The Dissertation Committee for Kwon Joong Son
certifies that this is the approved version of the following dissertation:

Impact Dynamics of Magnetorheological Fluid Saturated Kevlar and Magnetostrictive Composite Coated Kevlar

Committee:

Eric P. Fahrenthold, Supervisor

Michael D. Bryant

Mircea D. Driga

Mark F. Hamilton

Raul G. Longoria

Impact Dynamics of Magnetorheological Fluid Saturated Kevlar and Magnetostrictive Composite Coated Kevlar

by

Kwon Joong Son, B.S.; M.S.

DISSERTATION

Presented to the Faculty of the Graduate School of
The University of Texas at Austin
in Partial Fulfillment
of the Requirements
for the Degree of

DOCTOR OF PHILOSOPHY

THE UNIVERSITY OF TEXAS AT AUSTIN
May 2009

Dedicated to my Father.

Acknowledgments

First of all, I want to thank God for being You and for always being with me.

This dissertation is dedicated to all the people who have contributed to the production. I would like to thank my advisor Dr. Fahrenthold for his guidance, insight, patience, and most importantly, his thoughtfulness and understanding during my doctorial studies at the University of Texas at Austin. His unceasing enthusiasm for study and research has been academically challenging and enlightening me.

I would also like to thank my dissertation committee members: Dr. Michael D. Bryant, Dr. Mircea D. Driga, Dr. Mark F. Hamilton, and Dr. Raul G. Longoria for their advice and service.

I wish to thank the Office of Naval Research and NASA Johnson Space Center for their support for this research.

I am also thankful to the Texas Advanced Computing Center at the University of Texas at Austin and the Arctic Region Supercomputing Center at the University of Alaska at Fairbanks for high performance computing support.

I am pleased to thank Don Grosch, Explosives and Ballistics Range Manager, and the technical staff at Southwest Research Institute, for their work in the series of ballistic impact experiments.

This is a great opportunity to express my gratitude to all my friends who have been accompanying me to this moment from my days at Pohang University of Science and Technology (POSTECH), Carnegie Mellon University, and the University of Texas at Austin.

I thank my family in Christ at Austin Korean Presbyterian Church and Korean Central Church of Pittsburgh for their prayer, encouragement, perspective and love.

I wholeheartedly wish to thank to my parents Gye Sung Son and Hei Kyoung Kim, to my brother Kwon Ik Son, and to my sister Eun Jung Son, all of whom have unstintingly wholeheartedly and encouraged me in the name of the family regardless of my accomplishment or failure.

Finally, I wholeheartedly show my gratitude to my wife, Ji Hyun Park, who is my lifelong spouse and God's amazing gift to me, for supporting me with love and patience.

Kwon Joong Son

The University of Texas at Austin
May, 2009

Impact Dynamics of Magnetorheological Fluid Saturated Kevlar and Magnetostrictive Composite Coated Kevlar

Publication No. ____________________

Kwon Joong Son, Ph.D.
The University of Texas at Austin, 2009

Supervisor: Eric P. Fahrenthold

High strength, light weight and flexibility have made fabrics the preferred material for personal body armor and other impact protection applications such as passenger airbags, turbine blade containment systems, military and motorcycle helmets, and space debris shields. Recently, a shear thickening fluid has been used to treat a Kevlar fabric for an additional enhancement to the ballistic resistance of the neat fabric. Motivated by this technique of dissipation augmentation to high strength fabrics, this research aims at investigating the incorporation of other energy-dissipative materials into high strength fabrics. Specifically, two magnetic field-responsive materials (a magnetorheological fluid and Terfenol-D) have been used as a dissipation augmentation of Kevlar fabrics. No previous work has reported either experimental or computational research on the impact dynamics of Kevlar fabric treated with magnetorheological fluids or magnetostrictive solids. This research has investigated both computational modeling and experimental evaluation of the impact dynamics of textile composite armor, treated with magnetic field-responsive materials. Fragment simulating projectile impact tests have been conducted for the fabricated composite targets under an applied magnetic field. A computational model based on a hybrid particle-element method has been developed, to simulate the impact dynamics of composite fabric targets embodying magnetorheological fluids. This model is a mesoscale multiphysics model which can simulate impact dynamics including complex magneto-thermo-mechanical coupling effects as well as interactions among a projectile, fabric yarns, and magnetorheological fluid particles. Computer simulations have been performed to validate the hybrid particle-element method against experimental results. The computational method developed in this research has shown good agreement with the experimental data, in terms of the ballistic limit and residual velocity of a striking projectile. As fabric impact protection systems become more complex, and more expensive materials are introduced, computation may play a more important role in design. Therefore, the hybrid particle-element model in this dissertation may contribute to the improvement of the computational capability for virtual prototyping of fabric-interstitial fluid composites.

Table of Contents

List of Tables

List of Figures

Chapter 1

Introduction

1.1 Background

The main function of body armor is safety, to protect the life of the wearer from any possible ballistic threat in dangerous circumstances for military and police missions. Body armor systems can be classified into hard and soft body armor systems, based on the flexibility of armor materials. Hard armor systems are made from rigid materials with excellent mechanical strength such as metals or metal alloys (e.g. steel, Aluminum, Titanium, and their alloys), ceramic materials (e.g. Aluminum Oxide, Silicon Carbide, and Boron Carbide), and hard composite materials like glass-reinforced-plastic. On the other hand, soft body armor systems are manufactured from pliable materials (in most cases, high-strength woven fabrics and their composites). The principal requirements of soft body armor are high strength, lightweight, and flexibility. The strength of armor materials is the essential criterion for material selection in armor design, because stopping high-speed threatening objects depends on the mechanical strength of the armor materials. The light weight and flexibility of body armor can provide the wearer with better comfort and mobility, while performing police or military missions. However, the deformation of a body armor due to its flexibility should be limited, because excessive deformation of a soft body armor may contribute to blunt trauma caused by sudden deep strike on the human torso. Therefore, the control of the penetration depth of an impacting projectile is a very important design issue for a soft body armor. The advancement of soft body armor technology has been achieved by the development of bullet-proof fabrics having both high strength per unit mass and flexibility [116]. Examples of such high strength fabrics are aramid fabrics (e.g. Kevlar, Twaron, and Technora), ultra high molecular weight polyethylene fabrics (e.g. Spectra and Dyneema), fabrics made from thermoplastic liquid crystal polymers (e.g. Vectran), polybenzoxazole based fabrics (e.g. Zylon), polyamide based fabrics (e.g. Nylon), fabrics made from polypyridobisimidazole (e.g. M5), and fabrics from synthetic spider silk.

Advancement of soft body armor design has been accomplished by research on impact dynamics of fabrics and their composites under various impact conditions [26, 32]. The ballistic resistance of soft body armor has been evaluated based on the performance parameters such as the ballistic limit for a projectile [104, 119], the velocity profile of an impacted projectile (or simply the striking and exiting velocities [123]), and the penetration depth through a backing material simulating a human torso [72, 104]. Various types of constitutive relations for fabric materials have been developed, e.g. a linear (orthotropic) elastic model [37–39, 110], a visco-elastic model [65, 102, 119, 128], a statistical model [137, 138], a rate-dependent model [111, 118, 137], and a temperature-dependent model [138]. Fracture and damage mechanics have also been considered to model mechanical failure of fabric materials [119, 131]. In addition to material constitutive equations, frictional effects have been known to play an important role in ballistic resistance. Inter-yarn friction and the friction associated with yarn pull-out have been measured and evaluated under high-speed and quasi-static loading conditions [38, 39, 65, 100, 104, 146]. The structural configuration of woven fabrics has been investigated in terms of fabric weaving type [18], type of stitching [72], and other fabric specifications (e.g. the number of yarns per inch, number of fibers in a yarn, and yarn crimp) [65, 119, 128, 129]. The ballistic performance of multi-ply fabric systems has been studied for the systems by varying the number of fabric plies [32, 72, 130]. Boundary conditions have been considered as an important design parameter determining the performance of the fabric-based armor systems [37, 38, 145–147]. Finally, the effects of an impact threatening projectile have also been investigated in terms of the mass of the projectile, the shape of a projectile nose and, the impact velocity of a projectile [15, 26, 110]. These invaluable works have enabled more advanced and optimized soft body armor design. Due to the advancement of armor technology, recent soft body armor research has included multi-layered structures, composite structures, dissipation augmented structures, and intelligent structures with embedded smart structures for communication, energy harvesting, thermal protection, etc. [116].

Analytical, experimental, and computational approaches have coexisted in research and development of the soft armor systems, and these three principles of research have broadened the knowledge on impact dynamics of high strength fabrics.

In the first place, analytical research includes modeling kinetics and kinematics of fabrics impacted by a projectile, modeling geometry of a woven fabric, and modeling ballistic performance parameters like the ballistic limit and the penetration depth. Due to the complexity of textile impact physics, a problem simplification procedure is carried out for analytical methods in most cases. For example, if the transverse waveform associated with fabric deformation by a projectile and the wave propagation speed are assumed to be pre-determined, then the kinetic and strain energy absorbed in yarns and fabrics under a projectile impact can be analytically obtained [57]. In addition, with given information on the transverse wave propagation, the ballistic limit and the penetration depth can be analytically expressed in terms of surface density and Young's modulus [104]. A time-evolving tetrahedral deflection wave is generally chosen for a waveform generated in fabrics with plain weave. However, this perfectly tetrahedral waveform cannot explain the experimental observation of gradual distortion of the initial tetrahedral deflection due to yarn-yarn interaction, which finally causes bowing of the transverse deflection [26]. On the other hand, there exists an analytical way of treating impact problems with no pre-determined waveform. Phoenix and Porwal have derived equations of motion for a fabric impacted by a blunt projectile with a flat circular nose [109]. Modeling a fabric as a continuous membrane, Phoenix and Porwal were able to analytically predict the ballistic limit, the propagation of a fabric deflection wave, time history of the projectile velocity, and the strain field throughout the fabric [109]. Porwal and Phoenix have analytically solved the impact problem for a multi-layered fabric system, to study various system effects [110]. The continuum membrane model was chosen again to model each fabric layer, and an isotropic elastic model was used as a fabric constitutive equation. Porwal and Phoenix obtained the dynamic response of an impacted fabric considering system effects, such as the number of layers, a fabric separation distance, a failure strain of the fabric material, and contact area between a projectile and the fabric. However, this continuum membrane model, with an assumption of axisymmetric deformation about the linear path of a projectile, is not valid for the interlaced fabrics, which show a tetrahedral deflection with a symmetry about two orthogonal planes. An analytical approach has also been taken in developing fabric preprocessors to computationally represent the geometry of inter-woven fabrics. Various types of yarn structures (plain, basket, twill, etc) have been modeled by a computer-aided-design method [6]. For example, a yarn-level model for fabric geometry has been developed based on fabric data and the principle of minimum potential energy [82, 83, 115]. Other simple algebraic models for fabric impact dynamics have been analytically sought. For example, a model for the residual velocity and associated energy absorption capability for single yarn or single-ply fabric [57], a model for the residual velocity based on a constant penetration energy assumption [126], and a model for the ballistic limit and residual velocity based on regression of the experimental data [119] have been formulated. In spite of the reliability of an analytical method based on fundamental physics and mathematical induction, its practical use in solving fabric impact problems is generally limited to very simplified configurations.

Secondly, improvement of soft body armor design has primarily relied on ballistic experiments, because of the lack of reliable analytical and computational methods. To understand the influence of various design parameters on the ballistic performance of fabric systems, a large number of ballistic impact tests have been conducted. As a result, experimental data have increased the level of insight into impact dynamics of soft body armor. The experimental research in this area has included (1) impact tests for single-ply or multi-ply fabrics [32, 72, 123], (2) experiments to obtain mechanical models for material behavior, such as a strain-rate dependent strength model and a inter-yarn friction model [11, 28, 118, 137, 138] (3) experimental evaluation of system effects such as the aperture size of a target holder [32], the type of fabric stitching [72], and fabric clamping conditions [146].

Lastly, ballistic impact on woven fabrics is a challenging topic for computational methods, because fabric materials may have highly nonlinear characteristics (e.g., visco-plasticity, strain rate-dependency, anisotropy, temperature-dependency, etc) and structural complexity (e.g., woven structure, yarn crimping, inter- and intra-yarn structure, etc.) [28]. Representative numerical models in this area can be summarized as: (1) finite element models for fabrics based on two-dimensional membrane elements [65, 70, 73, 80, 99, 127], (2) three-dimensional finite element models for yarn-level computation [38, 39], (3) models based on pin-jointed bars or links [15, 102, 119, 128, 129, 146], (4) models based on discrete masses on a structured grid [20, 117, 151],

(5) a digital element model for fabric simulation at the yarn level [136] and fiber-level [94, 149], and finally (6) a meso-mechanical hybrid particle-element model for neat Kevlar fabrics and STF-Kevlar composites [111].

Analytical, experimental, and computational research have continuously sought significant improvements in body armor design. As advanced body armor systems incorporate novel armor structures such as resin-fabric composites [75], STF-fabric composites [139], and MRF-foam composites [36], computational methods become more important in the investigation of multi-scale and multi-physics effects. Therefore, reliable computational tools for virtual prototyping of advanced body armor designs need to be developed for future body armor systems.

1.2 Motivation

A variety of woven fabrics have been developed for use in ballistic protection applications, as stated in previous section. Although all these fabrics offer high strength and flexibility, Kevlar (one of the most widely used ballistic protection textiles) continues to play a central role in personal protection applications. Hence, there is a considerable interest in the development of Kevlar composites which might improve the ballistic performance of the standard (neat) fabric. The introduction of dissipative interstitial fluids (the bulk fabric has approximately fifty percent void space) has been proposed by the University of Delaware and the Army Research Laboratory [77, 78]. The dissipative fluid used was a shear thickening fluid (STF, composed of silica particles in polyethylene glycol). The STF-Kevlar composite has shown a significant improvement in ballistic performance in some test configurations. In a similar vein, MIT has suggested [87] the use of magnetorheological fluids in body armor, although their published research has studied only the energy dissipation characteristics of magnetorheological fluid-foam composites [36]. Magnetorheological (MR) fluids may offer opportunities to control both the stiffness and the dissipation properties of body armor. In this case the weight and power requirements associated with the application of a magnetic field to the MR fluid complicate considerably the body armor design problem.

In this dissertation, two specific magnetic field-responsive materials (magnetorheological fluids [25] and magnetostrictive materials [34]) are investigated, as a dissipation augmentation to neat Kevlar fabrics. Hereafter, "MRF-Kevlar" and "MSC-Kevlar" are used as abbreviations for MR fluid-treated Kevlar and magnetostrictive coated-Kevlar composites, respectively. Extensive experimental research has been performed to study the impact response of fabrics [31, 32, 111] but no previous work has reported experimental research on the impact performance on magnetomechanical Kevlar composites, either the MRF Kevlar or the MSC Kevlar, which are investigated in this dissertation. The most relevant previous experimental work has studied the basic properties of magnetorheological fluids [25] and magnetostrictive composites [34], the damping properties of Kevlar coated with a piezoceramic powder [98], and the development of electromagnetic hard armor [98, 125, 142]. Passive electromagnetic armor [148] renders conducting projectiles unstable, by applying a high voltage between parallel plates in order to flow current through the projectile during the penetration process. Active electromagnetic armor [125, 142] employs electromagnetic actuators to launch protective tiles against incoming projectiles. Other research has employed electric fields to distort shaped charge jets [140] and shape memory alloys to project circular rods against solid projectiles [71].

No applications of magnetomechanical soft armor have been reported. The most important practical use of MR fluids and magnetostrictive composites has been in controlled damping and actuator applications. MR fluids are used in controlled damping applications, such as automotive shock absorbers. Under an applied magnetic field they change (within few milliseconds) from a fluid to a semi-solid, due to chain-like alignment of iron particles (suspended in a carrier fluid) along the magnetic field direction. Magnetostrictive composites, which deform under an applied magnetic field, are used as actuators in audio and active machining applications [2]. Besides actuating or sensory applications, damping characteristics of magnetostrictive materials with giant magnetostriction (such as Terfenol-D [41]) have been investigated for use in energy dissipating applications [59, 92, 132, 141]. However, that work focused on the dissipation due to stress-strain hysteresis under cyclic loading conditions, not shock impact loading conditions.

No previous work has reported computational research on magnetomechanical Kevlar composites, for either the MRF Kevlar or the MSC Kevlar, which are the materials of focus in this dissertation. However, the body of computational work on fabric impact modeling is extensive [39, 80, 111, 128]. With one recent exception [111], previous work on fabric impact simulation has employed conventional finite element and particle methods. Conventional finite element methods employ element erosion algorithms, unsuitable for multi-layer fabric perforation problems since they discard failed elements. The most widely used finite element models of fabrics employ hex elements, which grossly overestimate yarn bending stiffness. Conventional particle methods suffer from numerical fracture and tensile instability problems, which severely hinder their use at the relatively low impact velocities of interest in body armor applications. Their use has been largely confined to hypervelocity impact problems [103]; even there the performance of particle methods has been problematic. In recent work Rabb [111] introduced, as an alternative to conventional finite element and particle methods, the use of hybrid particle-element methods [105, 120] in fabric modeling problems. This approach avoids the element erosion, tensile instability, and numerical fracture problems of conventional finite element and particle methods, and has been validated against experiment for multi-layer neat Kevlar impacts at velocities of interest in body armor applications.

1.3 Scope of the Research

This section presents the scope of the experimental and computational research on magnetomechanical Kevlar composites in this dissertation. The specific topics for this research are (1) design of magnetomechanically augmented Kevlar targets and the development of testing procedures for the fabricated Kevlar composites, (2) experimental data collection, in order to assess the ballistic performance of the augmented targets and to obtain FSP data to validate the developed computational model, (3) development of a numerical method suitable to describe the impact dynamics of augmented Kevlar composites, by extending the meso-mechanical hybrid particle-finite element method developed for neat- and STF-Kevlar fabrics, (4) modeling the kinematic and damping characteristics of magnetorheological fluids using Lagrangian particles , and (5) validation simulations.

1.3.1 Design of Targets, Testing Apparatuses, and Testing Procedures

The first research topic is to design magnetomechanical Kevlar targets, test fixtures, and testing procedures. This dissertation describes the design and fabrication of three types of magnetomechanical Kevlar composites, incorporating commercial magnetorheological fluids (MRF 140-CG from Lord Corporation) or magnetostrictive particles (Terfenol-D powder from Etrema, Inc.). Unlike impact tests on neat Kevlar fabrics, impact experiments for the magnetomechanical Kevlar composites require a special target fixture in order to apply a magnetic field to the mounted target. Impact tests should be conducted in a systematic way, based on well-organized experimental procedures.

1.3.2 FSP Impact Tests

The second task is to conduct FSP impact experiments, to measure ballistic performance data for the fabricated Kevlar composites. Impact tests were conducted not only to experimentally evaluate the ballistic performance of the fabrics treated with field-responsive materials, but also to provide experimental data for model validation simulations. In addition to impact tests on magnetized targets, non-magnetized baseline tests were also performed, to assess magnetic field effects on energy absorption in the magnetomechanical fabric composites.

1.3.3 Development of a Numerical Method

The third task was to develop a computational method for impact simulation of MRF-Kevlar composites. The computational model was developed by extending a meso-mechanical hybrid particle-element model for neat Kevlar and STF-Kevlar impact simulations. In this dissertation, a hybrid particle-element model was developed only for impact simulation on MRF-Kevlar composites, although not for MSC-Kevlar composites. Magnetorheological fluids were modeled as individual Lagrangian particles, occupying the void space in Kevlar woven fabrics. The model of interstitial particles included contact impact with neighboring particles and the shear yield stress due to magnetorheological effects, present in MR fluids under an applied magnetic field. Similar to the density calculation in Smoothed Particle Hydrodynamics (SPH) [97], a kernel-based interpolation scheme was used to calculate the mass density of the particles in a compressed state. Density and internal energy, together with an equation of state computationally determine the particle interactions via contact-impact.

1.3.4 Material Model Development

The fourth task was to develop a material model of magnetorheological fluids suitable for the hybrid particle-element modeling scheme. Thermodynamic model for MR fluids with and without PVC thin film wrapping were formulated, based on an equation of state for a mixture in equilibrium. This mixture theory, together with a Mie-Gruneisen equation of state for the constituents, can describe the thermodynamic state of MR fluids under shock compression. A magnetic field-dependent shear yield stress and a velocity dependent friction model were also developed. The nonlinear dependence of the shear yield stress on the applied field was modeled based on manufacturer's specifications for the MR fluid.

1.3.5 Validation Simulations

The last task was to conduct validation simulations against the experimental results for: (1) edge-clamped MRF-Kevlar impact tests, (2) neat Kevlar baseline tests, (3) magnetized MRF-Kevlar impact tests, and (4) non-magnetized MRF-Kevlar impact tests. These simulations require numerical treatment of the boundary conditions for the composite targets, the magnetic clamping on edge-treated MRF-Kevlar targets, and the characteristics of MRF-Kevlar composites enclosed by PVC film. Computer simulations were performed using a parallel hydrocode [42] based on the hybrid particle-element method. Simulation results were obtained at various impact velocities and compared with experimental results. Visualization of large-scale data was performed, and the post-processed graphics show the deformation of fabric composites, relative inter-particle motion due to solid-solid and/or solid-fluid interaction, fragmentation of the projectile and the fabric composites, target perforation, debris transport, and the distribution of thermodynamics states such as density, temperature, entropy, pressure etc.

1.4 Dissertation Organization

As stated in the previous section, the main tasks accomplished in this dissertation include: (1) design and fabrication of MRF-Kevlar and MSC-Kevlar composite targets, (2) conduct of FSP impact tests on the fabricated targets, (3) development of a numerical model for an armor system with a hybrid fluid-solid structure, and (4) validation simulations.

Chapter 2 describes experimental work on the edge-clamped MRF-Kevlar targets. A brief introduction to magnetorheological fluids and high strength fabrics is presented prior to describing the experimental work. A literature review on the yarn slippage effects is presented, to explain the motivation for testing the edge-clamped MRF-Kevlar composite. Once the schematic of the composite targets and the testing apparatus are described, the procedures for the MRF-Kevlar target fabrication and the testing apparatus are discussed in detail. This chapter describes also the impact testing procedures and provides experimental results in various forms, including residual velocity plots, an estimated ballistic limit, and images from a high speed camera.

Chapter 3 describes impact experiments on MRF-Kevlar composite targets placed inside an electromagnetic coil. While a neat Kevlar region is impacted by the projectile in an edge-clamped MRF-Kevlar test, an MRF treated Kevlar region is directly impacted by a projectile in this case. To investigate the effect of MR fluids on the ballistic protection capability of fabrics, a design for MRF-treated Kevlar composites and an associated testing apparatus are presented. A thick cylindrical coil was chosen to apply the magnetic field, since it has sufficient energized space for the MRF-Kevlar target and the target holder used in the impact experiments. In addition to impact tests on magnetized targets, two other series of impact tests were performed, as baseline tests: (1) MRF-Kevlar impact tests with no applied field and (2) neat Kevlar impact tests in the same target configuration. This chapter also describes testing procedures, and provides experimental data as well as an estimated ballistic limit.

Chapter 4 describes impact experiments on a Kevlar fabric composite coated with a polymer adhesive containing micron-sized magnetostrictive particles. The experimental setup is the same as the configuration in Chapter 3. Background information on magnetostriction and magnetostrictive materials is provided. Target fabrication procedures, for the mixture of Terfenol-D powders and polymer adhesive resins, are explained in detail. This chapter describes the impact experiments and provides impact test results.

Chapter 5 describes the development of a hybrid particle-element model for a fluid-solid composite, specifically woven Kevlar fabrics treated with MR fluids. This hybrid scheme is an extension to the work of Rabb [111] on a mesomechanical hybrid particle-element model for neat Kevlar and Kevlar treated with shear thickening fluids. Prior to the model development, a literature review is presented on conventional computational methods for modeling impact dynamics in woven fabrics. A detailed review of hybrid particle-element methods for impact simulations of multi-ply Kevlar fabrics is made in this chapter. To extend the hybrid method to MRF treated Kevlar fabrics, MR fluid particles are modeled as interstitial particles which occupy the void spaces in the Kevlar fabric. Equations of state for MR fluids consisting of iron particles in hydrocarbon oil are developed, based on the theory of mixtures. The composite structure of MR fluids wrapped in PVC heat shrink film is also modeled using a similar thermodynamic formulation. A field dependent shear yield stress model for MR fluids is developed to describe the interaction of MR fluid particles under a magnetic field. Validation simulations are performed for four cases: (1) magnetically edge-clamped MRF-Kevlar impact tests, (2) single-ply neat Kevlar impact tests, (3) magnetized MRF-Kevlar in a cylindrical coil, and (4) non-magnetized MRF-Kevlar impact tests. Simulation results are compared with the experimental results in each simulation configuration. Post-processing of the simulation data visualizes the numerical results obtained from the developed hybrid particle-element model.

Chapter 6 briefly summarizes the work of this dissertation and its contributions to body armor research . It also discusses future work on the impact dynamics of magnetomechanical Kevlar composites.

Chapter 2

Fragment Simulating Projectile Impact Tests on Magnetomechanically Edge-Clamped Magnetorheological Fluid-Kevlar Composites

2.1 Introduction

Personal body armor manufactured from high strength fabrics has in some cases been augmented with additional materials for improved ballistic performance (e.g., a multi-ply fabric structure and fabric-resin composites or laminates). Recently, University of Delaware and the Army Research Laboratory have developed a novel Kevlar composite treated with a Shear Thickening Fluid (STF). Ballistic impact test results have shown an improvement of ballistic performance in some test configurations [77, 78, 139]. Unlike Kevlar-epoxy laminates, STF-Kevlar composites maintain fabric flexibility due to the use of fluids which occupy the voids of the fabrics (approximately fifty percent in volume fraction for Kevlar of a plain weave type). If a small amount of void-filling fluid provides sufficient improvement in ballistic resistance of high strength fabrics, a fluid-treated fabric composite results in a smaller volume increment than adding another fabric layer. This dissertation investigates another type of fluid, called a magnetorheological fluid (MR fluids or MRF), which have shown a high dissipation capability in many engineering applications [23, 25, 36, 60, 122]. MR composites can mimic the flexibility advantage of STF-Kevlar composites since MR fluids behaves as a normal viscous fluid in the absence of a magnetic field [13, 14, 114].

Throughout this dissertation, two types of MRF-Kevlar composites have been studied. The first armor structure, presented in this chapter, is magnetomechanically edge-clamped MRF-Kevlar composites, designed to apply a shear yield stress at the clamped boundaries of Kevlar fabrics. Similar to the STF-Kevlar composite, the second armor system is the MRF-saturated Kevlar composite, which is directly impacted by a projectile. The edge-clamped MRF-Kevlar design utilizes a friction effect, the solidification of magnetorheological fluids under an external magnetic field. Friction effects have been known to influence the ballistic performance of high strength fabrics [145]. Fabric slipping at clamped edges has been observed during impact tests, when fabric targets are held by applying mechanical pressure on the fabric edges. Fabric slipping is primarily triggered by tension transmitted through the principal yarns (the yarns directly impacted by a projectile in contact [26]). In general, the boundary slipping effect is negligible for ballistic impact at high striking velocities, where the fabric perforation precedes the arrival of a fabric deflection wave at the clamped boundaries. On the other hand, at striking velocities low enough for the deflection wave front to hit the boundaries before the fabric perforation completes, boundary slipping affects the impact dynamics, by introducing dry friction between a fabric target and a target holder. Friction effects have been modeled in numerical codes, to more accurately simulate the impact dynamics of high-strength fabrics [37–39]. A novel clamping method has been suggested by Rabb to eliminate the significance of fabric slipping effects [111]. Rabb proposed the use of clinch buckle to achieve fixed boundary conditions on two edges and has experimentally verified the advantage of the buckle to completely clamp the fabric target on the target fixture. To avoid fabric slipping at the clamping boundaries, Rabb used a clinch buckle to firmly fix the fabric [111]. This no slip boundary condition is useful in developing a numerical model for high strength fabrics, because its numerical implementation is very straightforward. However, no ballistic system has been proposed that takes advantage of the frictional dissipation associated with fabric clamping. The magnetomechanical edge clamping methodology presented in this research employs the controllable shear yield stress (maximum up to 100 kPa) of commercial magnetorheological fluids [84].

The design, fabrication, and impact testing of edge-treated MRF-Kevlar composites are described in this chapter. The proposed design of the composites incorporates a field-responsive void-filling fluid to provide a supplementary mechanism for energy dissipation during fabric slipping. The associated clamping force is achieved by means of the shear resistance due to the solidification of MR fluids under the application of an external magnetic field. A fabrication procedure for MRF-Kevlar composites is introduced in detail. Fragment simulating projectile (FSP) impact tests have been performed to empirically evaluate the ballistic performance of magnetomechanically edge-clamped MRF-Kevlar composites, and also to investigate whether magnetic clamping by MR fluids can improve the ballistic protection of armor fabrics.

2.2 Materials

Three materials of interest in this chapter are fragment simulation projectiles, Kevlar fabrics, and magnetorheological fluids. This section presents characteristics and background information on each material.

2.2.1 Kevlar

Kevlar, the registered trademark of DuPont, is a synthetic aramid fiber invented in 1965. Kevlar is one of the most widely used high strength fabrics due to its high strength per unit weight. This remarkable mechanical characteristic can be explained by its molecular structure [88]. The strength of a synthetic fiber depends on the degree of parallel alignment of polymer chains, because the fracture of the polymer chain is caused by the breakage of carbon-carbon bonds in the polymer chains. Therefore, Kevlar needs to have tightly packed polymer chains oriented in parallel. Kevlar also has a radial strength enhancement, owing to the carbon-carbon interaction between neighboring chains. Due to this molecular structure, the Kevlar fiber is approximately five times stronger than steel wire, per unit mass. The main applications of Kevlar are high tension conveyer belts, ropes, cables [88], and protective ballistic fabrics (soft body armor) [116].

The Kevlar fabric used in this research is style 706 aramid fabric from Hexcel Corporation (Kevlar KM-2 fiber, 600 denier, 34 yarns/inch) [61, 111].

Denier is the unit for fineness of the yarn and measures the weight in grams of 9000 meters of yarn. This Kevlar fabric has 2.3 % yarn crimp. Yarn crimp is the unit used to measure the waviness in the yarn, and is determined by the ratio of the fully-stretched length of a yarn to the non-strentched length. The terminology “neat Kevlar” is used to distinguish Kevlar fabric treated with viscous fluids from the original fabric.

2.2.2 Magnetorheological Fluids

Magnetorheological fluid (MR fluid or MRF) was invented by Jacob Rabinow at the US National Bureau of Standards in the late 1940s [112]. In spite of its development in 1940s, MR fluid has only recently achieved commercial success in some engineering fields such as the automotive and exercise industries [69]. MR fluids are a mixture of the micron-sized magnetic particles, a non-magnetic viscous carrier fluid, and surfactants to prevent particle sedimentation. A schematic of dispersed iron particles in a suspension fluid is shown in Figure 2.1(a). The selection and composition of three constituents determine the magnetorheological properties of the blended fluids. This unique compositional characteristic makes MR fluids field-responsive smart fluids whose rheological properties can be controlled by an external magnetic field.

Rheological properties of MR fluids depend on the strength of an applied magnetic field, which causes structural evolution of the magnetic particles. With no applied magnetic field, MR fluids behave like Newtonian fluids whose viscous properties are similar to that of a base fluid [69]. However, application of a magnetic field results in the magnetic polarization of each iron particle. The polarization orientation is roughly parallel to the direction of the applied magnetic field. Consequently, mutual attraction and repulsion of magnetized dipolar particles is induced, due to the presence of the magnetic field, as depicted as in Figure 2.1(c). To attain the state of minimum potential energy, particles tend to align along the direction of the external magnetic field, so that they form a chain-like structure, as shown in Figure 2.1(b). The chains move apart from each other due to the repulsive force acting on two neighboring parallel dipoles (Figure 2.1(c)). As a result, they become dispersed over a magnetized domain. These columnar alignments of magnetic particles change MR fluids into semi-solids, bound together by dipole interactions.

Two important physical properties of MR fluids are the magnetization and the corresponding shear yield stress. The magnetization of MR fluids is determined by the structural evolution accompanying re-distribution of the magnetic particles, the volume fraction of the particles, the saturation magnetization of the magnetic particle, and the effects of surface adsorption of surfactant chemicals, which prevent the magnetization of the particle surface [114]. Because the relative permeability is about two times greater than that of paramagnetic materials, MR fluids are often referred to as a superparamagnetic materials [69]. Due to the field-induced solidification, MR fluids can withstand a shear traction and sustain a solidified state before yielding occurs. The maximum resistance can be characterized as the shear yield stress of magnetized MR fluids. Once the breakage of the chain structure starts taking place, due to external shear loading, the shear resistance of the MR fluids incorporates a viscosity as well as the shear yield stress. Among many constitutive models for MR fluids, a Bingham fluid model is one of the simplest and most widely used in describing the behavior of MR fluids [23, 60, 69, 122]. A field-dependent Bingham plastic model is used in the numerical model developed in this dissertation.

The specific MR fluid used in the fabrication of MRF-Kevlar composites is type MRF-140 CG manufactured by Lord Corporation [84]. It has 40% volume fraction iron particles in a hydrocarbon oil suspension. The maximum shear yield stress is about 60 kPa, in the case of saturation magnetization.

2.2.3 Projectile

The projectile used in the impact tests is a 0.22 caliber (0.56 cm) standard Fragment Simulating Projectile (FSP) MIL-P-36593A [96], whose schematic is shown in Figure 2.2. The projectile was made from 4340 steel and its weight is 1.1 grams.

2.3 Target Preparation and Experimental Procedure

Neat Kevlar fabrics (Hexcel Corporation Aramid Style 706 fabric) were cut into 22.86 cm by 5.08 cm strips. To draw guidelines for cutting, a marker with a soft tip was used to minimize any damage to fabric yarns. To increase the unmagnetized MR fluid viscosity, MR fluids were mixed with very small amount (1% in total mixture volume) of a vacuum grease (the silicon-free high-temperature grease model Aiezon H produced by M&I Materials Ltd. [93]). The prepared MR fluid mixture was applied to the clamped regions of Kevlar strips for the ballistic impact tests. The apparatus for target holding and magnetic clamping was designed by the University of Texas (UT) and fabricated by Southwest Research Institute (SwRI). The target holder is a mild steel plate (30.48 cm × 30.48 cm × 0.635 cm) with a rectangular aperture (10.16 cm × 6.35 cm) at the center. Ferromagnetic mild steel was chosen to minimize a magnetic reluctance in target holder, which was also used as a magnetic circuit for magnetic clamping on MRF-Kevlar composites. The front edges of the aperture were machined to prevent the Kevlar fabric from being damaged by sharp corners during the impact tests. Through holes, instead of threaded holes, were machined in order to avoid screw locking due to plastic deformation of the threads during the impact tests.

The FSP impact tests were conducted at the Small Arms Range of SwRI. In the first step, the magnet supports and air gap supports were assembled on the target holder. Next, one neat Kevlar layer (a vertical layer) was mounted on the target holder using clinch buckles. Then another layer of neat Kevlar (horizontal layer) was placed between the air gap supports on the target holder. The MR fluids prepared by UT were applied to one end of the Kevlar strip by brushing, then the MRF-treated strip was placed on the target holder. Before the other end of Kevlar strip was treated with MR fluids, an electromagnet (Model ESA-241 from Industrial Magnetics, Inc.) was placed, on brass metal shims, over the MRF-Kevlar target, to magnetically hold down the one edge. The other edge was then treated with MR fluids and magnetically clamped. A schematic of the edge-clamped MRF-Kevlar target assembly is shown in Figure 2.3. This assembled target was mounted on the target frame installed in the SwRI testing facility. A wood plate was clamped on top of the electromagnets to hold them in place during the impact tests (Figure 2.4). A laser pointer aligned with the Universal Gun was used to adjust the FSP striking point, to the center of the two crossed Kevlar strips. Each target was impacted by a 0.22 caliber FSP, at an impact velocity measured by two chronographs ahead of the target. Two high speed cameras were used, one to measure FSP residual velocities and one to record the target response. After each shot, the magnets were turned off and the impacted Kevlar strips were removed from the target holder.

2.4 Results of Impact Experiments

FSP impact tests on the edge-clamped MRF-Kevlar targets (Figure 2.4) were conducted to investigate the effectiveness of a fabric augmented with MR fluid as a ballistic protection system. In each test, the impact velocity of the FSP was measured by chronographs, and its residual velocity after target perforation was obtained, based on images captured by a high speed camera. Measured data for the FSP impact and residual velocities determine the projectile kinetic energy reduction that is the energy absorbed by a ballistic protection system. The ballistic performance of a ballistic protection system can be characterized by V_{50}. Statistically, V_{50} is defined as the velocity at which the probability of a striking projectile completely penetrating the target is 50%. The MRF-Kevlar targets in this chapter consist of two Kevlar layers (a vertical neat Kevlar strip and a horizontal MRF-Kevlar strip); the two layers are overlapped, to form a crossed configuration, where the overlapped region is impacted by a fragment simulating projectile (Figure 2.4).

Fifteen FSP impact tests were conducted for the magneomechanically edge-clamped MRF-Kevlar composites. The test results are sorted, in ascending order of impact velocity, in Table 2.1. The last column of the table describes the acceptability of the measured data based on closeness of the impact point to the center of the target. The data qualification scheme is illustrated in Figure 2.6(a). The measured velocity data is acceptable when a projectile hits the 2.54 cm × 2.54 cm region labeled as A. Experimental observations have shown that FSP impacts far away from the center of the target (i.e., target regions labeled B and C in Figure 2.6(a)) give rise to an underestimated energy absorption capability for the target. Off-centered FSP impact increases the residual velocity, as shown in Figure 2.6(b). This data screening process is used to increase the reliability of the experimental data.

Two Vision Research Phantom V7 monochrome cameras were used to capture an oblique rear view and a side view of the Kevlar fabric targets. Sequential images for an FSP test at an impact velocity of 426 m/s are shown in Figure 2.10. These pictures illustrate target perforation and yarn pull-out by a projectile, evolution of the fabric deflection (a pyramid-shaped deflection), slipping of the horizontal MRF-Kevlar strip, and the transport of MRF debris out of the clamped zone.

2.5 Analysis of Test Results

A constant energy absorption model is provides the expression of the relationship between the impact and residual velocities for a projectile striking armor material [33, 108, 147]. The basic assumption of this model is that the threshold energy for target penetration is constant, regardless of the geometric and kinematic features of a projectile (such as mass, shape, obliquity of impact, and velocity of impact). This model can represent the correlation between impact velocity and residual velocity of a projectile in the case of a small projectile impact onto a low thickness target. The constant ballistic limit model is also useful for estimating the overall ballistic performance using a single metric.

The measured impact and residual velocities of a projectile determine the kinetic energy reduction of the projectile. The absorbed kinetic energy (ΔE_p) is written as

$$\Delta E_p = E_i - E_r = \frac{1}{2} m_p V_i^2 - \frac{1}{2} m_p V_r^2 \tag{2.1}$$

where E_i is the initial kinetic energy of the projectile, E_r is the residual kinetic energy of the projectile, and m_p is the projectile mass.

For convenience, a dimensionless energy absorption $\Delta \bar{E}$ is defined here by normalizing ΔE_p with respect to the kinetic energy of the striking projectile such that

$$\Delta\bar{E} \equiv \frac{\Delta E_p}{E_i} = 1 - \left(\frac{V_r}{V_i}\right)^2 \tag{2.2}$$

In the case that $V_i < V_{50}$, $\Delta\bar{E} = 1$ because $V_r = 0$.

Assuming a constant ΔE_p for a target of interest, ΔE_p can be expressed in terms of the ballistic limit V_{50} as

$$\Delta E_p = \frac{1}{2} m_p V_{50}^2 = \text{const.} \tag{2.3}$$

Because, in this model, $V_r^2 = V_i^2 - V_{50}^2$ when $V_i \geq V_{50}$, $\Delta\bar{E}$ can be expressed in terms of the impact velocity and ballistic limit as

$$\Delta\bar{E} = \frac{V_i^2 - V_r^2}{V_i^2} = \left(\frac{V_{50}}{V_i}\right)^2 \tag{2.4}$$

In above equation, V_{50} can be estimated from the experimental data satisfying $V_i \geq V_{50}$.

$$V_{50} \approx \sqrt{\operatorname{Avg}\left(V_i^2 - V_r^2\right)} \tag{2.5}$$

Once V_{50} is specified from Equation (2.5), the projectile residual velocity can be expressed as a function of the impact velocity as

$$V_r = \sqrt{V_i^2 - V_{50}^2} \tag{2.6}$$

The estimated ballistic limit is 204 m/s for the ten acceptable experiments (listed in Table 2.1), according to the data screening strategy illustrated in Figure 2.6(a). The selected experimental data and its regression curve, obtained using Equation (2.6), are plotted on the same graph in Figure 2.7. A dimensionless energy absorption curve is shown in Figure 2.8. Figure 2.9 shows the experimental results for the impact tests on magnetomechanically edge-clamped MRF-Kevlar composites, versus single-ply and two-ply neat Kevlar FSP tests [111]. The ballistic performance of Kevlar fabrics with edge-treated MRF clamping is comparable to that of 2-ply neat Kevlar fabric, but not superior.

It should be noted that the above approximation made using a data set not uniformly distributed with respect to impact velocity. Hence the estimated V_{50} may be weighted toward the impact velocity with a higher data population. Hence, V_{50} approximation using an equally-spaced data set will be discussed in Chapter 5.

2.6 Summary

This chapter described impact experiments on MRF-Kevlar composites, where both target edges were clamped with electromagnets. The fundamentals of magnetorheological fluids were reviewed. Background information on high strength fabrics, especially Kevlar fabrics, was introduced. Target preparation and test procedures were described. A simple model to correlate V_r and V_i is used for the evaluation of the ballistic performance of the magnetomechanically edge-clamped MRF-Kevlar composites. A data screening method was applied to select acceptable test data to improve the precision of the experiments. This chapter provides impact test results, graphs of all test data, and images of the the experimental setup and impacted targets.

Table 2.1: Experimental results: FSP impacts on magnetomechanically edge-clamped MR Fluid-Kevlar composites (sorted in impact velocity ascending order)

Impact Velocity V_i (m/s)	Residual Velocity V_r (m/s)	Data Quality
122	0	A
199	38	A
199	0	A
216	122	B
243	163	B
252	167	A
257	136	A
260	183	B
277	212	B
291	256	B
300	219	A
335	261	A
360	298	A
426	371	A
435	395	A

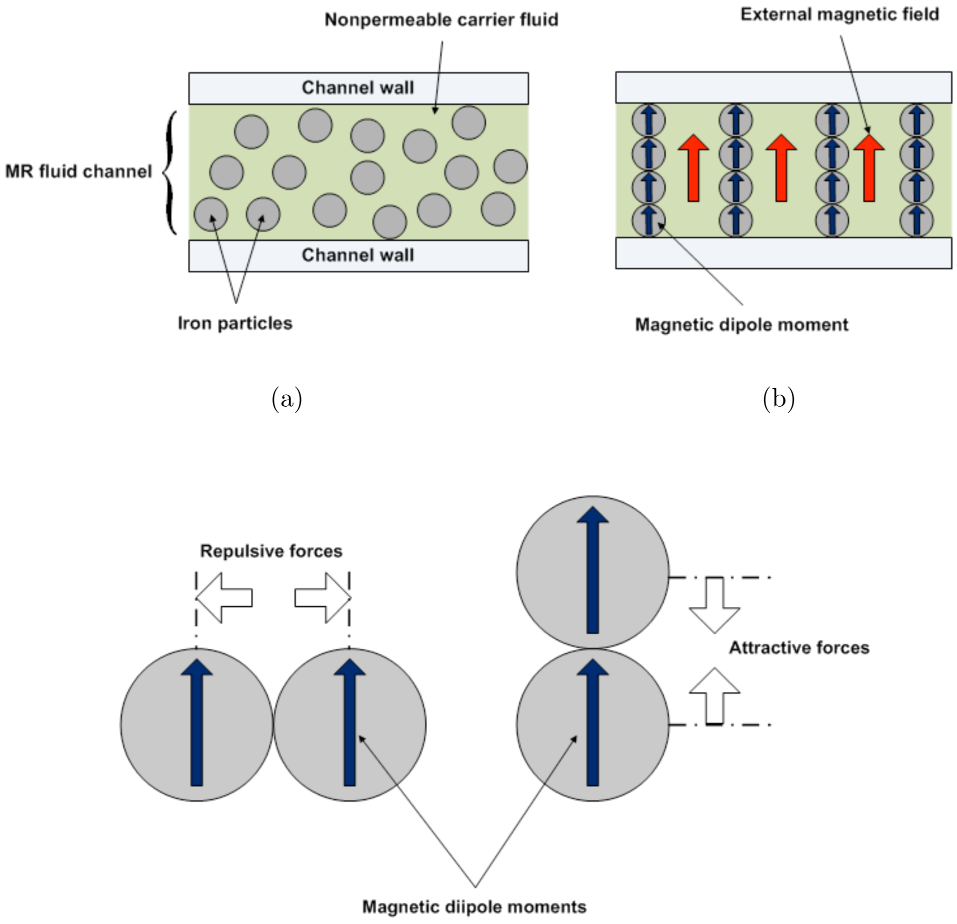

(a)

(b)

(c)

Figure 2.1: Microstructures of MR fluids (a) magnetic particles dispersed in nonmagnetic suspension (b) evolution of columnar structure under the application of an external magnetic field (c) interaction between two magnetic dipole moments in parallel depending on their relative positions in two cases

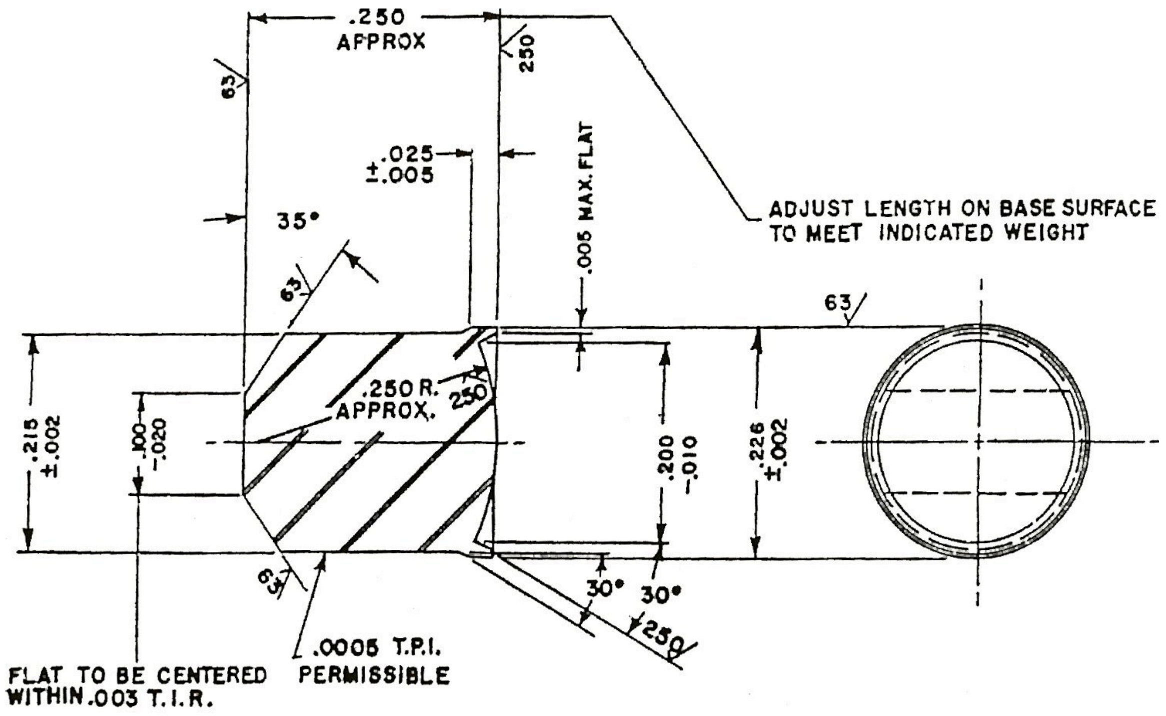

Figure 2.2: Fragment simulating projectile [96]

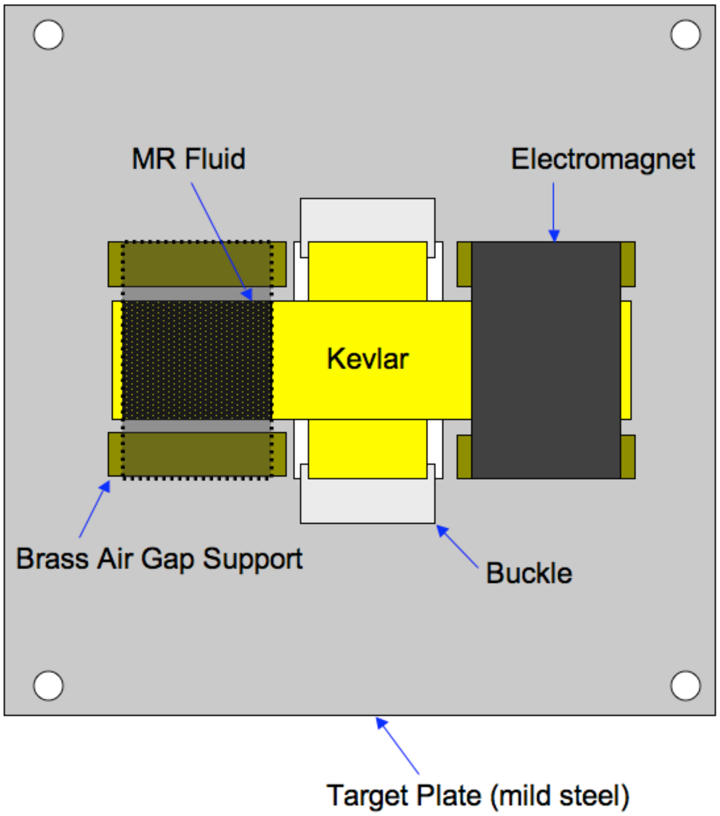

Figure 2.3: Schematic of target frame assembly

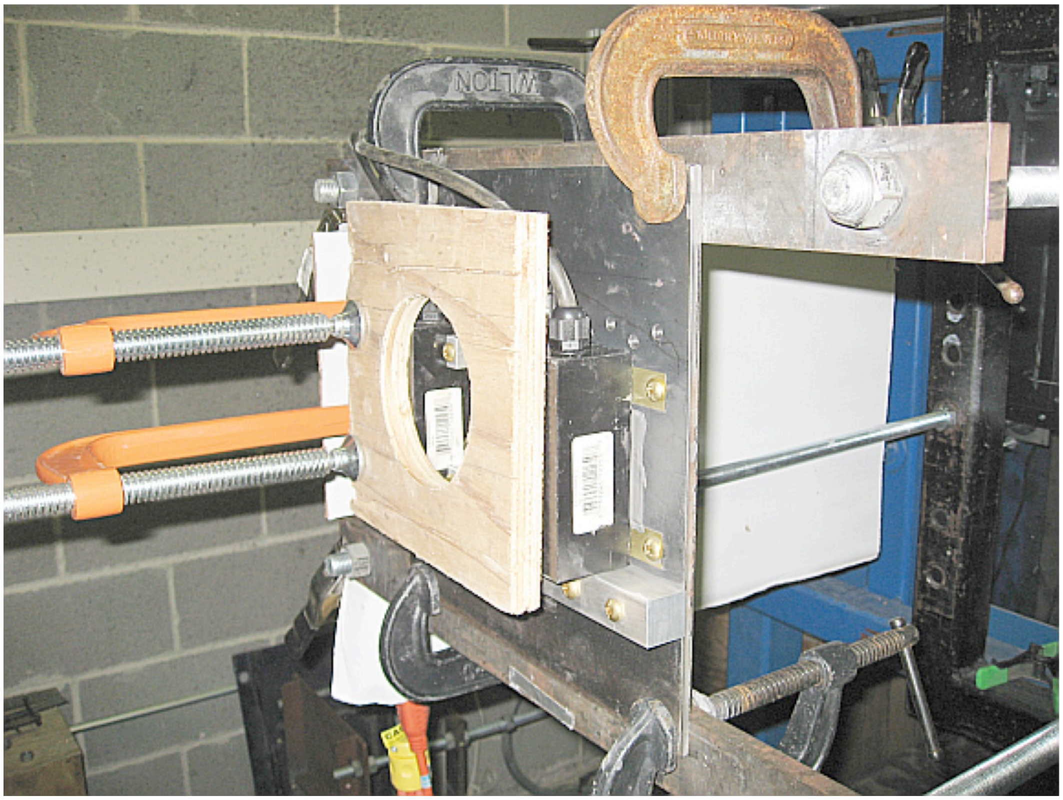

Figure 2.4: Target frame mounted on the target fixture

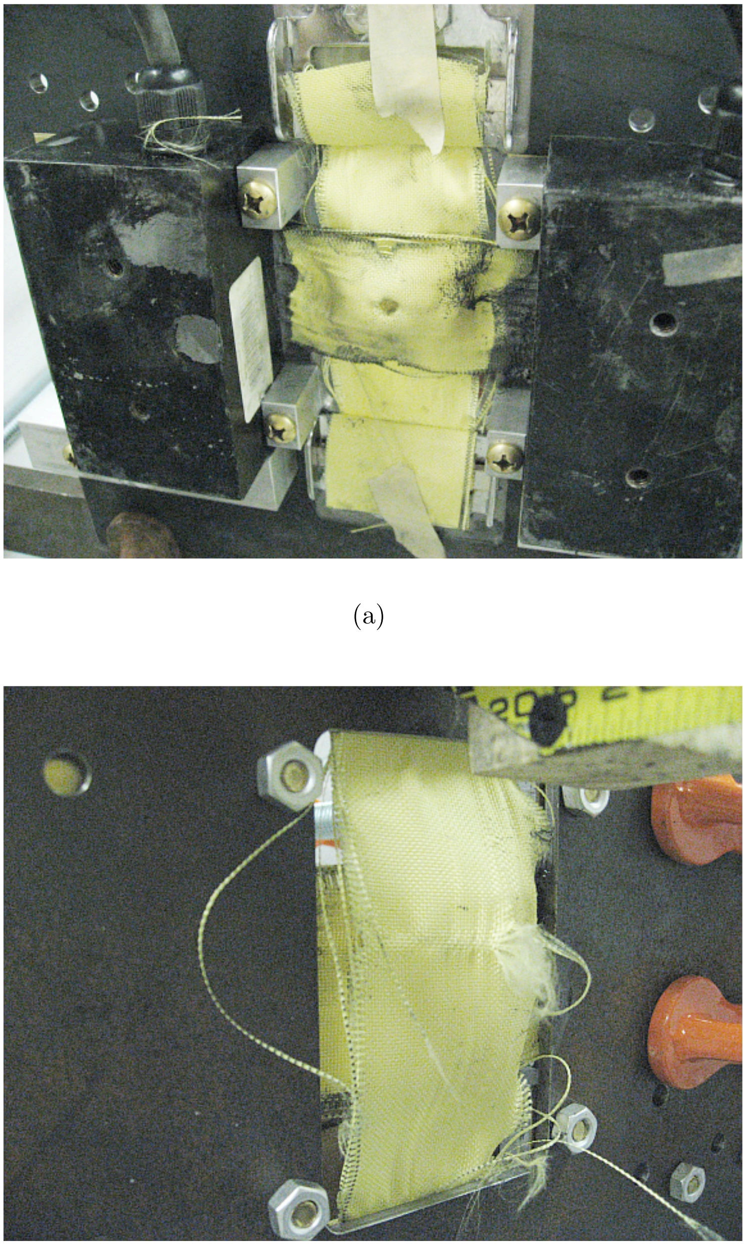

(a)

(b)

Figure 2.5: Impact damaged MRF Kevlar and neat Kevlar composite layers on the target frame (a) front view (b) back view

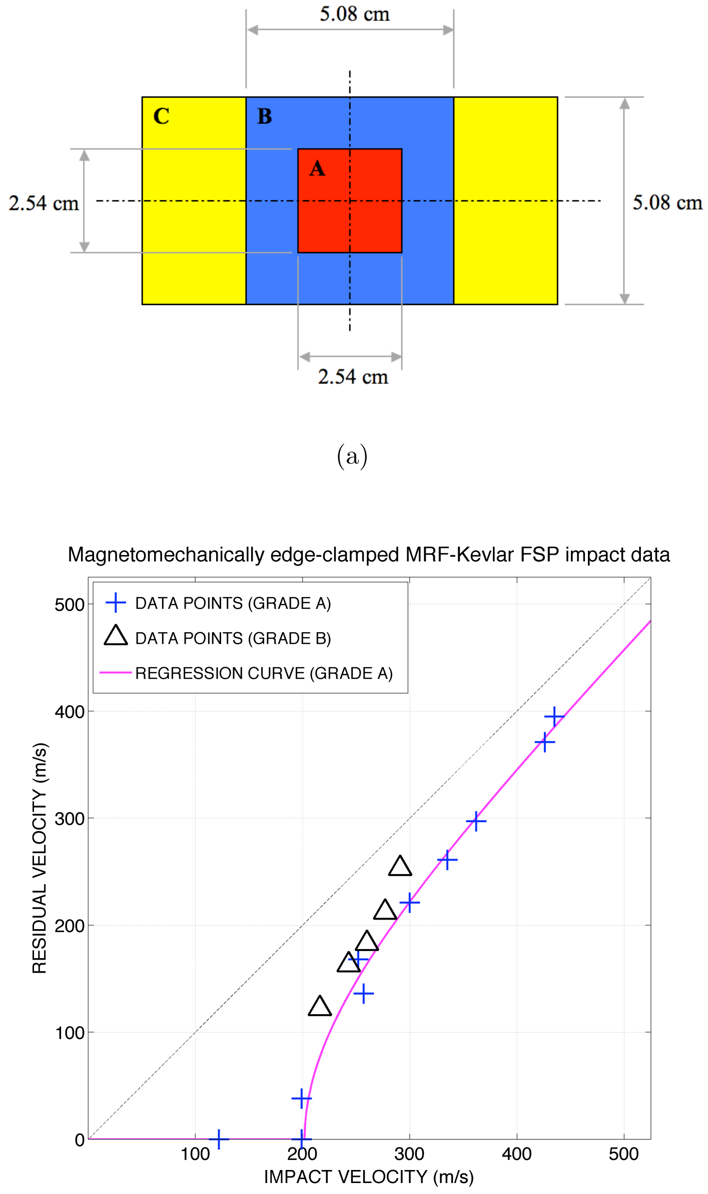

(a)

(b)

Figure 2.6: Data qualification strategy: (a) schematic of data screening (b) accepted and discarded experimental data in V_i-V_r curve

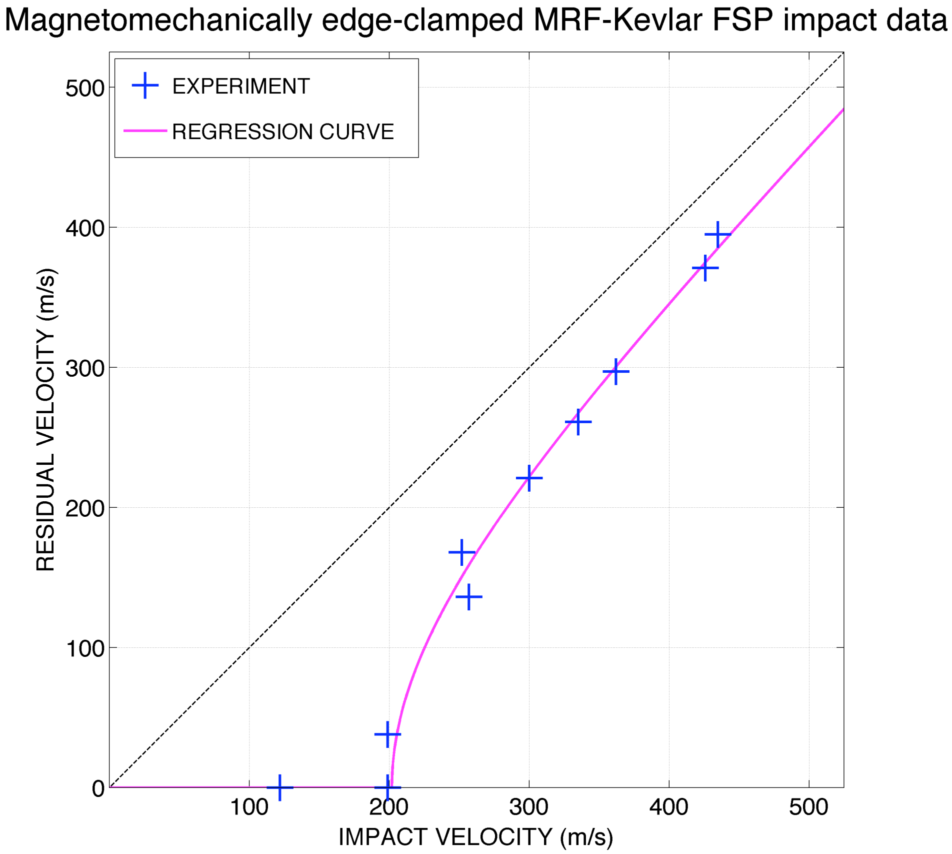

Figure 2.7: Experimental results: FSP impacts on magnetomechanically edge-clamped MR Fluid-Kevlar composites

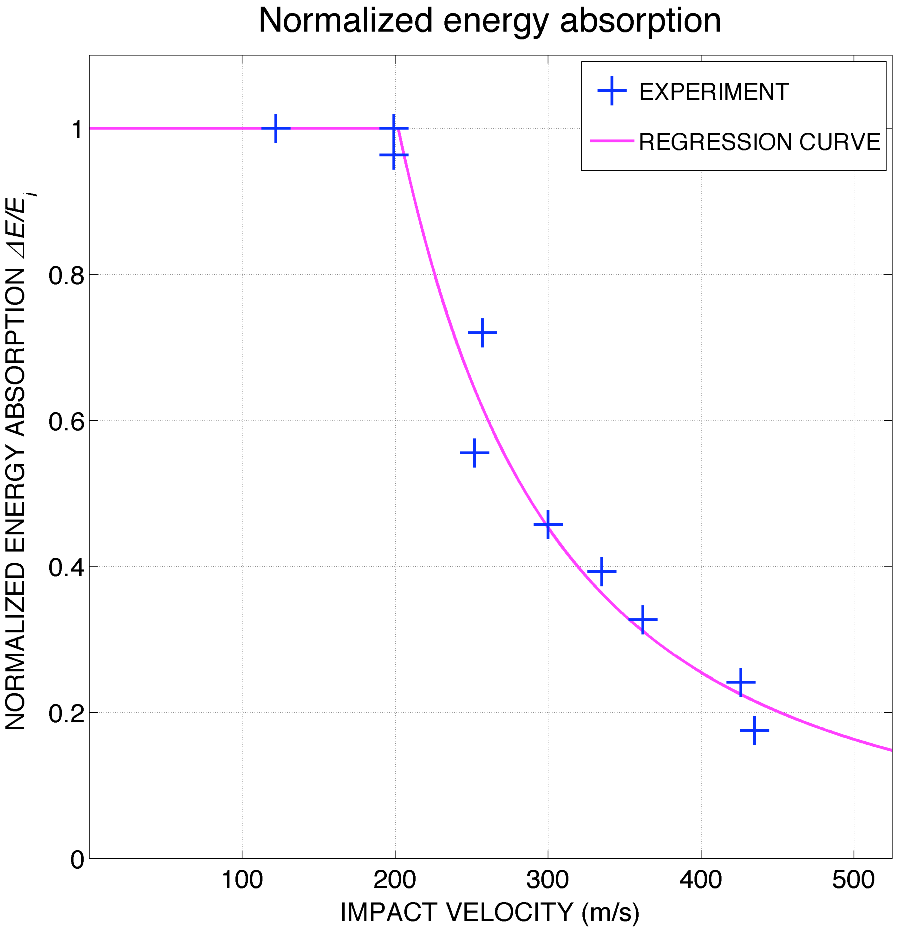

Figure 2.8: Experimental results: normalized absorbed energy for magnetomechanically edge-clamped MR Fluid-Kevlar composites with respect to the kinetic energy of a striking projectile

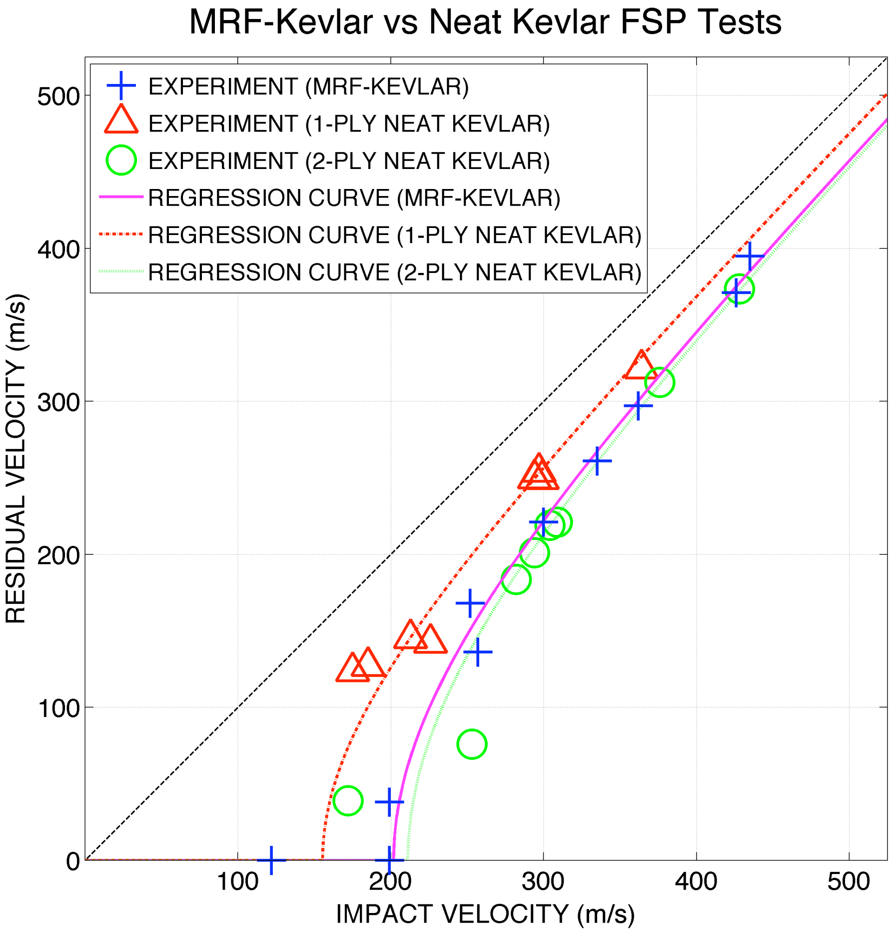

Figure 2.9: Experimental results: magnetomechanically edge-clamped MRF-Kevlar composite versus 1- and 2-ply neat Kevlar FSP tests

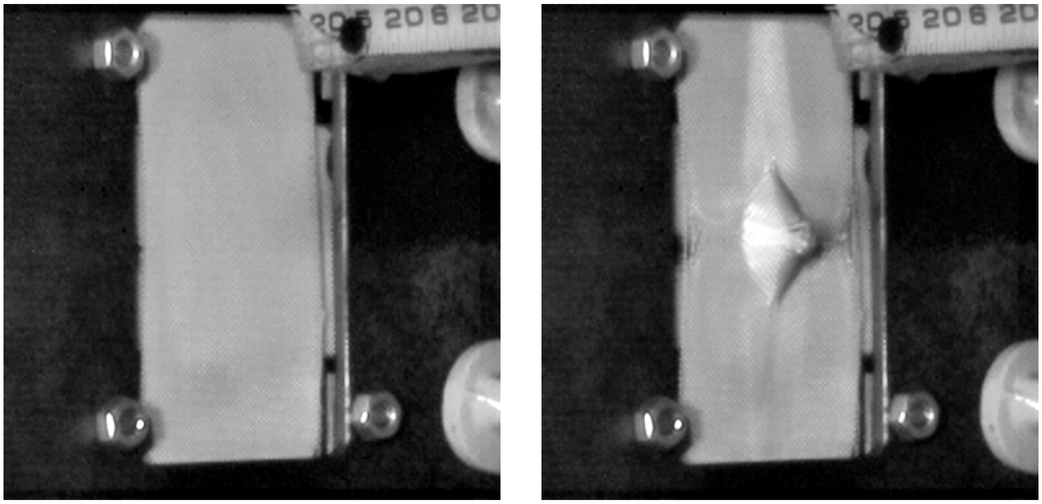

(a) $t = 0$ μsec

(b) $t = 50$ μsec

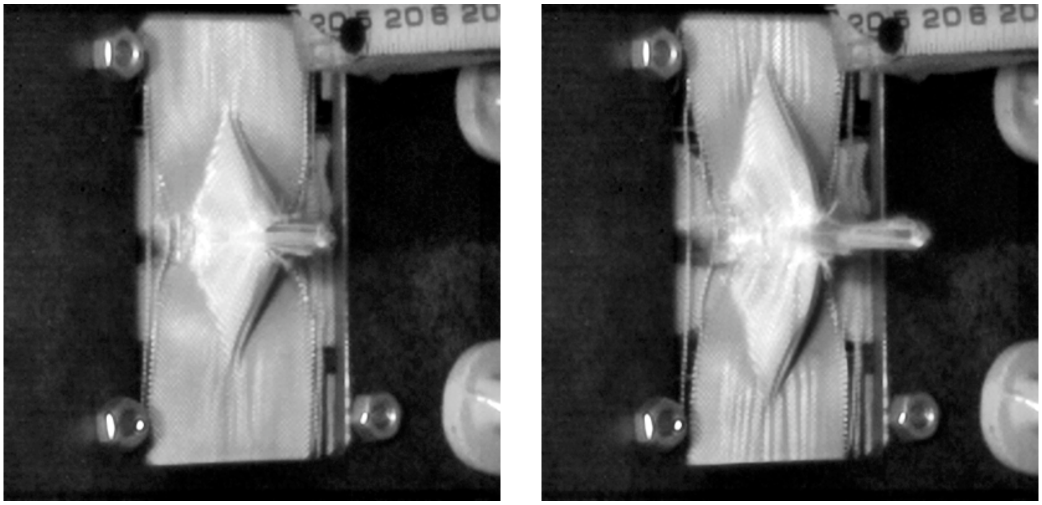

(c) $t = 100$ μsec

(d) $t = 150$ μsec

Figure 2.10: FSP impact experiment at 426 m/s on magnetomechanically edge-clamped MRF-Kevlar composite at 0 - 150 μsec

Chapter 3

Fragment Simulating Projectile Impact Tests on Magnetorheological Fluid Saturated Kevlar Composites

3.1 Introduction

Recent research on dissipative augmentation of high strength fabrics has been performed to develop an advanced body armor system to fulfill both strength and flexibility requirements. To improve the ballistic performance of textile armor systems, Kevlar fabric composites saturated with shear thickening fluids (STF) have been invented by the University of Delaware and the Army Research Laboratory [77, 78, 139]. The shear thickening fluids used for dissipation augmentation consist of silica nano-particles in a colloidal polyethylene glycol (PEG) suspension. Under a sudden increase in shear strain rate, the fluid behaves like a gel; it then quickly returns to its original structure upon removal of the shear strain rate [139]. Although the mechanism of STF-Kevlar impact performance is not fully understood [139], STF-Kevlar composites have shown higher energy absorption capability in certain testing configurations [77, 78, 130, 139]. Wetzel has shown that this improvement can be achieved when the impact velocity is low and the target size is small [139]. Magnetorheological fluids (MR fluids or MRF) may be used as an alternative dissipation mechanism since magnetized MR fluids can resist shear deformation. This shear resistance can hinder slip between fabric yarns under impact loading. Inspired by published research on the energy dissipative MRF-foam composite [36], researchers at Massachusetts Institute of Technology have proposed treating a high-strength fabric with magnetorheological fluids [87]. However, no experimental results on MRF-Kevlar composites have been published. An armor system with a hybrid solid-liquid structure is sometimes called liquid armor [133]; the MRF-based armor system is referred to as instant armor [87]. The key design issues on liquid armor include (1) the development of novel liquid materials with high energy absorption capability under ballistic impact, (2) the improvement of liquid armor durability, and (3) the development of lightweight structures to contain the fluid. Previously proposed conceptual design of an MRF-based liquid armor system has suggested field responsive MR fluids as the main protective part of the liquid armor structure and Kevlar fabric as containment for the MR fluids [87, 133]. However, besides difficulties in providing the source of a magnetic field, and in developing containment for MR fluids, the MRF-Kevlar armor system has another limitation. It is the problem of weight, since the density of commercial magnetorheological fluids is about three times greater than that of Kevlar fiber (in case of MRF with a 40% volume fraction of iron particles). Therefore, the effectiveness of this armor design must be compared with multi-ply neat fabrics, on a mass basis.

To avoid massive use of MR fluids in MRF-Kevlar armor fabrication, this dissertation proposes an MRF-Kevlar design similar to the STF-Kevlar composites in which fabric void space is filled with a viscous fluid. In this case, frictional effects associated with relative yarn slipping can be enhanced by the increased shear yield stress of MR fluids under an externally applied magnetic field. Shear thickening effects are due to cluster formation of silica particles in STF. However, in general, no shear thickening effects have been observed for MR fluids, even though the shear stress is dramatically increased under the application of a magnetic field. Moreover, unlike the STF-Kevlar composites, shear resistance can be controlled by adjusting the magnetic field strength in MRF-Kevlar composites.

This chapter presents an experimental evaluation of the ballistic performance of MRF treated Kevlar composites. The target preparation procedure is described, and the impact testing procedure is presented. Experimental data will also be used in computational research on the impact dynamics of MRF-Kevlar composites, described in Chapter 5. To provide baseline data, two additional sets of impact tests were conducted: (1) FSP impact tests on MRF-Kevlar composites with no applied magnetic field, and (2) FSP impact tests on neat Kevlar fabrics mounted on the same target holder.

3.2 Materials

3.2.1 Kevlar

Experimental research in this chapter investigates the ballistic performance of MRF-impregnated Kevlar fabrics. Among various available high strength fabrics, Kevlar was selected because it is the most widely used ballistic fabric. The specific Kevlar used in the fabrication of MRF-Kevlar composites was style 706 fabric from Hexcel Corporation [61]. The style 706 fabric has a plain weave, with both warp and fill yarns consisting of identical 600 denier KM-2 yarns. The yarn count for this fabric is 34 yarns per inch, and yarn crimp is 2.3%.

3.2.2 Magnetorheological Fluids

Magnetorheological fluids (MR fluids or MRF) are smart fluids whose rheological properties (e.g. the shear yield stress and the shear viscosity) are dependent on an externally applied magnetic field. This field-responsive behavior is due to the unique chemical composition of MR fluids. Typical magnetorheological fluids are a suspension of iron particles in a viscous carrier such as hydrocarbon oil, silicon oil, or water. The application of a magnetic field through MR fluids produces multiple dispersed columns of iron particles, aligned along the field direction (Figure 2.1(b)). The chain-like structures inside the MR fluid cause solidification of the MR fluid, and thus increase its shear resistance. The MR fluid used in this research is type MRF-140 CG from Lord corporation [84]. MRF-140 CG contains 40 % volume fraction of micron-sized iron particles. It has a maximum yield stress of approximately 60 kPa, at the saturated magnetization.

3.2.3 FSP

The type of projectile used in the ballistic impact experiments is the same as that used in Chapter 2. It is a fragment simulating projectile (FSP) MIL-P-46593A (Figure 2.2), which has a diameter of .22 caliber and mass of 1.1 g. However, all of the projectiles used in the impact tests in this chapter are made from nonmagnetic half hard brass, to avoid any unwanted interaction with magnetic fields.

3.2.4 PVC Shrink Tubing

Uline PVC shrink tubing model S-11801 from Uline Shipping Supplies was used to envelop the MRF treated region of the Kevlar. The tubing is 5.08 cm wide and has a density of 1.35 g/cc. The tensile strength is 52 MPa and the failure strain is approximately 300%.

3.3 Target Preparation and Experimental Procedure

The experimental tasks discussed in this section focus on the evaluation of the ballistic performance of MRF-Kevlar composite targets. The difference between this work and the edge-clamped MRF-Kevlar composites studied in Chapter 2 is that in this case the projectile directly impacts the MRF-treated fabric area. While Chapter 2 investigates MRF effects on fabric slippage at the clamped edges, this chapter evaluates MRF effects on the frictional forces between inter-woven yarns. Consequently, a magnetic field is applied to the impact region of the MRF-treated Kevlar fabric. This experimental configuration is difficult to achieve using a magnetic circuit like that used in Chapter 2, where the MRF-treated fabric is laying in the air gap between a magnet and a ferromagnetic substrate. To apply a magnetic field without blocking the passage of a projectile, a cylindrical coil was chosen as a source of the magnetic field for the MRF-Kevlar target tests. The target was placed inside the coil, as shown in Figure 3.1. The target holder must be compact enough to fit inside the coil. Because the target holder used in the magnetically edge-clamped MRF-Kevlar impact tests occupies too much space, a compact windowed frame was designed for targets placed in the coil. The target holder is supported by two parallel extensions which were connected to the target frame at the SwRI Small Arms Range. Clinch buckles were outer on both extensions, to hold the MRF-Kevlar composite, as shown in Figure 3.2.

A neat Kevlar fabric was cut into 5.08 cm-wide strips long enough to be mounted on the target holder. MR fluids were applied to a 5.08 cm × 5.08 cm region on the neat Kevlar strips. A total of 0.75 cc-MR fluid, ejected by a syringe, was used completely fill the voids of a 5.08 cm × 5.08 cm region of neat Kevlar fabric. In Chapter 2, the target plate and electromagnets naturally confined the MR fluids within the air gap. On the other hand, the MRF-Kevlar composites in this chapter require separate confinement. PVC shrink tubing was used to wrap the MRF-treated Kevlar region, to prevent MR fluids from escaping during both fabrication and testing. In order to investigate the ballistic performance of MR fluid impregnated Kevlar, the strength enhancement due to the wrapping material should be minimized. PVC film was chosen as an MRF-Kevlar wrapping material because of its low strength and high elongation, as compared to Kevlar.

The target holder was designed by the University of Texas (UT) and modified by Southwest Research Institute (SwRI) to attach it to the target frame in the SwRI Small Arms Range. The target holder, fabricated by SwRI, is shown in Figure 3.3. It was made from non-ferromagnetic aluminum which does not distort the magnetic field generated by the electromagnetic coil. The target holder has a 6.35 cm × 6.35 cm window, which allows for a target size of 5.08 cm × 6.35 cm for the MRF-Kevlar strip. This target configuration has two fixed and two free boundary conditions, as shown in Figure 3.4. There were four holes made through two extended target supports, shown in Figure 3.3, made by SwRI to align the coil. Hence the MRF-Kevlar target is placed at the center of the coil for each test, and is always normal to the path of a projectile.

The magnetic field source was an electromagnetic coil, Model 3473-70 manufactured by GMW Associates, Inc. Its specifications are listed in Table 3.1. The coil was supported by a sling connected to an overhead trolley crane, so that the vertical and horizontal position of the coil can be adjusted (Figure 3.4 (a)). The projectiles impacted the target with zero degree obliquity, as calibrated by a laser with a mirror placed on the flat surface of the coil. The magnetic field at the center of the cylindrical coil was measured by Gauss/Tesla meter model HHG-22 from Omega Engineering, Inc. before the impact tests. The field was measure to be 0.138 T for a constant current of 70 A (or equivalently 110 kA/m in the air).

The power supply for the coil was a Sorensen DLM32-95E 3kW DC power supply from Elgar Electronics Corporation. Per the coil specifications, the power supply was operated in constant current mode at a 70 A current. The coil incorporates thermal switches for emergency shutdown. The switches are on/off controlled with a sensor feedback signal connected to the power supply.

To prevent the coil from overheating, an adequate water cooling system must be provided to cool the coil under operation. The cooling system, attached to the cooling tubing of the coils, consists of flexible tubes, flow switches, a flowmeter, pressure gauges, and a water filter.

The powder gun used for the ballistic impact experiments was .22 caliber Universal Gun. The striking speed of the FSP was measured by a chronograph located between the gun muzzle and the target. A laser pointer was used to position the impact point on the target.

In a chronograph, the output signals from two sensing widows, with a specific spacing are triggered by the FSP passing through the windows. The time difference between the sequential triggerings provides the striking velocity of the projectile. Two high-speed monochrome video cameras (Vision Research Phantom V7) were used for the measurement of the residual velocity of the FSP and to observe the target deformation and perforation.

To evaluate the ballistic protection capability of the magnetized MRF-Kevlar composites, two sets of baseline tests were performed: (1) FSP impact tests on non-magnetized MRF-Kevlar composites, and (2) FSP impact tests on neat Kevlar fabrics mounted on the same target fixture.

Except for use of the magnetic coil and its supplementary subsystems (e.g. a power supply and a water cooling system), the baseline tests were performed using the same experimental procedures as the FSP impacts tests on magnetized MRF-Kevlar targets. In the interest of brevity, this section presents only the experimental procedures for the FSP impact tests on magnetized MRF-Kevlar composites. First, the target holder (Figure 3.3) was connected to the target fixture in the SwRI testing facility. The electromagnetic coil was then hooked up to a high-strength strap, and the coil was lifted into position by a trolley crane. The coil, hung by the strap, is shown in Figure 3.4. To connect the coil with the water cooling system and the power supply, the water cooling tubes, the power supply cables, the sensory feedback signal lines, and the grounding wire were then connected to the coil. Once an MRF-Kevlar target was mounted on the target holder (Figure3.4 (c)), the position and orientation of the coil were adjusted so that the target is correctly aligned. Two foam blocks were used to maintain the position of the hanging coil during the testing, as shown in Figure 3.4 (a) and (b). Next the circulation of the cooling water was started, then the power supply was turned on and set to a constant current mode. The constant current power supply generates a steady magnetic field around the target during the impact tests. Finally, the FSP impact test was performed, and the impact and residual velocities were measured by the chronograph and the high speed camera, respectively. After each shot, the coil was turned off, and the test procedure was repeated for the next shot.

3.4 Results of Impact Experiments

Three sets of impact tests have were conducted to study the impact dynamics of MRF-Kevlar composites: (1) FSP impact tests on magnetized MRF-Kevlar FSP composites, (2) FSP impact tests on non-magnetized MRF-Kevlar composites, and (3) FSP impact tests on neat Kevlar fabric. A total of thirty-nine MRF-Kevlar targets were tested at the SwRI Small Arms Range. Thirteen data points were discarded, based on the data screening scheme illustrated in Figure 2.6 (a). The remaining twenty-six V_i-V_r data points are listed in Table 3.2 and plotted in Figure 3.5. The associated energy absorption curve, from Equation (2.2), is displayed in Figure 3.6. The V_{50} estimated using Equation (2.5) is 150 m/s for the magnetized MRF-Kevlar composite targets. The corresponding data regression curve is shown in Figure 3.5. Figure 3.4 (c) and (d) show pictures of an intact MRF-Kevlar target mounted on the target holder and a post-impact image. Yarn pull-out and damage of the PVC film during the fabric perforation are observed in Figure 3.4(d). Figure 3.7 shows sequential images of an FSP impact test at 262 m/s. The yarns and fibers pulled out by the projectile, the transport of PVC debris, and fractured Kevlar fibers, and the released MR fluid particles can be observed in these figures.

A total of thirty FSP impact tests on non-magnetized MRF-Kevlar were performed to investigate the effect of a magnetic field on the energy absorption capability of MRF-Kevlar composite. Six data points were discarded, based on the data screening methodology used here (Figure 2.6 (a)) and the remaining twenty-four data points were accepted. The accepted data for these FSP impact tests are listed in Table 3.3 and plotted in Figure 3.8. The corresponding energy absorption curve for the non-magnetized MRF-Kevlar composites is shown in Figure 3.9. From the experimental data, V_{50} can be obtained using Equation (2.5). The calculated V_{50} is 146 m/s for the non-magnetized MRF-Kevlar composite targets. The V_i-V_r regression curve for non-magnetized targets and the dimensionless energy absorption are shown in Figure 3.8 and in Figure 3.9, respectively. The experimental results comparing the magnetized and non-magnetized MRF-Kevlar targets are compared in Figure 3.13. The magnetic field (with the flux density 0.138 T at the center of the coil) seems to provide no improvement in ballistic energy absorption for the MRF-impregnated Kevlar fabric.

A second set of baseline tests was conducted for neat Kevlar fabrics (not treated with any other material) mounted on the same target holder as shown in Figure 3.10(a). These neat Kevlar targets have the same boundary conditions as the MRF-Kevlar composites. A total of twenty-four neat Kevlar strips were tested, using .22 caliber fragment simulating projectiles, at various striking velocities. Nine data points were discarded based on the data screening scheme depicted in Figure 2.6 (a). The remaining fifteen data points are listed in Table 3.4. This data is plotted in Figure 3.11, and the associated energy absorption curve is shown in Figure 3.12. The V_{50} for these targets was obtained from Equation (2.5). The calculated V_{50} was 159 m/s for the single-ply neat Kevlar targets this baseline tests. This estimated V_{50} defines the regression curves for the residual velocity V_r and for the dimensionless energy absorption $\Delta\bar{E}$ as a function of V_i. These regression curves are shown, together with the experimental data, in Figures 3.11 and 3.12. Figure 3.10 shows pictures of: (a) an intact Kevlar strip mounted on the target holder and (b) a post-impact image. The results of these baseline tests show that MR fluid treatment of Kevlar fabric is not likely to improve energy absorption in a Kevlar fabric armor system (Figure 3.14).

3.5 Summary

This chapter presents results of FSP impact experiments on MRF-Kevlar composite targets. A target preparation procedure is described, for fabrication of an MRF-saturated Kevlar strip with PVC film wrapping. The target configuration and the test fixture were also described. The test procedure were described in detail. Test results are provided, in form of data tables, residual velocity graphs, estimated values for V_{50}, and high speed camera frames.

Table 3.1: Specifications of the electromagnetic coil model 3473-70 manufactured by GMW Associates

Property	Unit	Value
Number of coil turns	turns	460
Maximum field	T	0.14
Maximum DC power input	kW	2.07
Maximum DC current	A	70
Inductance	mH	60
Resistance	Ω	0.36-0.40
Flow rate for cooling water	l/min	6
Inner diameter	mm	177.8
Outer diameter	mm	390.5
Thickness	mm	130
Mass	kg	76

Table 3.2: Experimental results: FSP impacts on MRF-Kevlar with an applied magnetic field (H_0=111 kA/m) in the coil

Impact Velocity V_i (m/s)	Residual Velocity V_r (m/s)
113	0
124	8
134	0
147	0
169	89
173	92
174	67
176	124
183	116
222	111
236	172
254	183
262	214
277	248
301	271
301	272
352	319
354	327
356	318
362	333
376	349
384	354
390	357
451	427
466	430
472	443

Table 3.3: Experimental results: FSP impacts on MRF-Kevlar with no magnetic field

Impact Velocity V_i (m/s)	Residual Velocity V_r (m/s)
114	0
159	91
162	86
167	119
187	139
193	133
205	146
248	198
256	202
266	227
269	225
298	270
328	295
331	299
333	302
334	308
391	367
395	367
401	370
413	378
428	401
443	415
466	428
467	433

Table 3.4: Experimental results: FSP impacts on a neat Kevlar strip

Impact Velocity V_i (m/s)	Residual Velocity V_r (m/s)
161	38
176	97
177	128
208	127
257	193
295	255
299	256
352	298
369	333
391	356
403	366
415	385
437	407
453	426
470	440

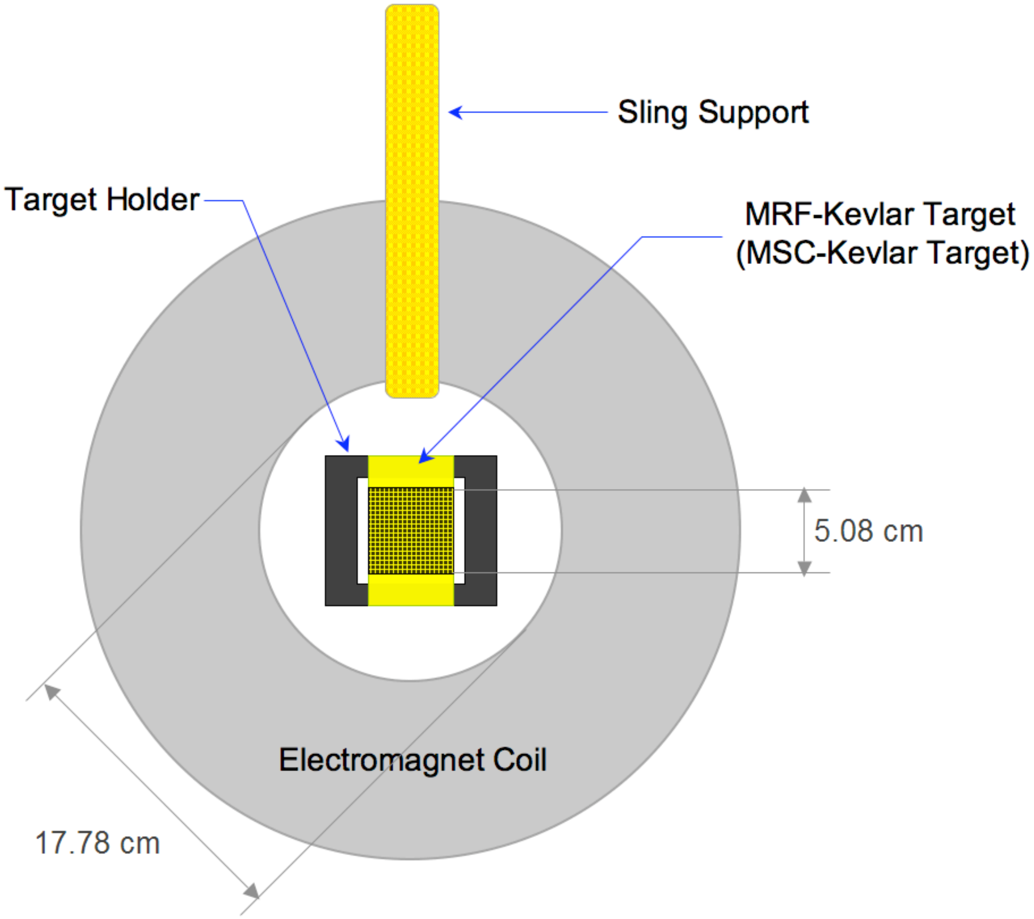

Figure 3.1: Schematic of target frame assembly in the coil

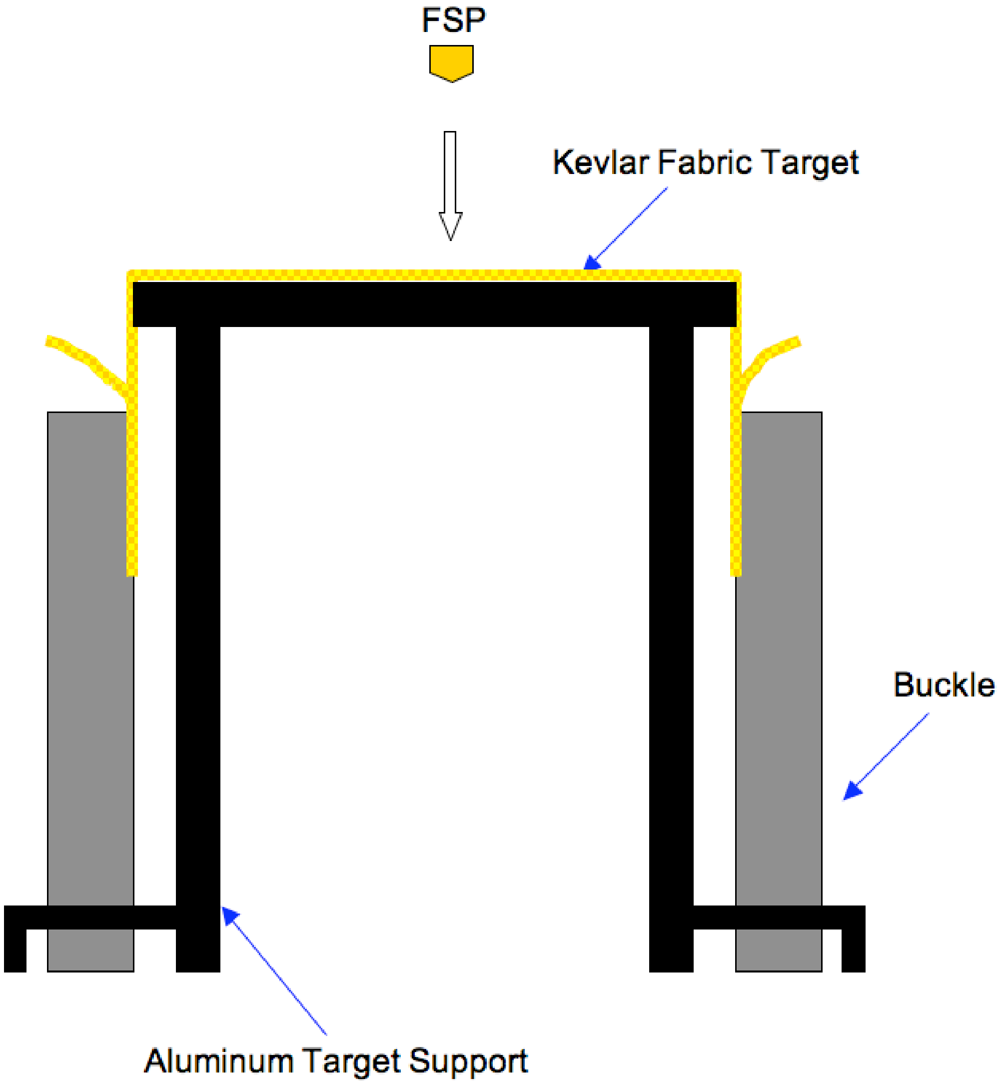

Figure 3.2: Schematic of FSP impact on the target fixed to the target holder

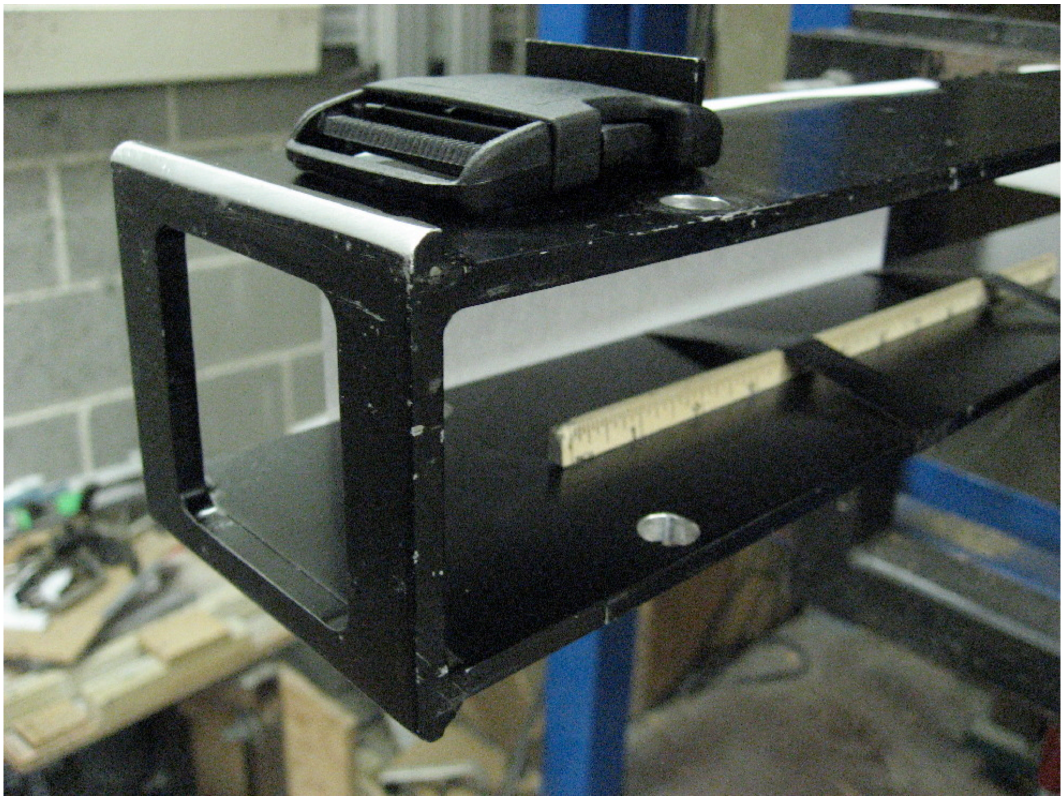

Figure 3.3: The target holder installed at Small Arms Range for FSP impact tests on neat-, MRF-, and MSC-Kevlar

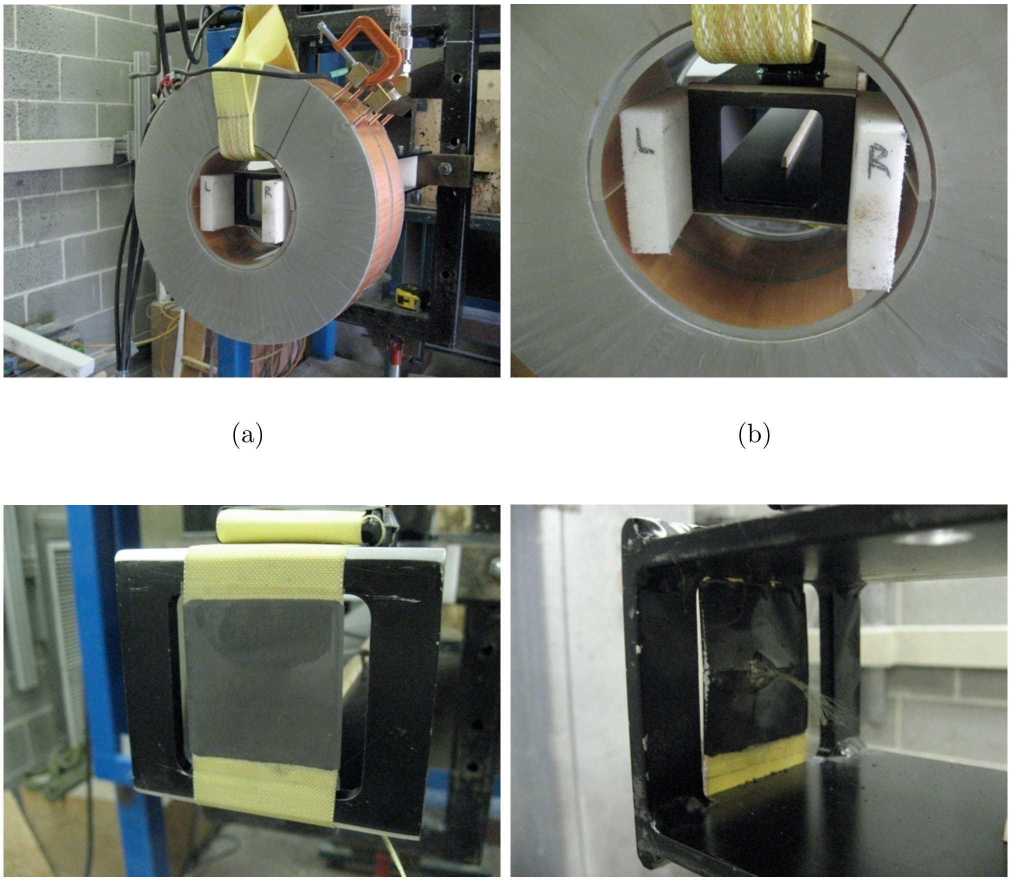

(a) (b)

(c) (d)

Figure 3.4: MRF-Kevlar impact FSP test (a) configuration of test setup (b) target fixture in the electromagnetic coil (c) MRF-Kevlar composite target mounted on the target fixture (d) post-impact image from the back of the target

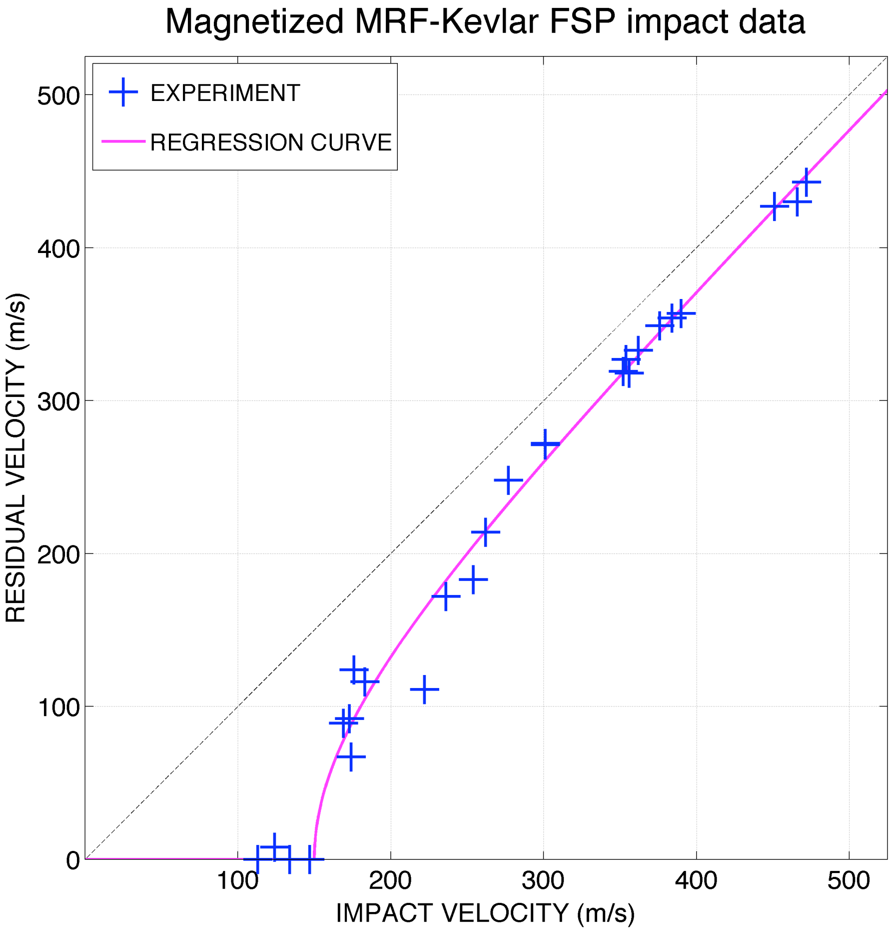

Figure 3.5: Experimental results: FSP impacts on MRF-Kevlar with an applied magnetic field (H_0=111 kA/m) in the coil

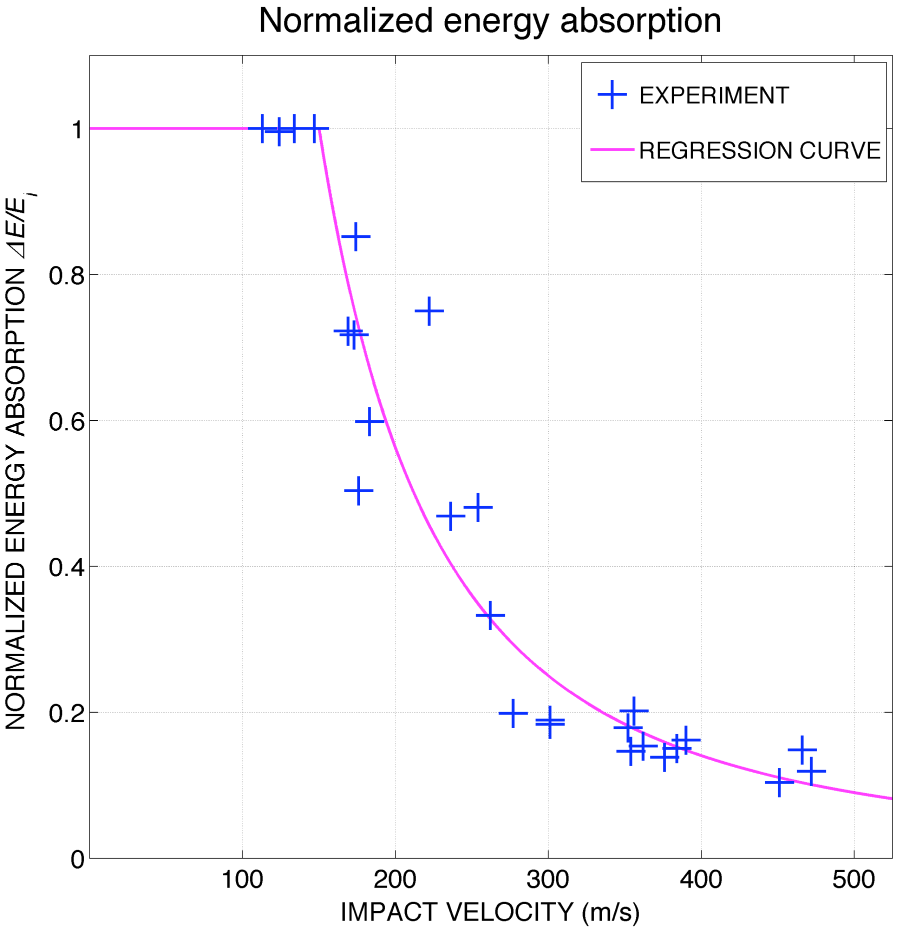

Figure 3.6: Experimental results: normalized absorbed energy for magnetized MRF-Kevlar composites in the coil where H_0=111 kA/m with respect to the kinetic energy of a striking projectile

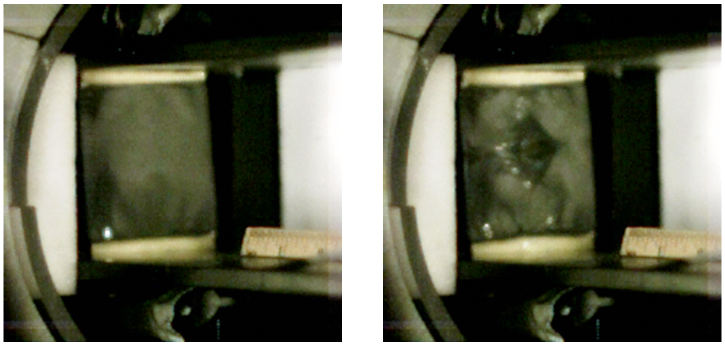

(a) $t = 0$ μsec (b) $t = 50$ μsec

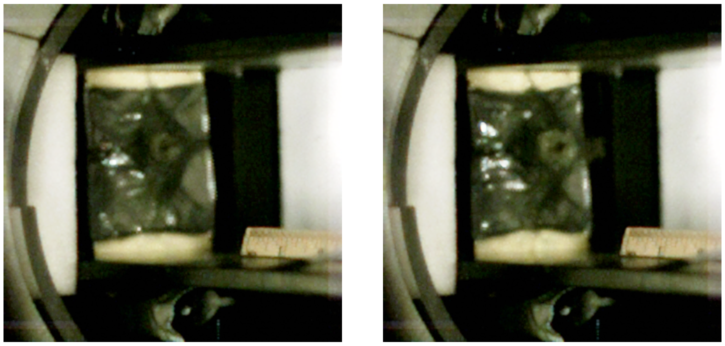

(c) $t = 100$ μsec (d) $t = 150$ μsec

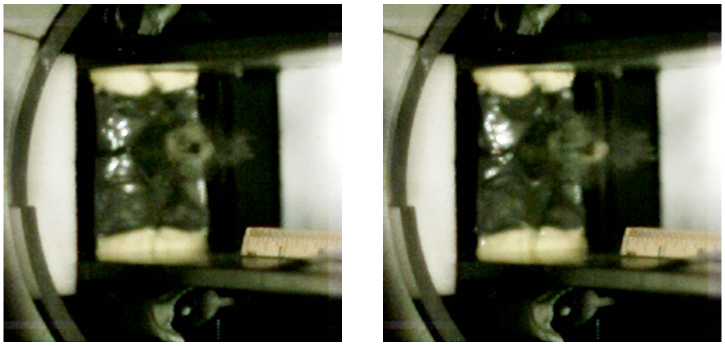

(e) $t = 200$ μsec (f) $t = 250$ μsec

Figure 3.7: FSP impact experiment at 262 m/s on magnetized MRF-Kevlar composite at 0 - 250 μsec

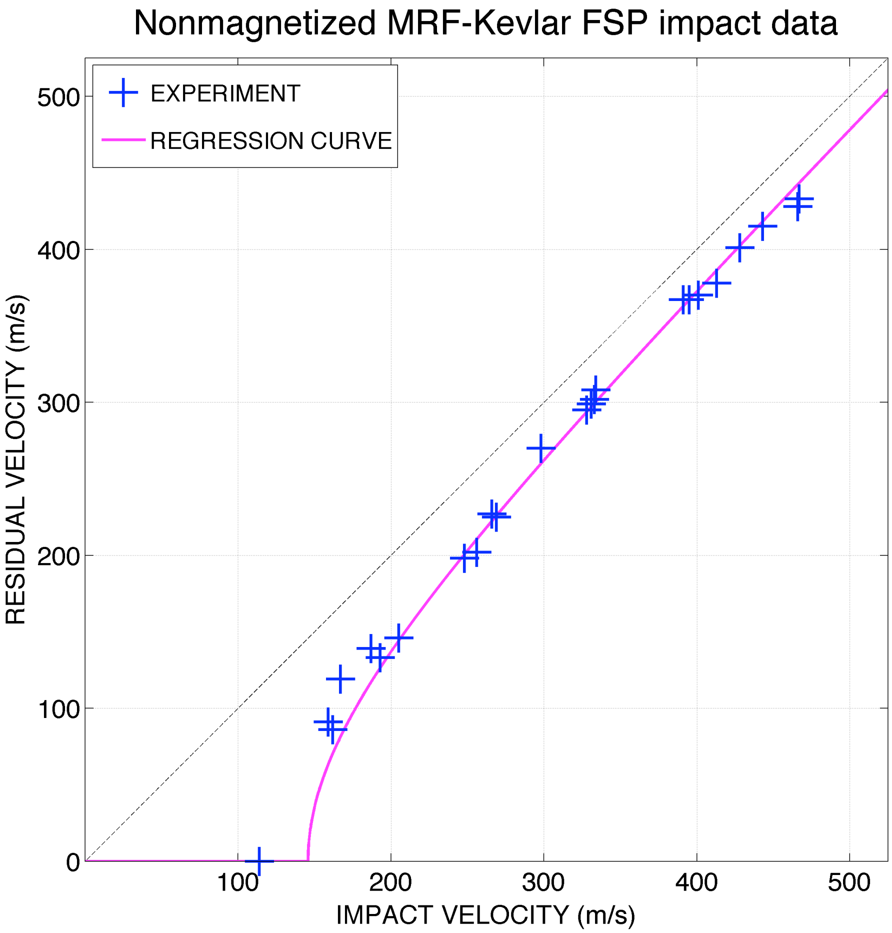

Figure 3.8: Experimental results: FSP impacts on MRF-Kevlar with no magnetic field

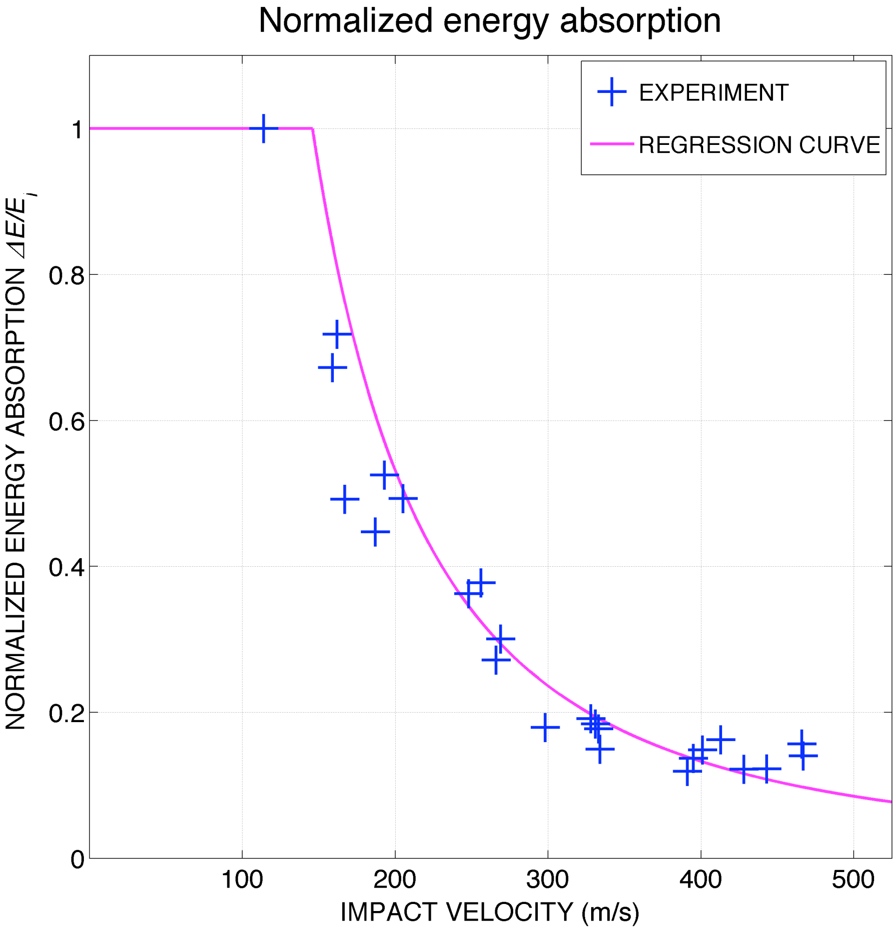

Figure 3.9: Experimental results: normalized absorbed energy for non-magnetized MRF-Kevlar composites with respect to the kinetic energy of a striking projectile

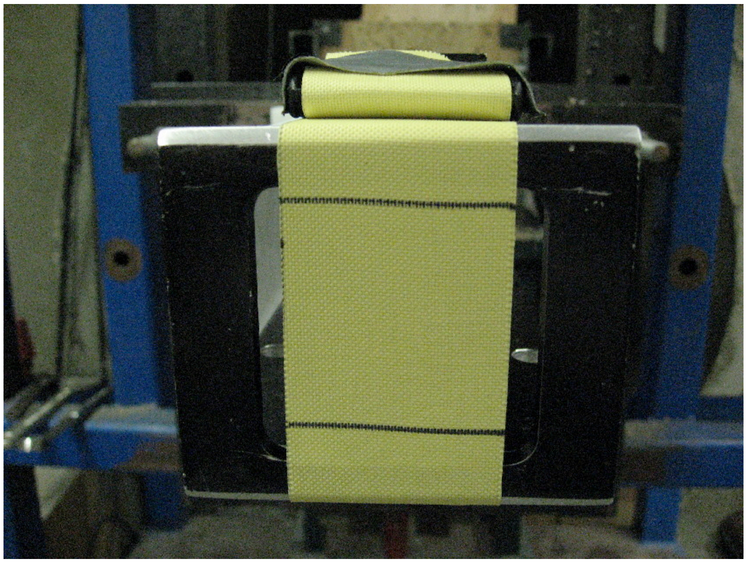

(a)

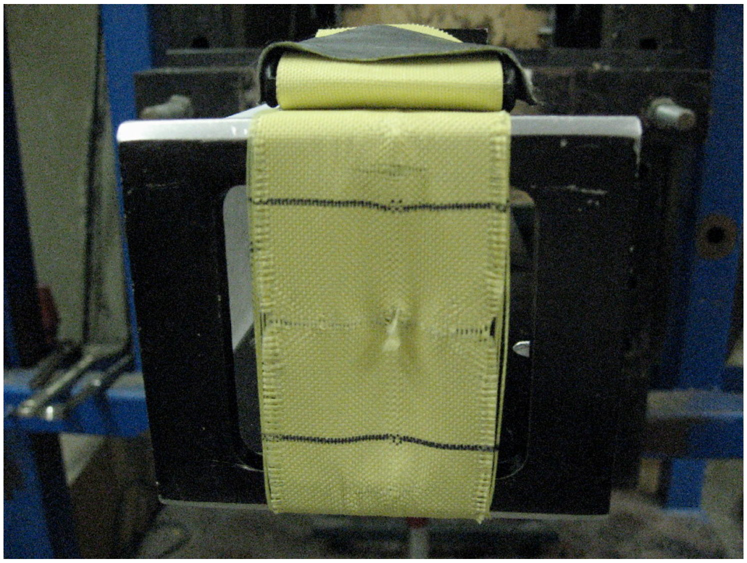

(b)

Figure 3.10: FSP impact baseline tests on neat Kevlar (a) intact Kevlar fabric mounted on the target holder (b) post-impact image

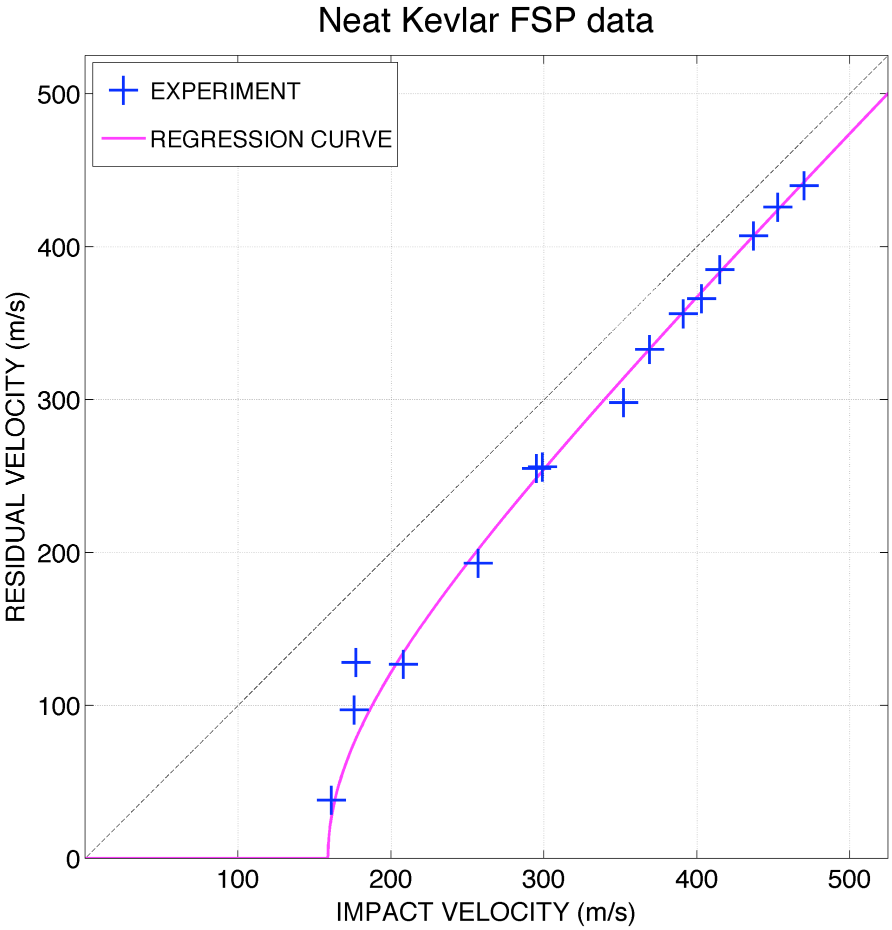

Figure 3.11: Experimental results: FSP impacts on a neat Kevlar strip

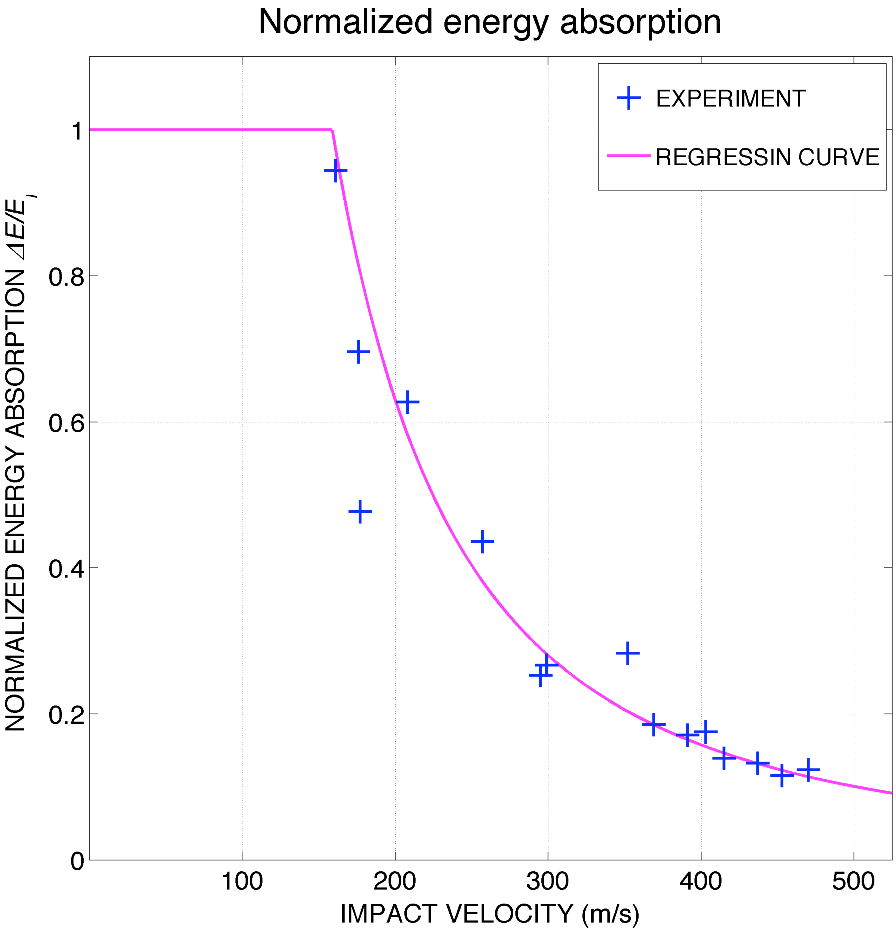

Figure 3.12: Experimental results: normalized absorbed energy for neat Kevlar baseline tests with respect to the kinetic energy of a striking projectile

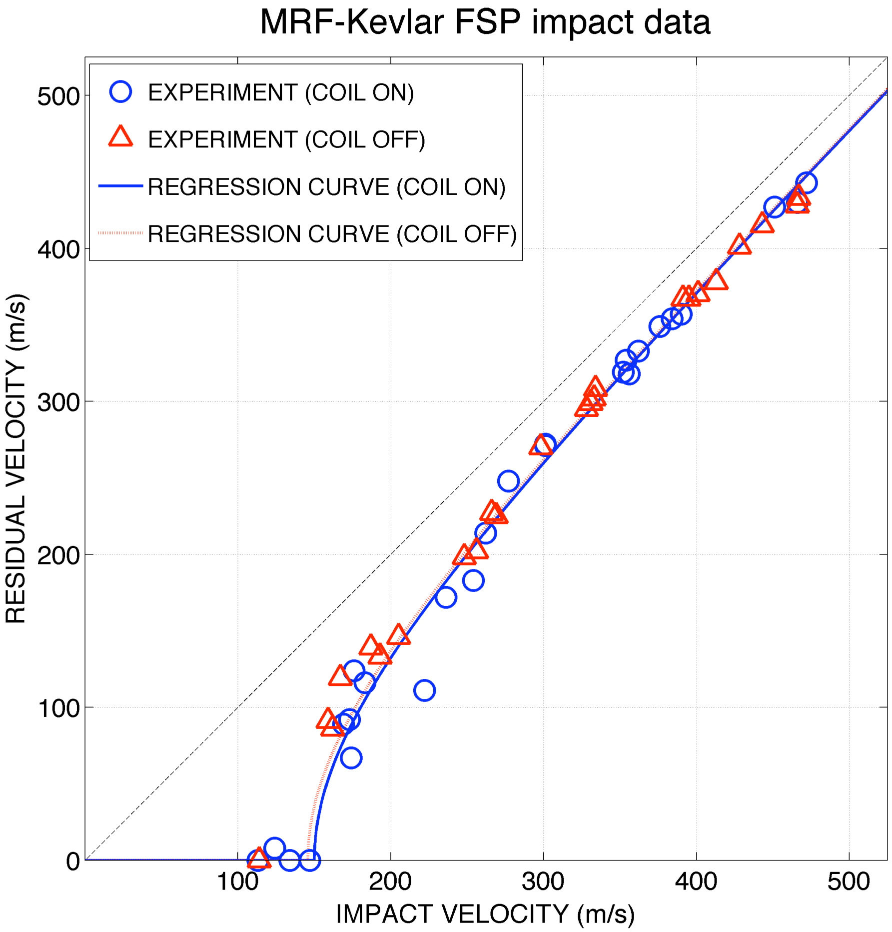

Figure 3.13: Experimental results: FSP impacts on MRF-Kevlar composites with an applied magnetic field in the coil v.s. with no magnetic field

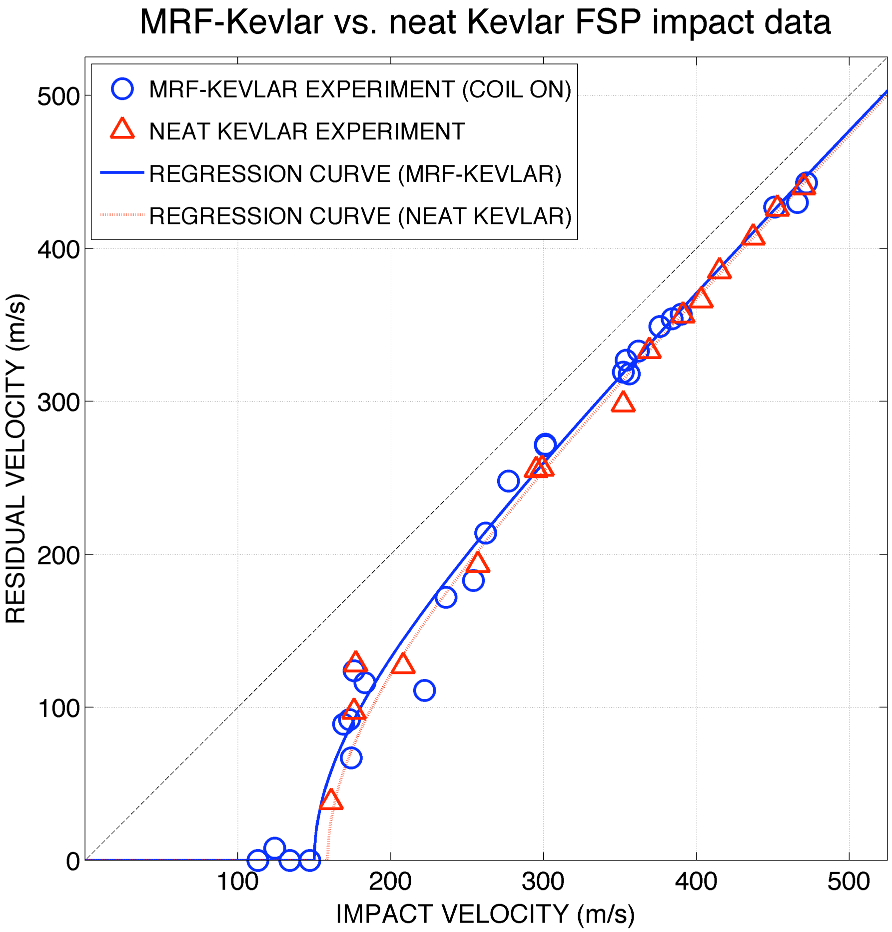

Figure 3.14: Experimental results: FSP impacts on Neat Kevlar v.s. MRF-Kevlar composites under an applied magnetic field

Chapter 4

Fragment Simulating Projectile Impact Tests on Magnetostrictive Composite Coated Kevlar Targets

4.1 Introduction

The development of high strength fabrics has made a breakthrough in the performance of soft body armor, by providing lightweight and flexibility [116]. This achievement is mainly due to their superior tensile strength, per unit mass, as compared to that of conventional armor materials such as metals and ceramics. For example, a Kevlar single fiber is known to have approximately five fold greater tensile strength per unit mass than steel [88]. In addition to excellent mechanical strength, high strength fabrics possess flexibility enough to provide the wearer with comfort and the manufacturer with the ease of tailoring. However, the flexibility of fabrics may lead to a fatal injury to the wearer (so called blunt force trauma) if the armor penetration depth exceeds a certain critical level, even in the case that the projectile is completely stopped by the ballistic fabric [11]. Therefore, the trade-off between comfort and safety determines a personal body armor with optimal flexibility. One way to address this problem is to add a stiff structure to an originally pliant armor system. A metallic or ceramic plate (like a hard armor vest), a separate layer from the ballistic fabric, has been used to enhance the safety for blunt trauma. In addition, the rigidity of fabric armor can be increased by using a fabric composite, such as Kevlar-Epoxy laminates. Another way to address the trade-off problem is to incorporate a viscous fluid, such as a Shear Thickening Fluid (STF), into neat woven fabrics [78]. This technique uses a void-filling or surface-coating fluids in order to improve the impact resistance of high strength fabrics. Although the dissipation augmenting mechanism of STF-Kevlar is not fully understood, it has been speculated that the improvement in impact energy absorption is achieved due to friction effects between the fabric yarns [139].

In previous two chapters, FSP impact tests have been conducted on Kevlar composite targets saturated with magnetorheological fluids, as a potential candidate for a dissipation augmenting viscous fluid. In this chapter, magnetostrictive particles are investigated as another material which may improve the impact resistance of high strength fabrics. Research regarding materials with giant magnetostriction, like Terfenol-D [41], has been focused on actuation or sensory applications. However, there have been several investigations of magnetostrictive material as an energy dissipating component in a vibrating system [59, 92, 132, 141]. These have shown that magnetostrictive materials, especially Terfenol-D, has a considerable damping capability for cyclic stress under magnetic loading conditions, due to stress-strain hysteresis.

This chapter presents FSP impact experiments on magnetostrictive coated-Kevlar composites (MSC-Kevlar) including target material preparation and experimental procedures. Polyurethane adhesive of a flexible type is chosen as a polymer adhesive. It is mixed with Terfenol-D powder, in order to coat the neat Kevlar fabric. This adhesive coating does not degrade the flexibility of the fabric. An introduction to magnetostriction is also presented in this chapter.

4.2 Materials

The experimental work in this chapter incorporates four key materials, which are brass, Kevlar, Terfenol-D, and Polyurethane.

4.2.1 Kevlar

All targets tested in this chapter were fabricated from the 706 style Kevlar KM2 woven fabric, manufactured by Hexcel Corporation [61]. Kevlar KM2 fabric is widely used in ballistic protection applications. Type 706 Kevlar fabrics have specifications of 600 denier, 34 yarns per inch, 0.023 cm thickness, 0.018 g/cm^2 areal density, and 46% void fraction.

4.2.2 Magnetostrictive Material: Terfenol-D

This section briefly introduces magnetostriction and magnetostrictive materials and presents a literature review on the damping characteristics of magnetostrictive materials.

Magnetostriction refers to a physical phenomenon of energy conversion, from magnetic energy to mechanical strain energy, and vice versa [64]. Because this energy conversion is bidirectional, magnetostrictive materials can be used as sensors as well as actuators. From the modeling point of view, the properties of magnetostrictive materials are highly nonlinear, since magnetostriction arises from very complex magnetomechanical coupling effects, including preload effects, magnetocrystalline anisotropy, rotation of magnetic moments, magnetic domain wall motion, temperature dependence of the magnetic and mechanical properties, and hysteresis [113].

Magnetostriction can be subdivided into direct and inverse magnetostrictive effects depending on the direction of energy transformation. Direct magnetostrictive effects refer to the mechanical strain induced by an internal or external magnetic field, while inverse effects refer to any change in magnetization due to the material deformation [34]. Magnetostrictive phenomena have been observed in most ferromagnetic materials [35]. Ferromagnetic materials can store magnetic energy in three forms: exchange energy, anisotropy energy, and demagnetizing energy. These three forms of magnetic energy are respectively associated with volume magnetostriction, linear magnetostriction, and the form effect [76]. The volume magnetostriction represents isotropic changes and the others describe anisotropic changes in deformation and magnetization. Among them, the direct linear magnetostriction, called Joule magnetostriction, is the most widely used magnetostrictive effect in actuating applications, due to the large strain (on the order of 1000 ppm) for the rare earth-iron compound $Tb_{0.3}Dy_{0.7}Fe_2$ (Terfenol-D). Its physical properties are listed in table 4.2 [30, 35]. For reference, the inverse effect, corresponding to Joule magnetostriction, is called the Villari effect, which describes the stress dependency of the magnetization of a material [35, 76].

Terfenol-D, developed by the Naval Ordnance Laboratory (now Naval Surface Warfare Center) in the 1960's, is a magnetostrictive compound of iron and two rare-earth metals, Terbium and Dysprosium. The name, Terfenol-D, is the abbreviation of its constituents (ter=Terbium, fe=Iron, D=Dysprosium) and its birthplace (nol = Naval Ordnance Lab). As shown in Table 4.1, pure Terbium and Dysprosium have a large magnetostriction compared to other magnetostrictive materials, even to Terfenol-D. However, those elements are not applicable for practical use, in a room temperature environment, because of their low Curie temperatures (-48 and -184 degrees Celsius, respectively). By producing an alloy with Iron, of high Curie temperature, their low Curie temperature can be overcome, with no significant degradation of their inherently high magnetostriction. The alloy, Terfenol-D, possess high strain and high force output with a large magnetomechanical coupling factor ($k_{33}^{max} = 0.75$) at room temperature, compared to the other magnetostrictive materials including Nickel, Alfer (Fe 13wt.% Al), magnetite (Fe_3O_4), Nickel ferrite ($NiFe_2O_4$), Ni 4wt.%Co, and so forth [35].

The major applications of magnetostrictive materials are sensors and actuators, due to their excellent energy transduction capability. Linear actuators [29] and rotary actuators [135] have been developed, based on Joule magnetostriction. Magnetostrictive material can be also used to generate sound waves, as a sonar transducer [34] or an ultrasonic transducer [143]. Hybrid magnetostrictive-piezoelectric devices have been studied as an application of magnetostrictive materials [22, 95]. In sensor applications, magnetomechanical sensors such as torque sensors, force sensors and magnetometers have been designed based on the inverse magnetostrictive effect [34].

The majority of research on design and analysis of magnetostrictive transducers has been focused on the energy coupling and conversion between mechanical strain energy and magnetic energy. However, there have also been studies on energy dissipation during the magnetostrictive processes. In general, stronger damping capability is observed in ferromagnetic materials than in non-ferromagnetic materials [141]. The energy loss in magnetostrictive materials is due to eddy currents on material surfaces and magnetization jumping within magnetic domains [59]. Hathaway *et al.* suggested a model for the energy loss in magnetostrictive materials, due to magnetization jumping within magnetic domains in terms of stress amplitude. Teter *et al.* measured energy dissipation due to stress-strain hysteresis at zero bias field, for magnetostrictive materials, including Terbium-Dysprosium-Iron compounds, in terms of the amplitude of the maximum applied stress [132]. Material damping of a Terfenol-D and polymer composite under cyclic axial and torsional loadings was measured by McKnight *et al.* [91, 92]. They obtained a high energy dissipation for magnetostrictive particulate composites in cyclic shear loading than in axial loading. The peak dissipation per cycle was about 20% for a composite containing Terfenol-D particulate 20% in volume [92].

In this research, Terfenol-D Powder manufactured by ETREMA Products, Inc. is used to fabricate a magnetostrictive particulate composite. Its material properties are listed in Table 4.2. Care should be taken to store and process Terfenol-D powder, since it is highly flammable.

4.2.3 Polyurethane Adhesive

To retain the inherent high strength and flexibility of ballistic protection fabrics, the coating material is required to have certain mechanical characteristics: lightweight, flexibility, strong adhesion and high toughness. From a manufacturing point of view, the coating process should be performed at room temperature, because heat can degrade the mechanical strength of Kevlar. The specific material chosen in this research was WC-753 A/B clear Polyurethane adhesive/coating system manufactured by BJB Enterprises, Inc. It is very flexible and can be cured at room temperature [16]. WC-753 system consists of two parts: a Polyurethane resin (part A) and a curing agent (part B). The density is 1.07 g/cc, less than that of Kevlar fiber.

4.2.4 Projectile

Projectiles used in impact tests were 1.2 gram, 0.22 caliber fragment simulating projectile made from half hard brass. Non-ferromagnetic brass was chosen to avoid magnetic field distortion. This projectiles were machined to have same geometry as a NATO standard FSP MIL-P-46593A, which is shown in Figure 2.2.

4.3 Target Preparation and Experimental Procedure

The experimental research was conducted in collaboration with Southwest Research Institute (SwRI). The testing procedure was developed by the University of Texas (UT), while the impact experiments were performed at SwRI Small Arms Range. The author designed and fabricated the MSC-Kevlar composite targets, provided and operated an electromagnetic coil, cooling system, and power supply, and developed the test procedure. The special target holder used for the MSC-Kevlar composites was originally designed by the author and modified by SwRI so that the target holder could be attached to the target fixture at the SwRI Small Arms Range. SwRI fabricated the target fixture (Figure 3.3), provided chronographs to measure the projectile impact velocity, and high speed cameras to measure the projectile residual velocity and observe the impact response of the target.

Before being coated with a magnetostrictive adhesive, the neat Kevlar fabric was cut into 5.08 cm × 25.4 cm strips and its weight was measured. To prepare the magnetostrictive coating material, Terfenol-D powder was mixed with WC-753 A/B Polyurethane adhesive with volume ratio of 1:2:2 (Terfenol-D: WC-753 Part A : WC-753 Part B). Since the mixture of polyurethane resin (WC-753 part A) and curing agent (WC-753 part B) begin solidifying after 7-10 minutes, the two chemicals were blended just at the moment of adding adhesive coating to the neat Kevlar fabrics. Hence the Terfenol-D powder was mixed with only one part of the WC-753 A/B adhesive before mixing the two adhesive parts. WC-753 part B was chosen to be mixed with the Terfenol-D powder because it is less viscous than part A. The mixing process for part B and Terfenol-D powder was conducted in an oxygen-free environment, due to the high flammability of Terfenol-D powder [41]. Terfenol-D and WC-753 part B (1:2 volume ratio) were mixed together in a glove box (Model 50600 made by Labconco Corporation) with an inert Argon gas atmosphere to prevent Terfenol-D powder oxidation. The Terfenol-D and WC-753 part B mixture was removed from the glove box and moved to a fume hood where the remaining fabrication steps took place. In the fume hood, the Terfenol-D and WC-753 part B mixture was blended with WC-753 part A resin. The final volume ratio among the three constituents was 1:2:2 (Terfenol-D : WC-753 part A : WC-753 part B). The adhesive stirring process was completed as quickly as possible, since the adhesive working time is about 7-10 minutes. The blended coating material was brushed into a marked rectangular area of 5.08 cm × 5.08 cm, on one side of the prepared Kevlar strips. The coated Kevlar strips were left in the hood to be cured for two days.

A sample of the cured MSC-Kevlar composite is shown in Figure 4.1. The weight of fabricated composite target was measured, and the weight of the neat Kevlar strip was subtracted, to obtain the mass of magnetostrictive coating for each target. The twenty-seven targets fabricated for impact tests had an average mass of magnetostrictive coating per target of 3.26 g (an areal density of 0.13 g/cm^2). For reference, the areal density of the Kevlar is 0.018 g/cm^2. Therefore, the ballistic performance of MSC-Kevlar targets should be compared with 8-ply neat Kevlar target of same weight as the MSC-Kevlar composite.

The experimental setup and testing procedures were the same as for the FSP impact tests on the MRF-Kevlar composite tested in a coil. The aluminum target holder with a 6.35 cm × 6.35 cm window (Figure 3.3) was connected to the pre-installed target frame in the SwRI Small Arms Range. The electromagnetic coil (model 3473-70 manufactured by GMW Associates, Inc.) was supported by a sling, connected to an overhead trolley crane, so that the vertical and horizontal positions of the coil could be adjusted. A Sorensen DLM32-95E 3kW Programmable DC power supply from Elgar electronics Corporation was connected to the coil, and was operated in constant current mode at 70 A. A laboratory-made water circulating system was used to cool the coil under operation. The magnetic field at the coil center was measured using a Gaussmeter (Model HHG-22 from Omega Engineering, Inc.) before the actual impact tests. The coil, when operated at 70 Ampere, generated a magnetic field of 138.7 mT (equivalently, 110 kA/m in air) at the coil center. This measured value was approximately the same as the calculated value, which was 133 mT (or 106 kA/m), based on the magnetic field modeled in Appendix C. A Universal Gun (0.22 calibe, chambered for the .22 Hornet cartridge held in a Universal Receiver.) was used to fire a brass fragment simulating projectile (type MIL-P-46593A) at the targets. Projectiles impacted the mounted target at normal incidence. Two sets of chronographs were used to measure the impact velocity of the incident projectile. Two vision Research Phantom V7 monochrome cameras were used to measure the residual velocity of the projectile and to record the fabric deformation and perforation.

All impact tests were conducted at the Small Arms Range at Southwest Research Institute. The University of Texas provided MSC-Kevlar targets, the design of the target holder, the electromagnetic coil with power supply, and the water cooling system. Targets were mounted on the target holder using polymer buckles, as shown in Fig 4.2(c). To align the coil, Nylon bars were inserted through the holes in the target holder extension, as shown in Fig 4.2(d). A laser was used to align the target with the gun, by adjusting horizontal and vertical positions of the target holder. Two polystyrene foam blocks were inserted into the space between the coil and the target holder, to avoid motion of the coil, as shown in Fig 4.2(b). The overall configuration of the target and coil is shown in Fig 4.2(a). The power supply for the coil, and lights for the high speed video, were turned on just before a projectile was fired and immediately turned off after each impact test. This avoided thermal degradation of the Kevlar or magnetostrictive coating. After the impact and residual velocities were measured and recorded, the impacted target was removed from the target holder. In the case of the non-magnetized MSC-Kevlar impact tests, the coil and cooling subsystems were excluded from the experiment.

4.4 Results of Impact Experiments

FSP impact tests were conducted on three different target configurations: magnetized MSC-Kevlar composites, non-magnetized MSC-Kevlar composites, and neat Kevlar fabric. The last two test series were performed as baseline tests, to evaluate the ballistic protection capability of energized MSC-Kevlar composites. The impact velocity was measured with chronographs and the residual velocity was obtained from the analysis of sequential images captured by the high speed video camera for each impact test.

The first set of experiments was conducted to investigate the ballistic performance of the MSC-Kevlar composite in a magnetic field. Twenty-six FSP impact tests were performed at SwRI. Nine test data points were discarded, based on the data qualification scheme shown in Figure 2.6(a). The remaining seventeen data points are listed in Table 4.3 and plotted in Figure 4.3. The kinetic energy reduction of the projectile was calculated and then normalized with respect to the incident kinetic energy for each test. This dimensionless energy absorption curve is shown in Figure 4.4. The value of V_{50}, estimated using Equation (2.5), was 183 m/s for the MSC-Kevlar composites. Figure 4.11 shows sequential images the target deformation for the FSP impact test at 159 m/s.

The second set of experiments was conducted with the same MSC-Kevlar targets, but without application of magnetic field on the target. Out of the twenty-four FSP impact tests conducted, eleven data points were discarded, based on data screening scheme shown in Figure 2.6 (a). The remaining thirteen data points are listed in Table 4.4. The data points are plotted in Figure 4.5. The estimated V_{50} is 200 m/s for the non-magnetized MSC-Kevlar composites. The corresponding normalized energy absorption curve is shown in Figure 4.6.

The last set of tests was conducted for neat Kevlar fabrics mounted on the same target holder used to test the MSC-Kevlar composites. The results for this set of baseline tests are provided in Chapter 3. Measured data for fifteen shots on neat Kevlar single-ply fabrics are listed in Table 4.5 and plotted in Figure 4.7. The estimated V_{50} is 159 m/s, and the associated regression curve is shown in Figure 4.7. The energy absorption curve for neat Kevlar is shown in Figure 4.8.

No improvement in ballistic performance was observed by applying an external magnetic field 111 kA/m to the MSC-Kevlar composites. On the other hand, the experimental results show that the non-magnetized targets have 9.3% larger V_{50} than the magnetized composites, equivalently 19.4% greater energy absorption capability (Figure 4.9). Compared to neat Kevlar fabrics, magnetized MSC-Kevlar composites have a 15.1% larger V_{50}, equivalently 32.5% greater energy absorption capability (Figure 4.10). Non-magnetized MSC-Kevlar composites have 25.8% larger V_{50} than neat Kevlar fabrics, on average, equivalently 58.2% greater energy absorption capability. The improvement in impact energy absorption was due to the coated material, not the composite interaction with the external magnetic field. Note that data scattering at low velocities (around V_{50}) was encountered.

4.5 Summary

Chapter 4 describes experimental research on MSC-Kevlar composite targets, using the same testing procedure as in Chapter 3. Background information on magnetostriction and magnetostrictive materials was discussed. Target fabrication procedures, including mixture of Terfenol-D powder and a polymer adhesive, were described in detail. This chapter included test in the form of, a data table, a graph, and estimated V_{50} values, and high speed camera images.

Table 4.1: Magnetostrictive properties of Terfenol-D and its constituting elements [34, 41]

Property	Unit	Material			
		Tb	Dy	Fe	Terfenol-D
Density	kg/m^3	8330	8560	7880	9250
Curie temperature	°C	-48	-184	770	380
Max. magnetostriction	*ppm*	3000	6000	-14	1620

Table 4.2: Material properties of Terfenol-D at room temperature [41]

Property	Unit	Value
Specific weight	kg/m^3	9250
Coefficient of linear thermal expansion	ppm/K	12
Young's modulus	GPa	25-35
Sound speed	m/s	1640-1940
Compressive strength	MPa	700
Tensile strength	MPa	28
Specific heat	$kJ/kg \cdot K$	0.35
Thermal conductivity	$W/m \cdot K$	13.5
Curie temperature	°C	380
Relative permeability		3-10
Joule magnetostriction	*ppm*	800-1200

Table 4.3: Experiment results: FSP impacts on MSC-Kevlar composites with an applied magnetic field (H_0=111 kA/m) in the coil

Impact Velocity V_i (m/s)	Residual Velocity V_r (m/s)
117	0
159	0
209	102
219	114
231	136
251	149
257	168
276	218
308	237
320	269
353	299
359	307
372	327
406	374
434	397
461	423
469	435

Table 4.4: Experiment results: FSP impacts on MSC-Kevlar composites with no magnetic field

Impact Velocity V_i (m/s)	Residual Velocity V_r (m/s)
144	0
228	80
231	107
232	109
251	124
254	131
258	147
312	260
331	267
352	285
405	369
418	379
464	419

Table 4.5: Experimental results: FSP impacts on a neat Kevlar strip

Impact Velocity V_i (m/s)	Residual Velocity V_r (m/s)
161	38
176	97
177	128
208	127
257	193
295	255
299	256
352	298
369	333
391	356
403	366
415	385
437	407
453	426
470	440

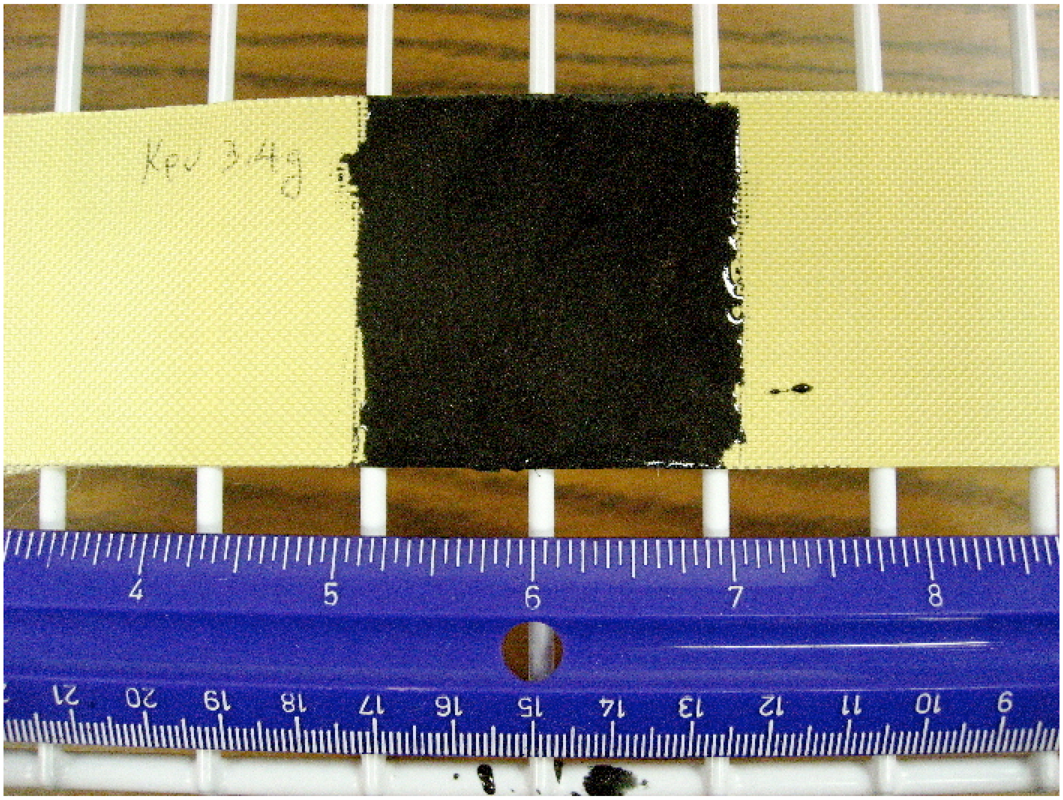

Figure 4.1: Fabricated MSC-Kevlar sample

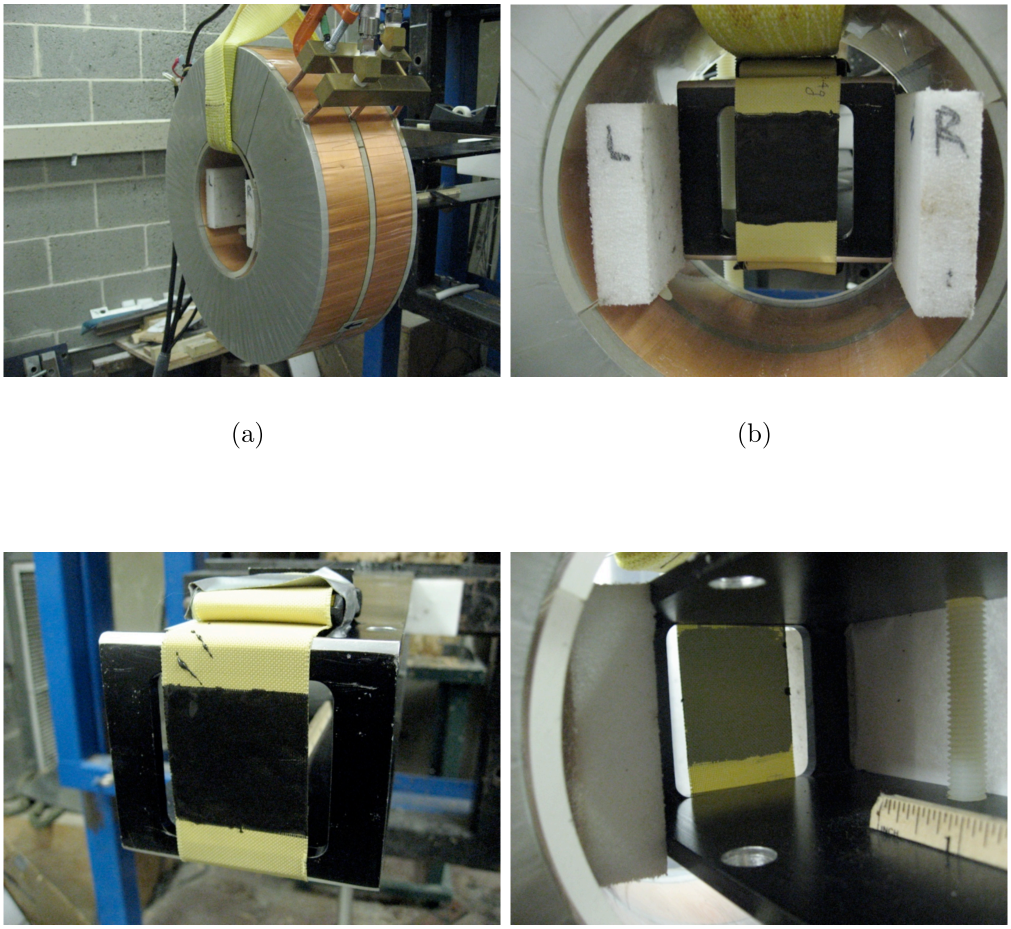

(a) (b)

(c) (d)

Figure 4.2: MSC-Kevlar impact FSP test (a) configuration of test setup (b) target fixture in the electromagnetic coil (c) MSC-Kevlar composite target mounted on the target fixture (d) view from the back of the target

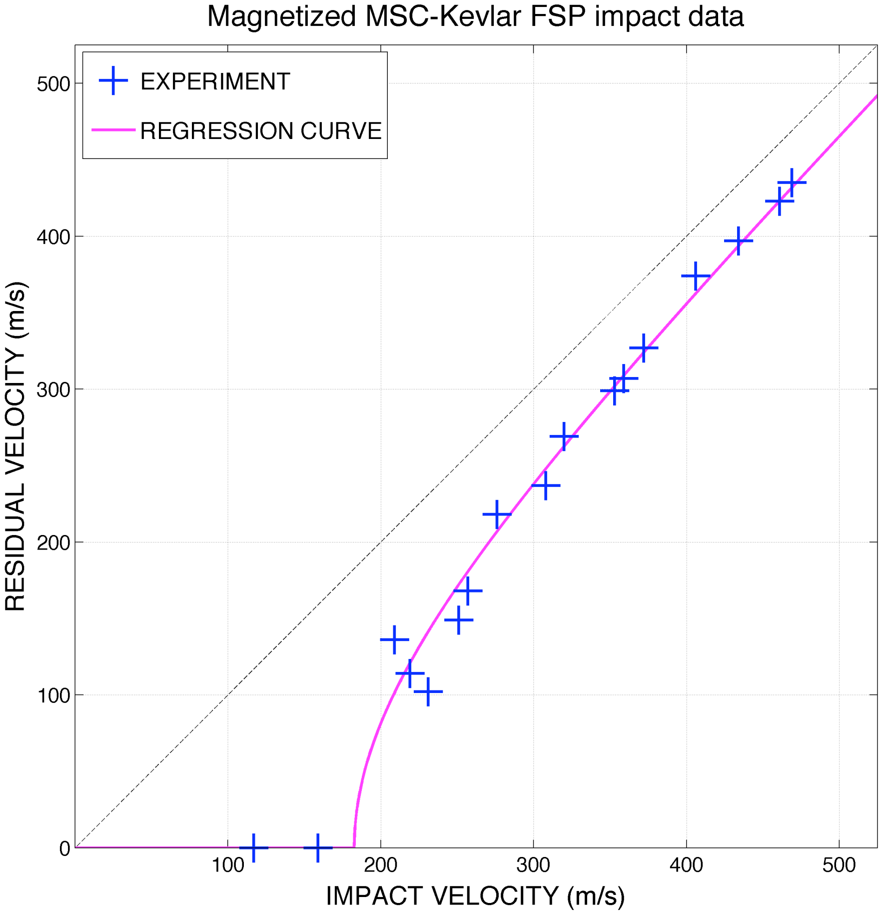

Figure 4.3: Experiment results: FSP impacts on MSC-Kevlar composites with an applied magnetic field (H_0=111 kA/m) in the coil

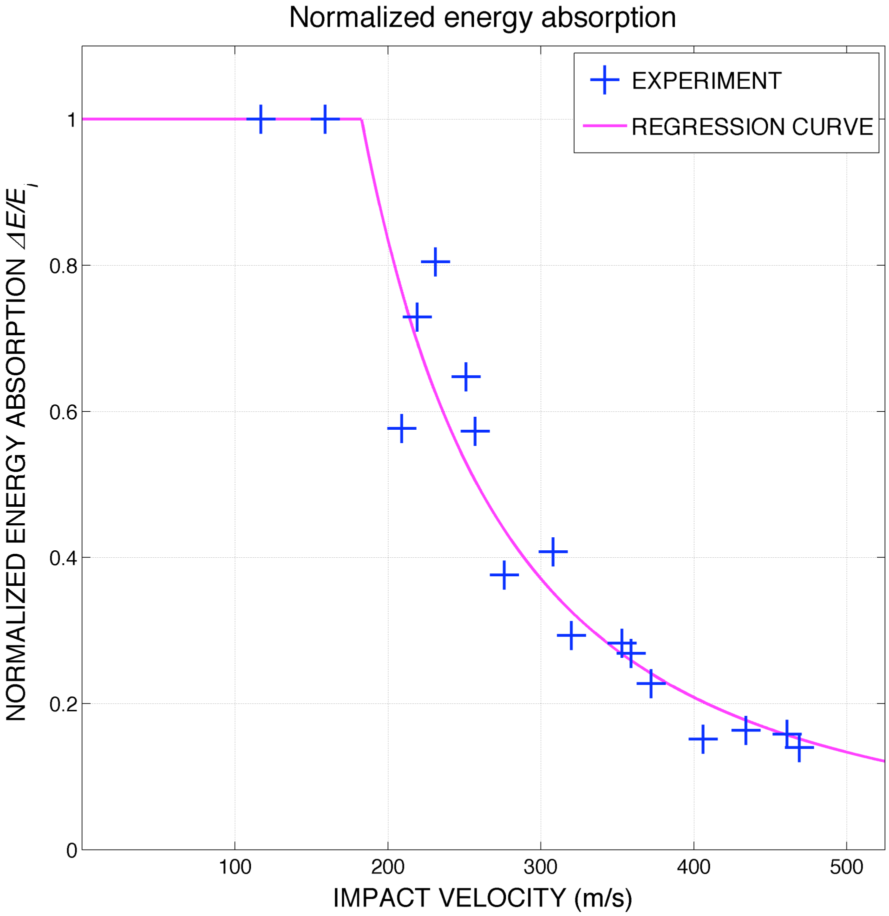

Figure 4.4: Experimental results: normalized absorbed energy for magnetized MSC-Kevlar composites in the coil where H_0=111 kA/m with respect to the kinetic energy of a striking projectile

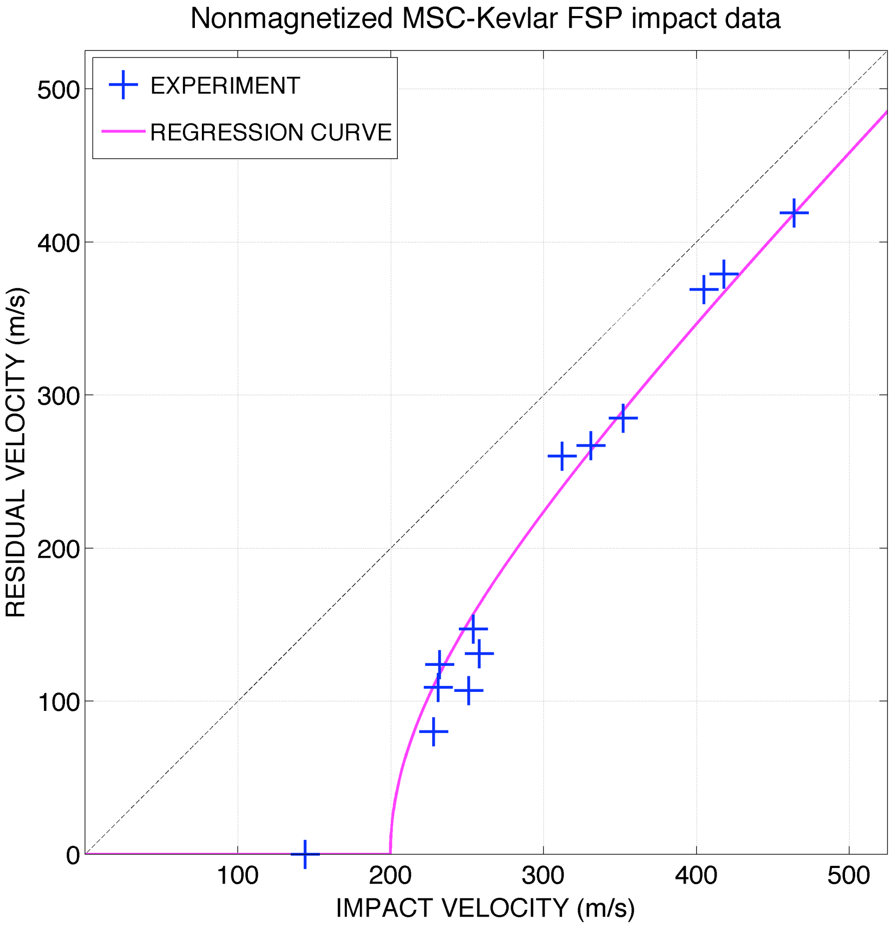

Figure 4.5: Experiment results: FSP impacts on MSC-Kevlar composites with no magnetic field

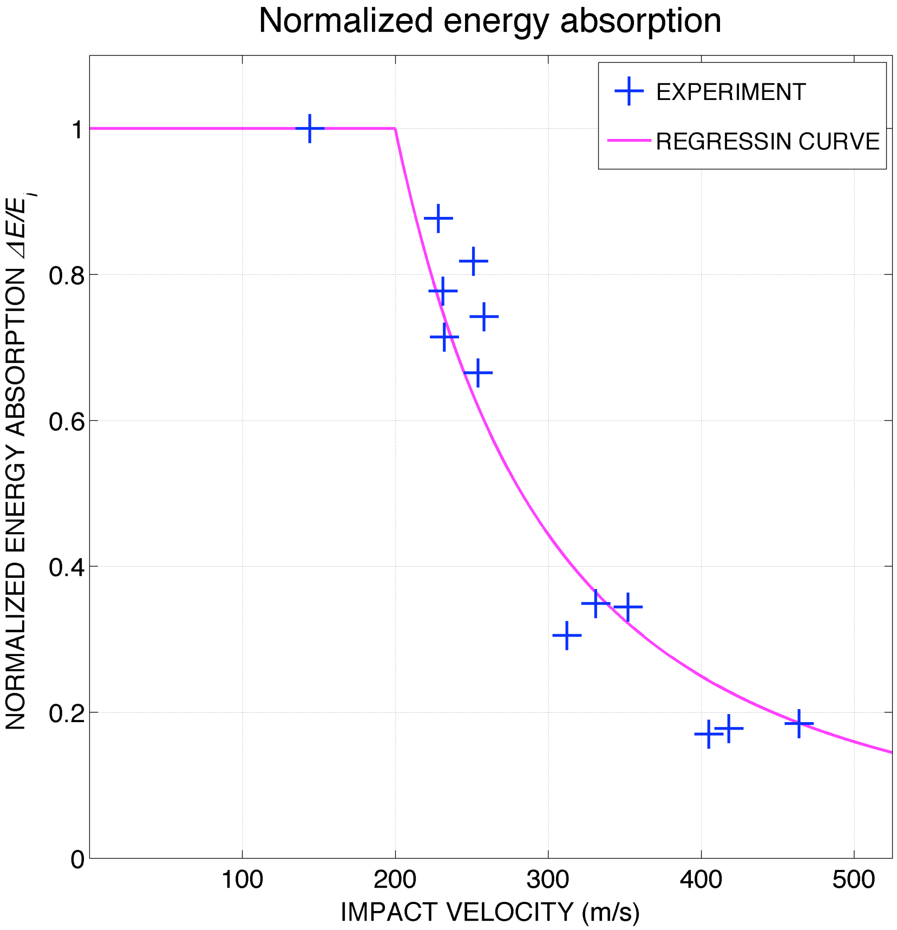

Figure 4.6: Experimental results: normalized absorbed energy for non-magnetized MSC-Kevlar composites with respect to the kinetic energy of a striking projectile

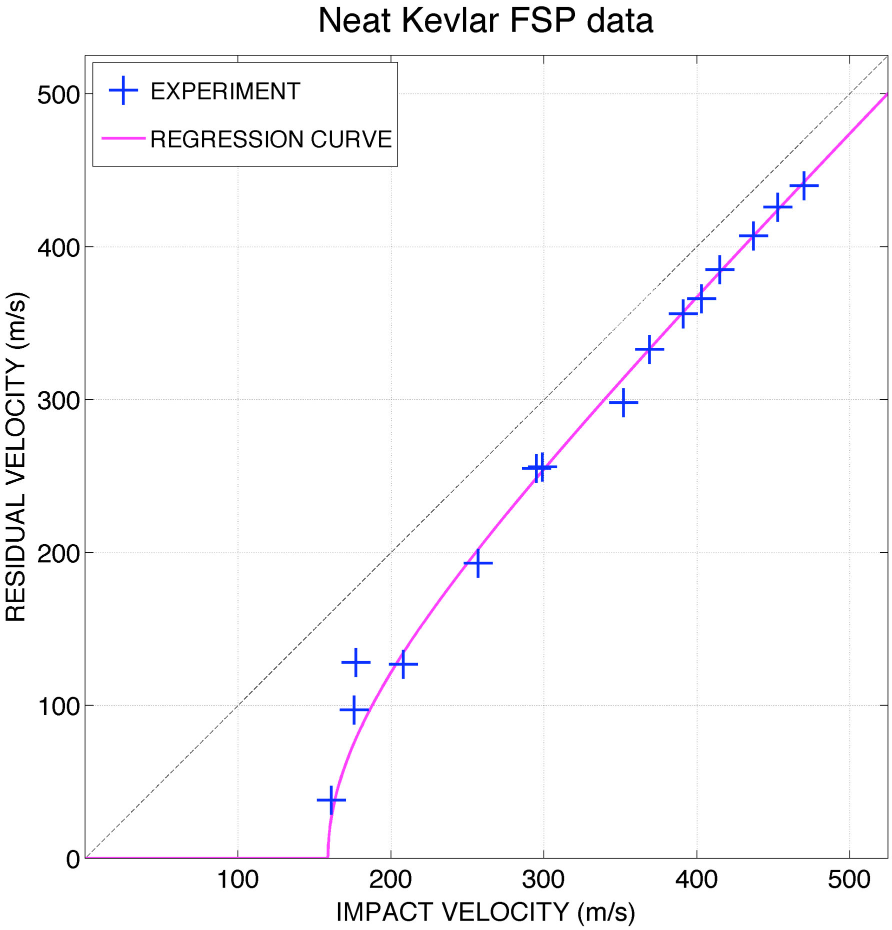

Figure 4.7: Experimental results: FSP impacts on a neat Kevlar strip

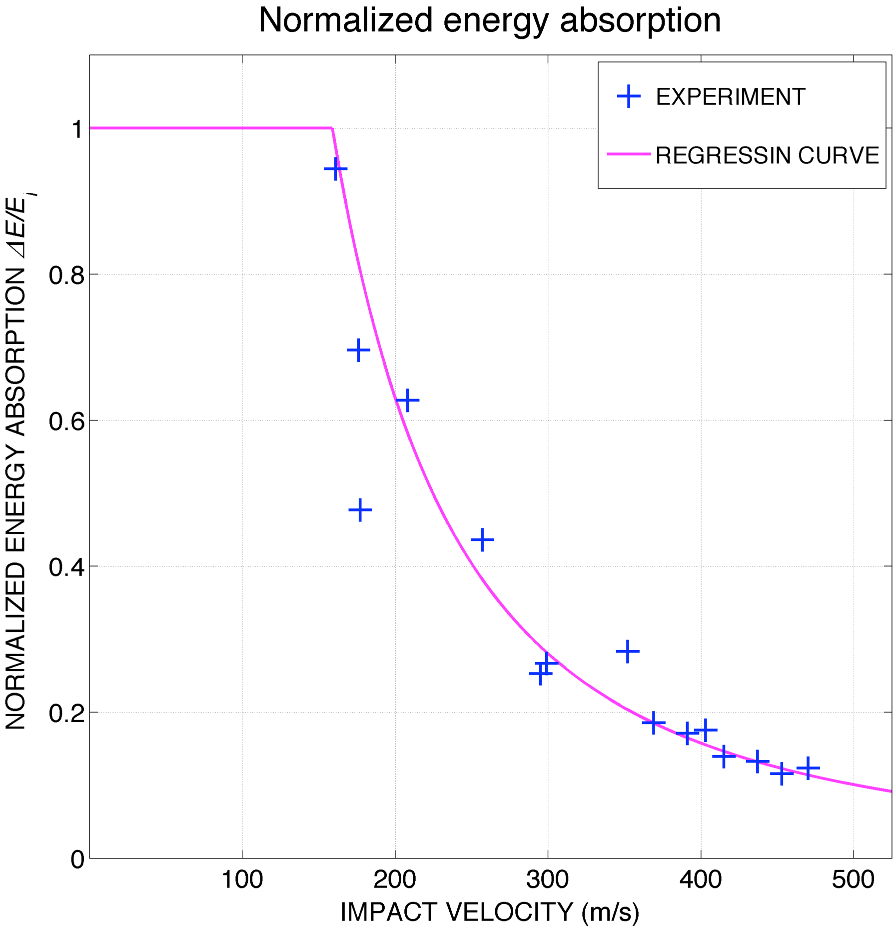

Figure 4.8: Experimental results: normalized absorbed energy for neat Kevlar baseline tests with respect to the kinetic energy of a striking projectile

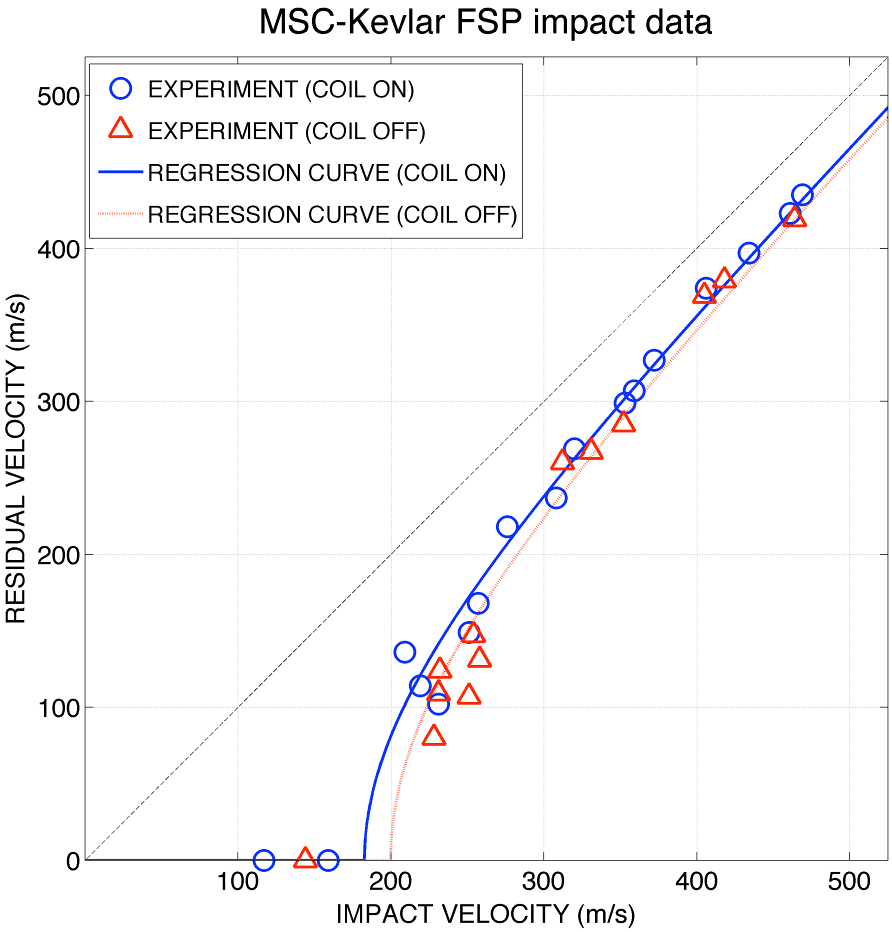

Figure 4.9: Experimental results: FSP impacts on MSC-Kevlar composites with an applied magnetic field in the coil v.s. with no magnetic field

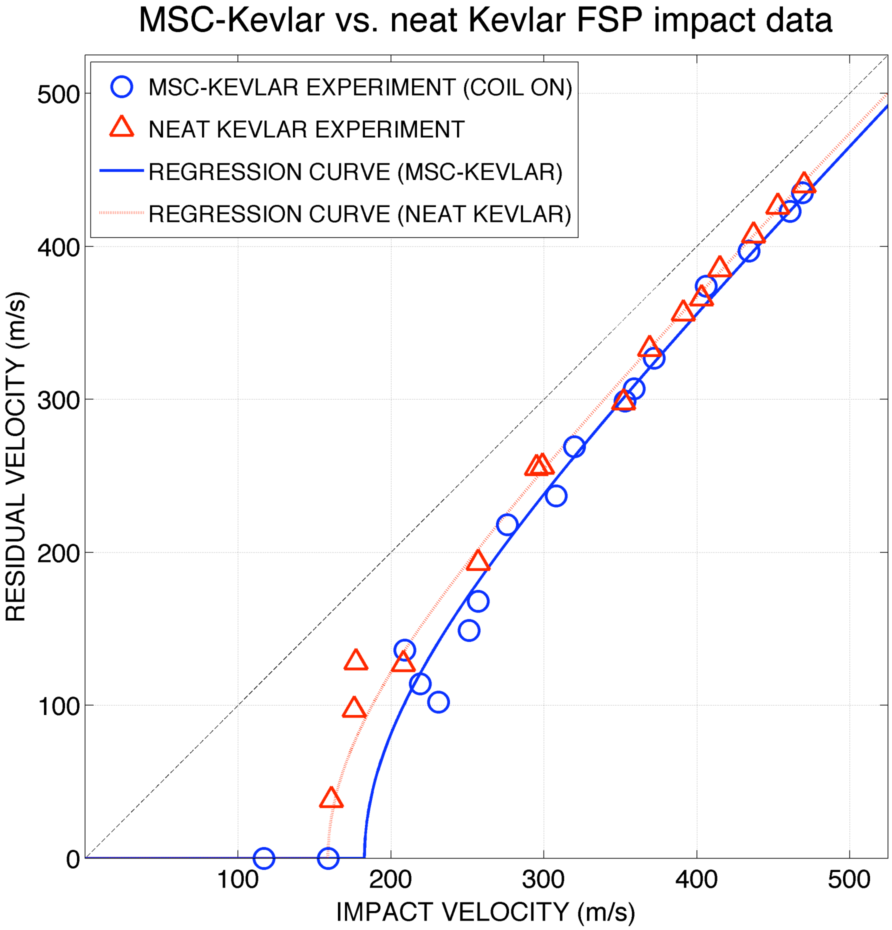

Figure 4.10: Experimental results: FSP impacts on Neat Kevlar v.s. MSC-Kevlar composites with an applied magnetic in the coil

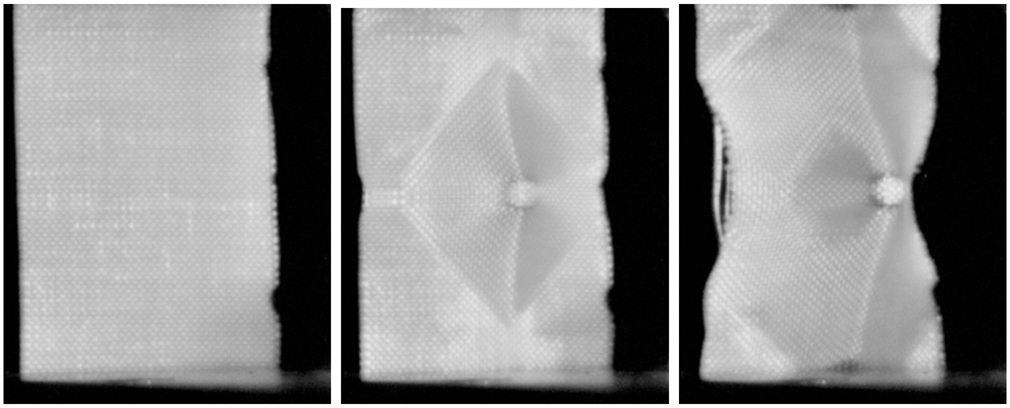

(a) $t = 0$ μsec (b) $t = 95$ μsec (c) $t = 190$ μsec

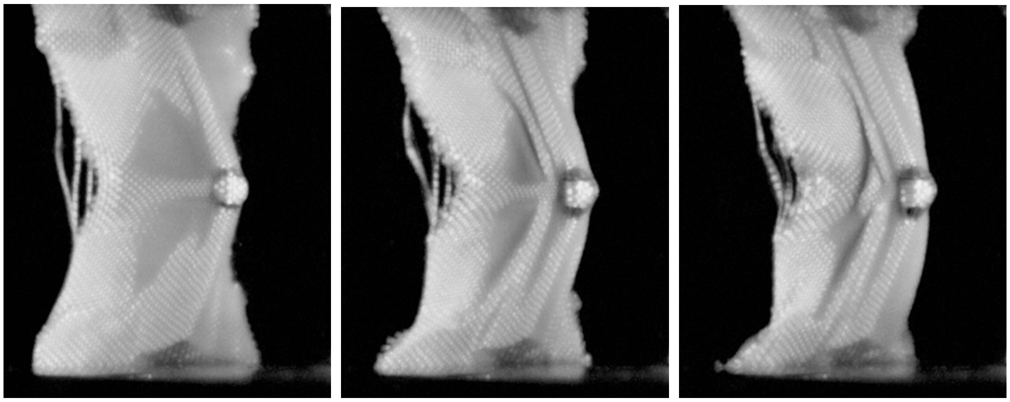

(d) $t = 285$ μsec (e) $t = 380$ μsec (f) $t = 475$ μsec

Figure 4.11: FSP impact experiment at 159 m/s on magnetized MRF-Kevlar composite at 0 - 475 μsec

Chapter 5

Development and Validation of a Particle-Element Model for Magnetorheological Fluid-Treated Kevlar Composites

5.1 Introduction

Computer aided virtual prototyping is the preferred way of designing and developing advanced armor systems due to the limitations of analytical methods and also due to very high cost of purely experimental research. Of course, analytical and experimental methods are indispensable in body armor research. Analytical research has provided an understanding of the fundamental physics of ballistic shielding performance under impact loading. Experimental research has been applied to evaluate and validate the reliability of armor prototypes. Moreover, any computational method should be supported by experimental validation, before being used as a practical design tool. The development of a reliable numerical method for body armor design becomes more and more important as novel protective materials and armor structures are developed.

Historically, computational methods for impact dynamics have been developed in academic and industrial fields as shock physics, car crashworthiness, spacecraft shielding, ballistic research, and so on. High- or hyper- velocity impact of materials in those fields is a complex thermomechanical phenomenon involving (1) intensive loading conditions (2) generation and propagation of shock induced discontinuities in thermomechanical state variables (3) large elastic-plastic deformation, with fracture and damage for even ductile materials (4) material vaporization and/or melting. Therefore, numerical methods for shock and impact physics should be capable of analyzing and predicting those thermomechanical effects.

In general, the computational methods for shock and impact physics may be classified into two categories, based on the frame of reference used to describe the motion of materials: Lagrangian method and Eulerian method [12]. One of the most popular Lagrangian methods is the Lagrangian finite element method (FEM) which uses deformable elements [24, 58]. The Lagrangian FEM is normally used for solids, because the meshed elements can easily represent the deformation of solid materials. For fluid problems, Lagrangian mesh-based techniques are not generally adequate, due to the highly advective nature of fluids. Instead, space-fixed Eulerian grids are preferred when computing the motion of fluids. Two representative methods are finite difference and finite volume methods [90]. To take advantage of both numerical techniques, Arbitrary Lagrangian-Eulerian (ALE) methods have been developed [21].

As an alternative to the mesh-based or grid-based methods, meshfree or meshless methods have also been developed to solve shock and impact problems [81, 85, 107]. Two popular meshfree methods are Smoothed Particle Hydrodynamics (SPH) [68, 124] and the Element-Free Galerkin (EFG) method [85]. These meshfree methods use moving interpolation functions, called kernels, to compute physical quantities of interest in terms of a finite number of nodal values. These interpolation kernels do not require any structural mesh. Therefore, unlike mesh-based methods, meshfree techniques do not suffer from mesh distortion problems for large material deformation. In addition, the particle description of a continuous or discontinuous medium allows contact-impact problems to be handled more easily than mesh-based methods. However, meshfree methods inherently have a numerical fracture problem, called tensile instability, due to the finite domain support of the interpolating kernels. Another challenging problem for meshfree methods is imposing boundary conditions.

Various numerical models for fabric impact simulation have been developed, using mesh-based, particle-based, and/or grid-based techniques, including: (1) fabric models based on 2-D membrane elements [65, 70, 73, 80, 99, 117, 127], (2) 3-D finite element models at the yarn level [38, 39], (3) fabric models with pin-jointed links [15, 102, 119, 128, 129, 146], (4) lumped mass models with discrete particles on a grid structure [20, 117, 151], (5) digital element method for fabric simulations at the yarn level [136] and at the fiber level [94, 149], and (6) a mesomechanical hybrid particle-element model for neat Kevlar and STF-Kevlar composite [111]. Each method has its owns numerical algorithm to describe the geometry of fabrics, material constitutive relations, contact algorithms, inter-yarn friction effects, and boundary conditions.

Among those methods, the hybrid particle-element method is a very promising computational strategy because it takes advantage of both mesh-based methods and mesh-free methods, by simultaneously using particles and elements [45, 46, 105]. The hybrid method differs from a coupled particle-element method, like the coupled FEM-SPH method in reference [67], in that the hybrid method uses particles and elements at the same time, but not redundantly. Particles are used to describe inertial effects, contact-impact between particles, and thermodynamic states of materials. Elements are used to represent material deformation and strength effects. The hybrid particle-element method has provided validated simulation results for various hypervelocity impact problems and for high-strength fabric impact problems [17, 43, 49, 106].

This chapter presents a literature review of a hybrid particle-element model for impact dynamics of single- or multi-ply Kevlar woven fabrics. The hybrid particle-element method is then extended to model fabric saturated by magnetorheological fluids. The geometry of the MRF treated Kevlar composite is constructed by inserting free fluid particles (with no inter-particle connectivity through a finite element) into the voids of a Kevlar fabric. Because the MR fluid is a mixture of synthetic hydrocarbon oil and iron micro-particles, the thermomechanical properties of MR fluids are modeled using the theory of mixtures. Interpolation kernels are defined to describe the mechanical interaction between neighboring particles in contact. These kernel functions are used to model the contact-impact between the particles and to compute the current density of the particles. A velocity-dependent Bingham plastic fluid model is used to represent field dependent shear yielding and shear viscosity of MR fluids under the application of a magnetic field. Four example simulations are presented to validate the extended hybrid particle-element method against the experimental results discussed in Chapters 2 and 3. The simulation work models (1) FSP impacts on magneto-mechanically edge-clamped MRF-Kevlar composites, (2) FSP impacts on neat Kevlar targets mounted on the target holder shown in Figure 3.3, (3) FSP impacts on PVC-wrapped MRF-Kevlar composites under the magnetic field generated by an electromagnetic coil, and (4) FSP impacts on PVC-wrapped MRF-Kevlar composites with no magnetic field.

5.2 Development of Hybrid Particle-Element Model for MRF-Kevlar Composites

5.2.1 Introduction

A hybrid particle element method has been developed to numerically solve impact problems for a general three-dimensional continuous medium [45, 46, 105, 120, 121]. The hybrid formulation takes advantage of both the energy-based particle hydrodynamics method (Hamiltonian particle hydrodynamics) of Fahrenthold and Koo [47, 48] and finite element based continuum mechanics [19]. In this formulation, classical Lagrangian or Hamiltonian mechanics [52, 55] has been extended to incorporate the thermal states of materials as generalized coordinates in the system Lagrangian or Hamiltonian. This extension has also included internal state variables, such as a plastic strain and damage [44], in a thermodynamically consistent fashion [63, 150].

Recently a mesomechanical hybrid particle-element model has been developed by Rabb to simulate FSP impacts on neat Kevlar fabrics and STF-treated Kevlar composites [111]. In this model, a hybrid particle-bar element structure was chosen to represent the yarn-level crimped geometry of Kevlar woven fabrics, and the theory of mixtures was used to compute the thermodynamic states of the STF-Kevlar composite. A rate dependent friction model was included to represent energy dissipation due to friction between the Kevlar yarns as well as and viscous friction.

The computational research in this dissertation aims at simulating FSP impacts on MRF-Kevlar fabric composites. Unlike Rabb's work, which modeled a fluid particle as a constituent of the STF-Kevlar mixture, MR fluids are modeled here as the individual particles interacting with other structural components, such as projectile and fabric. The separate geometry of the MRF fluid and Kevlar solid provides not only a higher computational resolution (to capture the dynamics of a complex fluid-solid interaction), but also a way of incorporating a field dependent shear strength and friction model for MR fluid in a hybrid particle-element formulation.

5.2.2 Geometric Modeling

In computer-aided-design (CAD) and computer-aided-analysis (CAE) in fabric impact dynamics, various methods for geometric modeling have been investigated. Adanur introduced CAD models for various weave types (plain, basket, twill, etc.) to represent the yarn-level geometry of woven fabrics [6]. A variational formulation based on the principle of minimum strain energy has been used to model a spatial curve for each interwoven yarn [82, 83, 115]. This mesomechanical CAD model for fabrics yarns can be used to impose a geometric constraint on the finite element analysis at each simulation time step. [115]. Nadler has investigated a two-scale model for a fabric [99]: (1) a membrane model in the macro-scale and (2) a micro-scale model for orthogonal yarns interacting inside each membrane. Fabrics have been modeled as a collection of mass particles located at the nodes of an orthogonal grid structure [20, 117, 151]. Membrane finite elements have been chosen, for simplicity and convenience, to model fabrics without yarn-level analysis [65, 70, 73, 80, 99, 127]. Interwoven yarn structures have been modeled using finite elements, by adopting a pre-determined curve for the yarns and a given shape for the yarn cross-section [38, 39]. The complex geometry of a woven fabric has been simplified by modeling only interlaced pin-jointed links [15, 102, 119, 128, 129, 146]. In the digital element method, individual fibers [94, 149], or yarns [136] have been modeled as chained spheres.

Compared to these modeling strategies, a hybrid-particle element model for woven fabric [111] provides a very direct way of modeling the mesomechanical geometry of a fabric. In addition to the fabric, a projectile and other structural components (e.g. MR fluids in this research) can be modeled using a hybrid particle-element method. Therefore, using the hybrid particle-element modeling methodology, complex geometries with various materials can be modeled in a unified fashion. For example, in modeling the impact and compression of materials, the particle based contact-impact algorithm can be applied for any type of particles (either solid or fluid) with any associated element type (either a hexahedral element or a bar element). The types of material geometry considered in work are (1) hybrid particle-hexahedral element models for the projectiles [45, 46, 105, 120], (2) hybrid particle-bar element model for the yarns and PVC-MRF composites [111], and (3) free Lagrangian particle models for MR fluids.

1. **Modeled Geometry of a Projectile**

   Steel and brass projectiles were used in the impact tests presented in Chapters 2 and 3 for MRF-Kevlar composite targets. A non-rigid model for these projectiles is adopted here, and describes a projectile's stiffness, material damping, and equation of state in [9]. The projectiles are modeled with eight-noded hexahedral elements, with an ellipsoidal particle at each node. This hybrid particle-hexahedral element scheme has been used to model various solid metallic, ceramic, and polymeric materials, including steel, aluminum, silicon carbide, carbon-carbon, Kevlar, and Nextel [43, 105, 106, 120]. More specifically, eight nodes are located at the vertices of each element, thus the particles are grouped in each element as shown in Figure 5.1(a). Ellipsoidal particles are used because they can significantly reduce computational costs, by reducing the total number of particles required for structures with a high aspect ratio. The ellipsoidal particle used here is a non-deforming material body whose translational and rotational motion can be described by rigid body kinematics. Material deformation is described by the relative separation distance between particles, as compared to the reference configuration.

Consider an hexahedral element with sides of lengths $2l_1$, $2l_2$, and $2l_3$ (Figure 5.1(b)) and define two aspect ratios with respect to l_2 as $\Phi_1 = \frac{l_1}{l_2} = \frac{h_1}{h_2}$ and $\Phi_3 = \frac{l_3}{l_2} = \frac{h_3}{h_2}$, then the volume of an hexahedral element is

$$V_e = 8l_1l_2l_3 = 8\Phi_1\Phi_3l_2^3 \tag{5.1}$$

Let each ellipsoidal particle have semi-axes h_1, h_2, and h_3 and aspect ratios the same as the element, so that $\Phi_1 = \frac{l_1}{l_2} = \frac{h_1}{h_2}$ and $\Phi_3 = \frac{l_3}{l_2} = \frac{h_3}{h_2}$ (Figure 5.1(b)), then the volume of the particles representing the element volume is

$$V_p = \frac{4}{3}\pi h_1h_2h_3 = \frac{4}{3}\pi\Phi_1\Phi_3h_2^3 \tag{5.2}$$

Because the inertia of the system is modeled by the particles, above two volumes V_e and V_p should be the same. Equating (5.1) and (5.2), the particle half lengths can be expressed in terms of the element lengths as

$$h_2 = \left(\frac{6}{\pi}\right)^{\frac{1}{3}} l_2, \quad h_1 = \Phi_1h_2, \quad h_3 = \Phi_3h_2 \tag{5.3}$$

If the modeled solid material is non-porous, then neighboring particles should be overlapped, according to Equation (5.3). To model contact impact between particles, the effective nodal separation length between neighboring particles is defined such that

$$2h_{\text{eff},i} = 2\beta h_i \tag{5.4}$$

where β is a coefficient depending on the particle packing scheme.

2. **Modeled Geometry of a Kevlar Woven Fabric**

Kevlar fabric is modeled here using the mesomechanical particle-bar element method developed by Rabb, in order to present yarn-level features of woven fabrics (such as yarn crimp and the weave pattern [111]). First, the fabric volume is divided into uniform hexahedral cells whose dimensions are $2l_1$, $2l_2$, and $2l_3$ in x-, y-, and z-direction respectively as shown in Figure 5.2. Here $2l_2$ is set to be the same as the thickness of fabric t that $l_2 = t/4$. Assuming that the warp and weft yarns have an identical shape, the condition $l_1 = l_3$ is imposed, and characterizes the plain weave fabric used in this research. For convenience, the aspect ratio of a unit cell is defined by

$$\Phi = \frac{l_1}{l_2} = \frac{l_3}{l_2} \tag{5.5}$$

The waviness of the warp and weft yarns is used to model the yarn geometry and it is measured by the fabric parameter (C), defined by

$$C = 100 \times \frac{Y - F}{F} \tag{5.6}$$

where F is the linear distance between two ends of a sampled non-stretched yarn and Y is the length of the same yarn after being straightened by tension.

Rabb derived the relationship between Φ and yarn crimp, which is written

$$\Phi^{-2} = \left(\frac{l_2}{l_1}\right)^2 = \frac{1}{4}\left[6(1+C)-2\right]^2 - 4 \tag{5.7}$$

For non-porous materials, the dimensions of an ellipsoidal particle can be determined by equating the element volume $V_e = 8l_1l_2l_3$ and the particle volume $V_p = \frac{4}{3}\pi h_1h_2h_3$,

$$h_2 = \left(\frac{6}{\pi}\right)^{\frac{1}{3}} \frac{t}{4} \tag{5.8}$$

The woven fabric is considered as a porous material, due to its high void fraction (about 0.5 in Kevlar plain weave fabric). Let the void fraction of a fabric be ϕ, then the real particle volume becomes

$$\hat{V}_p = (1-\phi)8l_1l_2l_3 \tag{5.9}$$

The corresponding dimensions of an ellipsoidal particle are $\hat{h}_1$, $\hat{h}_2$, and $\hat{h}_3$. The $\hat{h}_2$ is set to be the same as h_2 to maintain the particle representation of the fabric thickness, regardless of void fraction. In addition, from the similarity condition $\frac{\hat{h}_1}{h_1} = \frac{\hat{h}_3}{h_3}$, the other two particle dimensions are obtained as follows.

$$\begin{aligned} 8(1-\phi)l_1l_2l_3 &= \frac{4}{3}\pi\hat{h}_1h_2\hat{h}_3 && (5.10) \\ \hat{h}_1 = \hat{h}_3 &= (1-\phi)^{\frac{1}{2}}\,\frac{t}{4}\left(\frac{6}{\pi}\right)^{\frac{1}{3}}\Phi && (5.11) \end{aligned}$$

3. **Modeled Geometry of Magnetorheological Fluids**

   Magnetorheological fluids are modeled as a set of particles filling voids in the modeled Kevlar fabric. Figure 5.3(a) shows schematic of the particle representation for a woven Kevlar fabric, treated with MR fluids. Because two Kevlar particles are stacked, in the thickness direction, in the single-ply fabric shown in Figure 5.2(a), two fluid particles can occupy the void space in the woven fabric structure. Unlike the Kevlar particles, which are inter-connected by bar elements, the interstitial MR fluid particles do not have any connectivities. Figure 5.3(b) shows a post-processed image of the MRF-Kevlar composite geometry generated by this modeling strategy.

4. **Modeled Geometry of PVC wrapped Magnetorheological Fluids**

   PVC heat shrink tubing was used to confine the MR fluids in the neat Kevlar fabric. To model the geometry of MRF-Kevlar composites, the PVC-MRF composite structure was divided into two distinct parts: interior and exterior parts with respect to the fabric. The interior part of the fluid is modeled using interstitial fluid particles inside a woven fabric. The exterior part of the model incorporates elements in order to represent strength effects of the PVC tubing. The exterior interconnected bar elements take the forms of an orthogonally gridded 2-D membrane, as shown in Figure 5.4. The solid bar shown in Figure 5.4 is a part of the target frame.

5.2.3 Particle Kinematics

Translational motion of each ellipsoidal particle can be described by the following vector quantities for particle i

$$\mathbf{c}^{(i)} = \left[\begin{array}{ccc} c_1^{(i)} & c_2^{(i)} & c_3^{(i)} \end{array}\right]^T \tag{5.12}$$

$$\mathbf{p}^{(i)} = m^{(i)}\dot{\mathbf{c}}^{(i)} \tag{5.13}$$

where $\mathbf{c}^{(i)}$ is a center of mass position, $\dot{\mathbf{c}}^{(i)}$ is a center of mass velocity, $\mathbf{p}^{(i)}$ is a particle linear momentum, and $m^{(i)}$ is the particle mass. These vector quantities are represented by a 3 by 1 column matrix whose components are expressed with respect to a global coordinate system {OXYZ}, as shown in Figure 5.5 (b).

Rigid body rotation is described by singularity-free Euler parameters [10, 101] defined by

$$\mathbf{e}^{(i)} = \left[\begin{array}{cccc} e_0^{(i)} & e_1^{(i)} & e_2^{(i)} & e_3^{(i)} \end{array}\right]^T \tag{5.14}$$

$$e_0^{(i)} = \cos\left(\frac{\theta^{(i)}}{2}\right) \tag{5.15}$$

$$e_i^{(i)} = u_k^{(i)} \sin\left(\frac{\theta^{(i)}}{2}\right), \qquad k = 1, 2, 3 \tag{5.16}$$

where $\mathbf{u}^{(i)} = \left[\begin{array}{ccc} u_1^{(i)} & u_2^{(i)} & u_3^{(i)} \end{array}\right]^T$ is a unit vector of directed along an axis of rotation and $\theta^{(i)}$ is an angle of rotation for particle i. The Euler parameter vector $\mathbf{e}^{(i)}$ satisfies

$$\mathbf{e}^{(i)^T}\mathbf{e}^{(i)} = 1 \tag{5.17}$$

which is a holonomic constraint in the Lagrangian formulation.

Two coordinate systems are used to express the components of tensor quantities used to describe rotational motion. Those are the global coordinate system {OXYZ} and the co-rotating body fixed coordinate system {oxyz}, as shown in Figure 5.5 (b). Throughout this dissertation, a hat(ˆ) on any tensor quantity means that its components are expressed with respect to the co-rotating system {oxyz}. The particle orientation and angular velocity can be expressed in terms of the Euler parameters and their time derivatives for particle i as follows:

$$\mathbf{R}^{(i)} = \mathbf{E}^{(i)}\mathbf{G}^{(i)^T} \tag{5.18}$$

$$\hat{\boldsymbol{\omega}}^{(i)} = 2\mathbf{G}^{(i)}\dot{\mathbf{e}}^{(i)} \tag{5.19}$$

$$\hat{\boldsymbol{\Omega}}^{(i)} = 2\mathbf{G}^{(i)}\dot{\mathbf{G}}^{(i)^T} = -2\dot{\mathbf{G}}^{(i)}\mathbf{G}^{(i)^T} \tag{5.20}$$

$$\hat{\mathbf{h}}^{(i)} = \hat{\mathbf{J}}^{(i)}\hat{\boldsymbol{\omega}}^{(i)} = 2\hat{\mathbf{J}}^{(i)}\mathbf{G}^{(i)}\dot{\mathbf{e}}^{(i)} \tag{5.21}$$

with

$$\mathbf{E}^{(i)} = \begin{bmatrix} -e_1^{(i)} & e_0^{(i)} & -e_3^{(i)} & e_2^{(i)} \\ -e_2^{(i)} & e_3^{(i)} & e_0^{(i)} & -e_1^{(i)} \\ -e_3^{(i)} & -e_2^{(i)} & e_1^{(i)} & e_0^{(i)} \end{bmatrix} \tag{5.22}$$

$$\mathbf{G}^{(i)} = \begin{bmatrix} -e_1^{(i)} & e_0^{(i)} & e_3^{(i)} & -e_2^{(i)} \\ -e_2^{(i)} & -e_3^{(i)} & e_0^{(i)} & e_1^{(i)} \\ -e_3^{(i)} & e_2^{(i)} & -e_1^{(i)} & e_0^{(i)} \end{bmatrix} \tag{5.23}$$

where $\mathbf{R}$ is an orthogonal rotation matrix satisfying $\mathbf{a} = \mathbf{R}\hat{\mathbf{a}}$ for an arbitrary vector $\mathbf{a}$, $\hat{\boldsymbol{\omega}}$ is an angular velocity for a rotating rigid body with coordinates expressed in the co-rotating frame {oxyz}, $\hat{\boldsymbol{\Omega}}$ is a skew symmetric matrix associated with the vector $\hat{\boldsymbol{\omega}}$, satisfying $\hat{\boldsymbol{\Omega}}\hat{\mathbf{b}} = \hat{\boldsymbol{\omega}} \times \hat{\mathbf{b}}$ for an arbitrary vector

$\hat{\mathbf{b}}$, $\hat{\mathbf{h}}$ is the angular momentum of a rigid body, and $\hat{\mathbf{J}}$ is the mass moment of inertia of a rigid body.

5.2.4 Finite Element Kinematics

Element kinematics are described by strain definitions incorporating finite deformation. Because the hybrid particle-element method takes advantage of the energy methods used in Lagrangian or Hamiltonian mechanics, and general continuum thermomechanics, element kinematics plays a key role. An element strain is needed to describe various forms of strain energy associated with the element deformation. Two types of finite elements are used to model the geometry of a projectile and the Kevlar woven fabric; their kinematics are described in the following section.

1. **Kinematics of Three-Dimensional Hexahedral Elements**

   Eight-noded three-dimensional hexahedral finite elements are chosen to model the fragment simulating projectile. Their element strain is decomposed into volumetric and deviatoric strain parts and the deviatoric strain is further decomposed into a elastic strain and an isochoric plastic strain [46, 105, 120]. The volumetric deformation is measured by an element Jacobian. The shear deviatoric strain for element j is written as

   $$\bar{\mathbf{E}}^{(j)} = \frac{1}{2}\left(\bar{\mathbf{C}}^{(i)} - \mathbf{I}\right) \tag{5.24}$$

with

$$\begin{aligned}\bar{\mathbf{C}}^{(j)} &= \bar{\mathbf{F}}^{(j)T}\bar{\mathbf{F}}^{(j)} &(5.25)\\ \bar{\mathbf{F}}^{(j)} &= J^{(j)^{-\frac{1}{3}}}\mathbf{F}^{(j)} &(5.26)\\ J^{(j)} &= \det\left(\mathbf{F}^{(j)}\right) &(5.27)\end{aligned}$$

where $\bar{\mathbf{E}}$ is a deviatoric Euler-Lagrange strain tensor, $\bar{\mathbf{C}}$ is a deviatoric right Cauchy-Green strain tensor, $\mathbf{I}$ is the second-order identity tensor, $\mathbf{F}$ is a deformation gradient tensor, $\bar{\mathbf{F}}$ is its unimodular part (since $\det(\bar{\mathbf{F}}) = 1$), and J is the Jacobian of the deformation gradient tensor $\mathbf{F}$.

Decomposition of the deviatoric strain tensor is assumed, to separate its elastic and plastic parts in following additive manner:

$$\begin{aligned}\bar{\mathbf{E}}^{(j)} &= \bar{\mathbf{E}}^{e(j)} + \mathbf{E}^{p(j)} &(5.28)\\ \mathbf{E}^{p(j)} &= \frac{1}{2}\left(\mathbf{C}^{p(j)} - \mathbf{I}\right) &(5.29)\end{aligned}$$

where $\bar{\mathbf{E}}^e$ is an elastic deviatoric strain tensor, $\bar{\mathbf{E}}^p$ is a plastic strain tensor, and $\bar{\mathbf{C}}^p$ is a plastic right Cauchy-Green strain tensor. Assuming that plastic deformation is isochoric, the determinant of $\bar{\mathbf{C}}^p$ is constant, hence

$$\mathrm{tr}\left(\mathbf{C}^{p(j)^{-T}}\dot{\mathbf{C}}^{p(j)}\right) = 0 \qquad (5.30)$$

or equivalently,

$$\mathrm{tr}\left(\mathbf{C}^{p(j)^{-T}}\dot{\mathbf{E}}^{p(j)}\right) = 0 \qquad (5.31)$$

where $\mathrm{tr}(\cdot)$ is the trace of a matrix.

An effective plastic strain rate is defined by

$$\dot{\epsilon}^{p(j)} = \|\dot{\mathbf{E}}^{p(j)}\| \tag{5.32}$$

where $\|\cdot\|$ is a scalar-valued tensor operator defined by

$$\|\mathbf{A}\| = \sqrt{\frac{1}{2}\mathrm{tr}\left(\mathbf{A}^T\mathbf{A}\right)} \tag{5.33}$$

for an arbitrary second-order tensor A. The effective plastic strain (ϵ^p) is used later to express a yield criterion, including strain hardening and thermal softening effects.

2. **Kinematics of One-Dimensional Bar Elements**

One-dimensional bar elements were chosen to model the geometry of interwoven yarns in a hybrid particle-element formulation for impact dynamics of Kevlar woven fabrics [111]. Because each bar element connects two particles, a reference element volume can be simply obtained by averaging the associated particle volumes. Denoting an element linking two particles i and j with an index (i,j), the element reference volumes can be written as

$$V_0^{(i,j)} = \frac{1}{2}\left(V_0^{(i)} + V_0^{(j)}\right) \tag{5.34}$$

where V_0 is a reference volume.

An element strain is calculated using

$$\begin{aligned} \epsilon^{(i,j)} &= \frac{l^{(i,j)}}{l_0^{(i,j)}} - 1 && (5.35)\\ l^{(i,j)} &= |\mathbf{c}^{(i)} - \mathbf{c}^{(j)}| && (5.36)\\ l_0^{(i,j)} &= |\mathbf{c}_0^{(i)} - \mathbf{c}_0^{(j)}| && (5.37) \end{aligned}$$

where $l^{(i,j)}$ is a current nodal separation distance between particles i and j, its reference value is $l_0^{(i,j)}$.

To enable all state variables to be defined particles, a strain measure is assigned to particle i by

$$\epsilon^{(i)} = \frac{1}{n_n^{(i)}} \sum_{j=1}^{n} \alpha_{ij} \epsilon^{(i,j)} \tag{5.38}$$

where $n_n^{(i)}$ is number of bar elements connected to particle i.

5.2.5 Density Interpolation

The density interpolation scheme formulated by Shivarama and Fahrenthold [120] and Park and Fahrenthold [105] can be used for all particle types. The current density of particle i can be obtained by using an interpolation kernel

$$\rho^{(i)} = \rho_0^{(i)} + \sum_{j=1}^{n_n} \rho_0^{(j)} W^{(i,j)} \tag{5.39}$$

where $\rho^{(i)}$ is a particle current density, $\rho_0^{(i)}$ is a particle reference density, $n_n^{(i)}$ is the number of the neighboring particles for particle i, and $W^{(i,j)}$ is a density interpolation kernel defined by

$$W^{(i,j)} = \frac{1}{n_n}(1 - \delta_{ij}) \left[\left(\frac{1}{\zeta^{(i,j)}} \right)^3 - 1 \right] \hat{u}(\xi^{(i,j)}) \tag{5.40}$$

$$\xi^{(i,j)} = \min \left[1, \frac{3}{2} \left(\frac{\rho_0^{(i)}}{\rho^{(i)}} \right)^{\frac{1}{3}} \right] - \zeta^{(i,j)} \tag{5.41}$$

where δ_{ij} denotes the Kronecker delta function. The function $\zeta^{(i,j)}$ is the normalized nodal separation distance two particles; it can be obtained in a co-rotating frame fixed to the ellipsoidal particle j using

$$\begin{aligned}
\zeta^{(i,j)} &= \sqrt{\left(\mathbf{c}^{(i)} - \mathbf{c}^{(j)}\right)^T \mathbf{H}^{(j)} \left(\mathbf{c}^{(i)} - \mathbf{c}^{(j)}\right)} && (5.42) \\
\mathbf{H}^{(j)} &= \mathbf{R}^{(j)} \hat{\mathbf{H}}^{(j)} \mathbf{R}^{(j)T} && (5.43) \\
\hat{\mathbf{H}}^{(j)} &= \begin{bmatrix} 2\beta h_1^{(j)} & 0 & 0 \\ 0 & 2\beta h_2^{(j)} & 0 \\ 0 & 0 & 2\beta h_3^{(j)} \end{bmatrix}^{-2} && (5.44)
\end{aligned}$$

where $h_1^{(j)}$, $h_2^{(j)}$, $h_3^{(j)}$ are the principal semi-axis of the ellipsoidal particle j shown in Figure 5.5(a). The parameter β is determined by the close packing distance for ellipsoidal particles in the reference configuration.

5.2.6 Kinetic Energy and Kinetic Co-Energy

The total kinetic co-energy is an algebraic sum of the individual kinetic co-energies of the particles, hence

$$T^* = \sum_{i=1}^{n} T^{*(i)} \tag{5.45}$$

where $T^{*(i)}$ is a kinetic co-energy associated with particle i. It consists of a translational energy described by the center-of-mass velocity and a rotational energy represented by the Euler parameters,

$$\begin{aligned}
T^{*(i)} &= \frac{1}{2} m^{(i)} \dot{\mathbf{c}}^{(i)T} \dot{\mathbf{c}}^{(i)} + \frac{1}{2} \hat{\boldsymbol{\omega}}^{(i)T} \hat{\mathbf{J}}^{(i)} \hat{\boldsymbol{\omega}}^{(i)} && (5.46) \\
&= \frac{1}{2} m^{(i)} \dot{\mathbf{c}}^{(i)T} \dot{\mathbf{c}}^{(i)} + 2 \dot{\mathbf{e}}^{(i)T} \mathbf{G}^{(i)T} \hat{\mathbf{J}}^{(i)} \mathbf{G}^{(i)} \dot{\mathbf{e}}^{(i)} \\
&= \frac{1}{2} m^{(i)} \dot{\mathbf{c}}^{(i)T} \dot{\mathbf{c}}^{(i)} + 2 \mathbf{e}^{(i)T} \dot{\mathbf{G}}^{(i)T} \hat{\mathbf{J}}^{(i)} \dot{\mathbf{G}}^{(i)} \mathbf{e}^{(i)}
\end{aligned}$$

Generalized momenta associated with $\dot{\mathbf{c}}^{(i)}$, $\dot{\mathbf{e}}^{(i)T}$, and $\dot{\hat{\boldsymbol{\omega}}}^{(i)}$ are defined by reference [121], and are

$$\begin{aligned}
\mathbf{p}^{(i)} &= \frac{\partial T^*}{\partial \dot{\mathbf{c}}^{(\mathbf{i})}} = m^{(i)}\dot{\mathbf{c}}^{(\mathbf{i})} && (5.47)\\
\mathbf{h_e}^{(i)} &= \frac{\partial T^*}{\partial \dot{\mathbf{e}}^{(\mathbf{i})}} = 4\mathbf{G}^{(i)T}\hat{\mathbf{J}}^{(i)}\mathbf{G}^{(i)}\dot{\mathbf{e}}^{(i)} && (5.48)\\
\hat{\mathbf{h}}^{(i)} &= \frac{\partial T^*}{\partial \hat{\boldsymbol{\omega}}^{(i)}} = 2\hat{\mathbf{J}}^{(i)}\mathbf{G}^{(i)}\dot{\mathbf{e}}^{(i)} && (5.49)
\end{aligned}$$

The total system kinetic energy T can be obtained using the following Legendre transform of T^*,

$$T = \sum_{i=1}^{n}\left[\mathbf{p}^{(i)T}\dot{\mathbf{c}}^{(i)} + \hat{\mathbf{h}}^{(i)T}\hat{\boldsymbol{\omega}}^{(i)}\right] - T^* \tag{5.50}$$

which yields

$$T = \sum_{i=1}^{n}\left[\frac{1}{2m^{(i)}}\mathbf{p}^{(i)T}\mathbf{p}^{(i)} \; + \; \frac{1}{2}\hat{\mathbf{h}}^{(i)T}\hat{\mathbf{J}}^{(i)-T}\hat{\mathbf{h}}(i)\right] \tag{5.51}$$

5.2.7 Thermo-Mechanical System Potential Energy

As previously discussed in the discussion of the kinematics for the finite elements, the hexahedral elements and bar elements have different strain expressions. Therefore, unlike the system kinetic energy, the system potential energy, specifically the element strain energy, is formulated separately for those two cases.

1. **Potential Energy for the Particle-Hexahedral Element Model**

   The system potential energy is composed of a thermomechanical internal energy and a mechanical strain energy. In the hybrid particle-element formulation, the thermomechanical potential energy can be written as [105]

$$V = \sum_{i=1}^{n} U^{(i)} + \sum_{j=1}^{n_e} \alpha_{ij} V_0^{e(j)} \Psi^{(j)} + \sum_{j=1}^{n_e} \sum_{k=1}^{n_s} V_0^{e(j,k)} \Psi^{(j,k)} \tag{5.52}$$

where $U^{(i)}$ is an internal energy, n is the number of particles, n_e is the number of elements, n_s is the number of subelements per element, $V_0^{e(j)}$ is the reference volume for element j, $V_0^{e(j,k)}$ is the reference volume for subelement k associated with element j, $\Psi^{(j)}$ is the strain energy per unit volume in shear for element j, and $\Psi^{(j,k)}$ is the strain energy per unit volume in tension for subelement (j,k).

The shear and tensile strain energies, $\Psi^{(j)}$ and $\Psi^{(j,k)}$, are defined here by

$$\begin{aligned} \Psi^{(j)} &= (1 - d^{(j)}) \mu^{(j)} \mathrm{tr} \left(\mathbf{E}^{e(j)T} \mathbf{E}^{e(j)} \right) && (5.53) \\ \Psi^{(j,k)} &= \frac{1}{2} (1 - D^{(j)}) K^{(j)} \left\langle J^{(j,k)} - 1 \right\rangle^2 && (5.54) \end{aligned}$$

where $d^{(j)}$ is a shear damage variable, $\mu^{(j)}$ is a shear modulus, $\mathbf{E}^{e(j)}$ is an elastic deviatoric strain tensor, $D^{(j)}$ a volumetric damage variable, $K^{(j)}$ is a bulk modulus, $J^{(j,k)}$ is the subelement Jacobian associated with subelement (j,k), and $< \cdot >$ is the bracket function satisfying

$$\begin{array}{ll} < x > = x & \text{for} \quad x \geq 0 \\ < x > = 0 & \text{for} \quad x < 0 \end{array} \tag{5.55}$$

The system potential energy of Equation (5.52) has the following functional form:

$$V = V \left(\mathbf{c}^{(i)}, U^{(i)}, d^{(j)}, D^{(j)}, \mathbf{E}^{p(j)} \right) \tag{5.56}$$

Since

$$\begin{aligned} J^{(j,k)} &= J^{(j,k)}(\mathbf{c}^{(i)}) && (5.57) \\ \mathbf{E}^{e(j)} &= \bar{\mathbf{E}}^{(j)}(\mathbf{c}^{(i)}) - \mathbf{E}^{p(j)} = \mathbf{E}^{e(j)}(\mathbf{c}^{(i)}, \mathbf{E}^{p(j)}) && (5.58) \end{aligned}$$

Therefore, the generalized conservative forces derived from Equation (5.56) are

$$\begin{aligned} \mathbf{g}^{(i)} &= \frac{\partial V}{\partial \mathbf{c}^{(i)}} && (5.59) \\ 1 &= \frac{\partial V}{\partial \mathbf{U}^{(i)}} && (5.60) \\ \Gamma^{d(j)} &= -\frac{\partial V}{\partial d^{(j)}} && (5.61) \\ \Gamma^{D(j)} &= -\frac{\partial V}{\partial D^{(j)}} && (5.62) \\ \mathbf{S}^{(j)} &= -\frac{1}{V_0^{(j)}} \frac{\partial V}{\partial \mathbf{E}^{p(j)}} && (5.63) \end{aligned}$$

where $\mathbf{g}^{(i)}$ is a conservative force associated with the center of mass coordinates, $\Gamma^{d(j)}$ and $\Gamma^{D(j)}$ are energy release rates due to the shear and normal damage accumulation, and $\mathbf{S}^{(j)}$ is a plastic stress tensor.

2. **Potential Energy for Particle-Bar Element Model**

Total strain energy is derived for a hybrid particle-element model using bar elements [111] as:

$$V = \sum_{i=1}^{n} U^{(i)} + \sum_{i=1}^{n} \sum_{j=1}^{n} \alpha_{ij} V_o^{(i,j)} \psi^{(i,j)} + \sum_{i=1}^{n} \sum_{j=1}^{n} \alpha_{ij} V_o^{(i,j)} \phi^{(i,j)} \qquad (5.64)$$

where α_{ij} is a Boolean matrix specifying the connectivity between two particles i and j, $V_o^{(i,j)}$ is the average volume defined in Equation (5.34),

$\psi^{(i,j)}$ is an element strain energy per unit volume due to tension, and $\phi^{(i,j)}$ is a shear strain energy due to the relative rotational displacements of two interconnected particles. The function $\phi^{(i,j)}$ is used to represent a strain energy in torsion. These tensile and shear strain energies are defined by

$$\begin{aligned}
\psi^{(i,j)} &= \frac{1}{2}E^{(i,j)}(1-d^{(i,j)}) < \epsilon^e >^2 && (5.65)\\
\phi^{(i,j)} &= (1-d^{(i,j)})\kappa\mu^{(i,j)}(\mathbf{e}^{(i)}-\mathbf{e}^{(j)})^T(\mathbf{e}^{(i)}-\mathbf{e}^{(j)}) && (5.66)\\
E^{(i,j)} &= \frac{1}{2}\left(E^{(i)}+E^{(j)}\right) && (5.67)\\
d^{(i,j)} &= \frac{1}{2}\left(d^{(i)}+d^{(j)}\right) && (5.68)
\end{aligned}$$

where ϵ^e is the elastic tensile strain from Equation (5.35), $E^{(i,j)}$ is average elastic modulus and $d^{(i,j)}$ is an average damage, κ is a dimensionless penalty stiffness and $\mu^{(i,j)}$ is an average shear modulus.

If the internal energy $U^{(i)}$ for particle i is taken as a system generalized coordinate, the total potential energy takes the following functional form:

$$V = V(\mathbf{c}^{(i)}, \mathbf{e}^{(i)}, U^{(i)}, d^{(i)}, \epsilon^{p(i)}) \qquad (5.69)$$

and its associated generalized forces are

$$\mathbf{g}^{(i)} = \frac{\partial V}{\partial \mathbf{c}^{(i)}} \tag{5.70}$$

$$\mathbf{M_e}^{(i)} = \frac{\partial V}{\partial \mathbf{e}^{(i)}} \tag{5.71}$$

$$1 = \frac{\partial V}{\partial \mathbf{U}^{(i)}} \tag{5.72}$$

$$\Gamma^{d(i)} = -\frac{\partial V}{\partial d^{(i)}} \tag{5.73}$$

$$\sigma^{p(i)} = -\frac{1}{V_0^{(i)}}\frac{\partial V}{\partial \epsilon^{p(i)}} \tag{5.74}$$

where $\mathbf{g}^{(i)}$ is a conservative force associated with a particle translation, $\mathbf{M}^{(i)}$ is a conservative force associated with a particle rotation, $\Gamma^{d(j)}$is an energy release rate caused by damage accumulation, and $\sigma^{p(i)}$ is a plastic stress associated with an effective plastic strain ϵ^p. Specifically, explicit expressions for these generalized conservative forces are found in [111].

Unlike the potential energy for hexahedral element case, the bar element formulation adopts an averaging scheme to obtain element quantities from a mean value of two associated particle quantities. This averaging procedure means that the equations of motion for the bar particle-elements only incorporate particle state variables. Compared to a three-dimensional finite element formulation for yarns and fabrics using a linear orthotropic elasticity model [37–39, 110], the hybrid particle-element formulation gains computational efficiency, without losing accuracy. Any reliable stress-strain constitutive relation for a single fiber or yarn can be directly incorporated. The hybrid simulation methodology can also model intra- or inter-yarn friction and contact-impact between yarns.

A Mie-Grüneisen type of equation of state is used here to compute the pressure

$$P = P_H\left(1 - \frac{\Gamma\mu}{2}\right) + \Gamma\rho(u - u_0) \tag{5.75}$$

where ρ is a mass density, u is a specific internal energy, P_H is the pressure on the Hugoniot curve which can be approximated in the following polynomial form:

$$\begin{array}{rll} P_H = & K_1\mu + K_2\mu^2 + K_3\mu^3 & \text{for } \mu \geq 0 \\ P_H = & K_1\mu & \text{for } \mu < 0 \end{array} \tag{5.76}$$

where μ is is the material compression, and Γ is the Grüneisen parameter [144]

$$\mu = \frac{\rho}{\rho_0} - 1 \tag{5.77}$$

$$\Gamma = \frac{\beta_T K}{\rho_0 C_v} \tag{5.78}$$

Here β_T is a volumetric thermal expansion coefficient, K is an isothermal bulk modulus, ρ_0 is a reference mass density, and C_v a specific heat capacity at constant volume.

When modeling a mixture (e.g. magnetorheological fluids in this work), the theory of mixtures can be applied to describe the equation of state. A mixture equation of state can be derived when the mass fractions and thermodynamic properties for each constituent are known. Mixture equations of state have been derived for the hybrid particle-element formulation used to represent an STF-Kevlar composite [111].

Assuming a homogeneous mixture with a known mass fraction for each individual constituent, the total mass of a mixture can be written as

$$m = \sum_{i=1}^{n_m} m_i \tag{5.79}$$

where n_m is the number of materials in the mixture

Mass fraction of constituent material i is defined by

$$f_i = \frac{m_i}{m} \tag{5.80}$$

The total internal energy of the mixture

$$U = \sum_{i=1}^{n_m} m_i u_i \left(\rho_i, s_i\right) \tag{5.81}$$

where the specific internal energy u_i is expressed as a function of the density ρ_i and the specific entropy s_i.

Pressure P and temperature θ can be obtained from the following thermodynamic relations:

$$P = \rho^2 \frac{\partial u}{\partial \rho} \tag{5.82}$$

$$\theta = \frac{\partial u}{\partial s} \tag{5.83}$$

where ρ is a mass density, u is a specific internal energy, and s is a specific entropy. For any ellipsoidal body of mass m, in the hybrid particle-element model, the thermodynamic states are assumed to be homogeneous throughout each individual body. Therefore, the internal energy and entropy for particle

i are

$$U^{(i)} = m^{(i)} u^{(i)} \tag{5.84}$$

$$S^{(i)} = m^{(i)} s^{(i)} \tag{5.85}$$

From the work by Rabb [111], the mixture equation of state can be expressed

$$P = \sum_{i=1}^{n_m} f_i P_i \frac{\rho_0}{\rho_{i0}} \tag{5.86}$$

$$\theta = \sum_{i=1}^{n_m} f_i \theta_i \frac{c_{vi}}{c_v} \tag{5.87}$$

where ρ_0 is reference density for the mixture, ρ_{i0} is the reference density of a constituent, c_v is the specific heat for the mixture, and c_{vi} is the specific heat for a constituent.

5.2.8 Damage and Plasticity Models

Various damage evolution models can be conveniently incorporated into the hybrid particle-element formulation, in a thermodynamically consistent fashion, by defining damage variables as internal state variables. Fahrenthold and Horban [44] developed two continuum damage models, a Grady-Kipp type model and a Johnson-Holmquist type, to separately represent volumetric and shear damage mechanics. Here a simple damage model [45, 46, 105, 120] has been adopted, for a computational efficiency, to describe material failure in impact problems. The simple damage evolution equations for element j are

$$\dot{d}^{(j)} = \frac{\Lambda^{(j)}}{\hat{n}\Delta t}\hat{u}(1 - d^{(j)}) \tag{5.88}$$

$$\dot{D}^{(j)} = \frac{\Lambda^{(j)}}{\hat{n}\Delta t}\hat{u}(1 - D^{(j)}) \tag{5.89}$$

where $\Lambda^{(j)}$ is a Boolean parameter which indicates whether an element j has failed, $\hat{n}$ is the number of time steps over which damage fracture occurs, Δt is a computational time step, and $\hat{u}$ the Heaviside step function. The parameter $\Lambda^{(j)}$ is initially set to zero, and becomes one when one of the following failure criteria is met [120]: (1) a maximum plastic strain criterion (2) a maximum compression criterion, (3) a maximum tensile stress criterion, and (4) melt or char temperature criterion.

Experimental and analytical work has developed various strength models to describe the failure of fabric materials. These include statistical models using Weibull parameters [137, 138], rate-dependent strength models [111, 118, 137], and temperature-dependent yarn fracture models [138]. In this computational study, strain rate dependency is not modeled and a maximum strain failure criterion is used, so that fabric damage is initiated when

$$\epsilon^{(i)} \geq \epsilon_f \tag{5.90}$$

where $\epsilon^{(i)}$ is nodal strain at particle i and ϵ_f is the tensile strain at which yarn fracture occurs.

A plasticity model can also be incorporated into the hybrid particle-element model, by introducing plastic strain as an internal state variable and then modeling its time evolution equation. Here modeling plasticity is separately considered for the hexahedral element and the bar element cases.

1. Plasticity Model for the Hexahedral Elements

A non-associative flow rule satisfying the isochoric constraint of Equation (5.31) has been adopted to describe plastic deformation in hybrid particle-hexahedral element formulations [45, 105, 120]. The plastic flow rule for element j is

$$\dot{\mathbf{E}}^{p(j)} = \frac{\dot{\lambda}^{(j)}}{\|\mathbf{S}^{p(j)}\|} \underline{\underline{\mathbf{N}}}^{p(j)} \underline{\underline{\mathbf{N}}} \mathbf{S}^{p(j)} \tag{5.91}$$

where $\dot{\lambda}^{(j)}$ is a positive coefficient and $\| \cdot \|$ is a scalar-valued tensor operator defined by Equation (5.33), $\underline{\underline{\mathbf{N}}}^{p(j)}$ and $\underline{\underline{\mathbf{N}}}$ are fourth-order tensors defined for an arbitrary second-order tensor $\mathbf{A}$ by [105]

$$\begin{aligned} \underline{\underline{\mathbf{N}}}^{p(j)} \mathbf{A} &= \frac{1}{2\|\mathbf{C}^{p(j)}\|} \left(\mathbf{C}^{p(j)} \mathbf{A} + \mathbf{A} \mathbf{C}^{p(j)} \right) && (5.92) \\ \underline{\underline{\mathbf{N}}} \mathbf{A} &= \mathbf{A} - \frac{1}{3} \mathrm{tr}(\mathbf{A}) \mathbf{I} && (5.93) \end{aligned}$$

with $\mathbf{C}^{p(j)}$ a plastic right Cauchy-Green strain tensor for element j and $\mathbf{I}$ the second-order identity tensor. Here $\mathbf{S}^{p(j)}$ is an effective plastic stress given by

$$\mathbf{S}^{p(j)} = \underline{\underline{\mathbf{N}}}^T {\underline{\underline{\mathbf{N}}}^{p(j)}}^T \mathbf{S}^{(j)} \tag{5.94}$$

where $\mathbf{S}^{(j)}$ is the plastic stress tensor defined by the generalized force associated with the plastic strain tensor $\mathbf{E}^{p(j)}$ in Equation (5.63).

A yield function for each element, expressed in terms of the effective plastic stress, is

$$f^{(j)} = \|\mathbf{S}^{p(j)}\| - Y^{(j)} \tag{5.95}$$

where $Y^{(j)}$ is the yield stress and yielding of element j occurs when $f^{(j)} > 0$. The yield stress, including strain hardening and thermal softening effects, used here is [105]

$$Y^{(j)} = Y_0^{(j)}(1 - d^{(j)})(1 + \kappa^{p(j)}\epsilon^{p(j)})^{\alpha^{p(j)}}(1 - \eta^{p(j)}\theta^{H(j)}) \tag{5.96}$$

where $\epsilon^{p(j)}$ is the effective plastic strain from Equation (5.32), $Y_0^{(j)}$ is the reference yield stress, $\kappa^{p(j)}$ is a strain hardening coefficient, $\alpha^{p(j)}$ is a strain hardening exponent, $\eta^{p(j)}$ is a thermal softening coefficient, and $\theta^{H(j)}$ is the maximum historical homologous temperature.

The increment in $\mathbf{E}^{p(j)}$ for each computational time step Δt is obtained using

$$\Delta\lambda^{(j)} = \frac{< f^{(j)} >}{(1 - d^{(j)})2\mu^{(j)}} \tag{5.97}$$

2. **Plasticity Model for the Bar Elements**

The same yield function and yield stress determined by Equations (5.95) and (5.96) are used for bar elements, again computing a particle average,

$$f^{(i,j)} = \sigma^{p(i,j)} - Y^{(i,j)} \tag{5.98}$$

$$Y^{(i,j)} = Y_0^{(i,j)}(1 - d^{(i,j)})(1 + \kappa^{p(i,j)}\epsilon^{p(i,j)})^{\alpha^{p(i,j)}}(1 - \eta^{p(i,j)}\theta^{H(i,j)}) \tag{5.99}$$

where $\sigma^{p(i,j)}$ is the plastic stress for a bar element connecting two particles i and j and $\epsilon^{p(i,j)}$ is the plastic strain. The failure of a yarn occurs when the strain reaches a specified plastic failure strain.

5.2.9 Friction Models

Frictional effects associated with impact dynamics includes material damping in tension/compression, intra- and inter-material Coulomb friction in shear, and intra- and inter-material viscous friction. These friction effects can be modeled using the relative velocities between neighboring particles. The normal component of the relative velocity is used for material damping effects and a tangential component is used to model friction in shear. Material damping can be incorporated into a computational model as a constitutive relation, e.g. as a viscoelastic model for a fabric [65, 102, 119, 128]. In this hybrid particle-element formulation, an elastic-plastic constitutive model with damage variables is chosen to model Kevlar fabrics, and an artificial viscosity [62] is introduced in modeling material compression under shock and impact. Details of the artificial viscosity are presented in the next section. A general shear friction model was introduced by Rabb [111]. It is a velocity dependent friction model which can be used to represent Coulomb friction, viscous friction, and a Bingham plastic model [86].

1. **Velocity Dependent Friction Model in General Form**

   A scalar shear force can be calculated from the shear yield stress

   $$f_0 = \tau_0 A \tag{5.100}$$

   where τ_0 is the shear yield stress and A is the area in contact, defined by a particle cross-sectional area cut by the surface of an associated element

   $$A = \frac{\pi r^2}{\frac{N}{2}} \tag{5.101}$$

where r is the particle radius determined by $r = \sqrt[3]{h_1 h_2 h_3}$ for an ellipsoid and N is the number of neighboring particles in contact. A velocity dependent friction model has been adopted in the hybrid particle-element formulation, to avoid the singularity of Coulomb friction model, which may cause a physically inconsistent direction of friction force for a finite computational time step during which the sign of the relative velocity changes. The friction model for neighboring particles i and j used here [111] is

$$\mathbf{f}^{(i)} = \sum_{j=1}^{N} \alpha_{ij} \min\left(m^{(i)}, m^{(j)}\right) \frac{\mathbf{v}^{t(i,j)}}{\Delta t} \qquad \text{for} \quad |\mathbf{v}^{t(i,j)}| \leq v_c \quad (5.102)$$

$$\mathbf{f}^{(i)} = \sum_{j=1}^{N} \alpha_{ij} \tau^{(i,j)} A^{(i,j)} \frac{\mathbf{v}^{t(i,j)}}{|\mathbf{v}^{t(i,j)}|} \qquad \text{for} \quad |\mathbf{v}^{t(i,j)}| > v_c \quad (5.103)$$

where v_c is a critical velocity, α_{ij} a Boolean matrix identifying particle contact, $\tau^{(i,j)}$ is the average shear stress, $A^{(i,j)}$ is the average contact area, and $\mathbf{v}^{t(i,j)}$ is a tangential relative velocity between two particles i and j. The quantities $\tau^{(i,j)}$, $A^{(i,j}$, and $\mathbf{v}^{t(i,j)}$ are defined by

$$\tau^{(i,j)} = \frac{1}{2}\left(\tau^{(i)} + \tau^{(j)}\right) \quad (5.104)$$

$$A^{(i,j)} = \frac{1}{2}\left(A^{(i)} + A^{(j)}\right) \quad (5.105)$$

$$\mathbf{v}^{t(i,j)} = \mathbf{v}^{(i,j)} - \mathbf{v}^{n(i,j)} \quad (5.106)$$

with

$$
\begin{aligned}
\mathbf{v}^{(i,j)} &= \dot{\mathbf{c}}^{(i)} - \dot{\mathbf{c}}^{(j)} && (5.107) \\
\mathbf{v}^{n(i,j)} &= \left[\left(\dot{\mathbf{c}}^{(i)} - \dot{\mathbf{c}}^{(j)}\right) \cdot \left(\mathbf{c}^{(i)} - \mathbf{c}^{(j)}\right)\right] \frac{\mathbf{c}^{(i)} - \mathbf{c}^{(j)}}{\left|\mathbf{c}^{(i)} - \mathbf{c}^{(j)}\right|^2} && (5.108)
\end{aligned}
$$

If $\tau^{(i)}$ and $\tau^{(j)}$ are constant for particles i and j, Equations (5.102) and (5.103) represent a non-singular version of a Coulomb friction model.

2. **Bingham Fluid Model**

   A Bingham plastic model is a visco-plastic constitutive equation for a viscous fluid having a shear yield stress. Equations (5.102) and (5.103) can be used to model Bingham plastic flow, by specifying the stress term in the equations as

   $$\tau^{(i,j)} = \tau_0^{(i,j)} + \eta^{(i,j)}\dot{\gamma}^{(i,j)} \tag{5.109}$$

   where $\tau_0^{(i,j)}$ the shear yield stress, $\eta^{(i,j)}$ is the average shear viscosity, and $\dot{\gamma}^{(i,j)}$ is the shear strain rate for the particles i and j, defined by

   $$\dot{\gamma}^{(i,j)} = \frac{\left|\mathbf{v}^{t(i,j)}\right|}{l^{(i,j)}} \tag{5.110}$$

3. **Magnetic Field Dependent Bingham Fluid Model for MR Fluids**

   A magnetic field dependent Bingham plastic model has been used previously to model magnetorheological fluids[51, 122]. The field dependency can be written as

   $$
   \begin{aligned}
   \tau_0 &= \tau_0(\mathbf{B}_{\text{ext}}) && (5.111) \\
   \eta &= \eta(\mathbf{B}_{\text{ext}}) && (5.112)
   \end{aligned}
   $$

where $\mathbf{B}_{\text{ext}}$ is the magnetic flux density due to an applied magnetic field. Normally the field dependency of η is neglected and the value for η is chosen the same as the non-magnetized fluid viscosity. The shear yield stress $\tau_0(\mathbf{B}_{\text{ext}})$ for magnetorheological fluids can be derived using magnetostatic theory for the magnetization of iron particles [122], or can be determined based on the manufacturer's specification [84]. In this model, the field dependency of the shear stress is based on experimental data from the manufacturer of the MR fluid.

5.2.10 Artificial Viscosity

Artificial viscosity is introduced to impose damping effects during shock compression of converging particles. The objective of artificial viscosity is to smooth numerical solutions. Here the artificial viscous force [105] for particle i is defined by

$$\mathbf{f}^{v(i)} = \sum_{j=1}^{n} \nu^{(i,j)} \max\left\{0, v^{(i,j)}\right\} \mathbf{r}^{(i,j)} \hat{u}(1-\zeta^{(i,j)}) \tag{5.113}$$

where

$$\mathbf{r}^{(i,j)} = \frac{\mathbf{c}^{(i)} - \mathbf{c}^{(j)}}{|\mathbf{c}^{(i)} - \mathbf{c}^{(j)}|} \tag{5.114}$$

$$v^{(i,j)} = -\left(\dot{\mathbf{c}}^{(i)} - \dot{\mathbf{c}}^{(j)}\right) \cdot \mathbf{r}^{(i,j)} \tag{5.115}$$

and $\nu^{(i,j)}$ is a damping coefficient, chosen as

$$\nu^{(i,j)} = \frac{C_0}{2}\left(\rho^{(i)} c_s^{(i)} {V_0^{(i)}}^{\frac{2}{3}} + \rho^{(j)} c_s^{(j)} {V_0^{(j)}}^{\frac{2}{3}}\right)\left(1 + \frac{2c_1|v^{(i,j)}|}{c_s^{(i)} + c_s^{(j)}}\right) \tag{5.116}$$

where $c_s^{(i)}$ is the sound speed of particle i, c_0 and c_1 are dimensionless numerical viscosity coefficients, and $\zeta^{(i,j)}$ is the normalized nodal separation distance from Equation (5.42). Equation (5.113) includes a step function to introduce artificial viscosity only under compressed state.

An artificial viscous torque, damping the relative rotation of neighboring particles [105] is

$$\hat{\mathbf{M}}^{v(i)} = \sum_{1}^{n} \sigma^{(i,j)} \mathbf{R}^{(i)T} \left(\mathbf{R}^{(i)} \hat{\boldsymbol{\omega}}^{(i)} - \mathbf{R}^{(j)} \hat{\boldsymbol{\omega}}^{(j)} \right) \hat{u}(1 - \zeta^{(i,j)}) \tag{5.117}$$

where the artificial viscosity for rotation is defined by

$$\sigma^{(i,j)} = \frac{C_0}{2} \left(\rho^{(i)} c_s^{(i)} V_0^{(i)\frac{4}{3}} + \rho^{(j)} c_s^{(j)} V_0^{(j)\frac{4}{3}} \right) \tag{5.118}$$

5.2.11 Artificial Heat Diffusion

In the hybrid particle-element formulation used here, artificial heat diffusion [105] is used to model heat conduction under shock and impact loading conditions. The conducted power is

$$\dot{Q}^{\text{cond}} = \sum_{j=1}^{n} R^{(i,j)} \left(\theta^{(i)} - \theta^{(j)} \right) \hat{u}(1 - \zeta^{(i,j)}) \tag{5.119}$$

where

$$R^{(i,j)} = \frac{k_0}{2} \left(\rho^{(i)} c_s^{(i)} c_v^{(i)} V_0^{(i)\frac{2}{3}} + \rho^{(j)} c_s^{(j)} c_v^{(j)} V_0^{(j)\frac{2}{3}} \right) \tag{5.120}$$

with k_0 a numerical heat transfer coefficient and $c_v^{(i)}$ the isochoric specific heat.

5.2.12 Internal Energy Evolution Equations

The internal evolution equations for particle i can be determined from mechanical and thermal power flows [105], as

$$\dot{U}^{(i)} = \dot{U}^{\mathrm{wrk}(i)} + \dot{U}^{\mathrm{irr}(i)} - \dot{U}^{\mathrm{cond}(i)} \tag{5.121}$$

with

$$\begin{aligned} \dot{U}^{\mathrm{wrk}(i)} &= m^{(i)} \frac{P^{(i)}}{{\rho^{(i)}}^2} \dot{\rho}^{(i)} && (5.122) \\ \dot{U}^{\mathrm{irr}(i)} &= \mathbf{f}^{\mathrm{fr}(i)} \cdot \dot{\mathbf{c}}^{(i)} + \hat{\mathbf{M}}^{\mathrm{v}(i)} \cdot \hat{\boldsymbol{\omega}}^{(i)} + \sum_{j=1}^{n_e} \phi^{(i,j)} \dot{Q}^{\mathrm{irr}(j)} && (5.123) \end{aligned}$$

where $\dot{U}^{\mathrm{wrk}(i)}$ is a power flow into particle i due to mechanical work associated with material volume change, $\dot{U}^{\mathrm{irr}(i)}$ is a power flow due to irreversible entropy production, $\dot{U}^{\mathrm{cond}}$ is a power flow due to a heat diffusion (the same as $\dot{Q}^{\mathrm{cond}(i)}$), m^i is the particle mass, $\rho^{(i)}$ is a mass density, $P^{(i)}$ is the pressure, $\mathbf{f}^{\mathrm{fr}(i)}$ is the sum of the linear frictional forces (including an artificial viscous force, a velocity dependent Coulomb friction, and a friction due to Bingham plastic flow), $\hat{\mathbf{M}}^{\mathrm{v}(i)}$ is the numerical viscous torque, $\dot{Q}^{\mathrm{irr}(j)}$ is a power flow due to energy dissipation associated with the evolution of damage variables and plastic strain for element j, and $\phi^{(i,j)}$ is the fraction of the energy dissipation in element j which is transmitted to particle i.

Three different forms for $\dot{Q}^{\mathrm{irr}(j)}$ are used, based on the element type. For hexahedral elements,

$$\dot{Q}^{\mathrm{irr}(j)} = \Gamma^{d(j)} \dot{d}^{(j)} + \Gamma^{D(j)} \dot{D}^{(j)} + \mathrm{tr}\left(\mathbf{S}^{(j)T} \dot{\mathbf{E}}^{p(j)}\right) \tag{5.124}$$

for bar elements,

$$\dot{Q}^{\mathrm{irr}(j)} = \Gamma^{d(j)}\dot{d}^{(j)} + \sigma^{p(j)}\dot{\epsilon}^{p(j)} \tag{5.125}$$

and for element-free particles,

$$\dot{Q}^{\mathrm{irr}(j)} = 0 \tag{5.126}$$

5.2.13 Hamilton's Equations

The system Hamiltonian is the sum of the kinetic energy and potential energy,

$$H \; = \; T \; + \; V \tag{5.127}$$

In this hybrid particle-element formulation, the general functional form for the Hamiltonian is

$$H \; = H\left(\mathbf{c}^{(i)}, \mathbf{p}^{(i)}, \mathbf{e}^{(i)}, \hat{\mathbf{h}}^{(i)}, U^{(i)}, x_{\alpha}^{(j)}\right) \tag{5.128}$$

with

$$i = 1, 2, \cdots, n_p, \quad j = 1, 2, \cdots, n_e, \quad \text{and} \quad \alpha = 1, 2, \cdots, n_{ISV}$$

where n_p is the number of particles, n_e is the number of elements, $x_{\alpha}^{(j)}$s are the internal state variables associated with element j, and n_{ISV} is the number of internal state variables.

The governing equations for the system are obtained using Lagrange's equations or Hamilton's equations. The canonical Hamilton's equations [120] are

$$
\begin{aligned}
\dot{\mathbf{p}}^{(i)} &= -\frac{\partial H}{\partial \mathbf{c}^{(i)}} + \mathbf{q}^{\mathbf{c}(i)} && (5.129)\\
\dot{\mathbf{c}}^{(i)} &= \frac{\partial H}{\partial \mathbf{p}^{(i)}} && (5.130)\\
\dot{\mathbf{h}}_{\mathbf{e}}^{(i)} &= -\frac{\partial H}{\partial \mathbf{e}^{(i)}} + \mathbf{q}^{\mathbf{e}(i)} && (5.131)\\
\dot{\mathbf{e}}^{(i)} &= \frac{\partial H}{\partial {\mathbf{h}_{\mathbf{e}}}^{(i)}} && (5.132)\\
0 &= -\frac{\partial H}{\partial U^{(i)}} + q^{U(i)} && (5.133)\\
0 &= -\frac{\partial H}{\partial x_\alpha^{(j)}} + q^{x_\alpha(j)} && (5.134)
\end{aligned}
$$

where $\mathbf{q}^{\mathbf{c}(i)}$, $\mathbf{q}^{\mathbf{e}(i)}$, $q^{U(i)}$,and $q^{x_\alpha(j)}$ are generalized nonconservative forces associated with the generalized coordinates $\mathbf{c}^{(i)}$, $\mathbf{e}^{(i)}$, $U^{(i)}$, and $q^{x_\alpha(j)}$ respectively. The nonconservative forces are determined by the virtual work done by external forces and by the constraint forces, which are due to the nonholonomic constraints. Note that Equation (5.131) represents the time evolution of a 4×1 momentum vector (${\mathbf{h}_{\mathbf{e}}}^{(i)}$) for particle i, associated with the Euler parameter vector $\mathbf{e}^{(i)}$. This momentum evolution equation can be used to derive the evolution equation for a 3×1 angular momentum vector $\hat{\mathbf{h}}^{(i)}$, defined by Equation (5.49)[121]. The angular momentum vector evolution equation for particle i is

$$\dot{\hat{\mathbf{h}}}^{(i)} = 2\dot{\mathbf{G}}^{(i)}{\mathbf{G}^{(i)}}^T\hat{\mathbf{h}}^{(i)} - \frac{1}{2}\mathbf{G}^{(i)}\frac{\partial H}{\partial \mathbf{e}^{(i)}} + \frac{1}{2}\mathbf{G}^{(i)}\mathbf{q}^{\mathbf{e}(i)} \qquad (5.135)$$

Note that the generalized coordinates are constrained by Equation (5.17) and by the evolution equations for the internal energy, the damage variables, and the plastic strain. The nonholonomic constraints for particles associated with hexahedral elements takes the following functional form

$$\begin{aligned}\dot{U}^{(i)} &= \dot{U}^{(i)}\left(\mathbf{c}^{(i)}, \mathbf{e}^{(i)}, U^{(i)}, d^{(j)}, D^{(j)}, \mathbf{E}^{p(j)}\right) && (5.136)\\ \dot{d}^{(j)} &= \dot{d}^{(j)}\left(\mathbf{c}^{(i)}, \mathbf{e}^{(i)}, U^{(i)}, d^{(j)}, D^{(j)}, \mathbf{E}^{p(j)}\right) && (5.137)\\ \dot{D}^{(j)} &= \dot{D}^{(j)}\left(\mathbf{c}^{(i)}, \mathbf{e}^{(i)}, U^{(i)}, d^{(j)}, D^{(j)}, \mathbf{E}^{p(j)}\right) && (5.138)\\ \dot{\mathbf{E}}^{p(j)} &= \dot{\mathbf{E}}^{p(j)}\left(\mathbf{c}^{(i)}, \mathbf{e}^{(i)}, U^{(i)}, d^{(j)}, D^{(j)}, \mathbf{E}^{p(j)}\right) && (5.139)\end{aligned}$$

While the nonholonomic constraints for particles i associated with bar elements are

$$\begin{aligned}\dot{U}^{(i)} &= \dot{U}^{(i)}\left(\mathbf{c}^{(i)}, \mathbf{e}^{(i)}, U^{(i)}, d^{(i)}, \epsilon^{p(i)}\right) && (5.140)\\ \dot{d}^{(i)} &= \dot{d}^{(i)}\left(\mathbf{c}^{(i)}, \mathbf{e}^{(i)}, U^{(i)}, d^{(i)}, \epsilon^{p(i)}\right) && (5.141)\\ \dot{\epsilon}^{p(i)} &= \dot{\epsilon}^{p(i)}\left(\mathbf{c}^{(i)}, \mathbf{e}^{(i)}, U^{(i)}, d^{(i)}, \epsilon^{p(i)}\right) && (5.142)\end{aligned}$$

To identify generalized nonconservative forces in the canonical Hamilton's equations, the external forces and the constraint forces acting on each particle must be derived. External forces are determined by the loading conditions for the modeled system, and the corresponding generalized forces can be obtained from a virtual work expression. Suppose that $\mathbf{f}^{\text{ext}}(t)^{(i)}$ and $\hat{\mathbf{M}}^{\text{ext}}(t)^{(i)}$ represent time-varying external forces and torque for particle i, then the associated virtual work [121] is

$$\delta W^{\text{ext}(i)} = \mathbf{f}^{\text{ext}}(t)^{(i)T} \delta\mathbf{c}^{(i)} + 2\left[\mathbf{G}^{(i)T} \hat{\mathbf{M}}^{\text{ext}}(t)^{(i)}\right]^{T} \delta\mathbf{e}^{(i)} \tag{5.143}$$

Nonholonomic constraint forces can be determined by introducing Lagrange multipliers [105, 120]. The Lagrange multipliers can be computed in closed form, using the degenerate Hamilton's equations associated with the internal states [105, 120].

The final form of Hamilton's equations for the particle-element system is

$$\begin{aligned}
\dot{\mathbf{p}}^{(i)} &= -\mathbf{g}^{(i)} - \mathbf{f}^{\mathrm{fr}(i)} + \mathbf{f}^{\mathrm{ext}}(t)^{(i)} && (5.144)\\
\dot{\mathbf{c}}^{(i)} &= \frac{\mathbf{p}^{(i)}}{m^{(i)}} && (5.145)\\
\dot{\hat{\mathbf{h}}}^{(i)} &= \hat{\mathbf{\Omega}}^{(i)}\hat{\mathbf{h}}^{(i)} - \frac{1}{2}\mathbf{G}^{(i)}\mathbf{M_e}^{(i)} - \hat{\mathbf{M}}^{\mathrm{v}(i)} + \hat{\mathbf{M}}^{\mathrm{ext}}(t)^{(i)} && (5.146)\\
\dot{\mathbf{e}}^{(i)} &= \frac{1}{2}\mathbf{G}^{(i)T}\hat{\mathbf{J}}^{(i)-1}\hat{\mathbf{h}}^{(i)} && (5.147)
\end{aligned}$$

augmented by the evolution equations for the internal states.

In the particle-element modeling approach, the complete system level equations consist of Hamilton's equations for the particles and time evolution equations for the internal state variables (i.e., damage variables and plastic strains). The evolution equations for the nonholonomic constraints take the form of Equations (5.136) through (5.139) for the particles associated with hexahedral elements, and Equations (5.140) through (5.142) for the particles associated with bar elements. The system level equations are nonlinear ordinary differential equations in explicit state space form.

Since each material is modeled somewhat differently specific Hamilton's equations for the different materials involved in the MRF-Kevlar impact simulations are as follows.

1. **Hamilton's Equation for Projectiles**

A general functional form for the total Hamiltonian of a fragment simulating projectile is

$$H_{\mathrm{FSP}} = H_{\mathrm{FSP}}\left(\mathbf{c}^{(i)}, \mathbf{p}^{(i)}, \mathbf{e}^{(i)}, \hat{\mathbf{h}}^{(i)}, U^{(i)}, d^{(j)}, D^{(j)}, \mathbf{E}^{p(j)}\right) \tag{5.148}$$

where the superscript i is for a particle and the superscript j for an element.

The final form of the system-level equations for the projectile is

$$\begin{aligned}
\dot{\mathbf{p}}^{(i)} &= -\mathbf{g}^{(i)} - \mathbf{f}^{\mathrm{v}(i)} - \mathbf{f}^{\mathrm{C}(i)} - \mathbf{f}^{\mathrm{B}(i)} + \mathbf{f}^{\mathrm{ext}}(t)^{(i)} && (5.149)\\
\dot{\mathbf{c}}^{(i)} &= \frac{\mathbf{p}^{(i)}}{m^{(i)}} && (5.150)\\
\dot{\hat{\mathbf{h}}}^{(i)} &= \hat{\boldsymbol{\Omega}}^{(i)}\hat{\mathbf{h}}^{(i)} - \frac{1}{2}\mathbf{G}^{(i)}\mathbf{M}_{\mathbf{e}}{}^{(i)} - \hat{\mathbf{M}}^{\mathrm{v}(i)} + \hat{\mathbf{M}}^{\mathrm{ext}}(t)^{(i)} && (5.151)\\
\dot{\mathbf{e}}^{(i)} &= \frac{1}{2}\mathbf{G}^{(i)T}\hat{\mathbf{J}}^{(i)-1}\hat{\mathbf{h}}^{(i)} && (5.152)\\
\dot{U}^{(i)} &= \dot{U}^{(i)}\left(\mathbf{c}^{(i)}, \mathbf{e}^{(i)}, U^{(i)}, d^{(j)}, D^{(j)}, \mathbf{E}^{p(j)}\right) && (5.153)\\
\dot{d}^{(j)} &= \dot{d}^{(j)}\left(\mathbf{c}^{(i)}, \mathbf{e}^{(i)}, U^{(i)}, d^{(j)}, D^{(j)}, \mathbf{E}^{p(j)}\right) && (5.154)\\
\dot{D}^{(j)} &= \dot{D}^{(j)}\left(\mathbf{c}^{(i)}, \mathbf{e}^{(i)}, U^{(i)}, d^{(j)}, D^{(j)}, \mathbf{E}^{p(j)}\right) && (5.155)\\
\dot{\mathbf{E}}^{p(j)} &= \dot{\mathbf{E}}^{p(j)}\left(\mathbf{c}^{(i)}, \mathbf{e}^{(i)}, U^{(i)}, d^{(j)}, D^{(j)}, \mathbf{E}^{p(j)}\right) && (5.156)
\end{aligned}$$

where $\mathbf{g}^{(i)}$ is a conservative force associated with the particle center of mass coordinates, $\mathbf{f}^{\mathrm{v}(i)}$ is a viscous force due to neighboring particles, $\mathbf{f}^{\mathrm{C}(i)}$ is a Coulomb friction force acting on the particle, $\mathbf{f}^{\mathrm{B}(i)}$ is Bingham-plastic viscous friction force, $\mathbf{f}^{\mathrm{ext}}(t)^{(i)}$ is an external force, $\mathbf{M}_{\mathbf{e}}{}^{(i)}$ is a conservative force associated with the Euler parameters, $\hat{\mathbf{M}}^{\mathrm{v}(i)}$ is an artificial viscous torque, and $\hat{\mathbf{M}}^{\mathrm{ext}}(t)^{(i)}$ is an external torque.

2. **Hamilton's Equation for Kevlar Woven Fabrics**

   A general functional form for the total Hamiltonian of the Kevlar fabric is

$$H_{\text{Kevlar}} = H_{\text{Kevlar}}\left(\mathbf{c}^{(i)}, \mathbf{p}^{(i)}, \mathbf{e}^{(i)}, \hat{\mathbf{h}}^{(i)}, U^{(i)}, d^{(i)}\right) \tag{5.157}$$

   Since the Kevlar fabric is modeled with bar elements, There are no element state variables. The final form for the governing equations is

$$\begin{aligned}
\dot{\mathbf{p}}^{(i)} &= -\mathbf{g}^{(i)} - \mathbf{f}^{\text{v}(i)} - \mathbf{f}^{\text{C}(i)} - \mathbf{f}^{\text{B}(i)} + \mathbf{f}^{\text{ext}}(t)^{(i)} && (5.158)\\
\dot{\mathbf{c}}^{(i)} &= \frac{\mathbf{p}^{(i)}}{m^{(i)}} && (5.159)\\
\dot{\hat{\mathbf{h}}}^{(i)} &= \hat{\boldsymbol{\Omega}}^{(i)}\hat{\mathbf{h}}^{(i)} - \frac{1}{2}\mathbf{G}^{(i)}\mathbf{M_e}^{(i)} - \hat{\mathbf{M}}^{\text{v}(i)} + \hat{\mathbf{M}}^{\text{ext}}(t)^{(i)} && (5.160)\\
\dot{\mathbf{e}}^{(i)} &= \frac{1}{2}\mathbf{G}^{(i)T}\hat{\mathbf{J}}^{(i)-1}\hat{\mathbf{h}}^{(i)} && (5.161)\\
\dot{U}^{(i)} &= \dot{U}^{(i)}\left(\mathbf{c}^{(i)}, \mathbf{e}^{(i)}, U^{(i)}, d^{(i)}\right) && (5.162)\\
\dot{d}^{(i)} &= \dot{d}^{(i)}\left(\mathbf{c}^{(i)}, \mathbf{e}^{(i)}, U^{(i)}, d^{(i)}\right) && (5.163)
\end{aligned}$$

3. **Hamilton's Equation for Magnetorheological Fluids**

   A general functional form for the total Hamiltonian of the interstitial magnetorheological fluid particles is

$$H_{\text{MRF}} = H_{\text{MRF}}\left(\mathbf{c}^{(i)}, \mathbf{p}^{(i)}, \mathbf{e}^{(i)}, \hat{\mathbf{h}}^{(i)}, U^{(i)}\right) \tag{5.164}$$

   Because the fluid particles are modeled as free Lagrangian particles, no element state variables are needed to represent material strength effects.

The final form of the first-order state-space equations is

$$\begin{aligned}
\dot{\mathbf{p}}^{(i)} &= -\mathbf{g}^{(i)} - \mathbf{f}^{\mathrm{v}(i)} - \mathbf{f}^{\mathrm{B}(i)} + \mathbf{f}^{\mathrm{ext}}(t)^{(i)} && (5.165)\\
\dot{\mathbf{c}}^{(i)} &= \frac{\mathbf{p}^{(i)}}{m^{(i)}} && (5.166)\\
\dot{\hat{\mathbf{h}}}^{(i)} &= \hat{\boldsymbol{\Omega}}^{(i)}\hat{\mathbf{h}}^{(i)} - \frac{1}{2}\mathbf{G}^{(i)}\mathbf{M_e}^{(i)} - \hat{\mathbf{M}}^{\mathrm{v}(i)} + \hat{\mathbf{M}}^{\mathrm{ext}}(t)^{(i)} && (5.167)\\
\dot{\mathbf{e}}^{(i)} &= \frac{1}{2}\mathbf{G}^{(i)^T}\hat{\mathbf{J}}^{(i)^{-1}}\hat{\mathbf{h}}^{(i)} && (5.168)\\
\dot{U}^{(i)} &= \dot{U}^{(i)}\left(\mathbf{c}^{(i)}, \mathbf{e}^{(i)}, U^{(i)}\right) && (5.169)
\end{aligned}$$

The transport of fluid particles is governed by momentum transfer due to contact-impact effects and magnetic field-dependent viscous friction effects. Note that a mixture equation of state is used for these particles.

4. **Hamilton's Equation for PVC wrapped Magnetorheological Fluids**

   A general functional form for the thermomechanical Hamiltonian of the magnetorheological fluid-PVC mixture is

$$H_{\mathrm{MRF-PVC}} = H_{\mathrm{MRF-PVC}}\left(\mathbf{c}^{(i)}, \mathbf{p}^{(i)}, \mathbf{e}^{(i)}, \hat{\mathbf{h}}^{(i)}, U^{(i)}, d^{(i)}, \epsilon^{p(i)}\right) \qquad (5.170)$$

Because the MRF-PVC mixture is also modeled with bar elements, the system-level dynamic equations are written as

$$\dot{\mathbf{p}}^{(i)} = -\mathbf{g}^{(i)} - \mathbf{f}^{\mathrm{v}(i)} - \mathbf{f}^{\mathrm{B}(i)} + \mathbf{f}^{\mathrm{ext}}(t)^{(i)} \tag{5.171}$$

$$\dot{\mathbf{c}}^{(i)} = \frac{\mathbf{p}^{(i)}}{m^{(i)}} \tag{5.172}$$

$$\dot{\hat{\mathbf{h}}}^{(i)} = \hat{\boldsymbol{\Omega}}^{(i)}\hat{\mathbf{h}}^{(i)} - \frac{1}{2}\mathbf{G}^{(i)}\mathbf{M}_{\mathbf{e}}{}^{(i)} - \hat{\mathbf{M}}^{\mathrm{v}(i)} + \hat{\mathbf{M}}^{\mathrm{ext}}(t)^{(i)} \tag{5.173}$$

$$\dot{\mathbf{e}}^{(i)} = \frac{1}{2}\mathbf{G}^{(i)^T}\hat{\mathbf{J}}^{(i)^{-1}}\hat{\mathbf{h}}^{(i)} \tag{5.174}$$

$$\dot{U}^{(i)} = \dot{U}^{(i)}\left(\mathbf{c}^{(i)}, \mathbf{e}^{(i)}, U^{(i)}, d^{(i)}, \epsilon^{p(i)}\right) \tag{5.175}$$

$$\dot{d}^{(i)} = \dot{d}^{(i)}\left(\mathbf{c}^{(i)}, \mathbf{e}^{(i)}, U^{(i)}, d^{(i)}, \epsilon^{p(i)}\right) \tag{5.176}$$

$$\dot{\epsilon}^{p(i)} = \dot{\epsilon}^{p(i)}\left(\mathbf{c}^{(i)}, \mathbf{e}^{(i)}, U^{(i)}, d^{(i)}, \epsilon^{p(i)}\right) \tag{5.177}$$

These time evolution equations are similar to those of a Kevlar fabric; the difference is the fact that the PVC is modeled as elastic-plastic. Note that a mixture equation of state is again used for the particles, this time incorporating both MR fluid constituents and PVC.

5.3 Simulation Results

An extended hybrid particle-element method has been formulated in previous section, to model the thermomechanical interaction of woven fabrics and interstitial rheological fluids. The computational approach of modeling fluids as Lagrangian particles effectively incorporates the magnetic field-dependent shear yield stress and shear viscosity effects of magnetorheological fluids into the fabric model. This section presents validation simulations of FSP impacts on MRF-Kevlar composites, namely the experimental results from Chapters 2 and 3. The four target configurations for the impact simulation in this dissertation are: (1) the magnetomechanically edge-clamped MRF-Kevlar composites in Chapter 2, (2) the single-layer Kevlar fabric in Chapters 3 and 4, (3) the magnetized MRF-Kevlar composites in Chapter 3, and (4) the non-magnetized MRF-Kevlar composites in Chapter 3. The material properties used in the simulation are listed in Tables 5.1 and 5.2.

5.3.1 FSP Impact Simulation for Edge-Clamped MRF-Kevlar Composites

The first example simulation models the impact of a steel projectile on 2-ply Kevlar fabrics (one neat and one MRF treated). The experimental procedure and results are explained in Chapter 2. Two fabric strips are orthogonally crossed, as shown in Figure 2.3. The vertical 10.16 cm × 5.08 cm Kevlar strip has two fixed and two free boundary conditions, with two edges fastened by clinch buckles. The fixed boundary condition allows the particles at the boundary only two degree-of-freedom motion: rotation about the edge lines and translation along the edge lines. The horizontal 21.59 cm × 5.08 cm Kevlar strip is saturated with MR fluid represented by interstitial fluid particles. The black particles in Figure 5.9 are the modeled MR fluid particles. The boundary condition for this strip is a confinement of the particles placed in the air gap between the target plate and the magnet, as shown in Figure 2.3. In addition, an external loading condition is imposed on the particles, due to the magnet, which applies magnetic clamping effects on two edges of the target. The resultant shearing resistance prevents particles from sliding before a shear yielding takes place. The MR fluids under the magnets are magnetically saturated, based on the magnetic circuit analysis in Appendix A. Therefore, for the MR fluids, a maximum fluid shear yield stress (i.e., 60 kPa [84]) is induced by the electromagnet. In this simulation, the shear yield stress is chosen as 36 kPa which is two-fifth of the manufacturer's specification (60 kPa) due to the fact that the magnetized area constitutes two-fifths of the air gap area, as shown in Figure A.3(a).

This simulation incorporates 393,351 particles and 1,055,018 bar elements. The number of MR fluid particles is 23,120. Since the MR fluid particles have no element connectivities, their motion is constrained only by contact-impact with neighboring particles and external loading. The steel FSP is modeled using 17,805 particles and 8,204 hexagonal elements. Seven simulations were conducted over the impact velocity range $150 \leq V_i \leq 450$, with an equal spacing of 50 m/s.

The simulation results are summarized in Table 5.3 and plotted in Figure 5.6. A regression curve for the data is drawn on the same plot, based on the assumption of constant energy loss (Equation (2.1)). Energy absorption is shown in Figure 5.7, using the dimensionless energy absorption ratio defined by Equation (2.4). The value of V_{50} estimated from the simulations is 201 m/s, which is 1.47% less than the experimental value ($V_{50,\text{exp}} = 204$ m/s).

Figure 5.8 depicts sequential images of an FSP impact at 400 m/s on a magnetomechanically edge-clamped MR Fluid-Kevlar composite, for 0-60 μsec after impact. These simulation images show relative motion among the FSP, yarns, and interstitial MRF particles, as well as damaged fragments of each material. A block is added during post-processing to represent the target frame. Figure 5.9 shows an FSP impact simulation at 400 m/s, on a magnetomechanically edge-clamped MR Fluid-Kevlar composite, at 30 μsec after impact.

5.3.2 FSP Impact Simulation for Neat Kevlar

FSP impact simulations for a single-ply Kevlar fabrics were performed prior to simulation work on magnetized or non-magnetized MRF-Kevlar composites. Figure 3.10 (a) shows the configuration of the fabric target just before projectile impact on the target. The target is supported by the frame of the holder. The initial configuration of the modeled geometry is shown in Figure 5.12. The Kevlar held in the PVC buckles is modeled using spring acting on the particles along the bottom and top horizontal edges. Their stiffness is determined by the total length of the Kevlar strip and the elastic modulus of Kevlar. This simulation incorporated a total of 104,817 particles and 260,304 bar elements to model Kevlar fabrics. The brass FSP is modeled with 17,805 particles and 8,204 hexagonal elements. A total of seven simulations were performed in the impact velocity range of $150 \leq V_i \leq 500$ at an equal spacing of 50 m/s.

The simulation results are listed in Table 5.4. Figure 5.10 displays the simulation and experimental data on the same plot. The corresponding energy absorption curve is shown in Figure 5.11. Both plots show a regression curve obtained from the assumption of constant energy loss (Equation (2.1)). The value of V_{50} estimated from this simulation is 151 m/s, which is 5.03% less than the experimental value ($V_{50,\text{exp}} = 159$ m/s).

Figure 5.13 depicts sequential images of FSP impacts at 400 m/s on neat Kevlar fabric, for 0-60 μsec after impact. These simulation images show relative motion among the FSP, yarns, and damaged fragments of each material. Blocks are added during post-processing to represent the target frame. Figure 5.14 shows an FSP impact simulation at 100 μsec, for a single-ply Kevlar target. This image shows the complex transversal deflection of the fabrics due to the superposition of deflection waves and reflections imposed by the boundary blocks.

5.3.3 FSP Impact Simulation for Magnetized PVC-MRF-Kevlar Composites

The target MRF-Kevlar composites are composed of a single-ply of Kevlar fabric, treated with 0.75 ml MR fluids, and wrapped in 0.00254 cm-thick PVC heat shrink tubing. Figure 3.4(c) shows the target configuration for the FSP impact tests; the MRF treated area is 5.05 cm × 5.08 cm in size, as indicated in the figure. This target differs from that of the edge treated MRF-Kevlar composites in that a thin PVC tubing is used to confine the MR fluid. The PVC thin film is not modeled as an independent structure, because of high computational cost of modeling a very thin film with many small particles. Instead, the PVC material properties are incorporated in the mixture model for MR fluids, as an additional constituent. While interstitial MRF particles within the Kevlar voids are modeled as free Lagrangian particles, as shown in Figure 5.18, a hybrid particle-element formulation is used to model the PVC-MRF mixture surrounding the Kevlar fabric as shown in Figure 5.19. In this figure the element opacity is reduced to provide a clear visual description. This image shows an FSP impact simulation at 400 m/s, on an MRF-Kevlar composite target, at 20 μsec after impact. The shear yield stress for the PVC-MRF mixture is 45 kPa, based on the MR fluid manufacture's specification for a magnetic field intensity of 111 kA/m. This simulation incorporates total of 163,045 particles and 260,304 bar elements. The brass projectile is modeled with 17,805 particles and 8,204 hexagonal elements, while 117,552 bar elements represent the PVC-MRF-Kevlar mixture on the outer surface.

Total of fifteen simulations were completed over the impact velocity range of $125 \leq V_i \leq 475$, with an equal spacing of 25 m/s (Table 5.5). Figure 5.15 shows the simulation data and the regression curve obtained from the assumption of constant energy loss (Equation (2.1)). The curve for impact energy absorption is shown in Figure 5.16, which plots the dimensionless energy absorption ratio defined by Equation (2.4). The value of V_{50} estimated from these simulations is 149 m/s, which is 0.67% less than the experimental value ($V_{50,\text{exp}} = 150$ m/s).

Figure 5.20 depicts sequential images of an FSP impacts, at 400 m/s on an MRF-Kevlar target, at 0-60 μsec after impact. These images show relative motion among the FSP, yarns, MRF-PVC mixture particles/elements, plus damaged fragments of each material. The blocks are added during post-processing, to represent for the target frame. Figure 5.21 shows an image of an FSP impact simulation at 400 m/s, on an MRF-Kevlar composite target, at 100 μsec after impact (front view). Figure 5.22 shows the image of an FSP impact simulation at 400 m/s, on an MRF-Kevlar composite target at 100 μsec after impact (back view).

5.3.4 FSP Impact Simulation for Non-Magnetized MRF-PVC-Kevlar Composites

The simulation configuration for the non-magnetized MRF-Kevlar composites enclosed in PVC tubing is the same as the simulation for the magnetized targets (shown in Figure 5.20) except for the absence of a magnetic field. In this case, the shear yield stress is set to zero. The simulation results are listed in Table 5.6 and plotted in Figures 5.23 and 5.24. The value of V_{50} evaluated from the simulations is 149 m/s, which is 2.05% more than the experimental value ($V_{50,\text{exp}} = 146$ m/s).

5.4 Summary

This chapter has extended the hybrid particle-element formulation developed in previous work, in order to model augmenting fluids for high-strength fabrics using Lagrangian particles occupying the fabric void space. Ellipsoidal particles and bar elements are used to the model the MRF fluid and PVC mixture. Hence these simulations include three types of the particle-element models: (1) hybrid particle-hexahedral element to model the solid projectile, (2) hybrid particle-bar element to model the woven fabrics and the PVC thin film, and (3) free ellipsoidal particles to model the MR fluids. The hybrid particle-element formulation is an energy method, and was derived in a thermodynamically consistent fashion, using Hamilton's equations for a general thermo-mechanical system. The system Hamiltonian includes the translational and rotational kinetic energy of the modeled particles, the strain energy of the modeled elements, and the internal energy of the particles. Hence classical dynamics and continuum mechanics are simultaneously used to model the system. The formulation includes a density interpolation kernel which determines contact-impact forces between the near neighbor particles, elastic-plastic material models with damage variables, a flow rule for isochoric plasticity, dry and viscous frictional effects, artificial viscosity and artificial heat diffusion, equations of state for compressed medium, and mixture equation of state for heterogeneous materials. This work is the first hybrid particle-element formulation to incorporate fluid-structure interaction and model interstitial fluids. Hence it has extended the hybrid particle-element method, to simulate the impact dynamics of a rather complex system. Note that the field-dependence of smart fluids is included in the numerical model. Example simulations show good agreement with the experimental results obtained in Chapter 2 and Chapter 3.

Table 5.1: Magnetorheological fluid properties used in the impact simulations

Property	Iron		Hydrocarbon oil		PVC	
		Ref		Ref		Ref
Mass fraction (MRF)	0.865		0.135		0	
Mass fraction (PVC-MRF)	0.766		0.119		0.115	
Shear modulus ($Mbar$)	0.82	[4]	NA		0.00965	[89]
Reference density (g/cm^3)	7.86	[54]	0.819	[53]	1.35	[134]
Reference Sound Speed ($cm/\mu sec$)	0.491	[4]	0.1341	#	0.1993	[1]
Melt/char temperature (K)	1808	[79]	NA		416	[134]
Specific heat ($\frac{Mbar \cdot cm^3}{g \cdot kK}$)	0.0045	[79]	0.0222	[53]	0.01072	[89]
Thermal expansion coefficient (kK^{-1})	0.00166	[79]	0.72	[66]	0.145	[56]
Mie-Gruneisen gamma	1.66	[7]	0.5653	*	0.54	*
Mie Gruneisen slope coefficient	0.158	[7]	0.145	[1]	1.631	[1]

NA : not applicable
* : calculated from Equation (5.78)
# : calculated from the thermoelastic relation

Table 5.2: Kevlar and FSP properties used in the impact simulations

Property	Neat KM-2 fiber		Steel		Half hard Brass	
		Ref		Ref		Ref
Shear modulus ($Mbar$)	0.3714	[111]	0.801	[111]	0.37	[3]
Reference density (g/cm^3)	1.45	[111]	7.842	[111]	8.45	[1]
Reference Sound Speed ($cm/\mu sec$)	0.5352	[111]	0.5352	[111]	0.366	[1]
Melt/char temperature (K)	700	[111]	2310	[111]	1158	[3]
Specific heat ($\frac{Mbar \cdot cm^3}{g \cdot kK}$)	0.0142	[111]	0.00448	[111]	0.00377	[40]
Thermal expansion coefficient (kK^{-1})	0.012	[111]	0.00166	[111]	0.06156	[40]
Mie-Gruneisen gamma	0.7666	[111]	1.84	[111]	2.19	*
Mie Gruneisen slope coefficient	1.0	[111]	1.5	[111]	1.547	[1]

* : calculated from Equation (5.78)

Table 5.3: Simulation results: FSP impacts on magnetomechanically edge-clamped MR Fluid-Kevlar composites

Simulation No.	V_i (m/s)	V_r (m/s)	$\Delta\bar{E}_i$ $\left(\frac{V_i^2-V_r^2}{V_i^2}\right)$	Simulation Time (μsec)
1	150	0	1.00	458
2	200	57	0.92	329
3	250	92	0.86	280
4	300	184	0.62	146
5	350	268	0.41	132
6	400	354	0.22	74
7	450	413	0.16	56
Number of particles: 393,351 Estimated V_{50} = 201 m/s				

Table 5.4: Simulation results: FSP impacts on single-ply neat Kevlar fabrics

Simulation No.	V_i (m/s)	V_r (m/s)	$\Delta\bar{E}_i$ $\left(\frac{V_i^2-V_r^2}{V_i^2}\right)$	Simulation Time (μsec)
1	150	95	0.60	323
2	200	139	0.52	230
3	250	197	0.38	218
4	300	257	0.27	197
5	350	302	0.26	162
6	400	365	0.17	125
7	450	428	0.10	110
Number of particles: 104,817 Estimated V_{50} = 151 m/s				

Table 5.5: Simulation results: FSP impacts on magnetized MRF-Kevlar composites

Simulation No.	V_i (m/s)	V_r (m/s)	$\Delta \bar{E}_i$ $\left(\frac{V_i^2 - V_r^2}{V_i^2}\right)$	Simulation Time (μsec)
1	125	0	1.00	313
2	150	26	0.97	374
3	175	54	0.90	252
4	200	86	0.82	228
5	225	132	0.66	196
6	250	199	0.37	160
7	275	235	0.27	110
8	300	266	0.21	141
9	325	295	0.18	95
10	350	325	0.14	139
11	375	352	0.12	71
12	400	377	0.11	129
13	425	402	0.11	57
14	450	426	0.10	124
15	475	451	0.10	67
Number of particles: 163,405 Estimated $V_{50} = 149$ m/s				

Table 5.6: Simulation results: FSP impacts on non-magnetized MRF-Kevlar composites

Simulation No.	V_i (m/s)	V_r (m/s)	$\Delta \bar{E}_i$ $\left(\frac{V_i^2 - V_r^2}{V_i^2}\right)$	Simulation Time (μsec)
1	125	0	1.00	310
2	150	14	0.99	315
3	175	51	0.92	291
4	200	86	0.82	276
5	225	132	0.66	256
6	250	199	0.37	232
7	275	235	0.27	208
8	300	267	0.21	84
9	325	296	0.17	82
10	350	325	0.14	79
11	375	352	0.12	77
12	400	377	0.11	75
13	425	402	0.11	75
14	450	427	0.10	75
15	475	451	0.10	76
Number of particles: 163,405 Estimated V_{50} = 149 m/s				

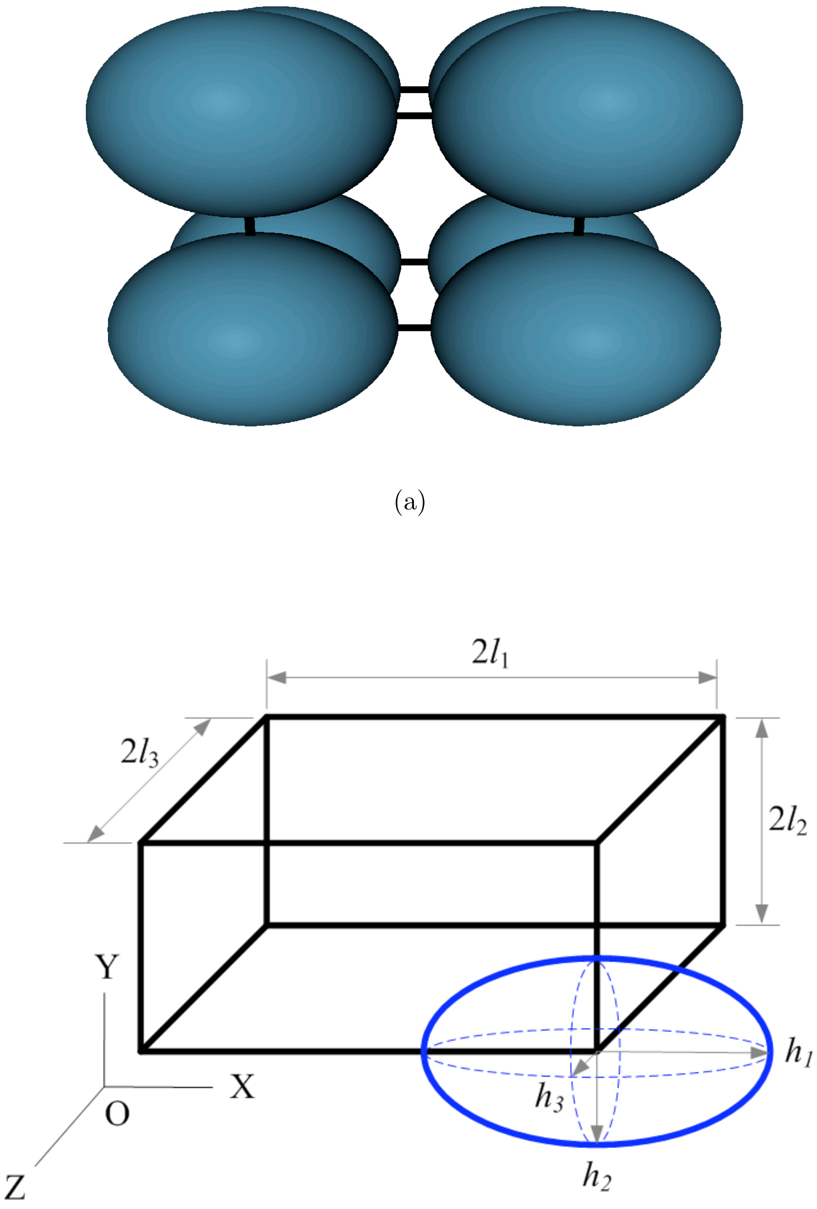
(a)

(b)

Figure 5.1: A geometric model for a projectile (a) 3-D view of the eight-noded hybrid ellipsoid-hexahedron model with perspective (b) schematic and dimensions of the ellipsoidal particle and hexahedral finite element

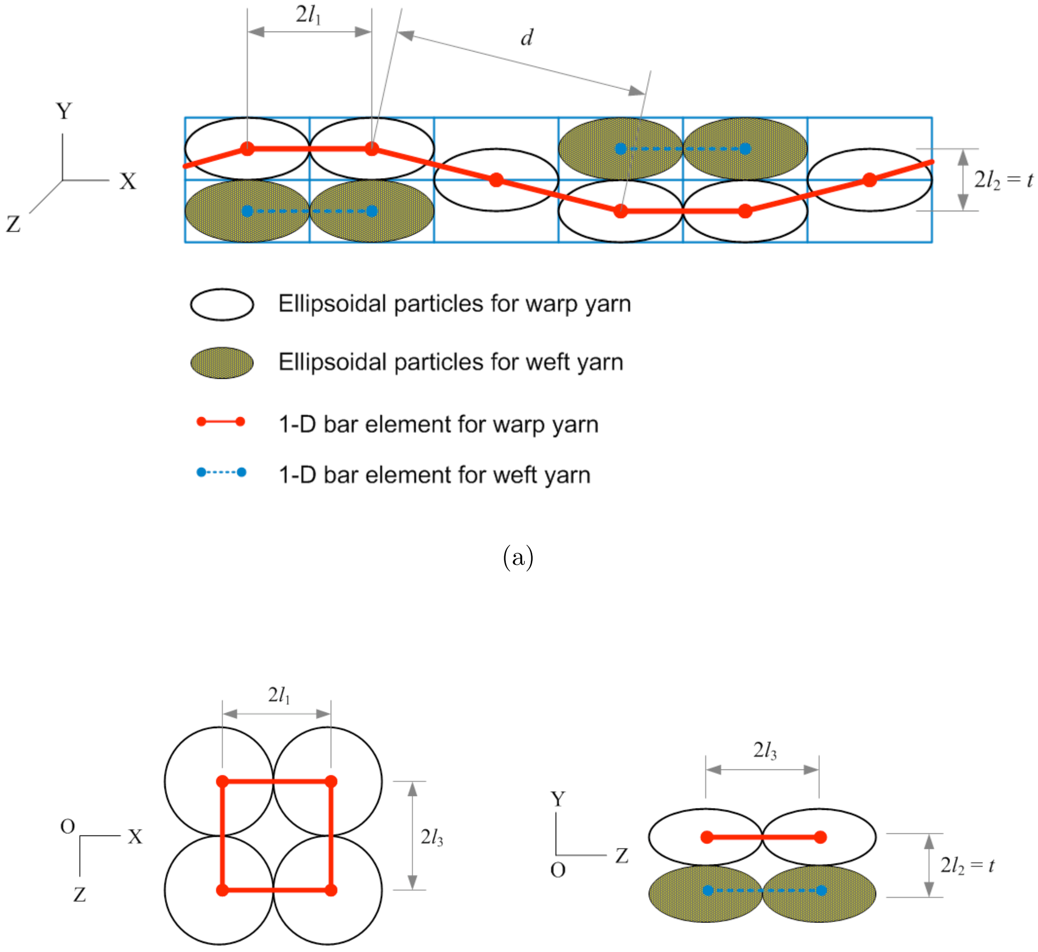

(a)

(b)

(c)

Figure 5.2: Mesomechanical yarn model of Kevlar KM-2 fabric in plain weaves (a) particle-element geometry model of crimped yarns (b) top view of a segmented warp yarn in Z-X plane (c) side view in Y-Z plane

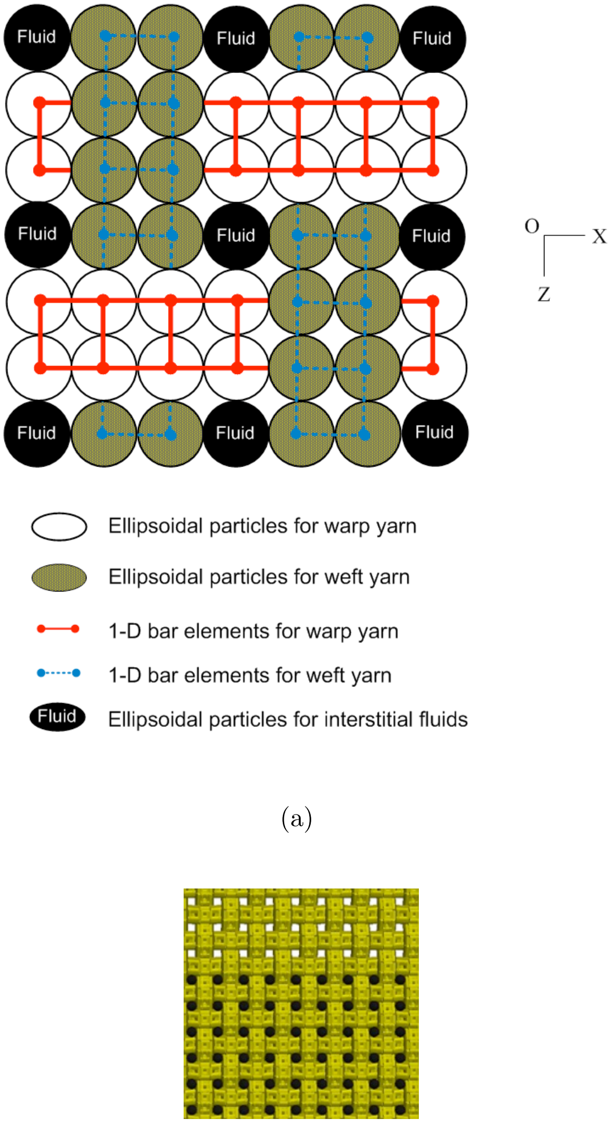

(a)

(b)

Figure 5.3: A geometric model for magnetorheological fluids (a) schematic of the particle representation for a MRF-Kevlar composite (b) post-processed configuration of the MRF-Kevlar composite

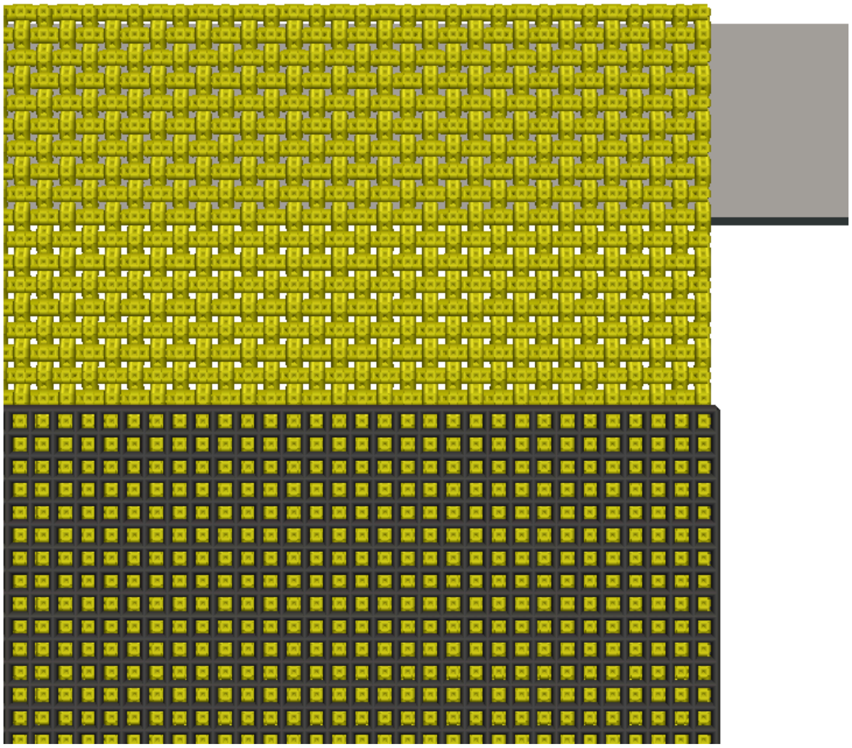

Figure 5.4: A geometric model for a MRF-Kevlar composite wrapped by PVC thin film

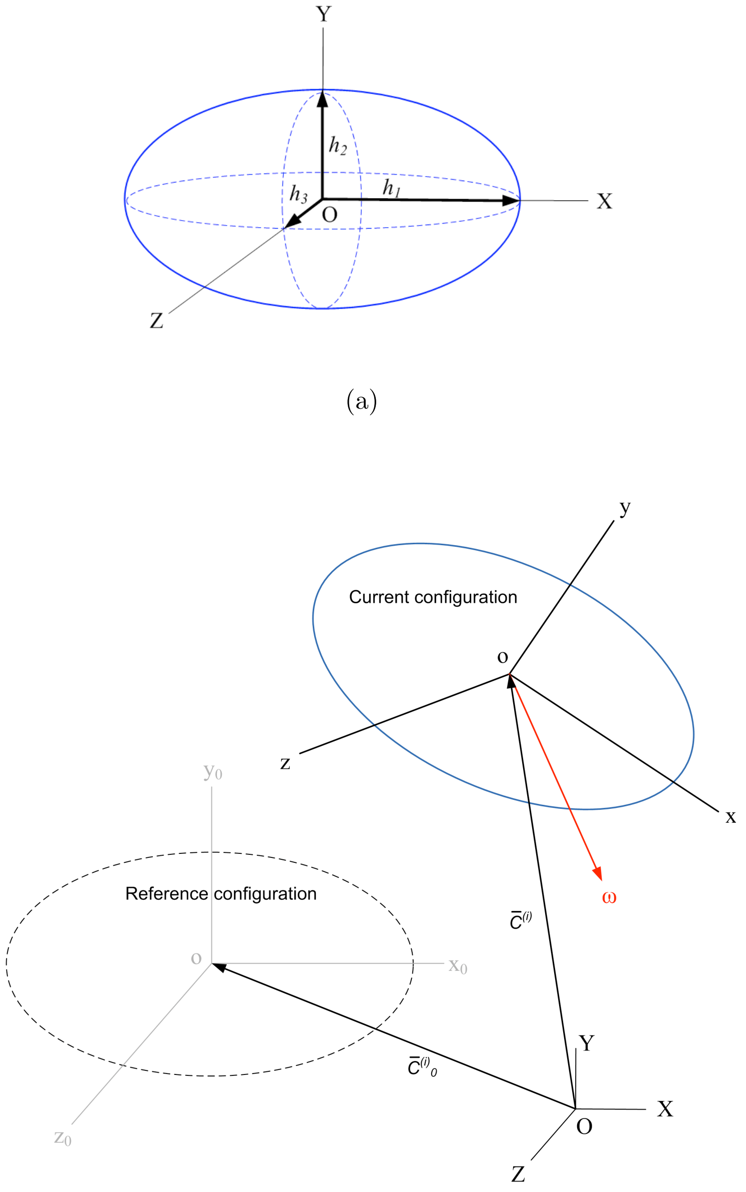

(a)

(b)

Figure 5.5: Schematic of an ellipsoidal particle (a): dimensions of half lengths (b) reference and current configuration of the ellipsoidal particle with the global reference frame $OXYZ$ and a body fixed co-rotating frame $oxyz$

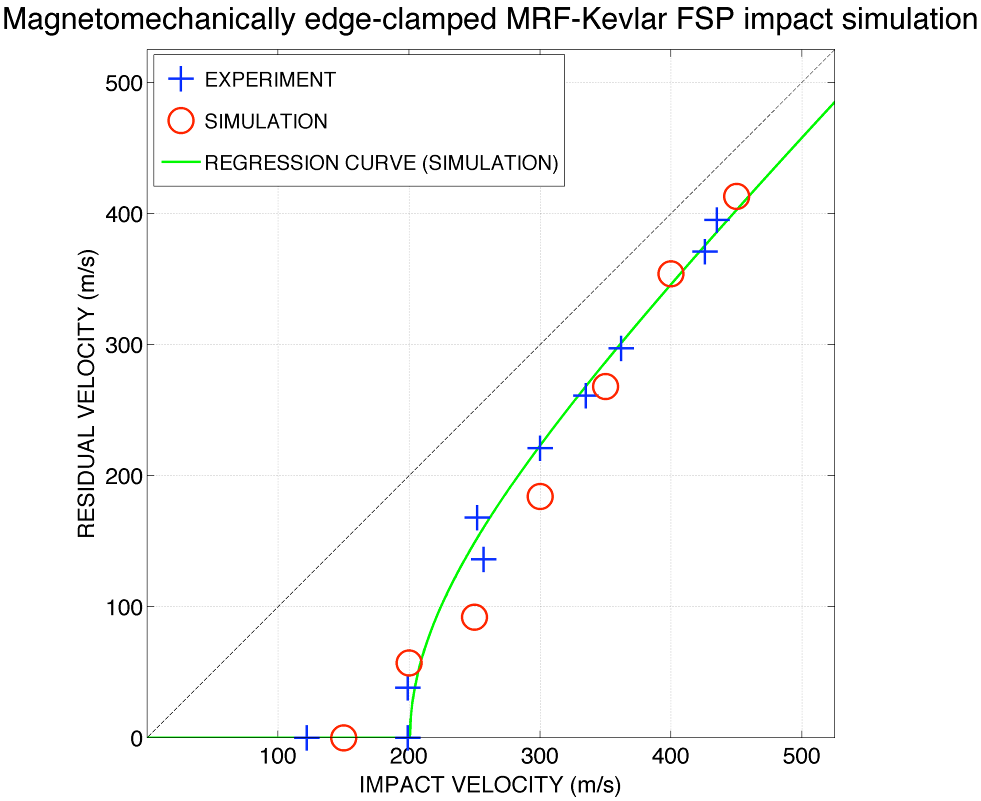

Figure 5.6: Simulation results: FSP impacts on magnetomechanically edge-clamped MR Fluid-Kevlar composites

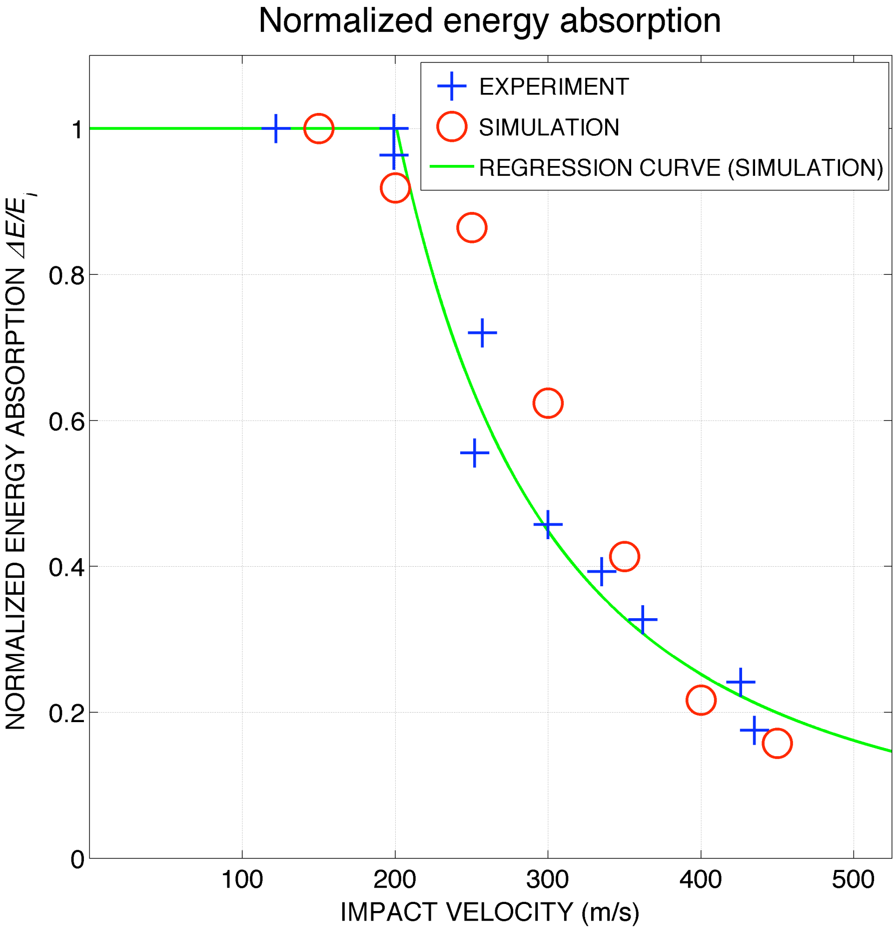

Figure 5.7: Simulation results: normalized absorbed energy for magnetomechanically edge-clamped MR Fluid-Kevlar composites with respect to the kinetic energy of a striking projectile

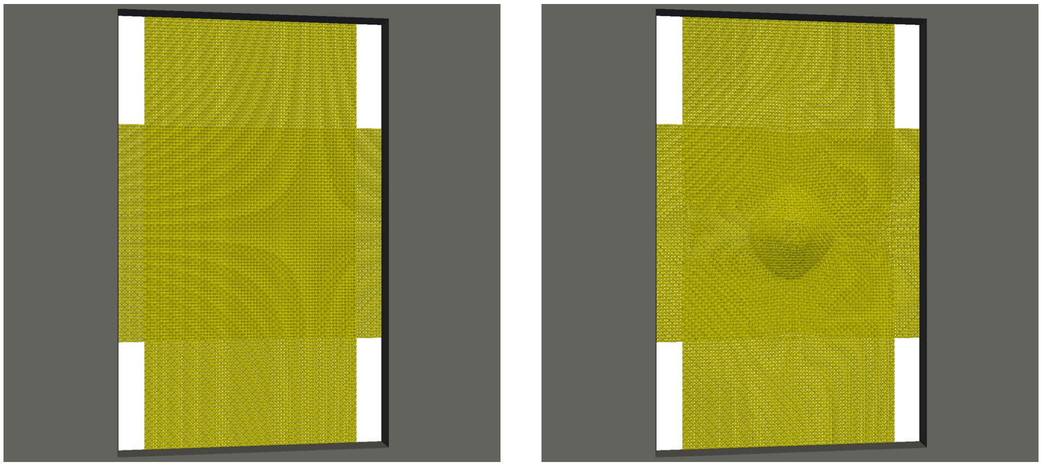

(a) $t = 0\ \mu sec$ (b) $t = 20\ \mu sec$

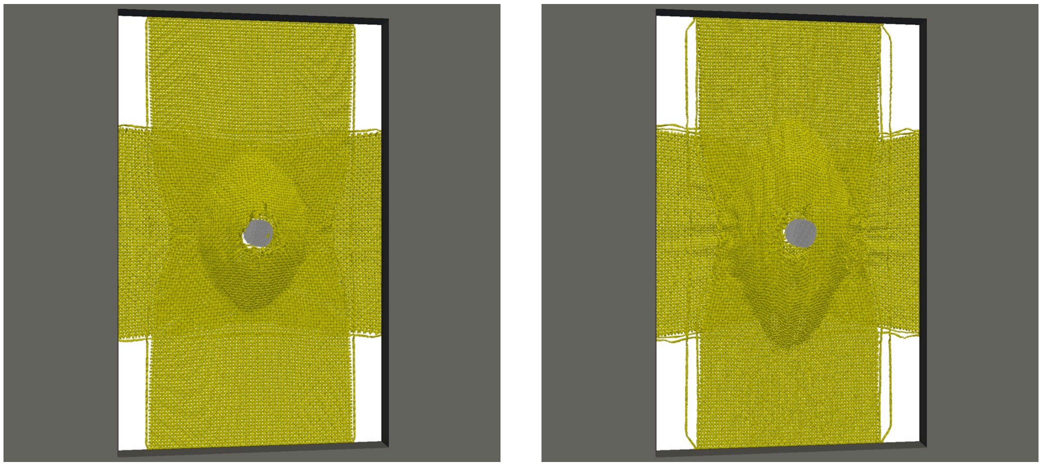

(c) $t = 40\ \mu sec$ (d) $t = 60\ \mu sec$

Figure 5.8: Simulation images: FSP impacts at 400 m/s on magnetomechanically edge-clamped MR Fluid-Kevlar composites at 0-60 μsec after impact

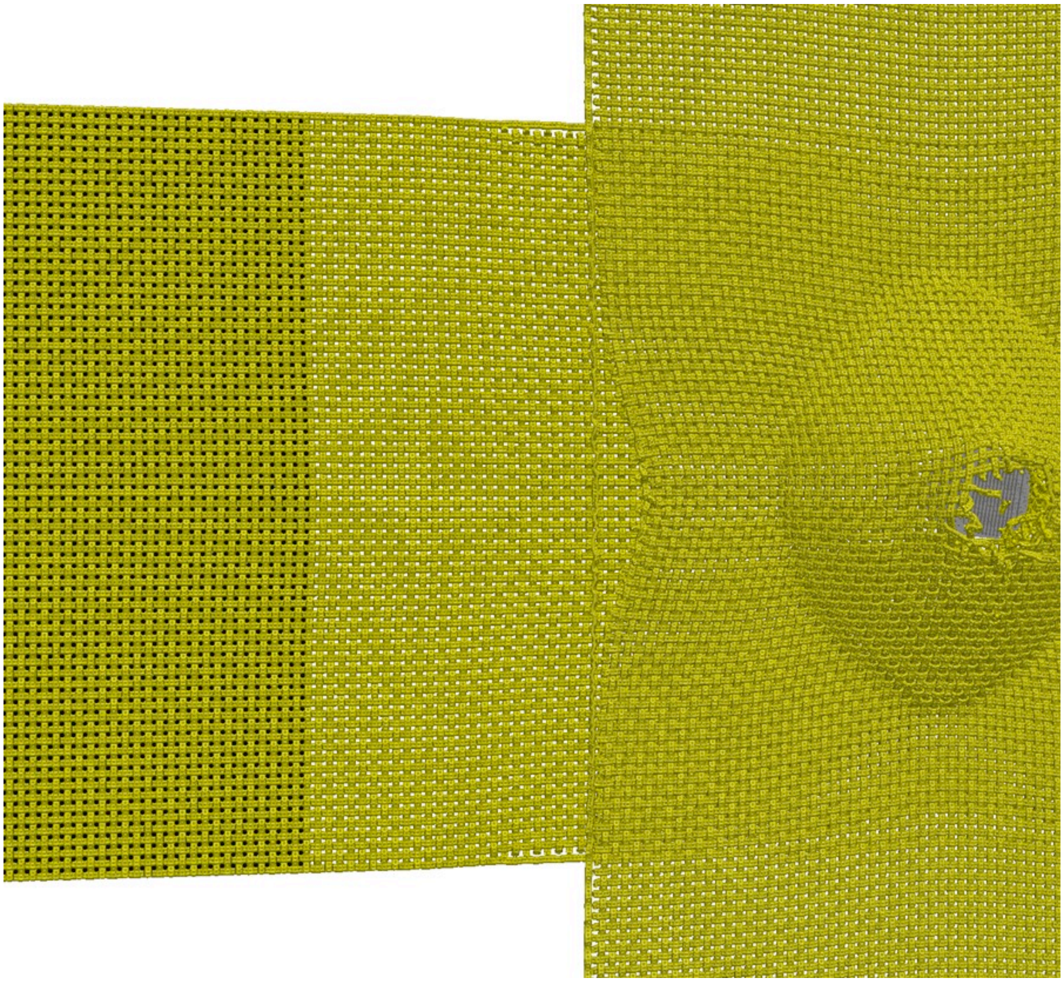

Figure 5.9: Interstitial MRF particles within voids between Kevlar yarns shown in FSP impact simulation at 400 m/s on magnetomechanically edge-clamped MR Fluid-Kevlar composites at 30 μsec after impact

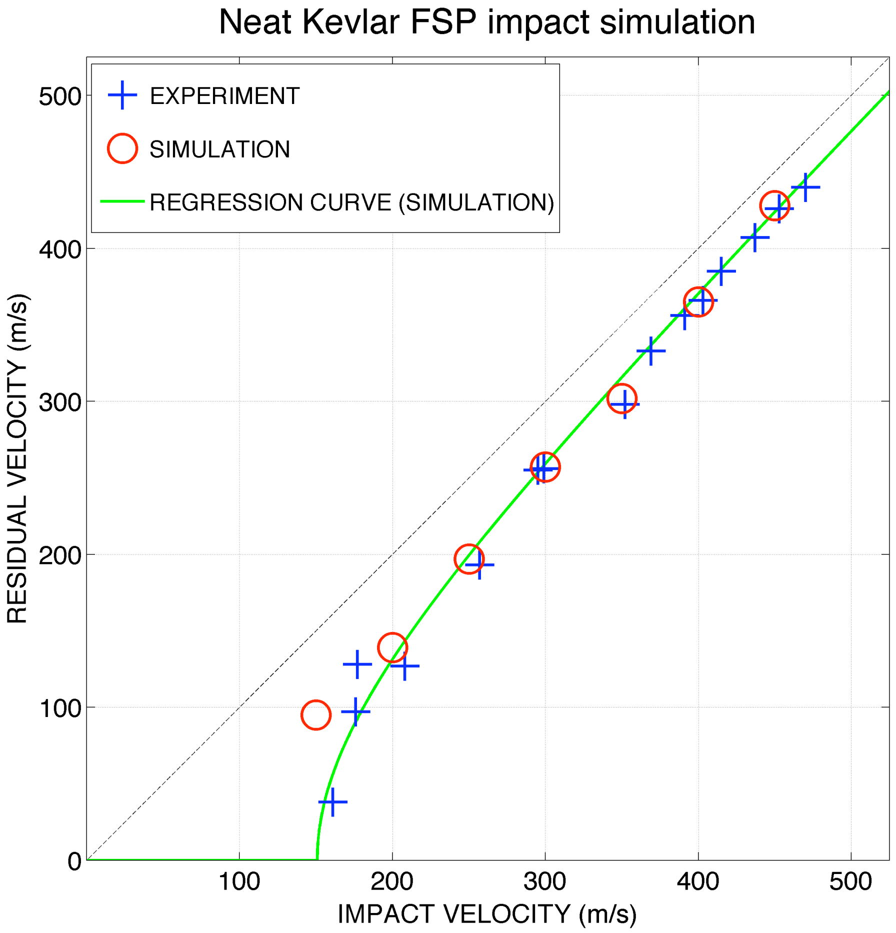

Figure 5.10: Simulation results: FSP impacts on a neat Kevlar strip

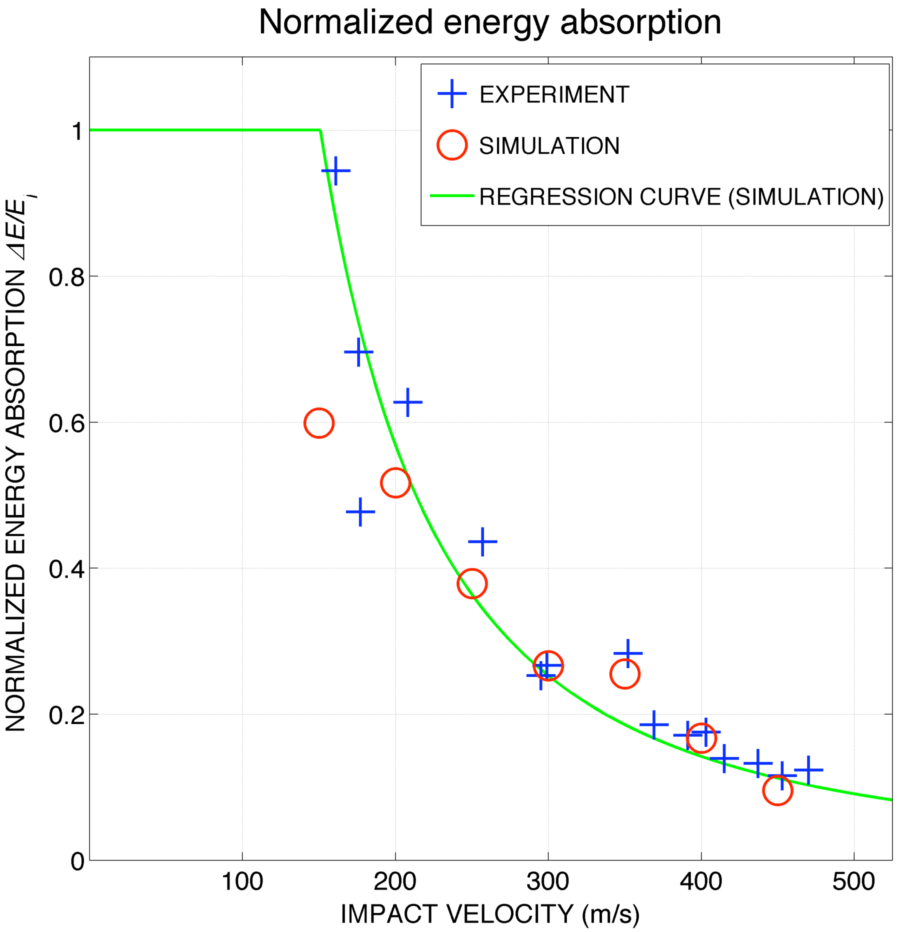

Figure 5.11: Simulation results: normalized absorbed energy for neat Kevlar baseline tests with respect to the kinetic energy of a striking projectile

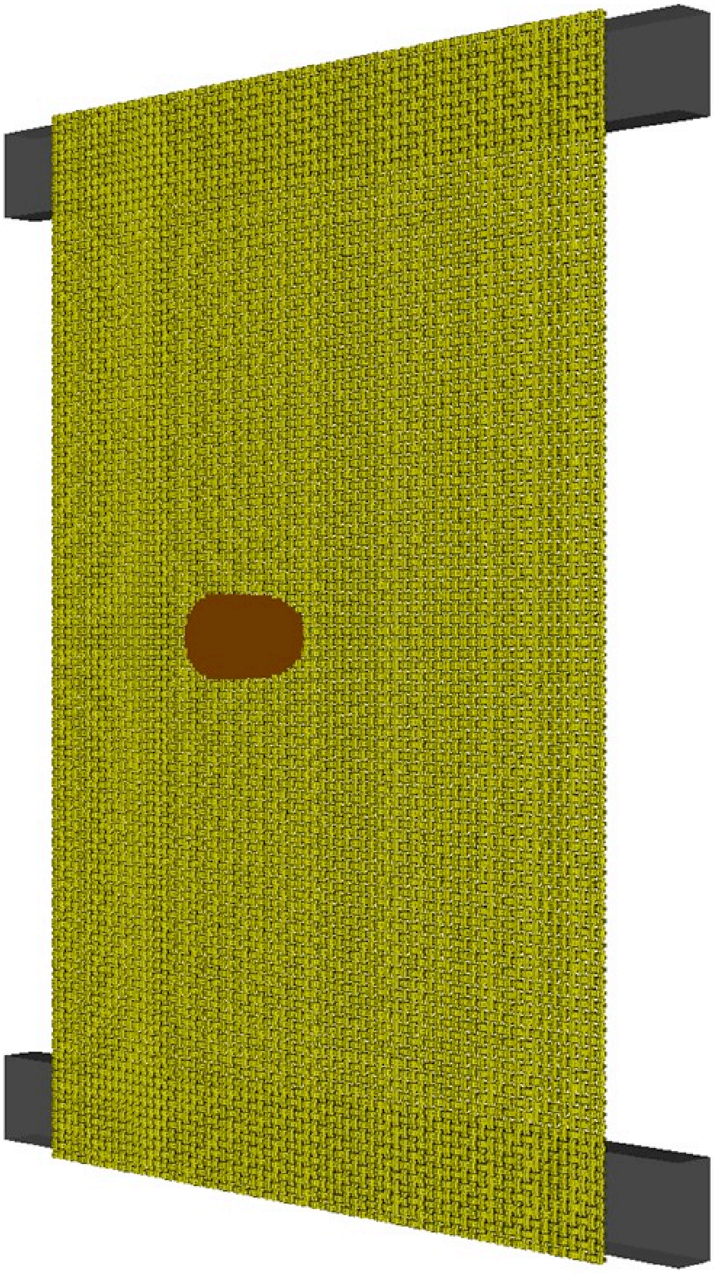

Figure 5.12: Initial configuration of FSP impact simulation on neat Kevlar target mounted on the target fixture

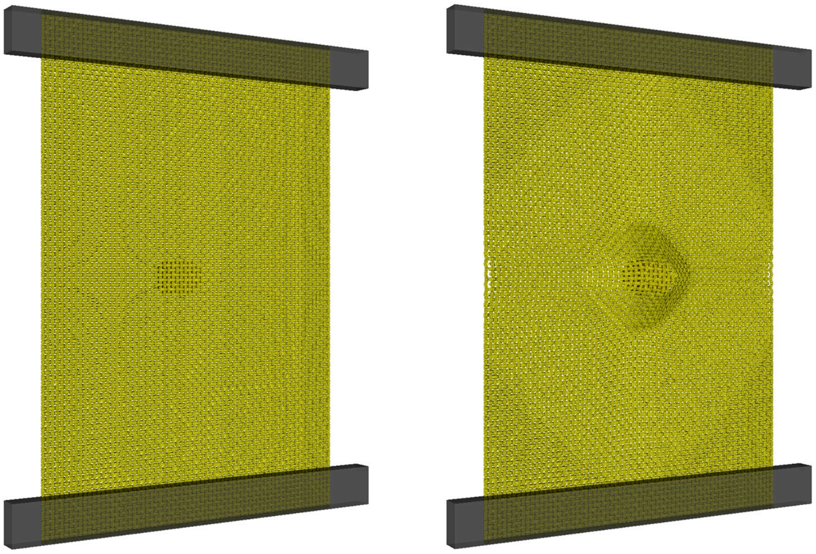

(a) $t = 0\ \mu sec$ (b) $t = 20\ \mu sec$

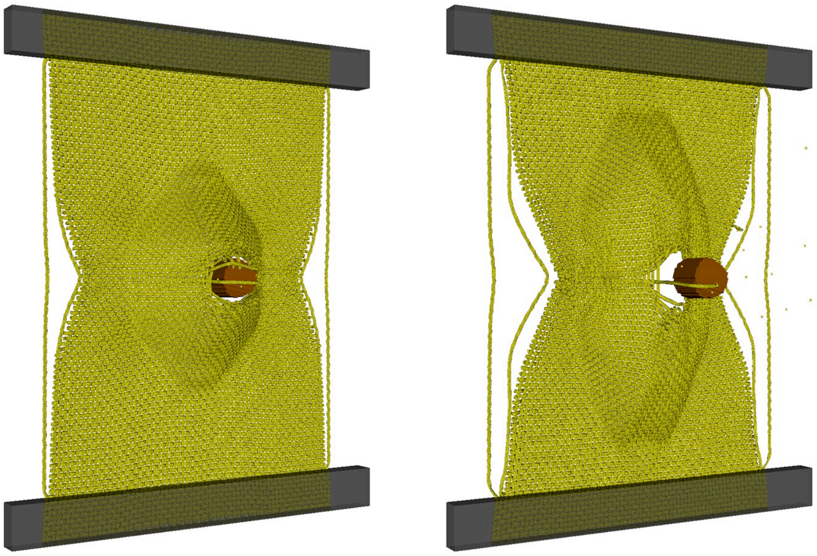

(c) $t = 40\ \mu sec$ (d) $t = 60\ \mu sec$

Figure 5.13: Simulation images: FSP impacts at 400 m/s on neat Kevlar fabric at 0-60 μsec after impact

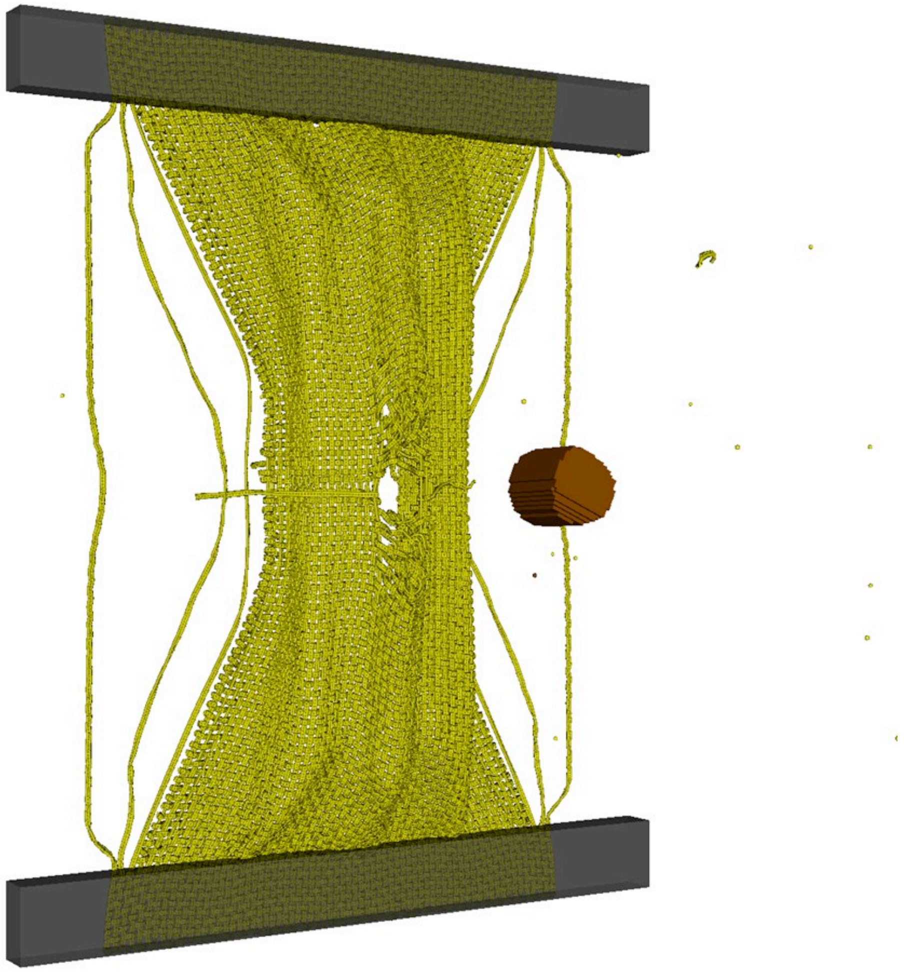

Figure 5.14: FSP impact simulation at 100 μsec on single-ply Kevlar mounted on the target fixture

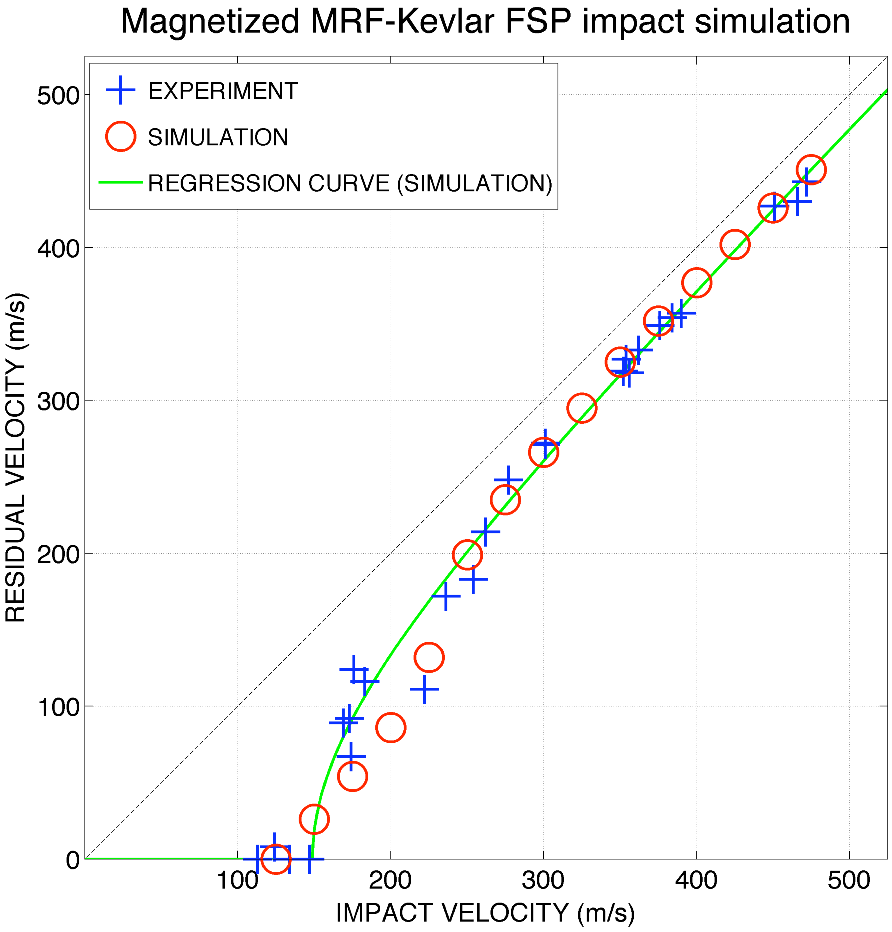

Figure 5.15: Simulation results: FSP impacts on MRF-Kevlar with an applied magnetic field (H_0=111 kA/m) in the coil

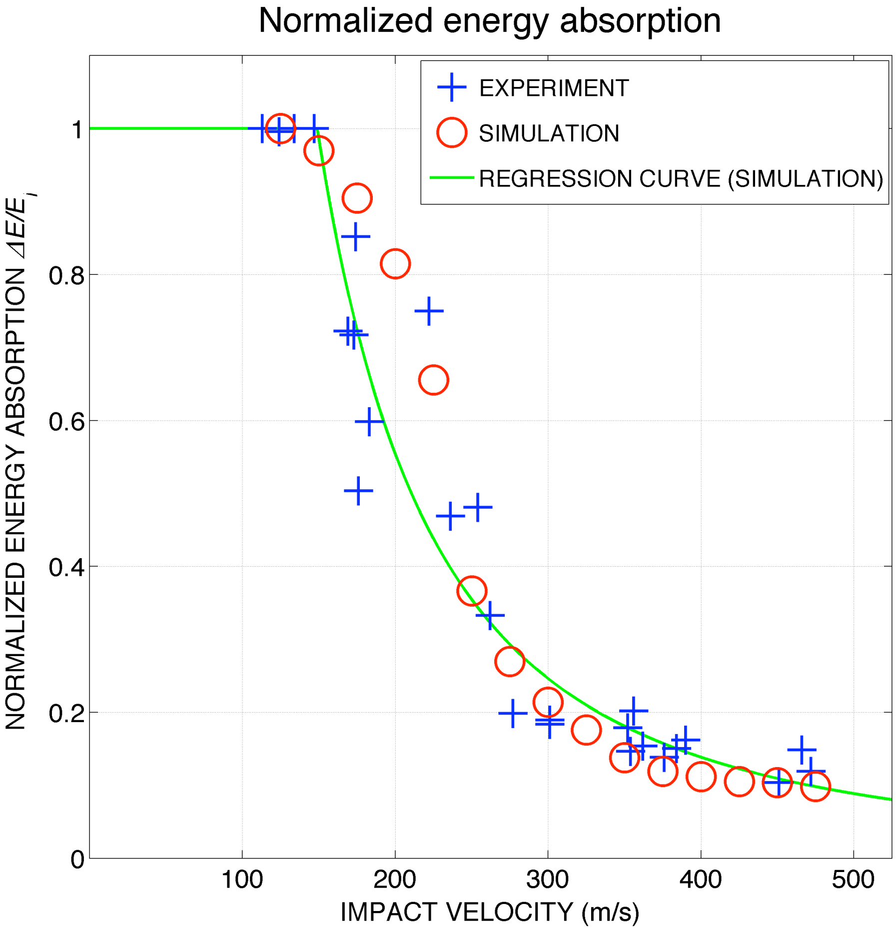

Figure 5.16: Simulation results: normalized absorbed energy for magnetized MRF-Kevlar composites in the coil where H_0=111 kA/m with respect to the kinetic energy of a striking projectile

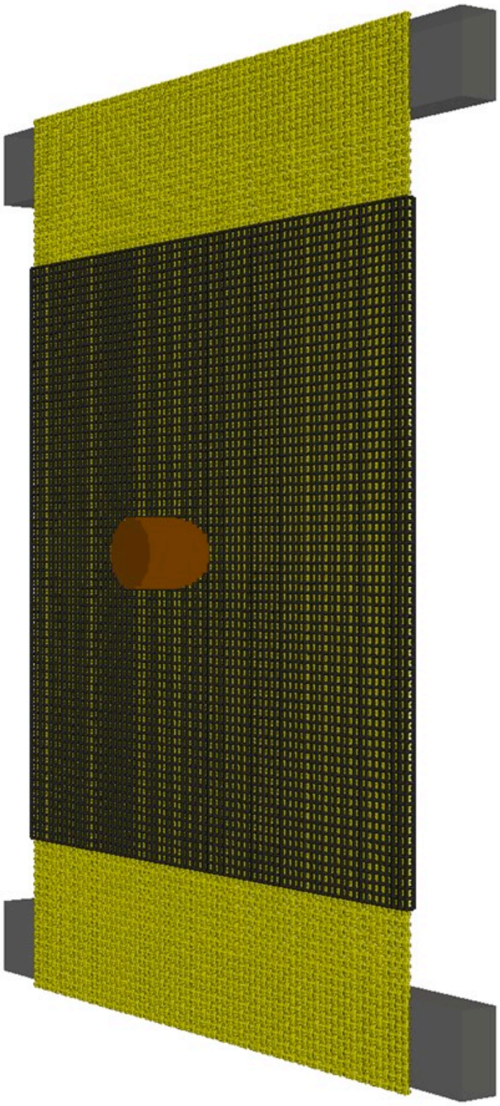

Figure 5.17: Initial configuration of FSP impact simulation on MRF-Kevlar target in the coil

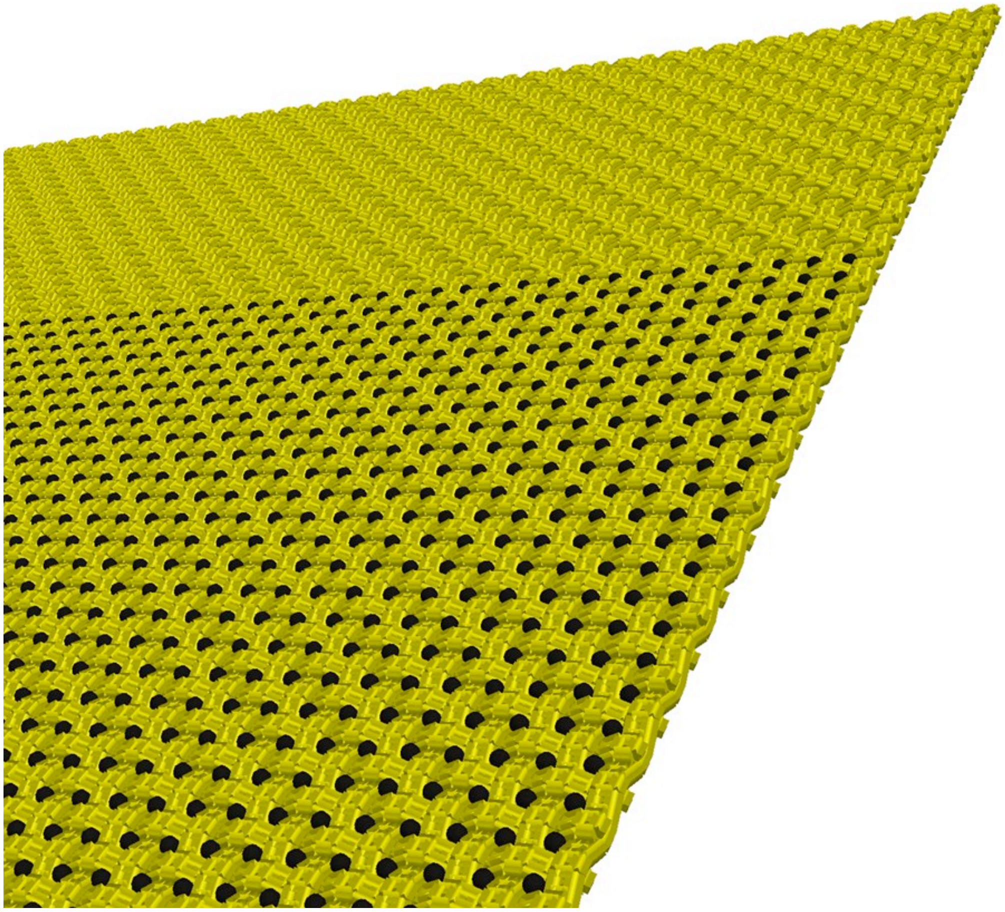

Figure 5.18: Interstitial MRF particles within voids between Kevlar yarns for MRF-Kevlar composites

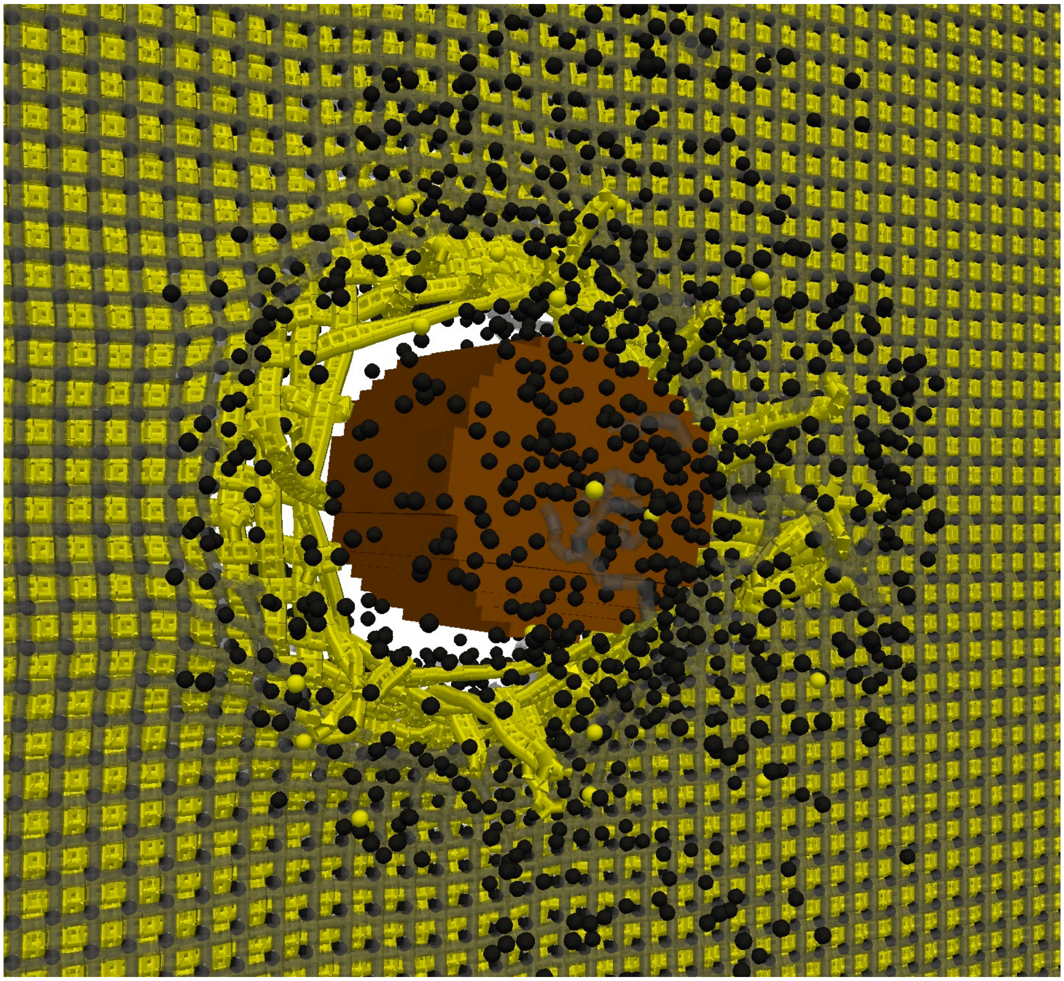

Figure 5.19: FSP impact simulation at 400 m/s on MRF-Kevlar composite target at 20 μsec after impact

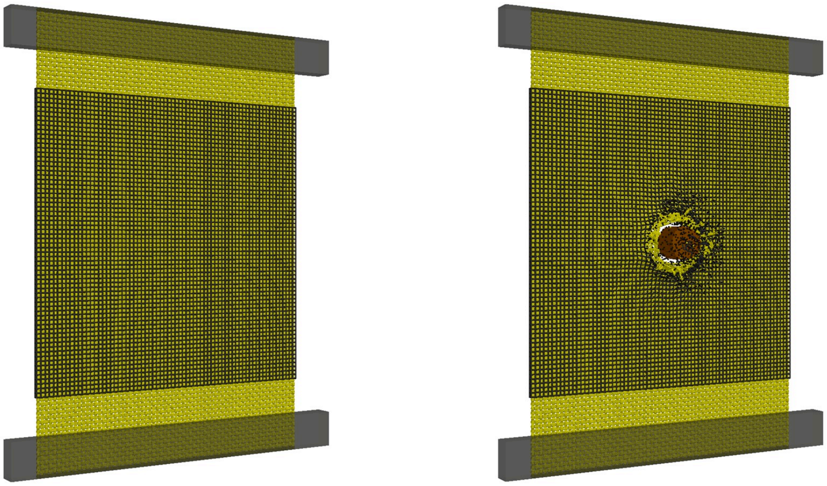

(a) $t = 0$ μsec (b) $t = 20$ μsec

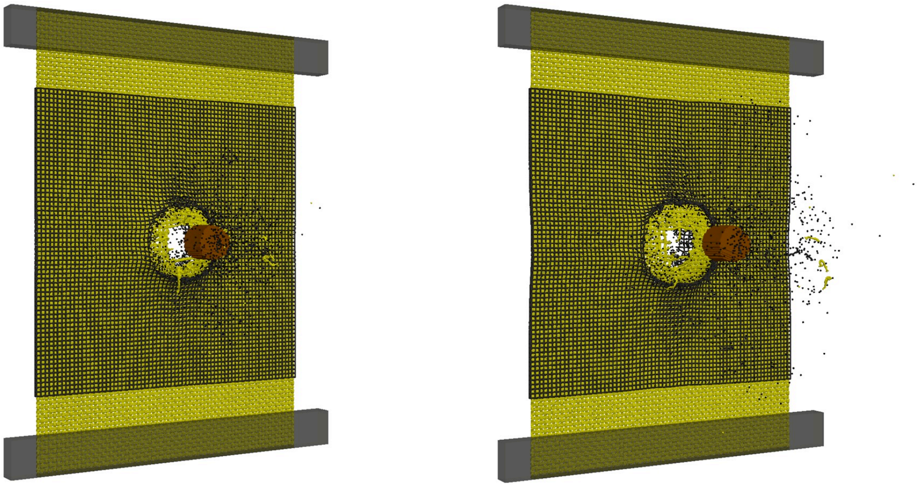

(c) $t = 40$ μsec (d) $t = 60$ μsec

Figure 5.20: Simulation images: FSP impacts at 400 m/s on MRF-Kevlar target in the coil at 0-60 μsec after impact

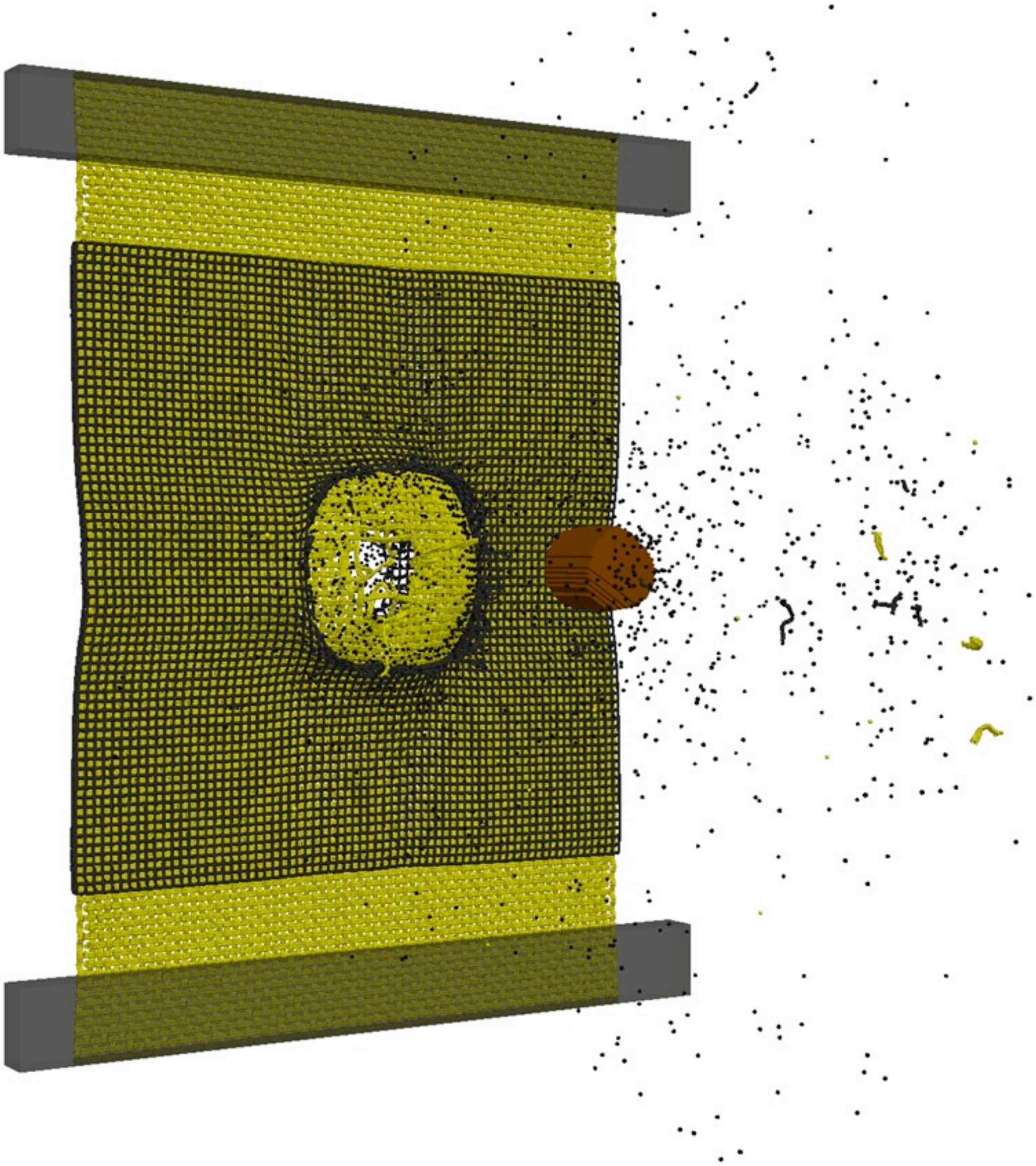

Figure 5.21: FSP impact simulation at 400 m/s on MRF-Kevlar composite target at 100 μsec after impact (front view)

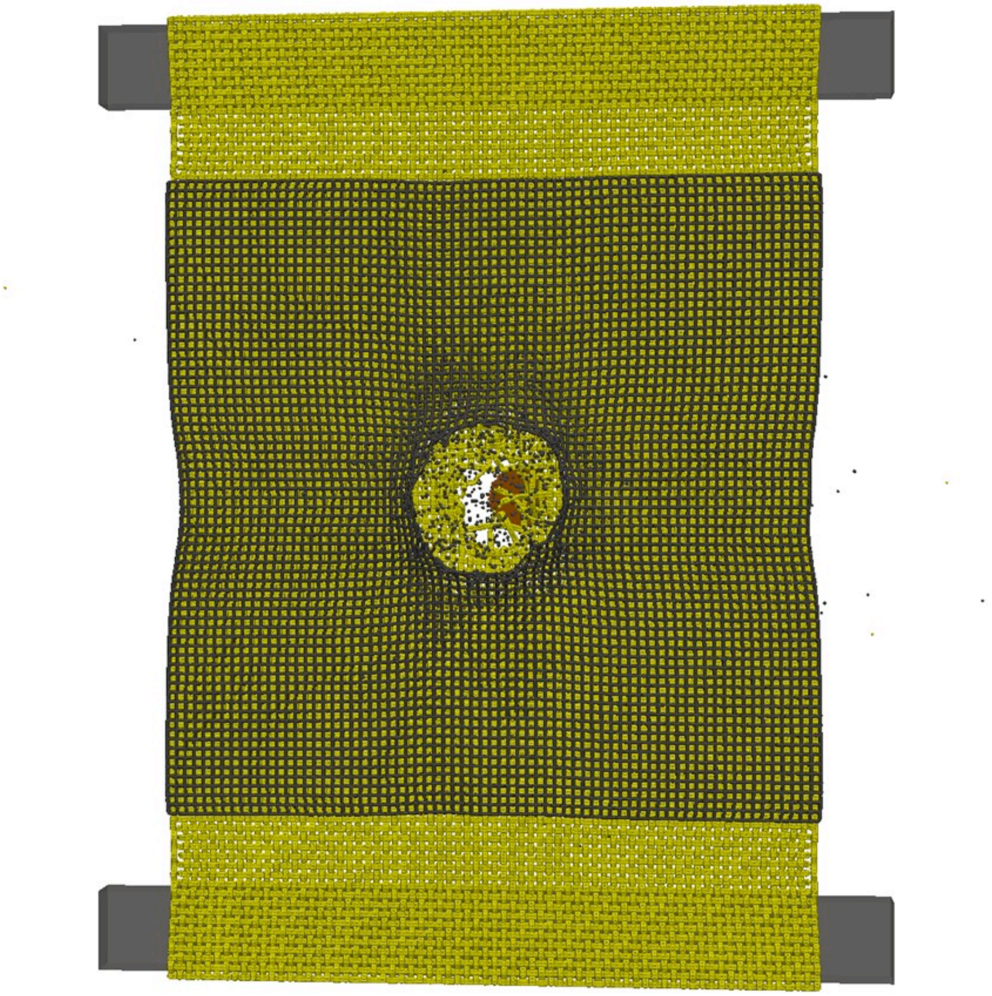

Figure 5.22: FSP impact simulation at 400 m/s on MRF-Kevlar composite target at 100 μsec after impact (back view)

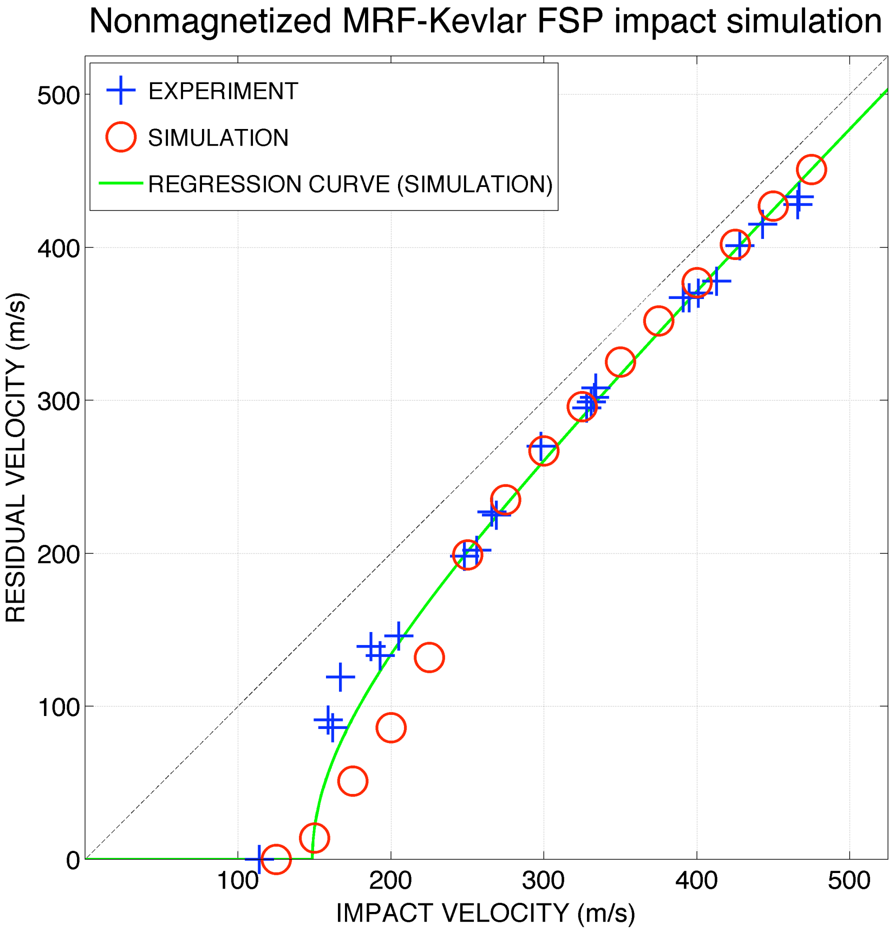

Figure 5.23: Simulation results: FSP impacts on MRF-Kevlar with no magnetic field

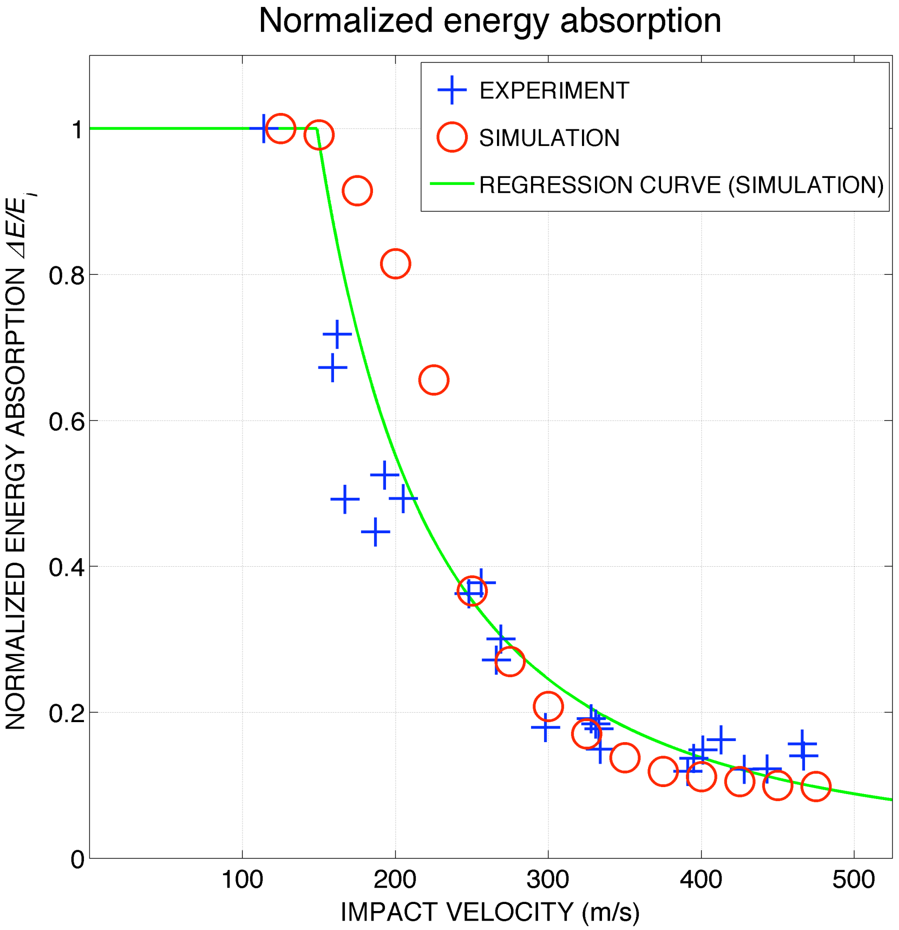

Figure 5.24: Simulation results: normalized absorbed energy for non-magnetized MRF-Kevlar composites with respect to the kinetic energy of a striking projectile

Chapter 6

Conclusion

The experimental and numerical research described in this dissertation was motivated by interest in adding dissipation augmentation to woven Kevlar fabrics. Magnetorheological fluids and a magnetostrictive composite coating have been studied as dissipation augmentations.

Micron-sized particles added to the fabric via magnetorheological fluids are magnetostrictive coating can occupy void spaces between the Kevlar yarns. These micro-particles were introduced to impede relative slippage between the fabric yarns under impact loading. To investigate the effectiveness of employing augmented fabrics for ballistic protection, this dissertation has studied the impact dynamics of three types of magnetomechanical Kevlar composites: (1) edge-clamped MRF-Kevlar composites, (2) MRF saturated-Kevlar composites enclosed by PVC film, and (3) Kevlar fabric coated with a Terfenol-D composite. FSP impact tests were conducted for all the magnetomechanical Kevlar composites, and neat Kevlar fabrics were tested to provide baseline data. Computational research has been conducted only for MR fluid treated Kevlar.

The FSP impact tests were performed in collaboration with Southwest

Research Institute. A new experimental procedure was developed, which consists of target preparation and the design of an experimental procedure for FSP impact tests on magnetomechanical Kevlar composite targets.

A computational model was formulated to describe projectile impact on magnetorheological fluid treated Kevlar. It consists of mesomechanical hybrid particle-element model for neat Kevlar fabrics with interstitial fluid and the associated overlap, used to confine the fluid. The MR fluid particles are loaded by contact impact with neighboring particles and by a shear yield stress due to the applied magnetic field. Mixture equations of state for MR fluids and MR fluids enclosed by PVC thin film have been derived. The damping characteristics of the MR fluids were modeled using a fleid-dependent Bingham plastic model, with the properties of the MR fluids specified by the manufacturer. The formulation models contact-impact and viscous interaction within the fabric and within the fluid, as well as corresponding fluid-fabric interaction. Validation simulations were performed for FSP impacts on MRF-Kevlar composites. Simulation results have shown good agreement with the experiment data. The hybrid particle-element formulation therefore extends previous work on a mesomechanical yarn-level fabric model. Element erosion and tensile instability problems common to other numerical methods are avoided by this unified, energy-based, modeling scheme. The experiments and simulations performed in this research provide a more thorough understanding for the impact dynamics of magnetomechanical composites. They contribute to future development of experimental and computational techniques for ballistic impact research, including multiphysics systems with complex geometry and incorporating advanced armor materials. Computer simulation work, based on the extended hybrid particle-element method, advances the state of the art in virtual prototyping of soft body armor systems.

Additional computational research is suggested to extend the current work in order to simulate MSC-Kevlar composites. An extended model could incorporate a magneto-dynamic model for dipole-field interaction of the magnetized Terfenol-D particles and a stiction model for the polyurethane adhesive coating. More material data is needed to study shock compression of Terfenol-D and polyurethane at very high velocities. A formulation of Hamilton's equanstions incorporating a dipole-field interaction model is presented in Appendix B. In order to quantify the distribution of impact energy for Kevlar fabric augmented by magnetorheological fluids or magnetostrictive solids, additional experimental and numerical work on energy accounting [145] is recommended as future work.

Appendices

Appendix A

Magnetic Circuit Model for an Electromagnet with Air-Gap Reluctance

A magnetic circuit model provides a useful simplification for calculating magnetic field quantities (such as magnetomotive force, magnetic reluctance and magnetic flux) for a magnetic system with a circuital configuration [27]. Here a circuit model is employed to estimate the magnetic field strength in an air gap between an electromagnet and a flat steel plate, since the gap length associated with the experimental research described in Chapter 2 is too small (l_g=16 mil = 0.4064 mm) to be probed by a conventional Gaussmeter. In this research, two commercial electromagnets, model EPA-242 (Figure A.1) and ESA-241 (Figure A.3) from Industrial Magnetics, Inc. were considered as candidates to provide a magnetic clamping force on a Kevlar strip saturated with MR fluid. The magnetic field strength calculated from the circuit model was used to estimate the shear yield stress of the MR fluid occupying the gap.

A.1 Magnetic Circuit Model for the Electromagnet EPA-242 without Fringing Effect

Figure A.1 shows: (a) the configuration of flat coplanar poles for the electromagnet EPA-242, (b) a schematic of a magnetic circuit, and (c) the associated magnetic circuit model.

Applying Kirchhoff's voltage law in the loop for the circuit model (Figure A.1(c)), the magnetomotive force can be expressed as the algebraic sum of all the voltage drops due to magnetic reluctance in the circuit.

$$V_m = \Phi(R_i + R_p + 2R_g) \tag{A.1}$$

where Φ is a magnetic flux, V_m is a magnetomotive force, R_i is the reluctance of the inner magnetic core, R_p is the reluctance associated with the mild steel plate, and R_g is the air-gap reluctance. By definition, the air gap reluctance R_g and the magnetic flux Φ can be written as

$$R_g = \frac{l_g}{\mu_0 A} \tag{A.2}$$

$$\Phi = BA \tag{A.3}$$

where l_g is the air gap length shown in Figure A.1(b), μ_0 is the permeability of free space, B is a magnetic flux density in the air gap, and A is the effective area through which the magnetic flux Φ passes in the air-gap region.

Substituting (A.2) and (A.3) into (A.1), V_m yields

$$V_m = BA\left(R_i + R_p + \frac{2l_g}{\mu_0 A}\right) \tag{A.4}$$

Rearrangement of this equation expresses B as a function of l_g in the form

$$B(l_g) = \left[\frac{A(R_i + R_p)}{V_m} + \frac{2l_g}{\mu_0 V_m}\right]^{-1} = \frac{1}{C_0 + C_1 l_g} \tag{A.5}$$

where C_0 and C_1 are fitted coefficients.

Neglecting fringing effect in the air gap, A is the pole area depicted in Figure A.1(c). Furthermore, since the system parameters V_m, R_i, and R_p are independent of l_g, the coefficients C_0 and C_1 in Equation (A.5) should be constant. Applying a linear regression technique to measured data $\{l_g,B\}$, these coefficients can be determined experimentally.

Figure A.2 shows the model-based curve for EPA-242, which has been obtained by fitting experimental data. In this plot, the magnetic field intensity H is shown instead of the magnetic flux density B, since H is normally used to estimate MR fluid properties.

A.2 Magnetic Circuit Model incorporating Fringing Effect for the Electromagnet ESA-241

Figure A.3 shows (a) the configuration of the poles for the electromagnet ESA-241, (b) a schematic of the magnetic circuit, and (c) the associated magnetic circuit model. Unlike the parallel pole configuration for EPA-242, the electromagnet ESA-241 has a rectangular pole at the center and much narrower rectangular poles along the four edges of its bottom face, as shown in Figure A.3(a). Magnetic field measurement reveals that fringing effects around the edge poles are not negligible, while fringing effects for the center pole are insignificant. Hence the fringing effect near the edge poles is considered here in calculating the air-gap reluctance (Figure A.4).

The circuit analysis used for EPA-242 can also be used for the island pole magnet. This magnetic flux B_c can be expressed as

$$B_c(l_g) = \left[\frac{A_c(R_i + R_p)}{V_m} + \left(1 + \frac{A_c}{A_e}\right)\frac{l_g}{\mu_0 V_m}\right]^{-1} \approx \frac{1}{E_0 + E_1 l_g} \tag{A.6}$$

where V_m is a magnetomotive force, l_g is an air gap length, R_i is the intrinsic reluctance of the magnet core, R_p is the reluctance associated with the metal plate, A_c is the area of the center pole, A_e is the total area of four edge poles, and μ_0 is the permeability of free space. Two coefficients E_0 and E_1 can be obtained using the same curve fitting method applied for EPA-242.

The fringing effect for the edge poles can be accounted in the magnetic circuit model by considering an effective area for magnetic flux passage. Figure A.5 shows a post-plate configuration and the magnetic fringing effect over an edge pole. The hexagonal post represents a magnetic core, associated with each edge pole. Regardless of the existence of magnetic fringing, Φ_1 should equal to Φ_2 in Figure A.5. Therefore, if the gap length l_g is small enough to neglect the spatial gradient of the magnetic flux, Φ_2 can be approximated as the product of two quantities, the magnetic flux density B_2 and the effective area A_e^{eff} through which B_2 passes. In the case of the magnet ESA-241, the effective area A_e^{eff} can be expressed as a function of l_g [8].

$$A_e^{\text{eff}} = A_e + \frac{4d}{\pi}\left[1 + ln\left(\frac{\pi h}{4l_g}\right)\right]l_g \tag{A.7}$$

where A_e is the total area of four edge poles.

Substituting, (A.6) and (A.7) into the equation $\Phi_1 = \Phi_2$ yields

$$B_e(l_g) = \frac{A_c}{A_e^{\text{eff}}}B_c = \frac{A_c}{\left[A_e + \frac{4d}{\pi}\left[1 + ln\left(\frac{\pi h}{4l_g}\right)\right]l_g\right](E_0 + E_1 l_g)} \tag{A.8}$$

Figure A.6 plots the magnetic field intensity as a function of the air-gap length l_g. Once E_0 and E_1 are determined by the data regression, the magnetic field intensity H_e satisfying $H_e = \frac{B_e}{\mu_o}$ can be calculated for the given geometric parameters d and h of the magnetic core. Hence, the field measurements for the edge poles can be used to estimate the accuracy of the derived model. In this analysis, the modeled field equations (A.6) and (A.8) show good agreement with the experimental data, as indicated in Figure A.6. The estimated field intensities for ESA-241 with an air-gap length of 0.4064 mm are H_c=809 kA/m and H_e=596 kA/m. These values are high enough to induce saturated magnetization for the MR fluid (MRF-140 CG manufactured by Lord Corporation) used in this research.

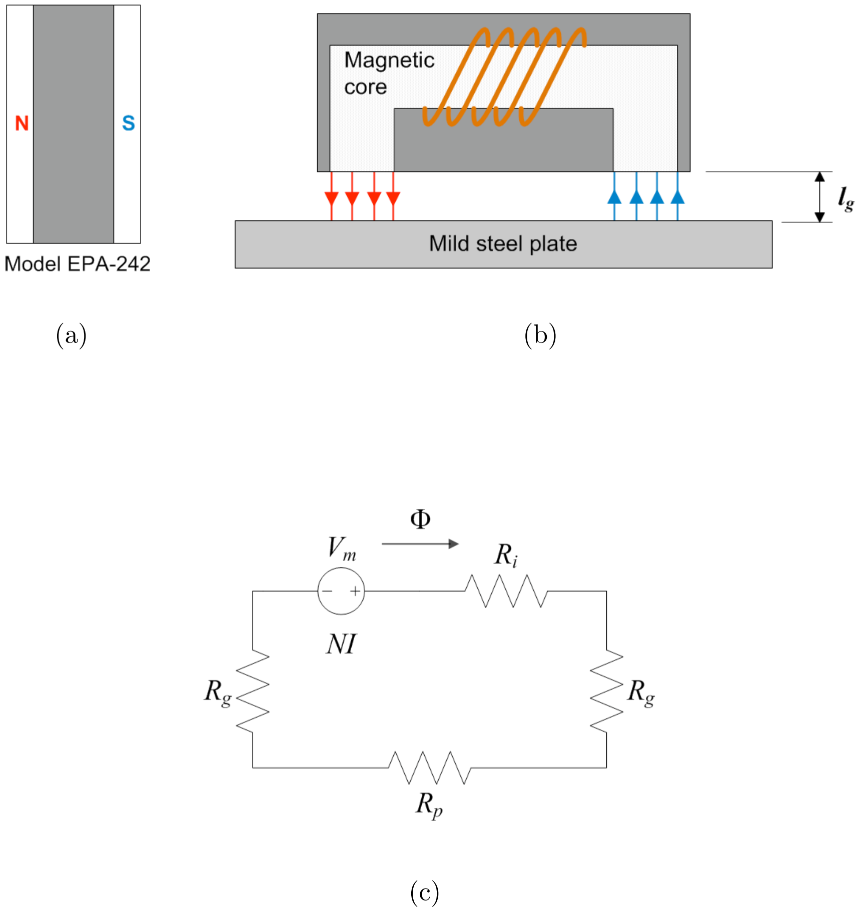

Figure A.1: Electromagnet (model EPA-242) and its magnetic circuit design : (a) pole configuration (b) schematic of the magnet and ferromagnetic plate with a specific air gap length (c) modeled magnetic circuit diagram

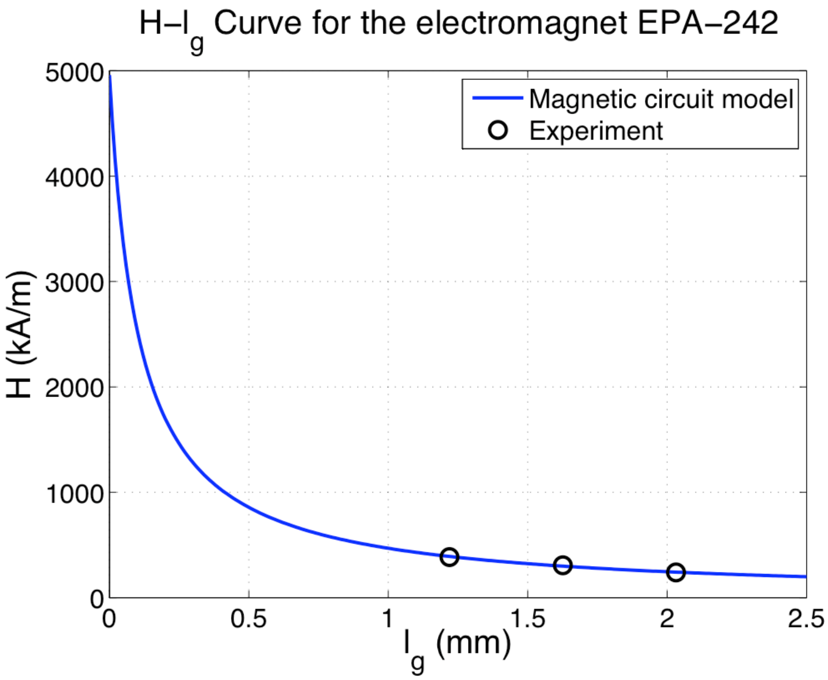

Figure A.2: Magnetic field intensity versus air gap length graph for the electromagnet EPA-242 which has two parallel rectangular poles

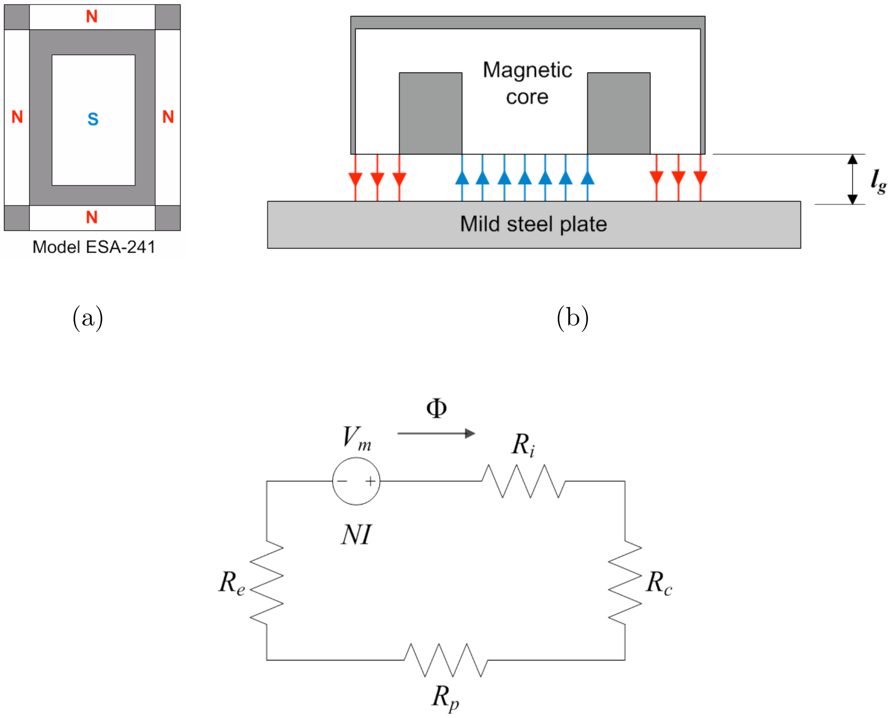

(a) (b)

(c)

Figure A.3: Electromagnet (model ESA-241) and its magnetic circuit design : (a) pole configuration (b) schematic of the magnet and ferromagnetic plate with a specific air gap length (c) modeled magnetic circuit diagram

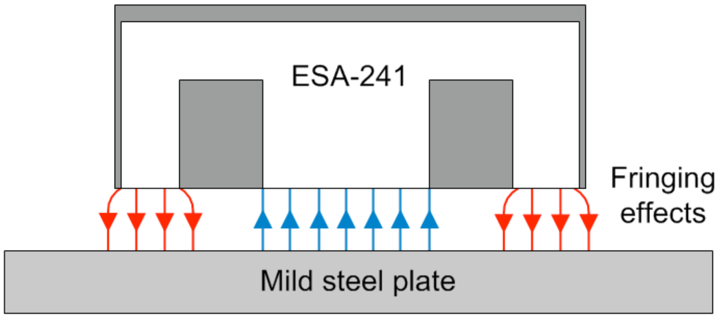

Figure A.4: Diagram showing the fringing effects at the edge poles of ESA-241

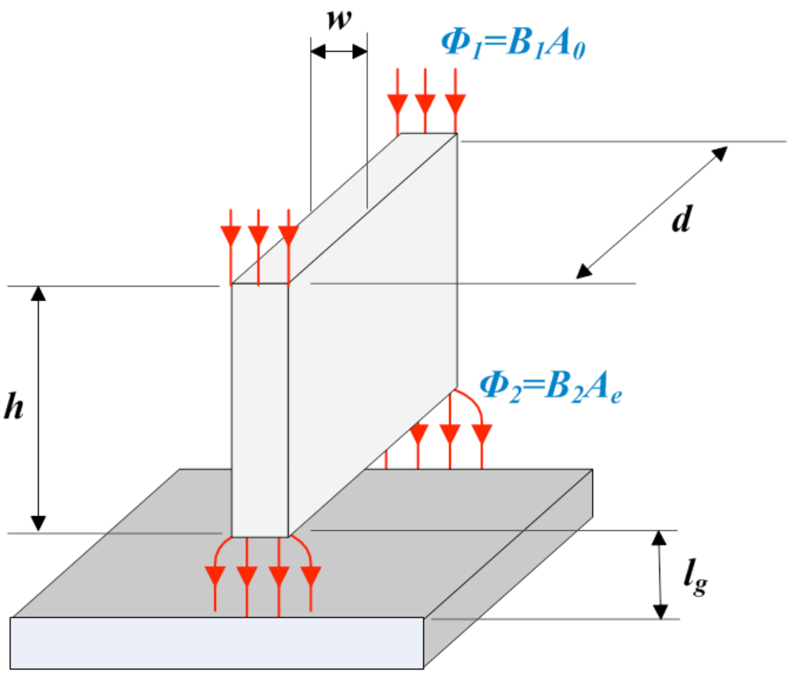

Figure A.5: Schematic of the ferromagnetic plate-post configuration with an air gap

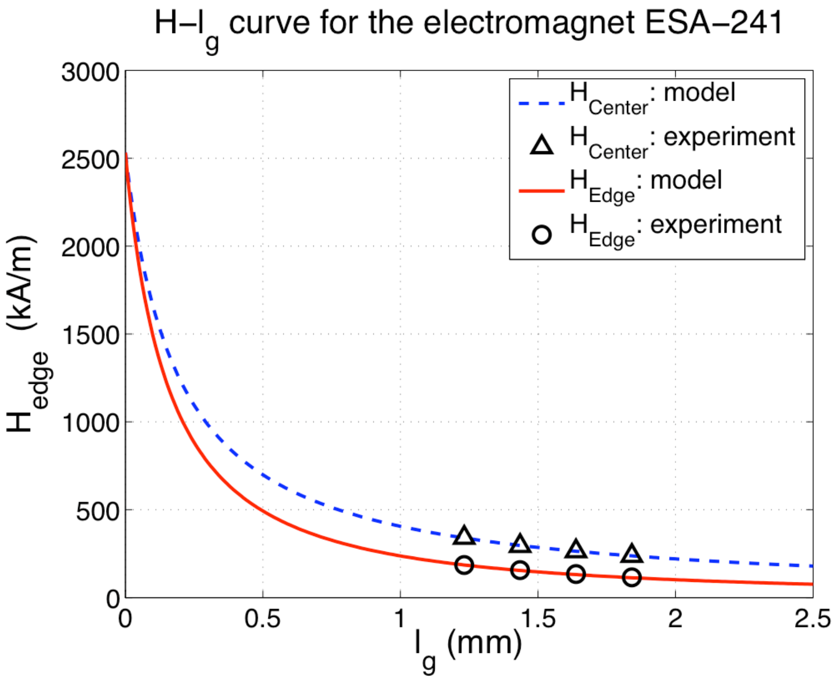

Figure A.6: Magnetic field intensity versus air gap length graph for the electromagnet ESA-241 which has a rectangular south pole at the center and four rectangular north poles along magnet edges

Appendix B

Hamilton's Equations of a Magnetic Dipole Moment in a Uniform Magnetic Field

In this appendix, a dipole-field interaction model is formulated for a permanently magnetized spherical particle under an external magnetic field. This model can be used for the future development of a hybrid particle-element model to simulate the impact dynamics of magnetized MSC-Kevlar composites, introduced in Chapter 4.

A schematic of the magnetized sphere in a magnetic field is depicted in Figure B.1. In this formulation, two coordinate systems are adopted, which are the global coordinate system {OXYZ} and the body-fixed co-rotating coordinate system {oxyz}. Hamilton's equations in canonical form are derived for this permanently magnetized particle, under the application of a uniform magnetic field. In this formulation, the rotational dynamics of the sphere are described by Euler parameters which provides a singularity-free parametric presentation of rigid-body rotation [101].

The finite rotation of a rigid body can be expressed in terms of the unit vector for the axis of rotation **u** and the angle of rotation (or the angular displacement) about the axis φ, defined in a counterclockwise sense,

$$\mathbf{u} = [\ u_x\ u_y\ u_z\ ]^T = [\ \cos\theta_x\ \ \cos\theta_y\ \ \cos\theta_z\ ]^T \tag{B.1}$$

where $\cos\theta_x$, $\cos\theta_y$, and $\cos\theta_z$ are the direction cosines of $\mathbf{u}$. The Euler parameters e_i $(i = 0, 1, 2, 3)$ are defined in terms of $\cos\theta_i$ and φ as below.

$$\mathbf{e} = \begin{bmatrix} e_0 \\ e_1 \\ e_2 \\ e_3 \end{bmatrix} = \begin{bmatrix} \cos\left(\frac{\varphi}{2}\right) \\ \cos\theta_x \sin\left(\frac{\varphi}{2}\right) \\ \cos\theta_y \sin\left(\frac{\varphi}{2}\right) \\ \cos\theta_z \sin\left(\frac{\varphi}{2}\right) \end{bmatrix} \tag{B.2}$$

Euler parameters can be used to express the Euler angles associated with the rotational displacement. If the Euler angles (ϕ, θ, ψ) are using **z-x-z** sequential rotations [10], they can be expressed in terms of the corresponding Euler parameters as

$$\phi = \arctan\left(\frac{e_3}{e_0}\right) + \arctan\left(\frac{e_2}{e_1}\right) \tag{B.3a}$$

$$\theta = 2\,\mathrm{arcsin}\left(\sqrt{{e_1}^2 + {e_2}^2}\right) \tag{B.3b}$$

$$\psi = \arctan\left(\frac{e_3}{e_0}\right) - \arctan\left(\frac{e_2}{e_1}\right) \tag{B.3c}$$

The rotation matrix $\mathbf{R}$ representing the coordinate transform from the co-rotating to the global system, with a common origin, can be represented by the Euler parameters.

$$\mathbf{R} = \mathbf{E}\mathbf{G}^T = 2\begin{bmatrix} {e_0}^2 + {e_1}^2 - \frac{1}{2} & e_1e_2 - e_0e_3 & e_1e_3 + e_0e_2 \\ e_1e_2 + e_0e_3 & {e_0}^2 + {e_2}^2 - \frac{1}{2} & e_2e_3 - e_0e_1 \\ e_1e_3 - e_0e_2 & e_2e_3 - e_0e_1 & {e_0}^2 + {e_3}^2 - \frac{1}{2} \end{bmatrix} \tag{B.4}$$

where

$$
\begin{aligned}
\mathbf{E} &= \begin{bmatrix} -e_1 & e_0 & -e_3 & e_2 \\ -e_2 & e_3 & e_0 & -e_1 \\ -e_3 & -e_2 & e_1 & e_0 \end{bmatrix} && \text{(B.5)} \\
\mathbf{G} &= \begin{bmatrix} -e_1 & e_0 & e_3 & -e_2 \\ -e_2 & -e_3 & e_0 & e_1 \\ -e_3 & e_2 & -e_1 & e_0 \end{bmatrix} && \text{(B.6)}
\end{aligned}
$$

The angular velocity $\mathbf{w}'$ in the coordinate system co-rotating with the rigid body is

$$\mathbf{w}' = 2\mathbf{G}\dot{\mathbf{e}} \tag{B.7}$$

The angular momentum $\mathbf{h}'$ in the co-rotating frame is

$$\mathbf{h}' = \mathbf{J}'\mathbf{w}' \tag{B.8}$$

where $\mathbf{J}'$ is the moment of inertia of the rigid body, expressed in terms of co-rotating coordinates.

Hamilton's equations for this dynamic system can be written as [121]:

$$
\begin{aligned}
\dot{\mathbf{p}} &= -\frac{\partial V}{\partial \mathbf{c}} + \mathbf{f}(t) && \text{(B.9a)} \\
\dot{\mathbf{h}}' &= -\Omega\mathbf{h}' - \frac{1}{2}\mathbf{G}\frac{\partial V}{\partial \mathbf{e}} + \mathbf{T}(t) && \text{(B.9b)} \\
\dot{\mathbf{c}} &= m^{-1}\mathbf{p} && \text{(B.9c)} \\
\dot{\mathbf{e}} &= \frac{1}{2}\mathbf{G}^T\mathbf{J}'^{-1}\mathbf{h}' && \text{(B.9d)}
\end{aligned}
$$

where $\mathbf{p}$ is the linear momentum of the sphere, V is the potential energy associated with the sphere, $\mathbf{f}(t)$ is a time-varying external force acting on the sphere, $\mathbf{h}'$ is the angular momentum of the sphere, $\mathbf{T}(t)$ is a time-dependent external torque acting on the sphere, and m is the mass of the sphere. The tensor quantities Ω and $\mathbf{J}'$ are defined by

$$\Omega = 2\mathbf{G}\dot{\mathbf{G}}^T \tag{B.10}$$

$$\mathbf{J}' = \begin{bmatrix} J_o & 0 & 0 \\ 0 & J_o & 0 \\ 0 & 0 & J_o \end{bmatrix}, \qquad J_o = \frac{2}{5}MR^2 \tag{B.11}$$

The potential energy of a magnetic dipole moment $\mathbf{m}_0$, placed in a uniform magnetic field $\mathbf{H}_0$ [114] is

$$\begin{aligned} V_d &= -\mu_0 \mathbf{m}_0^T \mathbf{H}_0 \\ &= -\mu_0 (\mathbf{R}\mathbf{m}_0')^T \mathbf{H}_0 \\ &= -\mu_0 \mathbf{m}_0'^T \mathbf{R}^T \mathbf{H}_0 \end{aligned} \tag{B.12}$$

where μ_0 is the permeability in free space, $\mathbf{m}_0 = [\ m_{0x}\ m_{0y}\ m_{0z}\ ]^T$, $\mathbf{m}_0' = [\ m_{0x}'\ m_{0y}'\ m_{0z}'\ ]^T$, $\mathbf{H}_0 = [\ H_{0x}\ H_{0y}\ H_{0z}\ ]^T$.

Assume that V_d is the only potential energy function, so that $V = V_d$ and V_d is independent of the position of the vector $\mathbf{c}$, the partial derivatives of V with respect to $\mathbf{c}$ and $\mathbf{e}$ become, respectively,

$$\frac{\partial V}{\partial \mathbf{c}} = \mathbf{0} \tag{B.13}$$

$$\frac{\partial V_d}{\partial \mathbf{e}} = -\mu_0 \mathbf{m}_0'^T \frac{\partial \mathbf{R}^T}{\partial \mathbf{e}} \mathbf{H}_0 \tag{B.14}$$

with

$$\frac{\partial \mathbf{R}^T}{\partial e_0} = 2 \begin{bmatrix} 2e_0 & e_3 & e_3 \\ e_2 & 0 & e_0 \\ e_3 & -e_0 & 0 \end{bmatrix} \tag{B.15a}$$

$$\frac{\partial \mathbf{R}^T}{\partial e_1} = 2 \begin{bmatrix} 2e_1 & e_2 & e_3 \\ e_2 & 0 & e_0 \\ e_3 & -e_0 & 0 \end{bmatrix} \tag{B.15b}$$

$$\frac{\partial \mathbf{R}^T}{\partial e_2} = 2 \begin{bmatrix} 0 & e_1 & -e_0 \\ e_1 & 2e_2 & e_3 \\ e_0 & e_3 & 0 \end{bmatrix} \tag{B.15c}$$

$$\frac{\partial \mathbf{R}^T}{\partial e_3} = 2 \begin{bmatrix} 0 & e_0 & e_1 \\ -e_0 & 0 & e_2 \\ e_1 & e_2 & 2e_3 \end{bmatrix} \tag{B.15d}$$

Equation (B.14) can be re-written, in terms of the vector components of $\mathbf{m}'_0$ and $\mathbf{H}_0$, as

$$\begin{aligned} \frac{\partial V_d}{\partial e_0} &= -2\mu_0 \big[m'_{0x}(2e_0 H_x + e_3 H_y - e_2 H_z) + \\ &\quad m'_{0y}(e_3 H_x + 2e_0 H_y + e_1 H_z) + m'_{0z}(e_2 H_x - e_1 H_y + 2e_0 H_z) \big] \end{aligned} \tag{B.16}$$

$$\begin{aligned} \frac{\partial V_d}{\partial e_1} &= -2\mu_0 \big[m'_{0x}(2e_1 H_x + e_2 H_y + e_3 H_z) + \\ &\quad m'_{0y}(e_2 H_x + e_0 H_z) + m'_{0z}(e_3 H_x - e_0 H_y) \big] \end{aligned} \tag{B.17}$$

$$\begin{aligned} \frac{\partial V_d}{\partial e_2} &= -2\mu_0 \big[m'_{0x}(e_1 H_y - e_0 H_z) + \\ &\quad m'_{0y}(e_1 H_x + 2e_2 H_y + e_3 H_z) + m'_{0z}(e_0 H_x + e_3 H_y) \big] \end{aligned} \tag{B.18}$$

$$\begin{aligned} \frac{\partial V_d}{\partial e_3} &= -2\mu_0 \big[m'_{0x}(e_0 H_y + e_1 H_z) + \\ &\quad m'_{0y}(-e_0 H_x + e_2 H_z) + m'_{0z}(e_1 H_x + e_2 H_y + 2e_3 H_z) \big] \end{aligned} \tag{B.19}$$

A simple example problem is solved here for the configuration shown in Figure B.2, which depicts a magnetized rigid sphere placed in a uniform magnetic field. The external magnetic field $\mathbf{H}_0$ is assumed to be parallel to the positive Y-axis, i.e. $\mathbf{H}_0 = H_0\hat{\mathbf{J}}$. The magnetic dipole moment $\mathbf{m}_0$ is further assumed to be in the x-y plane, so that $\mathbf{m}_0$ and the positive x-axis form a counter-clock-wise angle ϕ about the z-axis, as shown in Figure B.2. The ϕ-rotation about the positive Z-axis yields $\mathbf{u} = [\ 0\ 0\ 1\ ]^T$. Moreover, ϕ is the same as one Euler angle (see Equation (B.9a)). Therefore, using (B.2), the Euler parameters associated with this configuration can be expressed as

$$\mathbf{e} = [\ e_0\ e_1\ e_2\ e_3\ ]^T = [\ 1\ 0\ 0\ 0\ ]^T \tag{B.20}$$

Solutions of Hamilton's equations, (B.9a) through (B.9d), were obtained by numerical integration. A simple problem for a magnetized iron particle was solved, for the system parameters and initial conditions are listed in Table B.1. The time-domain solutions for ϕ, the particle kinetic energy, and the magnetic potential energy are shown in Figure B.3. Figure B.3(a) shows an oscillatory rotational motion of the iron particle, so the motion of this permanently magnetized sphere in a uniform magnetic field is very similar to the motion of a rigid sphere constrained by a torsional spring. Figure B.3(b) illustrates the principle of conservation of energy in the case where no dissipative effect is present in the system.

Table B.1: System parameters and initial conditions for the example problem

Parameter	Value
External magnetic field	$\mathbf{H}_0 = 111 \times [\ 0\ 1\ 0\ ]^T\ kA/m$
Magnetization of the sphere	$\mathbf{M} = 100 \times [\ 1\ 0\ 0\ ]^T\ kA/m$
Radius of the sphere	$r = 250\ \mu m$
Density of the sphere	$\rho = 3540\ kg/m^3$
Initial ϕ	$\phi(0) = 0^\circ$
Initial linear momentum	$\mathbf{p} = \mathbf{0}\ kg \cdot m/s$
Initial angular momentum	$\mathbf{h}' = \mathbf{0}\ kg \cdot m^2/s$
Initial position of the sphere	$\mathbf{c} = \mathbf{0}\ m$
Initial Euler parameters	$\mathbf{e} = [\ 1\ 0\ 0\ 0\ ]^T$

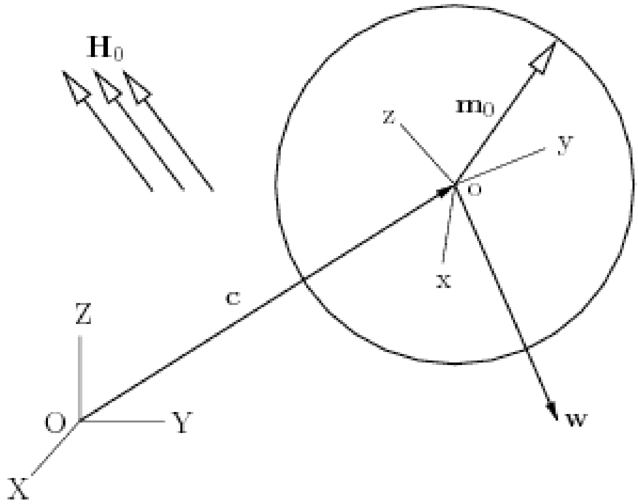

Figure B.1: Schematic of a magnetic dipole moment $\mathbf{m}_0$ fixed to a spherical ferromagnetic particle in a uniform external magnetic field $\mathbf{H}_0$

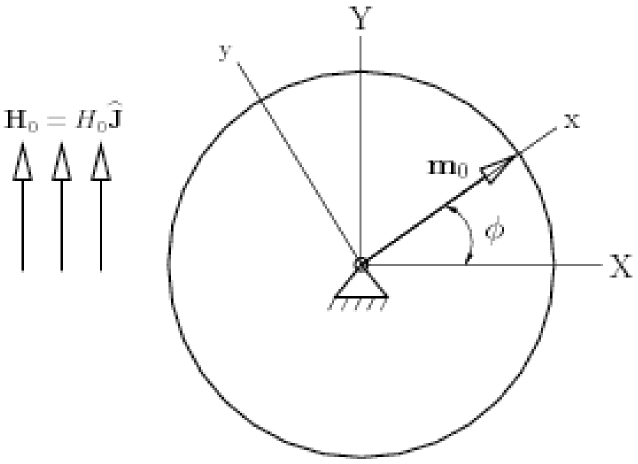

Figure B.2: Schematic of the 2-D configuration of a magnetic dipole moment $\mathbf{m}_0$ and a uniform external magnetic field $\mathbf{H}_0$ with the angular difference ϕ

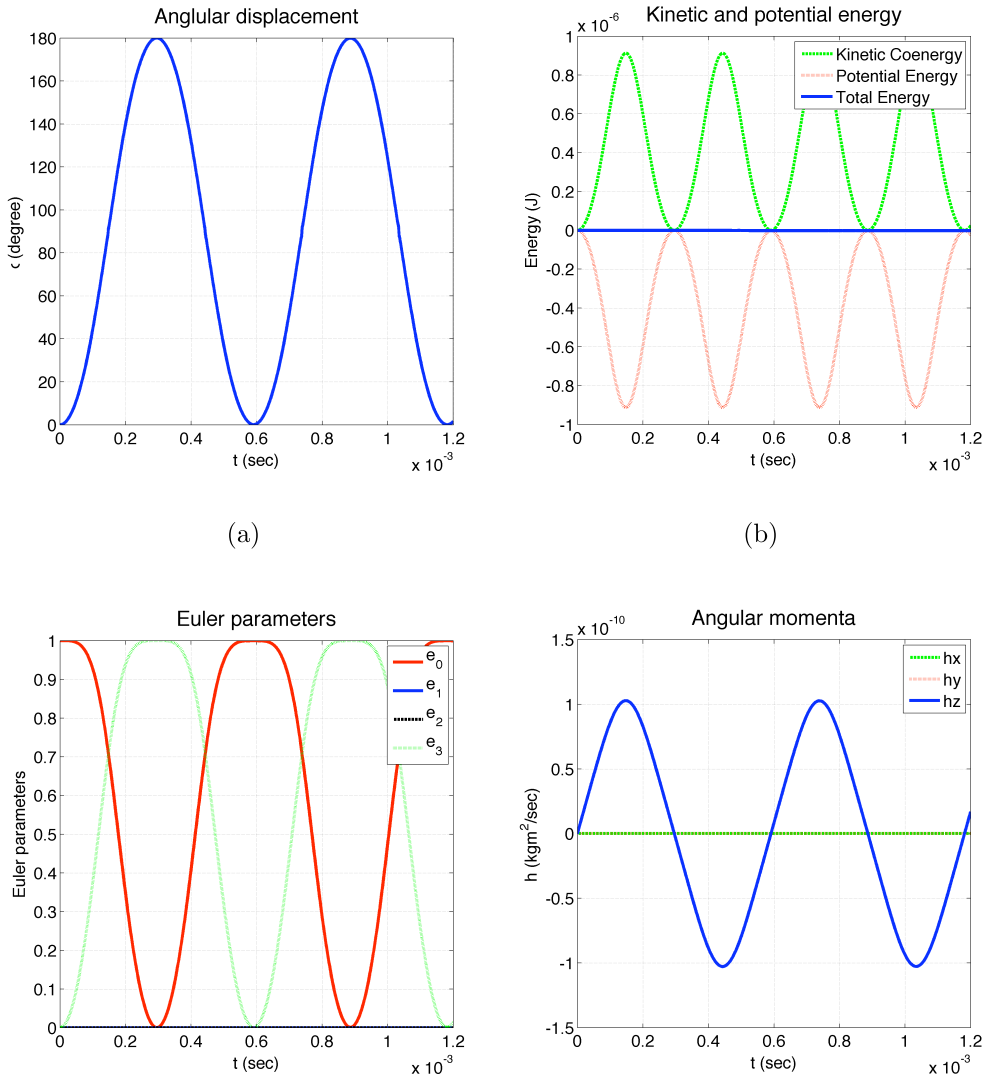

(a)

(b)

(c)

(d)

Figure B.3: Numerical solutions for (a) Euler angle ϕ versus time (b) kinetic energy and potential energy versus time (c) Euler parameters versus time and (d) angular momenta versus time when $\phi(0) = 0^\circ$

Appendix C

Calculation of the Magnetic Field of a Cylindrical Coil and Evaluation of its Magnetic Safety

In Chapter 3 and Chapter 4, a cylindrical coil was used to generate a magnetic field for the MRF-Kevlar and MSC-Kevlar testing. The magnetization of the MR fluid and Terfenol-D particles used for composite fabrication is due to an applied magnetic field. Hence, their induced mechanical properties can be predicted from the field distribution. The magnetic field distribution for the cylindrical electromagnetic coil has been computed using fundamental magneto-static field theory. Published solutions have been computed numerically to determine the field distribution around the coil, and also to evaluate safety of the coil in laboratory use.

C.1 Magnetic Field Calculation

This section presents a field calculation for the cylindrical electromagnetic coil used to magnetize MRF-Kevlar and MSC-Kevlar composites during the FSP impact tests. The coil is assumed to have a uniform and steady current density in operation. The magnetic field generated by this constant current condition can be computed by volume integration of a magnetic field generated due to a current in an infinitesimal circular loop [74]. The magnetic field solution is expressed in integral form, and can be computed by using numerical integration technique. In this study, the cylindrical coordinate system (ρ,ϕ,z) defined in [74] has been used, however, the coordinate origin is located at the centroid of a cylinder. A schematic of the cylindrical coil is shown in Figure C.1. Due to the change in coordinate origin, the field equations in [74] are now

$$\begin{aligned} \mathbf{B} &= B_\rho \hat{\mathbf{e}}_\rho + B_z \hat{\mathbf{e}}_z && \text{(C.1)} \\ B_\rho(\rho, z) &= B_\infty \frac{a^2 \pi}{4(b-a)} \int_0^\infty J_1(k\rho) \left(e^{-k\left|z-\frac{L}{2}\right|} - e^{-k\left|z+\frac{L}{2}\right|} \right) g(k) dk && \text{(C.2)} \\ B_z(\rho, z) &= B_\infty \frac{a^2 \pi}{4(b-a)} \int_0^\infty J_0(k\rho) f(k; z) g(k) dk && \text{(C.3)} \end{aligned}$$

where B_ρ and B_z are the components of the magnetic field in the ρ and z directions. In above equations, a is the inner radius of the coil, b is the outer radius of the coil, J_0 is a Bessel function of the first kind of order zero, J_1 is a Bessel function of the first kind of order one [5], and the quantity B_∞ s the magnetic field inside an infinitely long solenoid defined by

$$B_\infty = \frac{\mu_o N I}{L} \tag{C.4}$$

where I is the current flowing through the solenoid and N/L is the number of coil turns per unit length. In addition, the two functions $f(k; z)$ and $g(k)$ in the integrands of (C.2) and (C.3) are defined by

$$f(k; z) = \begin{cases} \left| e^{-k\left|z-\frac{L}{2}\right|} - e^{-k\left|z+\frac{L}{2}\right|} \right| & \text{for } |z| \geq \frac{L}{2} \\ 2 - e^{-k\left(\frac{L}{2}-z\right)} - e^{-k\left(\frac{L}{2}+z\right)} & \text{for } |z| < \frac{L}{2} \end{cases} \tag{C.5}$$

$$\begin{aligned} g(k) = \tfrac{1}{ka}\Big[- J_1(ka)H_0(ka) \quad & + \tfrac{b}{a} J_1(kb)H_0(kb) \\ & + J_0(ka)H_1(ka) - \tfrac{b}{a} J_0(ka)H_1(ka)\Big] \end{aligned} \tag{C.6}$$

where H_0 and H_1 are Struve functions [5].

The electromagnetic coil used in this study is the model 3473-70 manufactured by GMW Associates, Inc. The coil specifications are listed in Table C.1. Equations (C.2) and (C.3) are numerically integrated with the recursive adaptive Simpson quadrature integration function *quad* in MATLAB (which is a registered trademark of MathWorks). Figures C.2 and C.3 show contour plots of the magnitude of the magnetic field for the region $\rho < a$, inside the coil. The numerical results indicate that the magnetic field at the center of the coil is 0.133 Tesla, or equivalently 106 kA/m. To test this calculation, the magnetic field was measured at the center of the coil, using a Gauss/Tesla meter model HHG-22 from Omega Engineering, Incorporated. The measured value was 0.138 Tesla, or equivalently 110 kA/m, at the origin when a constant current of 70 A was applied. The error between the analytical and measured data is approximately 3.6%, therefore, the field equations C.2 and C.3 produce an acceptable prediction of the magnetic field for the coil. More intensive validation of this model has been already performed, by comparison of the computed field to measurements for a single-layer solenoid and a cylindrical thick coil [74].

C.2 Evaluation of the Magnetic Safety of an Electromagnetic Coil

This section presents a safety evaluation, for a magnetic field generated by an electromagnetic coil. Since there are many tools and machine components made from ferromagnetic metals in the SwRI test facility, a high-strength electromagnet may move objects in the neighborhood of the magnet. This safety evaluation considers only on the potential for movement of ferromagnetic objects in a static magnetic field. In general, other effects should also be considered, for example possible electromagnetic interference which may cause the malfunction of cardiac pacemakers, magnetohydrodynamic effects which may hinder the flow of blood in vessels, etc. [50].

A criterion published by the Fermi National Accelerator Laboratory may be used to estimate safe magnetic forces on ferromagnetic objects. The estimated safe magnetic force F_m on a spherical object normalized by its own gravity force F_g, should be less than 0.1, in order to avoid possible translation of the object [50], i.e.,

$$\frac{F_m}{F_g} \leq 0.1 \tag{C.7}$$

The force acting on a ferromagnetic sphere due to an external magnetic field $\overline{B}_0$, can be expressed as:

$$\overline{F}_m = \nabla(\frac{V}{\mu_0}\overline{B}_0 \cdot \overline{B}_0) \tag{C.8}$$

where V is the volume of the sphere and μ_0 is the permeability of free space. Since the weight of the sphere is $F_g = \rho V g$, the critical condition F_m/F_g in

Equation (C.7) can be expressed as:

$$\frac{F_m}{F_g} = \frac{1}{\rho g \mu_0} \nabla (\overline{B}_0 \cdot \overline{B}_0) \tag{C.9}$$

where ρ is the density of the material and g is the acceleration of gravity. Therefore, the safety criterion can be evaluated with Equation C.9 if the external field is known. The field calculation results in the previous section (i.e. Equation (C.2) and Equation (C.3)) provide an analytical description of the magnetic field strength around the coil, hence the normalized magnetic force can also be calculated from those equations. Figure C.4 plots the normalized magnetic force around the coil. As shown in the figure, F_m/F_g vanishes for $\rho > 1.2a$ and $z > 3l$ in each direction. This calculation indicates that the safety criterion is satisfied at a distance of about 198 mm away from the center of the coil.

Table C.1: Parameters of the cylindrical coil

Electromagnetic Coil Model 3473-70 manufactured by GMW Associates			
Property	symbol	Unit	Value
Number of turns	N	turns	460
Maximum current	I	A	70
Inner radius	a	mm	88.9
Outer radius	b	mm	195.26
Coil thickness	L	mm	130
Coil half length	l	mm	65

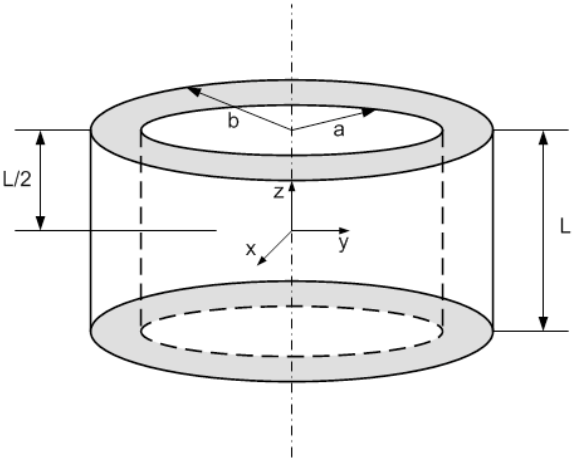

Figure C.1: Schematic of a cylindrical electromagnetic coil with a finite length

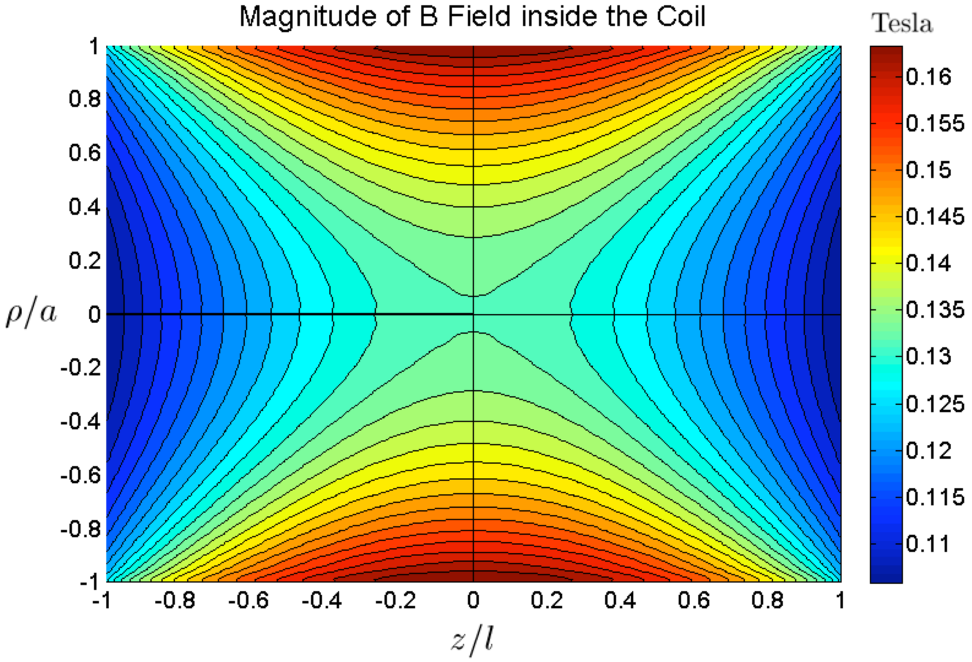

Figure C.2: Contour plot for the magnetic field calculation inside the coil. The color bar indicates the magnitude of the magnetic flux density in Tesla.

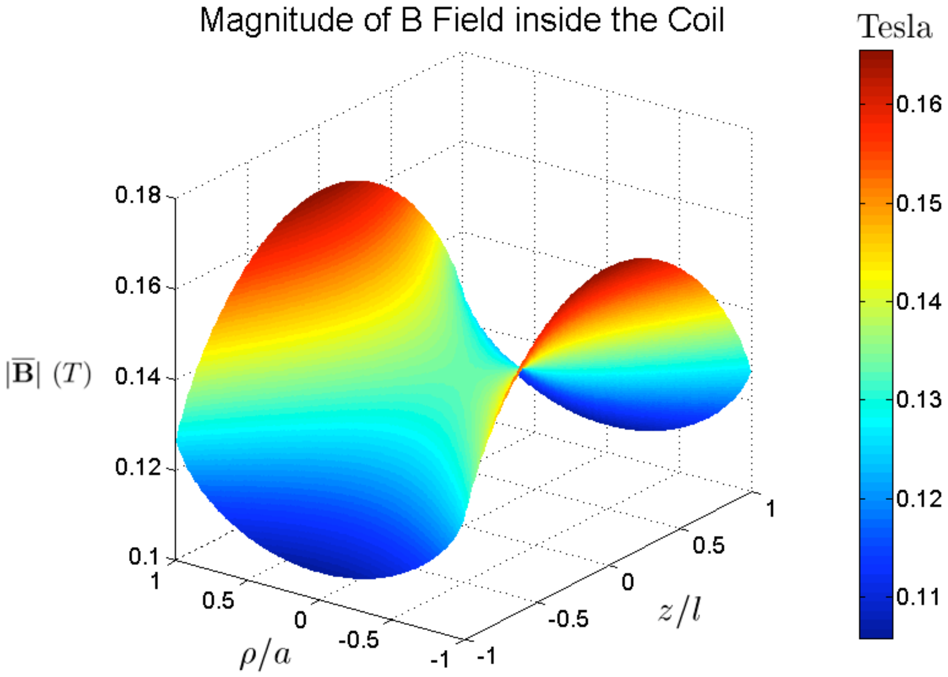

Figure C.3: 3D plot for the magnetic field inside the coil. The color bar indicates the magnitude of the magnetic flux density in Tesla.

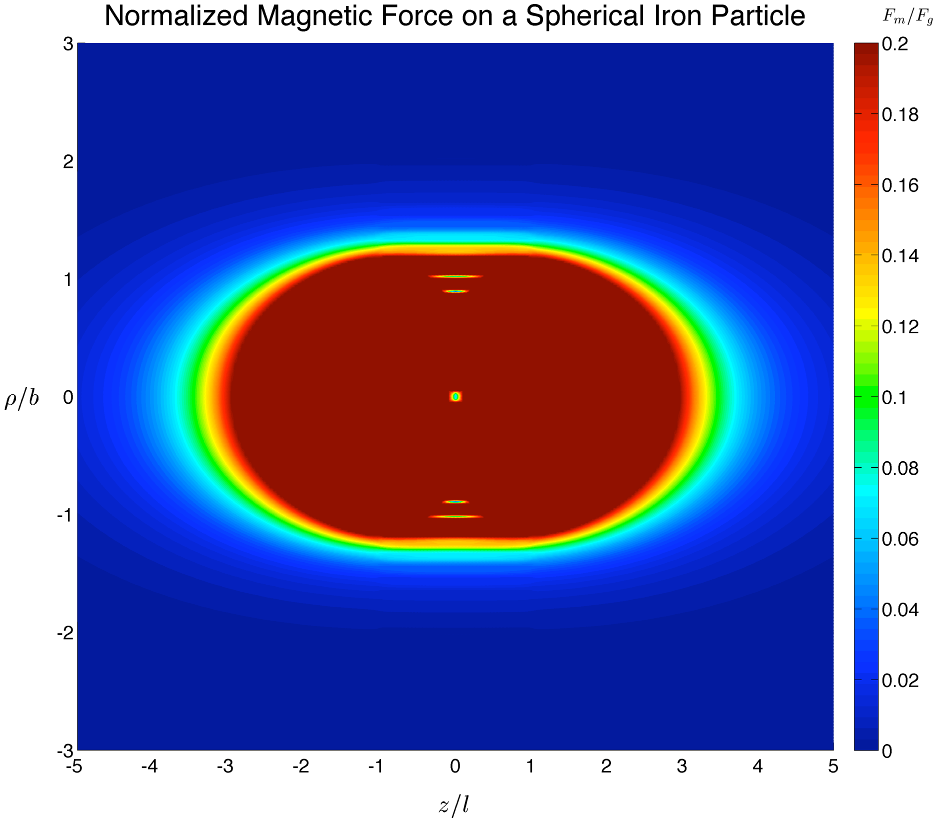

Figure C.4: Normalized force of a spherical iron objects around the electromagnetic coil with respect to its own gravity.

Bibliography

[1] http://teos.ficp.ac.ru/rusbank.

[2] http://www.etrema-usa.com.

[3] http://www.ezlok.com/technicalinfo/mpbrass.html.

[4] http://www.webelements.com.

[5] M. Abramowitz and I.A. Stegun, editors. *Handbook of Mathematical Functions*. National Bureau of Standards, 10th edition, December 1972.

[6] S. Adanur and T. Liao. 3D modeling of textile composite preforms. *Composites Part B: Engineering*, 29(6):787–793, 1998.

[7] O.L. Anderson. *Equation of State of Solids for Geophysics and Ceramic Science*. Oxford University Press, 1995.

[8] A. Balakrishnan, W.T. Joines, and T.G. Wilson. Air-gap reluctance and inductance calculations for magnetic circuits using a Schwarz-Christoffel transformation. *IEEE Transactions on Power Electronics*, 12(4):654–663, 1997.

[9] R. Barauskas and A. Abraitiene. Computational analysis of impact of a bullet against the multilayer fabrics in LS-DYNA. *International Journal of Impact Engineering*, 34(7):1286–1305, 2007.

[10] H. Baruh. *Analytical Dynamics*. McGraw-Hill, 1999.

[11] S Bazhenov. Dissipation of energy by bulletproof aramid fabric. *Journal of Materials Science*, 32(15):4167–4173, 1997.

[12] D.J. Benson. Computational methods in Lagrangian and Eulerian hydrocodes. *Computer Methods in Applied Mechanics and Engineering*, 99(2-3):235–394, 1992.

[13] B. Berkovski and V. Bashtovoy. *Magnetic Fluids and Applications Handbook*. Begell hous, Inc., 1996.

[14] B.M. Berkovsky, V.F. Medvedev, and M.S. Krakov. *Magnetic Fluids: Engineering Applications*. Oxford University Press, 1993.

[15] H.H. Billon and D.J. Robinson. Models for the ballistic impact of fabric armour. *International Journal of Impact Engineering*, 25(4):411–422, 2001.

[16] BJB Enterprises, Inc. WC-753 A/B clear 55 Shore D Polyurethane adhesive/coating system, October 2003.

[17] A. Bohannan and E.P. Fahrenthold. Hypervelocity impact simulation using membrane particle-elements. *International Journal of Impact Engineering*, 35(12):1497–1502, 2008.

[18] P. Boisse, A. Gasser, and G. Hivet. Analyses of fabric tensile behaviour: determination of the biaxial tension-strain surfaces and their use in form-

ing simulations. *Composites Part A: Applied Science and Manufacturing*, 32(10):1395–1414, 2001.

[19] J. Bonet and R.D. Wood. *Nonlinear Continuum Mechanics for Finite Element Analysis*. Cambridge University Press, 1997.

[20] D.E. Breen, D.H. House, and Wozny M.J. A particle-based model for simulating the draping behavior of woven cloth. *Textile Research Journal*, 64(11):663–685, 1994.

[21] K.G. Budge and J.S. Peery. RHALE: A MMALE shock physics code written in C++. *International Journal of Impact Engineering*, 14:107–120, 1993.

[22] J.L. Butler, A.L. Butler, and S.C. Butler. Hybrid magnetostrictive / piezoelectric tonpilz transducer. *Journal of the Acoustical Society of America*, 94(2):636–641, 1993.

[23] T. Butz and O. von Stryk. Modelling and simulation of electro- and magnetorheological fluid dampers. *ZAMM - Journal of Applied Mathematics and Mechanics*, 82(1):3–20, 2002.

[24] J. Campbell and R. Vignjevic. Development of Lagrangian hydrocode modelling for debris impact damage prediction. *International Journal of Impact Engineering*, 20(1-5):143–152, 1997.

[25] J.D. Carlson, D.M. Catanzarite, and K.A.St. Clair. Commercial magneto-rheological fluid devices. *International Journal of Modern Physics B*, 10:2857–2865, 1996.

[26] B.A. Cheeseman and T.A. Bogetti. Ballistic impact into fabric and compliant composite laminates. *Composite Structures*, 61(1-2):161–173, 2003.

[27] D.K. Cheng. *Field and Wave Electromagnetics*. Addison-Wesley Publishing Company, Inc., 2nd edition, 1989.

[28] M. Cheng, W. Chen, and T. Weerasooriya. Experimental investigation of the transverse mechanical properties of a single Kevlar KM2 fiber. *International Journal of Solids and Structures*, 41(22-23):6215–6232, 2004.

[29] F. Claeyssen, N. Lhermet, R. Le Letty, and P. Bouchilloux. Design and construction of a resonant magnetostrictive motor. *IEEE Transactions on Magnetics*, 32(5):4749–4751, 1996.

[30] A.E. Clark. *Ferromagnetic Materials*, chapter 7, pages 531–589. North Holland Publishing, Co., 1980.

[31] C.R. Cork and P.W. Foster. The ballistic performance of narrow fabrics. *International Journal of Impact Engineering*, 34(3):495–508, 2007.

[32] P.M. Cunniff. An analysis of the system effects in woven fabrics under ballistic impact. *Textile Research Journal*, 62(9):495–509, 1992.

[33] G.J. Czarnecki. Estimation of the V_{50} using semi-empirical (1-point) procedures. *Composites Part B: Engineering*, 29B:321–329, 1998.

[34] M.J. Dapino. On magnetostrictive materials and their use in adaptive structures. *Structural Engineering and Mechanics*, 17:303–329, 2004.

[35] E. du T. de Lacheisserie. *Theory and Applications of Magnetoelasticity.* CRC press, Inc., 1993.

[36] S.S. Deshmukh and G.H. McKinley. Adaptive energy-absorbing materials using field-responsive fluid-impregnated cellular solids. *Smart Materials and Structures*, 16(1):106–113, 2007.

[37] Y. Duan, M. Keefe, T.A. Bogetti, and B.A. Cheeseman. Modeling friction effects on the ballistic impact behavior of a single-ply high-strength fabric. *International Journal of Impact Engineering*, 31(8):996–1012, 2005.

[38] Y. Duan, M. Keefe, T.A. Bogetti, and B.A. Cheeseman. Modeling the role of friction during ballistic impact of a high-strength plain-weave fabric. *Composite Structures*, 68(3):331–337, 2005.

[39] Y. Duan, M. Keefe, T.A. Bogetti, B.A. Cheeseman, and B. Powers. A numerical investigation of the influence of friction on energy absorption by a high-strength fabric subjected to ballistic impact. *International Journal of Impact Engineering*, 32(8):1299–1312, 2006.

[40] ESPICorp. Inc. Technical data sheet: Brass 360, undated.

[41] Etrema Products, Inc. Data sheet Terfenol-D, undated.

[42] E.P. Fahrenthold. *User's Guide for EXOS©: A Three Dimensional Hybrid Particle-Finite Element Code for Hybpervelocity Impact Simulation.* The University of Texas at Austin, November 2007.

[43] E.P. Fahrenthold and R.J. Hernandez. Simulation of orbital debris impact on the space shuttle wing leading edge. *International Journal of Impact Engineering*, 33(1-12):231–243, 2006.

[44] E.P. Fahrenthold and B.A. Horban. Thermodynamics of continuum damage and fragmentation models for hypervelocity impact. *International Journal of Impact Engineering*, 20(1-5):241–252, 1997.

[45] E.P. Fahrenthold and B.A. Horban. A hybrid particle-finite element method for hypervelocity impact simulation. *International Journal of Impact Engineering*, 23(1, Part 1):237–248, 1999.

[46] E.P. Fahrenthold and B.A. Horban. An improved hybrid particle-element method for hypervelocity impact simulation. *International Journal of Impact Engineering*, 26(1-10):169–178, 2001.

[47] E.P. Fahrenthold and J.C. Koo. Energy based particle hydrodynamics for hypervelocity impact simulation. *International Journal of Impact Engineering*, 20(1-5):253–264, 1997.

[48] E.P. Fahrenthold and J.C. Koo. Hamiltonian particle hydrodynamics. *Computer Methods in Applied Mechanics and Engineering*, 146(1-2):43–52, 1997.

[49] E.P. Fahrenthold and Y.-K. Park. Simulation of hypervelocity impact on aluminum-Nextel-Kevlar orbital debris shields. *International Journal of Impact Engineering*, 29(1-10):227–235, 2003.

[50] Fermi National Accelerator Laboratory. *Fermilab ESH&Q Manual Chapter 5062.2-1: Static Magnetic Fields*, December 2005.

[51] S. Genc and P.P. Phule. Rheological properties of magnetorheological fluids. *Smart Materials and Structures*, 11(1):140–146, 2002.

[52] J.H. Ginsberg. *Advanced Engineering Dynamics*. Harper and Row Publishers, Inc., 1988.

[53] S.B. Glavatskih, M. Fillon, and R. Larsson. The significance of oil thermal properties on the performance of a tilting-pad thrust bearing. *Journal of Tribology*, 124:377–380, 2002.

[54] D.E. Gray, editor. *American Institute of Physics Handbook*. McGraw-Hill, Inc., 3rd edition, 1972.

[55] D.T. Greenwood. *Principles of Dynamics*. Prentice-Hall, Inc., 2nd edition, 1988.

[56] R. Greiner and F.R. Schwarzl. Thermal contraction and volume relaxation of amorphous polymers. *Rheologica Acta*, 23:378–395, 1984.

[57] B. Gu. Analytical modeling for the ballistic perforation of planar plain-woven fabric target by projectile. *Composites Part B: Engineering*, 34(4):361–371, 2003.

[58] J.O. Hallquist. *Theoretical Manual for DYNA3D.* Lawrence Livermore National Laboratory, Livermore, CA, 1983.

[59] K. Hathaway, A. Clark, and J. Teter. Magnetomechanical damping in giant magnetostriction alloys. *Metallurgical and Materials Transactions A*, 26(11):2797–2801, 1995.

[60] J. Hesselbach and C. Abel-Keilhack. Active hydrostatic bearing with magnetorheological fluid. *Journal of Applied Physics*, 93(10):8441–8443, 2003.

[61] Hexcel Schwebel. 706 Aramid and high performance fabrics product data, 2006.

[62] S. Hiermaier. *Structures under Crash and Impact: Continuum Mechanics, Discretization and Experimental Characterization.* Springer, 2008.

[63] G.T. Houlsby and A.M. Puzrin. *Principles of Hyperplasiticity.* Springer, 2006.

[64] IEEE. IEEE standard on magnetostrictive materials: piezomagnetic nomenclature. *IEEE Std 319-1990*, 1991.

[65] I. Ivanov and A. Tabiei. Loosely woven fabric model with viscoelastic crimped fibres for ballistic impact simulations. *International Journal for Numerical Methods in Engineering*, 61(10):1565–1583, 2004.

[66] B.O. Jacobson. *Rheology and Elastohydrodynamic Lubrication*. Elsevier Science Publishers, 1991.

[67] G.R. Johnson, E.H Petersen, and R.A. Stryk. Incorporation of an SPH option into the EPIC code for a wide range of high velocity impact computations. *International Journal of Impact Engineering*, 14:385–394, 1993.

[68] G.R. Johnson, R.A. Stryk, and S.R. Beissel. SPH for high velocity impact computations. *Computer Methods in Applied Mechanics and Engineering*, 139:347–373, 1996.

[69] MR. Jolly, J.W. Bender, and J.D. Carlson. Properties and applications of commercial magnetorheological fluids. In *Proc. SPIE*, volume 3327(1), pages 262–275, San Diego, CA, USA, June 1998. SPIE.

[70] Levent K. and Ahmed K.N. Frictional contact impact response of textile composite structures. *Composite Structures*, 37:269–280, 1997.

[71] G.M.A. Kamel. Smart armors made from shape memory materials. In *44th AIAA / ASME / ASCE / AHS / ASC Structures, Structural Dynamics, and Materials Conference*, Norfolk, VA, April 2003.

[72] M. Karahan, A. Kus, and R. Eren. An investigation into ballistic performance and energy absorption capabilities of woven aramid fabrics. *International Journal of Impact Engineering*, 35(6):499–510, 2008.

[73] M.J. King, P. Jearanaisilawong, and S. Socrate. A continuum constitutive model for the mechanical behavior of woven fabrics. *International Journal of Solids and Structures*, 42(13):3867–3896, 2005.

[74] V. Labinac, N. Erceg, and D. Kotnik-Karuza. Magnetic field of a cylindrical coil. *American Journal of Physics*, 74(7):621–627, 2006.

[75] B.L. Lee, T.F. Walsh, S.T. Won, Patts H.M., J.W. Song, and A.H. Mayer. Penetration failure mechanisms of armor-grade fiber composites under impact. *Journal of Composite Materials*, 35(18):1605–1633, 2001.

[76] E.W. Lee. Magnetostriction and magnetomechanical effects. *Reports on Progress in Physics*, 18(1):184–229, 1955.

[77] Y.S. Lee, E.D. Wetzel, R.G. Egres, and N.J. Wagner. Advanced body armor utilizing shear thickening fluids. In *23rd Army Science Conference*, December 2002.

[78] Y.S. Lee, E.D. Wetzel, and N.J. Wagner. The ballistic impact characteristics of Kevlar woven fabrics impregnated with a colloidal shear thickening fluid. *Journal of Materials Science*, 38(13):2825–2833, 2003.

[79] D.R. Lide, editor. *CRC Handbook of Chemistry and Physics.* CRC Press, 2006.

[80] C.T. Lim, V.P.W. Shim, and Y.H. Ng. Finite-element modeling of the ballistic impact of fabric armor. *International Journal of Impact Engineering*, 28(1):13–31, 2003.

[81] G.R. Liu and M.B. Liu. *Smoothed Particle Hydrodynamics.* Singapore, World Scientific Publishing Co. Pte. Ltd, 2003, 2003. Bibliography and Index.

[82] S.V. Lomov, A.V. Gusakov, G. Huysmans, A. Prodromou, and I. Verpoest. Textile geometry preprocessor for meso-mechanical models of woven composites. *Composites Science and Technology*, 60(11):2083–2095, 2000.

[83] S.V. Lomov and I. Verpoest. Model of shear of woven fabric and parametric description of shear resistance of glass woven reinforcements. *Composites Science and Technology*, 66(7-8):919–933, 2006.

[84] LORD Corporation. *Lord Technical Data: MRF-140CG Magneto-Rheological Fluid*, May 2006.

[85] Y.Y. Lu, T. Belytschko, and M. Tabbara. Element-free Galerkin method for wave propagation and dynamic fracture. *Computer Methods in Applied Mechanics and Engineering*, 126(1-2):131–153, 1995.

[86] J. Lubliner. *Plasticity Theory.* Collier Macmillan, 1990.

[87] K. Lurie. Instant armor. ScienCentral News, December 2003.

[88] E.E. Magat. Fibres from extended chain aromatic polyamides. *Philosophical Transactions of the Royal Society of London. Series A, Mathematical and Physical Sciences*, 294(1411):463–472, 1980.

[89] R.D. Maksimov, T. Ivanova, J. Zicans, S.N. Negreeva, and E. Plume. Thermal and elastic properties of poly(vinyl chloride) (PVC) + chlorinated polyethylene (CPE) blends. *Materials Research Innovations*, 7:326–330, 2003.

[90] J.M. McGlaun, S.L. Thompson, and M.G. Elrick. CTH: A three-dimensional shock wave physics code. *International Journal of Impact Engineering*, 10(1-4):351–360, 1990.

[91] G.P. McKnight and G.P. Carman. Energy absorption and damping in magnetostrictive composites. *Materials Research Society Symposium*, 604:267–272, 2000.

[92] G.P. McKnight and G.P. Carman. Energy absorption in axial and shear loading of particulate magnetostrictive composites. 3992(1):572–579, 2000.

[93] M&I Materials Ltd. Apeizon H grease safety data sheet, January 2008.

[94] Y. Miao, E. Zhou, Y. Wang, and B.A. Cheeseman. Mechanics of textile composites: Micro-geometry. *Composites Science and Technology*, 68(7-8):1671–1678, 2008.

[95] J.E. Miesner and J.P. Teter. Piezoelectric/magnetostrictive resonant inchworm motor. In *Proc. SPIE*, volume 2190(1), pages 520–527, Orlando, FL, USA, May 1994. SPIE.

[96] MIL-P-46593A. Projectile, calibers.22,.30,.50 and 20 mm fragment-stimulating, DoD, USA, 1962.

[97] J.J. Monaghan. Smoothed particle hydrodynamics. *Annual Review of Astronomy and Astrophysics*, 30:543–574, 1992.

[98] B.S. Munjal, H.V. Trivedi, and P.V.B.A.S. Sarma. Vibration damping on graphite and kevlar composites using piezoceramic powder coatings: a review. *The Shock and Vibration Digest*, 39(1):3–17, 2007.

[99] B. Nadler, P. Papadopoulos, and D.J. Steigmann. Multiscale constitutive modeling and numerical simulation of fabric material. *International Journal of Solids and Structures*, 43(2):206–221, 2006.

[100] B. Nadler and D.J. Steigmann. A model for frictional slip in woven fabrics. *Comptes Rendus Mecanique*, 331(12):797–804, 2003.

[101] P.E. Nikravesh. *Computer-Aided Analysis of Mechanical Systems*. Prentice Hall, Inc., 1988.

[102] W.R. Novotny, E. Cepus, A. Shahkarami, R. Vaziri, and A. Poursartip. Numerical investigation of the ballistic efficiency of multi-ply fabric armours during the early stages of impact. *International Journal of Impact Engineering*, 34(1):71–88, 2007.

[103] D. Palmieri. Simulation of shaped charge projectiles normal impact on the Columbus advanced shield. Technical Report ESA Report EWP-2173, ESA Report, undated.

[104] B. Parga-Landa and F. Hernandez-Olivares. An analytical model to predict impact behaviour of soft armours. *International Journal of Impact Engineering*, 16(3):455–466, 1995.

[105] Y.-K. Park and E.P. Fahrenthold. A kernel free particle-finite element method for hypervelocity impact simulation. *International Journal for Numerical Methods in Engineering*, 63(5):737–759, 2005.

[106] Y.-K. Park and E.P. Fahrenthold. Simulation of hypervelocity impact effects on reinforced Carbon-Carbon. *Journal of Spacecraft and Rockets*, 43(1):200–206, 2006.

[107] A.N. Parshikov and S.A. Medin. Smoothed particle hydrodynamics using interparticle contact algorithms. *Journal of Computational Physics*, 180(1):358–382, 2002.

[108] J.M. Pereira, G.D. Roberts, and D.M. Revilock. Elevated temperature ballistic impact testing of PBO and Kevlar fabrics for application in supersonic jet engine fan containment systems. Technical memorandum, National Aeronautics and Space Administration, Lewis Research Center, Cleveland, Ohio 44135-3191, 1997.

[109] S.L. Phoenix and P.K. Porwal. A new membrane model for the ballistic impact response and V_{50} performance of multi-ply fibrous systems. *International Journal of Solids and Structures*, 40(24):6723–6765, 2003.

[110] P.K. Porwal and S.L. Phoenix. Modeling system effects in ballistic impact into multi-layered fibrous materials for soft body armor. *International Journal of Fracture*, 135(1):217–249, 2005.

[111] R.J. Rabb. *A Mesomechanical Particle-Element Model of Impact Dynamics in Neat and Shear Thickening Fluid Kevlar.* PhD thesis, The University of Texas at Austin, 2007.

[112] J. Rabinow. The magnetic fluid clutch. *AIEE Transactions*, 67:1308–1315, 1948.

[113] M.M. Roberts, M. Mitrovic, and G.P. Carman. Nonlinear behavior of coupled magnetostrictive material systems analytical/experimental. In *Proc. SPIE*, volume 2441(1), pages 341–354, San Diego, CA, USA, May 1995. SPIE.

[114] R.E. Rosensweig. *Ferrohydrodynamics*. Cambridge University Press, 1985.

[115] T.V. Sagar, P. Potluri, and J.W.S. Hearle. Mesoscale modelling of interlaced fibre assemblies using energy method. *Computational Materials Science*, 28(1):49–62, 2003.

[116] R.A. Scott. *Textiles for Protection*. Woodhead Publishing Ltd, 2005.

[117] A. Shahkarami and R. Vaziri. A continuum shell finite element model for impact simulation of woven fabrics. *International Journal of Impact Engineering*, 34(1):104–119, 2007.

[118] V.P.W. Shim, C.T. Lim, and K.J. Foo. Dynamic mechanical properties of fabric armour. *International Journal of Impact Engineering*, 25(1):1–15, 2001.

[119] V.P.W. Shim, V.B.C. Tan, and T.E. Tay. Modelling deformation and damage characteristics of woven fabric under small projectile impact. *International Journal of Impact Engineering*, 16(4):585–605, 1995.

[120] R.A. Shivarama and E.P. Fahrenthold. An ellipsoidal particle-finite element method for hypervelocity impact simulation. *International Journal for Numerical Methods in Engineering*, 59(5):737–753, 2004.

[121] R.A. Shivarama and E.P. Fahrenthold. Hamilton's equations with Euler parameters for rigid body dynamics modeling. *Journal of Dynamic Systems, Measurement, and Control*, 126(1):124–130, 2004.

[122] B.F. Spencer Jr., S.J. Dyke, M.K. Sain, and J.D. Carlson. Phenomenological model for magnetorheological dampers. *Journal of Engineering Mechanics*, 123(3):230–238, 1997.

[123] D. Starratt, T. Sanders, E. Cepus, A. Poursartip, and R. Vaziri. An efficient method for continuous measurement of projectile motion in ballistic impact experiments. *International Journal of Impact Engineering*, 24(2):155–170, 2000.

[124] R.F. Stellingwerf and C.A. Wingate. Impact modeling with smooth particle hydrodynamics. *International Journal of Impact Engineering*, 14:707–718, 1993.

[125] K. Sterzelmeier, V. Brommer, and L. Sinniger. Active armor protection-conception and design of steerable launcher systems fed by modular pulsed-power supply units. *IEEE Transactions on Magnetics*, 37(1):238–241, 2001.

[126] C.T. Sun and S.V. Potti. A simple model to predict residual velocities of thick composite laminates subjected to high velocity impact. *International Journal of Impact Engineering*, 18(3):339–353, 1996.

[127] A. Tabiei and I. Ivanov. Computational micro-mechanical model of flexible woven fabric for finite element impact simulation. *International Journal for Numerical Methods in Engineering*, 53(6):1259–1276, 2002.

[128] V.B.C. Tan and T.W. Ching. Computational simulation of fabric armour subjected to ballistic impacts. *International Journal of Impact Engineering*, 32(11):1737–1751, 2006.

[129] V.B.C. Tan, V.P.W. Shim, and X. Zeng. Modelling crimp in woven fabrics subjected to ballistic impact. *International Journal of Impact Engineering*, 32(1-4):561–574, 2005.

[130] V.B.C. Tan, T.E. Tay, and W.K. Teo. Strengthening fabric armour with silica colloidal suspensions. *International Journal of Solids and Structures*, 42(5-6):1561–1576, 2005.

[131] K. Tanaka, K. Minoshima, T. Oya, and K. Komai. Influences of stress waveform and wet environment on fatigue fracture behavior of aramid single fiber. *Composites Science and Technology*, 64(10-11):1531–1537, 2004.

[132] J.P. Teter, K.B. Hathaway, and A.E. Clark. Zero field damping capacity in $(\mathrm{Tb_xDy_{1-x}})\mathrm{Fe_y}$. *Journal of Applied Physics*, 79(8):6213–6215, 1996.

[133] S. Trivedi. The next wave of innovation nanotech with defense. In *Electro/Information Technology, 2007 IEEE International Conference on*, pages 594–599, 2007.

[134] Uline Shipping Supplies. Material safety data sheet: PVC shrink film bags, undated.

[135] J.M. Vranish, D.P. Naik, J.B. Restorff, and J.P. Teter. Magnetostrictive direct drive rotary motor development. *IEEE Transactions on Magnetics*, 27(6):5355–5357, 1991.

[136] Y. Wang and X. Sun. Digital-element simulation of textile processes. *Composites Science and Technology*, 61(2):311–319, 2001.

[137] Y. Wang and Y. Xia. The effects of strain rate on the mechanical behaviour of Kevlar fibre bundles: an experimental and theoretical study. *Composites Part A: Applied Science and Manufacturing*, 29(11):1411–1415, 1998.

[138] Y. Wang and Y.M. Xia. Experimental and theoretical study on the strain rate and temperature dependence of mechanical behaviour of Kevlar fibre. *Composites Part A: Applied Science and Manufacturing*, 30(11):1251–1257, 1999.

[139] E.D. Wetzel, Y.S. Lee, R.G. Egres, K.M. Kirkwood, J.E. Kirkwood, and N.J. Wagner. The effect of rheological parameters on the ballistic properties of shear thickening fluid (STF)-Kevlar composites. In *AIP Conf. Proc.*, volume 712(1), pages 288–293, Columbus, Ohio (USA), June 2004. AIP.

[140] M. Wickert. Electric armor against shaped charges: Analysis of jet distortion with respect to jet dynamics and current flow. *IEEE Transactions on Magnetics*, 43(1):426–429, 2007.

[141] M. Wun-Fogle, J.B. Restorff, A.E. Clark, and J. Snodgrass. Magnetomechanical damping capacity of $\mathrm{Tb_xDy_{1-x}Fe_{1.92}}$ ($0.30 \leq$ x ≤ 0.50) alloys. *IEEE Transactions on Magnetics*, 39(5):3408–3410, 2003.

[142] L. Xiaopeng, M. Tao, Z. Chun, and L. Liyi. Multiprojectile active electromagnetic armor. *IEEE Transactions on Magnetics*, 43(1):460–462, 2007.

[143] C.S. Yung, C.Y. Lo, and S.W. Or. A 64 kHz Langevin sandwich transducer fabricated using giant magnetostrictive composites. In *Magnetics Conference, 2005. INTERMAG Asia 2005. Digests of the IEEE International*, pages 1445–1446, 2005.

[144] Ya B. Zel'dovich and Yu. P Raizer. *Physics of Shock Waves and High-Temperature Hydrodynamic Phenomena.* Dover Publications, Inc., 2002.

[145] X.S. Zeng, V.P.W. Shim, and V.B.C. Tan. Influence of boundary conditions on the ballistic performance of high-strength fabric targets. *International Journal of Impact Engineering*, 32(1-4):631–642, 2005.

[146] X.S. Zeng, V.B.C. Tan, and V.P.W. Shim. Modelling inter-yarn friction in woven fabric armour. *International Journal for Numerical Methods in Engineering*, 66(8):1309–1330, 2006.

[147] G.M. Zhang, R.C. Batra, and J. Zheng. Effect of frame size, frame type, and clamping pressure on the ballistic performance of soft body armor. *Composites Part B: Engineering*, 39(3):476–489, 2008.

[148] P. Zheng, Y. Liu, S. Cheng, Z. Li, and J. Hu. Research on the passive electromagnetic armor. *IEEE Transactions on Magnetics*, 41(1):456–459, 2005.

[149] G. Zhou, X. Sun, and Y. Wang. Multi-chain digital element analysis in textile mechanics. *Composites Science and Technology*, 64(2):239–244, 2004.

[150] H. Ziegler. *An Introduction to Thermomechanics*. North-Holland Publishing Company, 1983.

[151] T.I. Zohdi and D. Powell. Multiscale construction and large-scale simulation of structural fabric undergoing ballistic impact. *Computer Methods in Applied Mechanics and Engineering*, 195(1-3):94–109, 2006.

Vita

Kwon Joong Son was born in Dangjin-gun, South Chungcheong Province, Republic of Korea, on June 12, 1978. He is the second of three children born to Gye Sung Son and Hei Kyoung Kim. After graduating from Chungnam High School in Daejeon, Korea, in 1996, he pursued his undergraduate education at Pohang University of Science and Technology (POSTECH) where he graduated in February 2003 with a Bachelor of Science degree in Mechanical Engineering. After working as a researcher at Advanced Materials Processing Laboratory in POSTCH for six months, he attended Carnegie Mellon University in 2003 and achieved a Master of Science degree in Mechanical Engineering in May 2005. In the same year, he entered the Graduate School of the University of Texas at Austin to pursue a Ph.D degree in Mechanical Engineering. He received POSTECH General Scholarship (1996-1998, 2001-2002) and POSTECH Honor Scholarship (2001) for his academic accomplishments during his undergraduate studies. He received the KOSEF Korea Science and Engineering Foundation (KOSEF) Scholarship (2003 - 2005), the University of Texas Preemptive Fellowship (2005-2006), and a student scholarship sponsored by the Zienkiewicz Foundation to support for conference participation in the 8th World Conference on Computational Mechanics (July 2008). He has been married to Ji hyun Park since July 17, 2007.

Permanent address: 164-1 Munhwa-1-Dong Jung-Gu, Daejeon
301-131, Republic of Korea

This dissertation was typeset with LaTeX[†] by the author.

[†] LaTeX is a document preparation system developed by Leslie Lamport as a special version of Donald Knuth's TeX Program.